X-RAY INVESTIGATION OF DEFECTS IN III-NITRIDES AND THEIR ALLOYS

Zur Erlangung des akademischen Grades eines
DOKTORS DER NATURWISSENSCHAFTEN
von der Fakultät für Physik des
Karlsruher Instituts für Technologie (KIT)

genehmigte

DISSERTATION

von

M.Sc. Sergey Lazarev
aus Petropavlovsk, Kazakhstan

Tag der mündlichen Prüfung: 06.12.2013
Referent: Prof. Dr. Gerd Tilo Baumbach
Korreferent: Prof. Dr. Václav Holý

ACKNOWLEDGMENTS

Firstly, I would like to thank my mother, Lazareva Marina, and my aunt, Voloshuk Oksana, who raised me with all the patience they could muster and gave me this opportunity to reach the high level of education I have been fortunate enough to receive. I would also like to express my gratitude to my physics teacher in high school, Mrs. Alimova Rachima, to whom I owe my heartfelt gratitude for guiding me towards choosing physics as the main direction in my life.

I especially wish to thank my supervisor, Prof. Dr. Tilo Baumbach, for his constant support while I was writing my Ph.D.

I would also like to extend my sincere thanks and great respect to my second supervisor, Dr. Sondes Bauer, who spent many hours, days and weeks working with me on these various projects, the results of which are presented here in this work. Moreover, I would like to thank her for all her personal support and encouragement throughout the time I was preparing my doctorate, for organizing the micro-focus experiment at the NANO beamline at the synchrotron ANKA, Karlsruhe, Germany and for the many scientific discussions we enjoyed together.

Furthermore, I would like to thank Prof. Dr. Ferdinand Scholz and his group from Ulm University and Dr. Kamran Forghani for his generous and fruitful collaboration, for our many scientific discussions, and for providing the samples investigated in this thesis.

I am also very thankful to Prof. Dr. Vaclav Holy and Dr. Mychailo Barchuk from Charles University in Prague, for our effective collaboration and many scientific discussions.

I would like to thank Dr. Daniil Grigoriev, with whom I studied the theory of X-rays and various X-ray diffraction techniques.

My thanks also goes to Dr. Gernot Buth for his support during the beamtime at the SCD beamline at synchrotron ANKA.

Lastly, I would like to extend my thanks to Dr. Taras Slobodskyy and Dr. Andrey Minkevich, for their help at the beginning of my study for my Ph.D. I must also thank the many other people who have played both an important role in my life and have helped me on the way to preparing this doctorate, but who I have failed to mentioned here.

Contents

1 Introduction

1.1 Motivation behind the research

Group III-nitrides such as GaN, AlN, InN and their compounds, are attractive semiconductor materials for high-power, high-frequency and high-temperature electronic applications, due to their excellent structural properties and high levels of thermal and chemical stability compared to other group III-V compound semiconductors [1].

III-group nitrides have band gaps of 0.7 eV (InN) to 3.4 eV (GaN) to 6.0 eV (AlN) [2], with a high breakdown of voltage and a high electron mobility [3]. Ternary alloys, based on group III-nitrides, allow for the tuning of the band gap, ranging from near infrared (IR) to deep ultraviolet (UV) regions, which enables the emission of deep ultraviolet ($\lambda \leq 300$ nm or photon energy ≥ 4.1 eV based on high Al content $Al_xGa_{1-x}N$ quantum wells (QWs)), ultraviolet ($\lambda \leq 400$ nm or photon energy ≥ 3.1 eV), blue ($\lambda \approx 455$ nm or photon energy $= 2.7$ eV based on $In_yGa_{1-y}N$ QWs), green ($\lambda \approx 525$ nm or photon energy $= 2.4$ eV) emitters based on $In_xGa_{1-x}N$ QWs, and longer wavelength light-emitting diodes (LEDs) and violet and blue laser diodes (LDs). Comparison of the band gaps of the III-nitride materials and binary cubic semiconductors versus their lattice constant at 300 K are presented in the fig.1 [4, 5], shows that no other material systems could offer such large range of direct band gaps [6]!

III-nitrides have direct band gap [2], meaning that the momentum of electrons and holes is the same for both the conduction band and the valence band. An electron can emit a photon directly but not transfer momentum to the crystal lattice. Thus, they are well suited not only for optical emitters spanning the entire visible spectrum but they can also be used for the absorption of photons over a large wavelength range, which makes them attractive candidates for solar cell applications. Moreover, InN has a small band gap, which also boasts the smallest electron effective mass and highest carrier mobilities among the III-V nitrides. As such, it also makes an exciting material for high-speed electronic devices. The reason for the development of nitrides as an optoelectronic material is that there are no alternative ultraviolet, blue LDs and green LEDs based on other semiconductor materials (InGaAlAs, ZnMgS, ZnMgSe, AlGaP, etc.) which are as efficient. Moreover, these have limited lifetimes due to the dislocation generated in the areas where they are active [7].

As a result of their optoelectronic properties, group III-nitrides have attracted much attention over the last two decades.

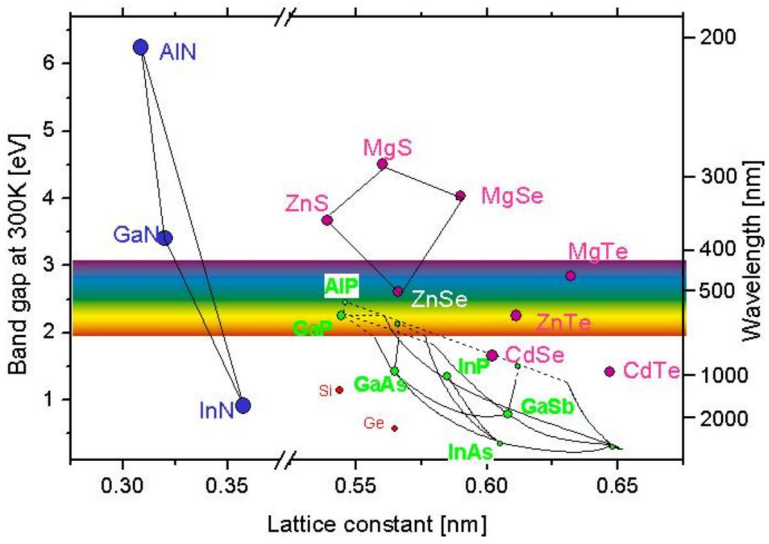

Figure 1: Band gaps of different compound semiconductors, plotted against their lattice constant. The right-hand scale gives the light wavelength that corresponds to the band gap energy, taken from [4].

1.2 The problem with III-nitrides

The problem with III-nitrides relates to two areas:

a) the decrease in Al(In)GaN alloys optoelectronic efficiency with a corresponding increase in Al(In) content due to defects formation;

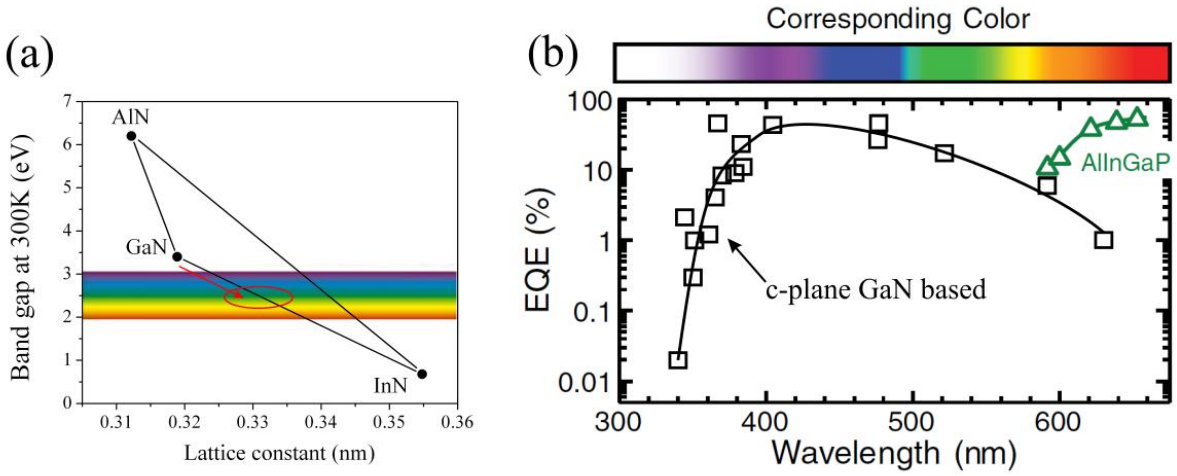

Figure 2: InN, GaN and AlN band gap triangle (a) and external quantum efficiencies of GaN-based and AlInGaP-based materials (b), taken from [6].

b) a reduction of optoelectronic devices based on GaN efficiency due to internal polarization. This is, known as the quantum-confined Stark effect.

The following sub-chapter sets out to investigate these issues in greater detail.

1.2.1 Decrease in Al(In)GaN alloy optoelectronic efficiency as the content increases

The growth of high quality AlN and InN is a challenging task since these are more mismatched in terms of lattices to the traditional substrata used for nitride growth, such as sapphire or SiC, as opposed to GaN [6, 8]. This lattice mismatch leads to the formation of dislocations, the result of which decreases the efficiency of the devices based on group III-nitrides. However, the efficiency of LED can be shown by applying external quantum efficiency (EQE) methods i.e. the fraction of injected electron-hole pairs that form a photon that can escape from the semiconductor (the highest possible EQE being 100%). Fig.2.b summarizes the dependence of the EQE on GaN-based LEDs and AlInGaP materials [6]. As expected, the EQE has a maximum of 400 nm, which corresponds to the emission wavelength of GaN. See fig.2.b.

When Al is incorporated into the GaN, the photons emitted by the AlGaN are able to reach a UV range with a wavelength of less than 400 nm. The EQE device decreases as the Al content increases because of the formation of dislocations due to this lattice mismatch. To produce the LED in a visible spectrum, either the InGaN or the AlInN should be grown on a Si or sapphire substrate. With this lattice mismatch, it is preferable to grow InGaN on sapphire, as this contains a lower lattice mismatch. See fig.2.a. The EQE of the InGaN-based materials also decreases as the content increases (the wavelength of the light emitted increases). By using AlInGaP materials, the spectrum in the red part can be covered with greater efficiency than that of the InGaN. However, the minimum of EQE corresponds to the range of green and yellow lights. Moreover, the drop in efficiency, known as the "efficiency droop" brought about with a high injection current density in this part of spectrum is known [5]. Therefore, there are still many challenges remaining for the highly efficient, bright LEDs in the green region of the optical spectrum. In scientific literature this problem is known as the "green gap" problem [9, 6].

1.2.2 Decrease in III-nitrides optoelectronic efficiency due to internal polarization fields

Most standard optoelectronic devices are generally based on (0001) III-nitride (c-oriented) films since the growth speed is higher and the lattice mismatch lower in the c-orientation in GaN [7, 10]. However, the wurtzite (hexagonal) structure is non-centrosymmetric (i.e. absence of inversion symmetry); it is polar with the polarization occurring parallel to the –c-axis [11, 6], as shown in fig.3.a.(above). Therefore, the two oppositely charged "-Ga" and "+N" faces are formed in the layer. As for GaN (and similarly for AlN and InN) the metal-terminated (0001) surface has a negative fixed polarization sheet of charge [6], see fig.3.a.(below).

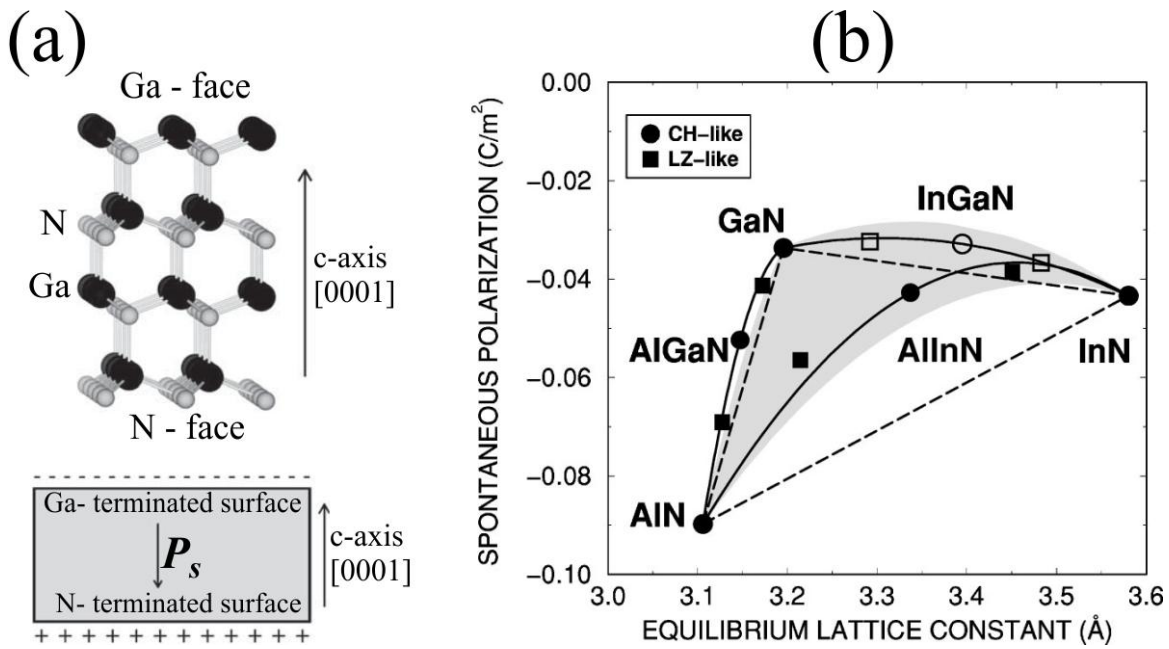

Figure 3: (a) Ball-and-stick model of the wurtzite GaN crystal structure (upper schema). The gallium atoms are represented as large dark spheres and the nitrogen atoms as small light spheres. The upper face of the crystal (0001) also is referred to as the gallium face. The bottom schema depicts a slab of GaN, with the (0001) surface at the top showing negative fixed polarization charges; while the bottom shows a $(000\bar{1})$ nitrogen face with positive fixed polarization charge. Fig.(b) shows spontaneous polarization as against the lattice constant equilibrium, as taken from [13].

The built-in electric field should be evaluated by accounting for the accumulation of a polarization charge at the interfaces between the GaN/AlGaN and GaN/InGaN heterostructures. The total polarization charge can be written as [12]:

$$P_{tot} = P_p + P_s, \tag{1}$$

where P_p is the piezoelectric charge caused by the lattice mismatch and by the strain (thermal strain) and other mechanical deformations of the crystal. P_s represents the spontaneous polarization charge of the GaN/Al(In)GaN interface, as clearly demonstrated by the works of Bernardini et al. [13, 14, 15]. The polarization discontinuities at interfaces in the III-nitride-based heterostructures grown along the [0001] direction, which induces a strong electric field, leading to the so-called quantum-confined Stark effect (QCSE).

Bernardini et al. [13] have calculated the spontaneous polarization and piezoelectric constants for GaN, AlN and InN, as shown in the tab.1. In addition, Bernardini has shown that piezoelectric polarization is also clearly non-linear [15, 13], as shown in fig.3.b.

	P_s, C/m^2
AlN	-0.081
GaN	-0.029
InN	-0.032

Table 1: Calculated spontaneous polarization of III-V wurtzite nitrides [13].

For LEDs (e.g., based on GaN barriers and $In_xGa_{1-x}N$ QWs), the fixed sheet charges at the heterointerfaces cause large electric fields which is perpendicular to the quantum well (QW) plane (fields on the order of 1 to 2 MV/cm depending on the InN molar fraction x). These internal polarization-related electric fields cause a spatial separation between the electron and hole wave functions. In the fig.4.a the separation of the electron and hole wave functions is shown as polar oriented $GaN/In_{0.10}Ga_{0.90}N$ (2.5 nm)$/GaN$ QW [6].

When the electron and hole wave functions are spatially separated due to the internal polarization-related electric field in the QW (QCSE), the likelihood that a radiative recombination event would yield the desired photon, is

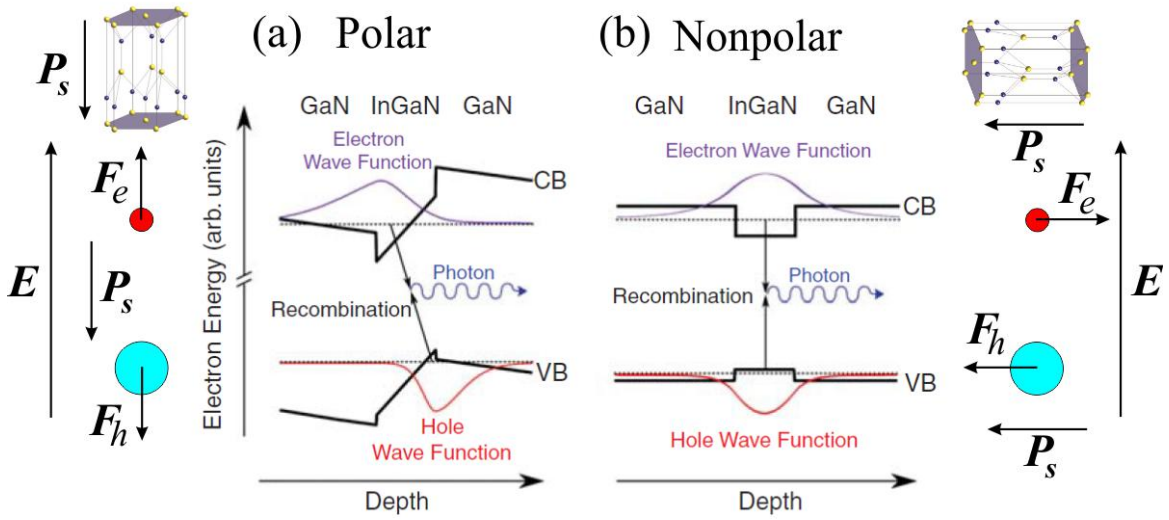

Figure 4: Self-consistent Schroedinger-Poisson solutions for the band profile (conduction band [CB] and valence band [VB]) for the $GaN/In_{0.10}Ga_{0.90}N(2.5\,\mathrm{nm})/GaN$ quantum well (QW) for the conventional polar (0001) Ga-face orientation (a). Non-polar orientation corresponds to either a-plane or m-plane orientation (b) [6].

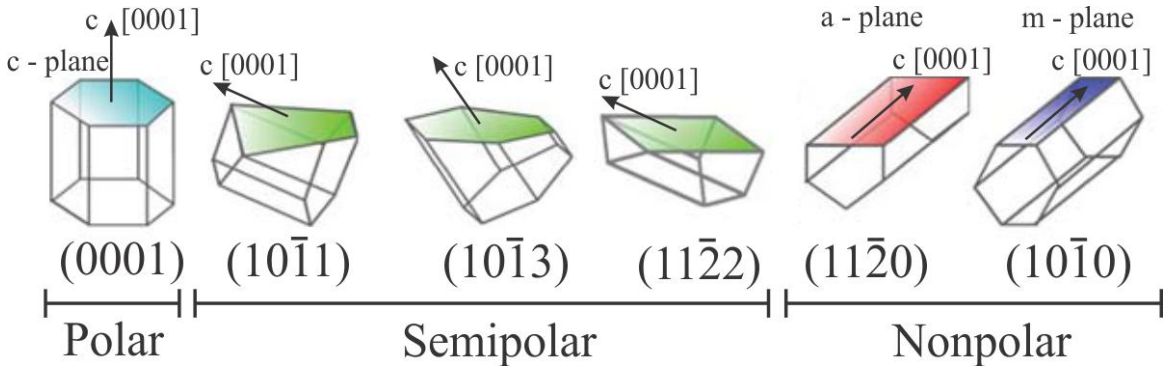

Figure 5: Polar, semipolar and nonpolar III-nitrides unit cell orientations.

reduced, thus increasing the likelihood that the injected electrons or holes would recombine non-radiatively (Auger recombination) and that the energy would be expended as heat [16].

For long-wave length emission of GaN based devices, high indium concentrations are required. This gives rise to strain in the piezoelectric GaN material because of the significant lattice mismatch between GaN and the active InGaN quantum wells. The outcome is high level internal electric fields with a drastic drop in efficiency [17].

However, III-nitrides can be grown when crystallographic orientations of the sample surface are altered or different. Due to the polarization properties of the cell unit along c- direction the surface orientations are split into three groups: polar, semipolar and nonpolar, as it is shown in the fig.5. The position of the c - orientation defines the surface. The sample grown in c-direction ([0001] perpendicular to the surface), with the surface (0001) is polar, see fig.5. There is only one c-plane polar orientation of the WZ structure.

If the position of with respect to the surface is inclined, the $(hkil)$ plane of the surface should have a nonzero h or k index and a nonzero l index and the sample semipolar, see fig.5. There are three common semipolar surface orientations: $(10\bar{1}1)$, $(10\bar{1}3)$ and $(11\bar{2}2)$. If the c-direction is lying in the sample surface, this means that the $(hkil)$ plane of the surface has index $l = 0$ and that the surface orientation is nonpolar. See fig.5. There are two common nonpolar surface orientations: $(11\bar{2}0)$ a-plane and $(10\bar{1}0)$ m-plane.

Nonpolar orientation	Mismatch, %	N (nm)	1/N ($10^5 cm^{-1}$)
a-GaN $\perp$(0001)	16.1	1.7	
a-GaN $\parallel$(0001)	1.2	23	4.3
m-GaN $\perp$(0001)	26	0.6	
m-GaN $\parallel$(0001)	9	2.85	35

Table 2: In-plane lattice mismatches of nonpolar a-GaN with r-sapphire and m-GaN with m-sapphire along the two main perpendicular in-plane directions. N is the distance between interfacial misfit dislocations necessary for a full relaxation. The expected densities of misfit dislocations (1/N) along [0001] direction are also given [20].

1.3 Nonpolar GaN films on sapphire substrate

The growth of GaN along nonpolar directions is expected to improve the efficiency of LEDs [18]. In 2000, Waltereit et al demonstrated the absence of internal electric fields in m-plane GaN QWs with AlGaN barriers [19]. Due to the crystal symmetry, there is no polarization discontinuity at the heterointerface and the wave functions of the electron and the hole overlap, as shown in fig.4.b.

The nonpolar GaN is grown mainly with $(10\bar{1}0)$ m-plane surface orientation on $(10\bar{1}2)$ r-sapphire or with $(11\bar{2}0)$ a-plane surface orientation on $(10\bar{1}0)$ m-sapphire [6]. The in-plane lattice mismatches between GaN and sapphire are different for different orientations in surface plane. In the tab.2 the in-plane lattice mismatches parallel and and transverse to [0001] direction are summarized [20]. The mismatches are higher for m-GaN. Additionally to the mismatches, the distance N between interfacial misfit dislocations necessary for a full relaxation, and expected densities of misfit dislocations $(1/N)$ along [0001] direction are presented.

In case of polar surface orientation of the GaN, lattice mismatch leads to the formation of misfit dislocations, which than propagate as threading edge and screw dislocations. For nonpolar GaN material grown on foreigner substrate, lattice mismatch influences on the [0001] in-plane crystallographic orientation, which is close parked direction for *hcp* structure. The misfit dislocations are formed as partial dislocations, produce mistakes in the atomic layers packing and begin the formation of two dimensional defects known as basal plane stacking faults (BSF). The BSF density is expected to be in the same order of magnitude as misfit dislocations $(1/N)$ in [0001] direction necessary for a full relaxation. Therefore, from the tab.2 one can predict higher BSF density in m-GaN films.

In spite of absence of polarization fields influence of caries recombination in nonpolar GaN and reduction of pure edge, screw and mixed dislocation densities in comparison with polar GaN [21], huge amount of BSFs with a typical density in the range $10^5 cm^{-1}$ to $10^6 cm^{-1}$ is found [22]. Since BSFs are two dimensional defects, they significant influence on optoelectronic devices efficiency reduction [8].

1.4 Semipolar GaN films on sapphire substrate

Despite of the reduction in polarization fields in nonpolar GaN, the BSFs density is considered to be high. Therefore, other crystallographic orientations should be considered. The fig.6 shows the spontaneous polarization discontinuity $P_\perp$ and wave function overlap for 3 nm wide $Ga_{0.75}In_{0.25}N$ quantum well layer coherently strained to GaN for crystallographic orientations ranging from the polar c-plane ($\theta = 0°$) to nonpolar ($\theta = 90°$) [9]. There is a zero crossing in the total polarization discontinuity at $\theta = 45°$ orientation and significantly reduced polarization discontinuity at inclination angles of $\theta \approx 60°$, which are close to two low-index semipolar orientations, $(10\bar{1}1)$ and $(11\bar{2}2)$, with $\theta = 62.3°$ and $\theta = 58.4°$, respectively.

Therefore, one can grow the semipolar GaN films with $(10\bar{1}1)$ and $(11\bar{2}2)$ surface orientation on sapphire [23]. However, the growth speed depends on the crystallographic orientations (see Chapter 2.2). For the semipolar GaN growth in surface direction is combined by growth in two orientations $[10\bar{1}0]$ or $[11\bar{2}0]$ and [0001] c-direction for $(10\bar{1}1)$ and $(11\bar{2}2)$ semipolar, respectively. The growth in c [0001] direction is faster and growth of $(10\bar{1}1)$ or $(11\bar{2}2)$ surfaces has three dimensional mode, and therefore leads inhomogeneous and rough surface.

To solve the problems with growth speed and quality of the layer semipolar film could be grown in the sidewalls of patterned sapphire substrates (PSSs) [9]. During this growth, sapphire substrate is etched to organize c-plane-like sapphire sidewalls, see fig.7. This technique has been first proposed by Honda et al. [24] to grow semipolar GaN planes on Si and later applied to various directions of GaN by Okada et al. [25, 26, 27].

The structure could be grown with or without SiO_2 mask using selective area growth in c-direction on the c-plane-like sapphire sidewalls. The direction of the growth is shown in the fig.7. When the GaN grows out of the trench, it will continue to grow laterally over the ridges separating the trenches in "+c" - [0001] direction

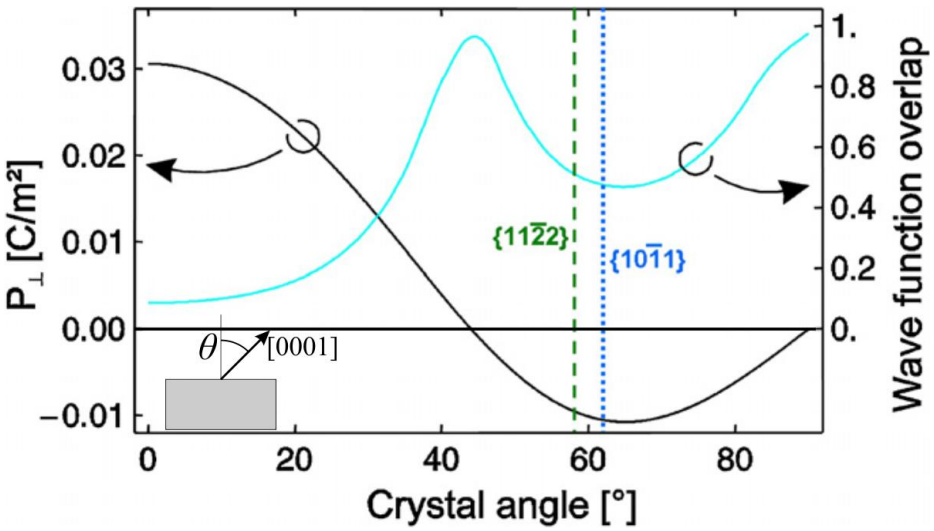

Figure 6: Piezoelectric polarization (left axis) and wave function overlap of the electrons in the conduction band and the holes in the valence band (right axis) in a 3 nm wide $Ga_{0.75}In_{0.25}N$ quantum well pseudomorphically strained with respect to GaN barriers as a function of the angle between substrate normal and the nitride c-axis. a- and m-plane quantum wells are at the right end of the diagram (90°); some semipolar planes are indicated by vertical lines around 60°, taken from [9].

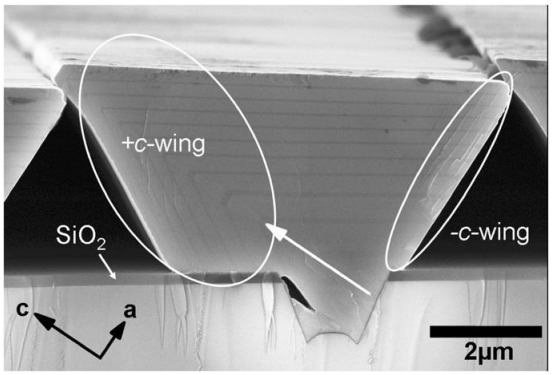

Figure 7: SEM micrograph of GaN stripes nucleated from the c-plane-like sidewall of grooves etched into r-plane sapphire, taken from [9].

organizing "+c" wing and in "-c" - [000$\bar{1}$] direction forming "-c" wings. Later the GaN blocks coalesce to a closed layer. Depending on etching process and orientation of sapphire substrate the semipolar (11$\bar{2}$2) or (11$\bar{2}$2) GaN could be grown.

In the initial stages of growth, influence of the lattice mismatch between sapphire trench bottom and GaN, leads the defects formation. Hence, the "-c" wings are dislocation rich (especially BSF rich), unlike the "+c" wings are dislocation free. A known method to reduce defects in GaN is the in-situ integration of SiN interlayers during crystal growth. This method could be adopted to the PSS semipolar GaN structures. The SiN mask could be deposited in the early stages of growth in "-c" wing in order to reduce the defect density (BSF density) [9].

The relation between dislocation density and polarization in GaN with different surface orientation could be summarized in four LED GaN/sapphire heteroepitaxial structures shown in the fig.8. The threading dislocations (TDs) are shown as black curved lines, and BSFs as yellow straight lines. An energy diagram drawing is shown on the right side of InGaN QWs for each structure (see fig.8).

In case of polar c-plane GaN on c-plane sapphire fig.8.a, the mismatch leads big number of threading dislocations, and polarization shift wave functions of electron and hole. For nonpolar a-plane GaN grown on r-plane sapphire fig.8.b, the polarization problem is solved, but additionally to TDs the BSFs are formed perpendicular to the surface. The semipolar (11$\bar{2}$2) GaN on m-plane sapphire fig.8.c decrease the polarization and BSF density, but their surface

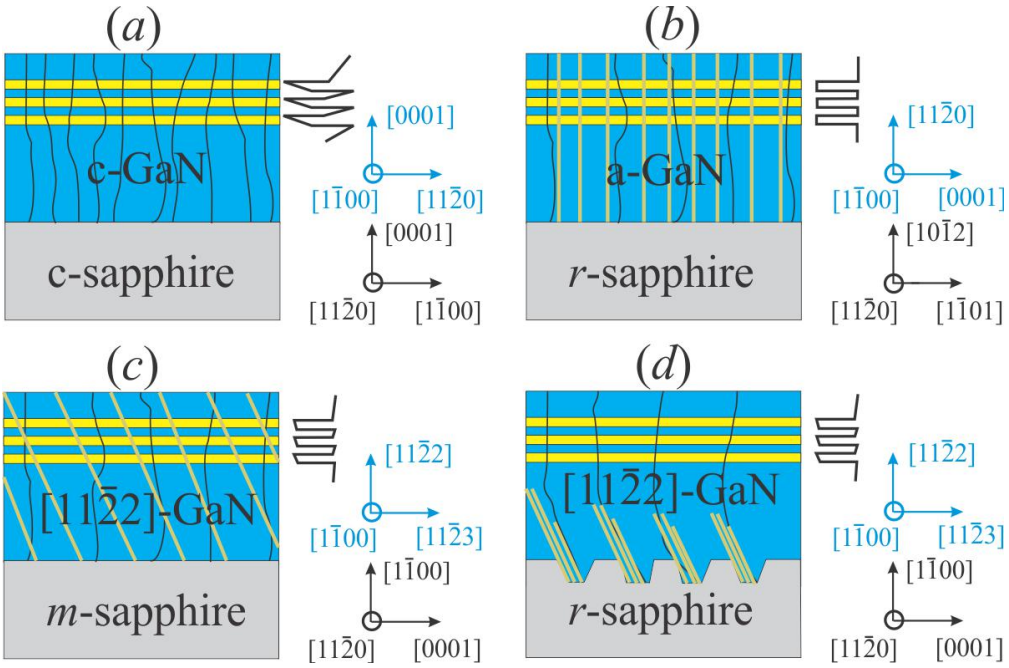

Figure 8: Schematic LED based on polar c-GaN (a), nonpolar a-GaN (b), semipolar (11$\bar{2}$2) GaN (c), and PSS semipolar (11$\bar{2}$2) GaN.

is relatively rough. And the best quality with decreased polarization is expected for semipolar (11$\bar{2}$2) GaN grown on patterned r-plane sapphire fig.8.d.

The PSS semipolar GaN samples grown in (10$\bar{1}$1) and (11$\bar{2}$2) directions will be investigated in this work. Additionally, the influence of SiN-mask on the BSFs density reduction will be studied.

1.5 Aims of the research

The main aim of this research is to present a comprehensive study of the dislocations and stacking faults in III-nitrides. The influence of the growth parameters and SiN mask intercalation on structural defects density has also been investigated in order to explore the optimization of the III-nitrides growth process and an increase in EQE in optoelectronic devices, based on GaN materials in the ultraviolet and visible spectrum of light.

Further to this, the threading dislocations in $Al_{0.2}Ga_{0.8}N$ epilayers with different layer thicknesses will be studied in Chapter 6. Stacking faults in semipolar (10$\bar{1}$1) and (11$\bar{2}$2) GaN layers with and without a SiN mask, grown on patterned sapphire substrata, will be investigated in Chapter 8.

Structural defects are investigated in the work, and introduced in Chapter 3, using mainly a non-destructive X-ray diffraction method that allows ex-situ and in-situ investigation of crystalline structures. The diffuse X-Ray scattering, which results from defects enables defect density determination using different models, is described in Chapter 4. Traditional Williamson-Hall plots and more sophisticated Monte Carlo based simulations will be used in Chapter 6 to determine the density of the threading dislocation in $Al_{0.2}Ga_{0.8}N$ epilayers with different layer thicknesses and to establish the variations according to the thickness of layers in dislocation density.

In Chapter 8, the density of the stacking faults of the basal plane in semipolar (10$\bar{1}$1) and (11$\bar{2}$2) GaN layers that are derived from the width and numerical simulation of the intensity distribution and the dependence of crystallographic orientation of the layers and the SiN mask intercalation on structure perfection, will also be examined. In addition, an investigation of local distribution of stacking faults in semipolar (10$\bar{1}$1) GaN will be investigated in Chapter 8.10 and the influence of the SiN mask demonstrated.

2 Growth and characterization of III-nitrides

2.1 Structure and physical properties of III-nitrides

2.1.1 III-nitrides unit cell and physical properties

Group III-nitrides can exist in three crystal structures: wurtzite (WZ), zincblende (ZB) and rocksalt crystallographic modifications [2]. In rocksalt structure (with space group $Fm\bar{3}m$) they can be possibly grown only under very high pressures of 22.9 GPa for AlN, 52.2 GPa for GaN and 12.1 GPa for InN. Therefore, rocksalt group III-nitrides cannot be produced by any epitaxial growth [2]. In cubic ZB structure or β- phase (space group $F\bar{4}3m$) the primitive unit cell contains two atoms. The ZB III-nitrides are metastable structures and can be stabilized under specific growth conditions such as on some suitable substrates [2].

In hexagonal WZ structure or α- phase (space group $P6_3mc$) the primitive unit cell is a parallelepiped and contains four atoms (two group III- and two nitrogen atoms) [2], as depicted in the fig.9.a. Each atom in the structure can be seen as located at the center of a tetrahedron with its four nearest atomic neighbors of the other type at the four corners of the tetrahedron as depicted in the fig.9. The wurtzite structure consists of two interpenetrating hexagonal close packed (hcp) sublattices, one of group III-atom lattice and another of nitrogen-atom lattice. Each lattice displaces from the other along the c-axis ideally by 3/8 of the cell height, (3/8c), related to u- parameter. The internal parameter u of the cation-anion bond length ratio along the c-axis in a unit of c is shown in the fig.9.b. In an ideal wurtzite crystal, the c/a ratio is 1.6330 and u- parameter is 0.375. The group III-nitrides and their alloys in hexagonal (WZ) have the thermodynamically most stable structure. Thus, in this work we will focus mostly on the wurtzite GaN and its compounds. Many slightly different unit cell parameters in lateral and vertical directions at room temperature are known from the literature [8]. However, the average parameters for the wurtzite GaN, InN and AlN are summarized in the tab.3 [28].

There are several equivalent ways to define the unit cell. For the purposes of this investigation the structures will be defined as follows: the shape of the wurtzite cell is a vertically oriented prism, with the base defined by the primitive lattice vectors **a** and **b** which are of equal lengths and are separated by an angle of 60°. The height of the cell is defined by the vector **c**. which is oriented vertically at 90° to both **a** and **b**. In the "ideal" wurtzite structure $a = b$ and c is related to a as:

$$c = 2\sqrt{\frac{2}{3}}a \tag{2}$$

To specify the positions of atoms within the cell the fractional coordinates are usually used for convenience. If a point **r** has Cartesian coordinates (x, y, z), then its fractional coordinates [x', y', z'] are defined as:

$$\mathbf{r} = x'\mathbf{a} + y'\mathbf{b} + z'\mathbf{c} \tag{3}$$

The Ga atoms are positioned in the corners of the unit cell parallelepiped (one is at the origin [0, 0, 0]) and an atom at [$\frac{1}{3}$, $\frac{1}{3}$, $\frac{1}{2}$]. The N atoms are placed directly above the Ga atoms and shifted in c direction in u. So, for [0, 0, 0] and [$\frac{1}{3}$, $\frac{1}{3}$, $\frac{1}{2}$] Ga atoms, N atoms have coordinates: [0, 0, $\frac{3}{8}$] and [$\frac{1}{3}$, $\frac{1}{3}$, $\frac{7}{8}$], see fig.9.a.

The shape of the primitive two-atom ZB cell is an equal-sided parallelepiped that can be most easily visualized by a larger 8-atom cubic cell. This cubic cell has Ga-atoms at the origin and in the center of each of the three faces that touch the origin. Each N-atom is shifted with respect to Ga-atom at a displacement of [$\frac{1}{4}$, $\frac{1}{4}$, $\frac{1}{4}$]. The lattice vectors defining the primitive cell are the three vectors going from the origin to the center of the three faces where the Ga-atoms are located. These vectors are of equal length and are separated from each other by angles of 90°. The three Ga-atoms on the faces of the cube are not in the primitive cell as they are simply the periodic repetitions of the atom at the origin. The primitive cell thus contains a Ga-atom at [0, 0, 0] and N-atom at [$\frac{1}{4}$, $\frac{1}{4}$, $\frac{1}{4}$].

Crystal	a, nm^{-1}	c, nm^{-1}	a/c	u	E_g(eV), [29]
AlN	3.122	4.982	1.601	0.380	5.1
GaN	3.189	5.186	1.626	0.376	3.51
InN	3.548	5.760	1.623	0.377	0.76[30]
Sapphire	4.758	12.991			

Table 3: III-nitrides unit cell parameters.

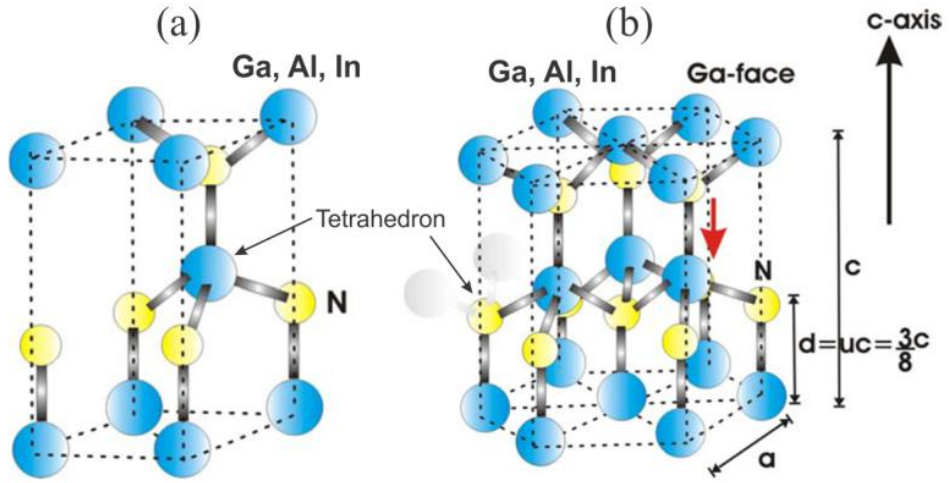

Figure 9: A stick-and-ball stacking model of wurtzite structure unit cell of (Ga, Al, In)N (a) and wurtzite structure of (Ga, Al, In)N (b), taken from [2].

Miller	Miller-Bravais	Meaning
203	$20\bar{2}3$	Reflection
(203)	$(20\bar{2}3)$	Plane
203	$\{20\bar{2}3\}$	Family of planes
[203]	$[20\bar{2}3]$	Directions
$\langle 203 \rangle$	$\langle 20\bar{2}3 \rangle$	Family of directions

Table 4: Miller and Miller-Bravais indexation of a reflection, plane, direction and their families.

2.1.2 Crystallographic directions in III-nitride crystals

For WZ hexagonal crystal systems, a Miller-Bravais or four-index $(hkil)$ notation is often used instead of Miller or three-index (hkl) notation [31]. The additional redundant index i, equal to $-(h+k)$, helps to show the equivalency of crystallographic planes such as $(11\bar{2}0)$ and $(\bar{2}110)$ [8]. Sometimes for simplicity instead of additional redundant $-(h+k)$ index, "dot" sign $hkil \Longleftrightarrow hk.l$ could be used ("dot" sign is kept to underline the hexagonal unit cell). A summary of notation conventions is given in the tab.4, and in the work reflections are marked as $hk\bar{i}l$, planes as $(hk\bar{i}l)$ and directions as $[hk\bar{i}l]$ [8] (see tab.4).

The unit cell of WZ structure with crystallographic directions is shown in the fig.10.a and its (0001) basal plane in the fig.10.b. In the fig.10.a some common planes with their names are shown. The c- plane or basal plane is a plane (0001), a - plane $(11\bar{2}0)$, m - plane $(10\bar{1}0)$ and r - plane is inclined $(1\bar{1}02)$ plane (see fig.10.a).

2.1.3 Stacking sequences in III-nitrides structure

The crystal structures of a large number of materials and their alloys, including III-nitrides, can be described geometrically in terms of a close-packing of equal spheres, held together by interatomic forces. The close-packed arrangement of equal spheres in a plane is shown in the fig.11.a where each sphere is in contact with six other spheres. Since the symmetry of this layer is 6 mm, such a layer is called a hexagonal close-packed layer. Let this layer be called an A layer. The next spherical layer could be placed in two different positions depicted in the fig.11.a as B and C. Either B or C layer could be formed due to their intersection, as it is visible in the figure.

The identity period of the close-packed structure is determined by the number of layers after which the stacking sequence repeats itself. There are two most common close-packed structures which occur in nature. They have identity periods of two and three layers, and are shown in the fig.11.b and fig.11.c. The first one is hexagonal close-packing (hcp) with a layer stacking ABAB..., see fig.11.b. The second is the cubic close-packing (ccp) with a layer stacking ABCABC..., see fig.11.c.

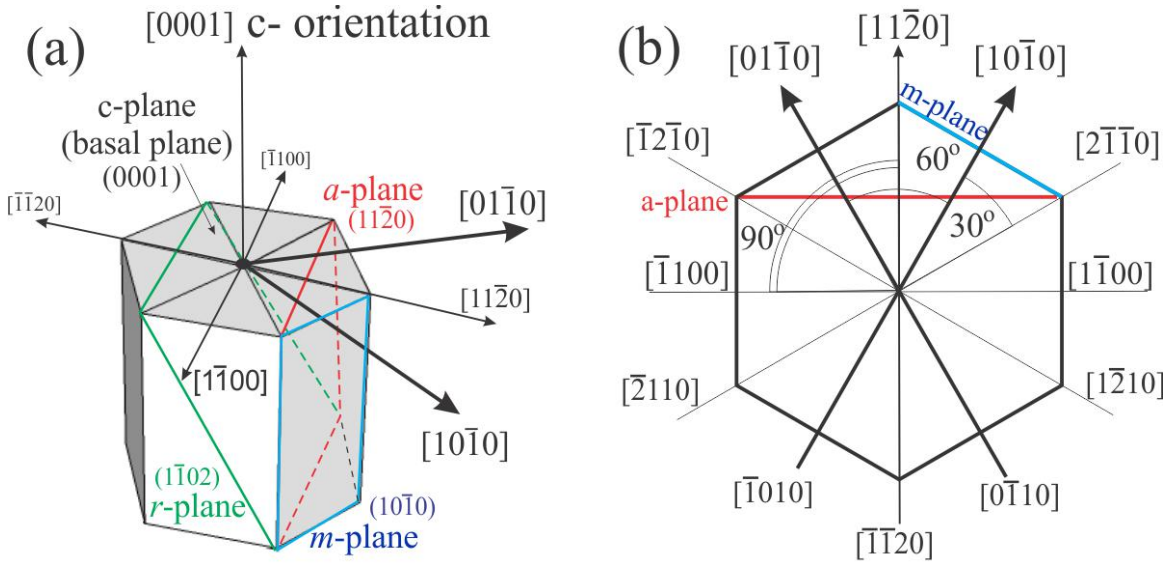

Figure 10: Hexagonal unit cell (a) and its basal plane (b) with crystallographic directions.

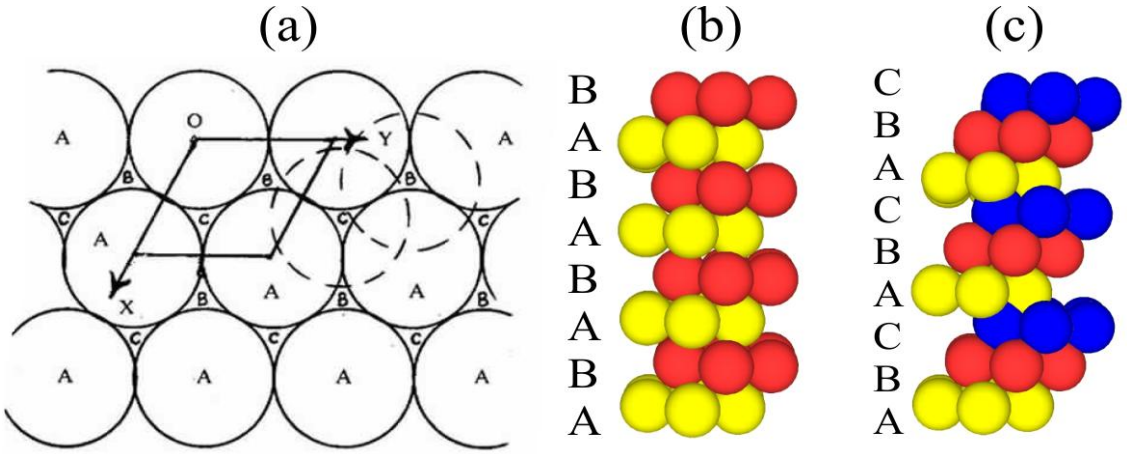

Figure 11: Close-packed arrangement of equal spheres in A, B and C layers (a), ABAB hcc structure (b), and ABCABC ccp structure (c).

ABC sequence	Ramsdell notation	Zhdanov number	h-c notation
AB	2H	(11)	h
ABC	3C	∞	c
ABCB	4H	(22)	hc
ABCACB	$6H_1$	(33)	hcc
ABCBAB	$6H_2$	(2211)	hchchh
ABACACBCB	9R	(12)	hhc

Table 5: Different notations for describing general close-packed structures.

2.1.4 Notations of close-packed structure

The close packed structures could be described in different notations. Krishna and Pandey [32] made complete summary of the different notations of the closed pack structures.

- The classical ABC notation:

As pointed out previously, the actual arrangement of layers in all close packed structures can be described in terms of the ABC notation for close-packing of spheres.

- Ramsdell's notation:

Close-packed structures can be designated by specifying the total number of layers in the hexagonal unit cell followed by the letter H, R or C to indicate the lattice type. Thus a symbol nH represents a structure with n layers in the primitive hexagonal unit cell while mR denotes a structure whose primitive lattice is rhomboidal and contains m layers in its hexagonal unit cell. In order to distinguish structures with same lattice type as well as the same repeat period along c, subscripts a, b, c or 1, 2, 3 are often used. This notation is applicable to all close-packed structures but it does not reveal the actual arrangement of the layers in the unit cell.

- Zhdanov notation:

The relationship between the three orientations, A, B and C of the close-packed layers may be visualized in terms of clockwise or counterclockwise rotation about [0001] through 60°. Hagg denoted the passage in clockwise direction A→B→C→A by a plus sign "+" and the passage in counterclockwise A→C→B→A by a minus sign "-". As structure such as ABCB is thus represented as ++−. No compactness results from the use of these "+" and "-" signs for representing a close-packed structure because their number remains the same as the number of layers in the ABC sequence of the structure. Therefore, Zhdanov suggested summing up the consecutive "+" and "-" signs and putting them down in numeral figures. Thus, the sequence ABCACB in Ramsdell notation 6H and a Hagg sequence +++— is denoted by the symbol (33) in the Zhdanov notation.

- The h-c notation:

In the h-c notation, one specifies each layer in terms of the orientation of layers above and below it. A layer is said to be in hexagonal configuration and is denoted as "h" if it is surrounded on either side by layers in similar orientations. A layer is said to be in cubic configuration and is denoted as "c" if it is surrounded on either side by layers in different orientations.

It is quite easy to transform from one notation to another. For this it is convenient to write first the complete ABC sequence.of the structure and then express this in the desired notation. The general close-packed structures expressed in different notations are listed in the tab.5.

2.2 Growth of III-nitrides

2.2.1 Introduction

The growth of III-nitrides with different crystallographic orientations can be performed on various foreigner substrates or III-nitrides substrates with different crystallographic orientations [8]. However, nonpolar and semipolar GaN bulk substrates are generally very small in size and expensive on account of the fact that, they are sliced vertically and cut at an angle from a thick c-plane GaN substrate [33]. Moreover, the speed of their growth depends on the crystallographic orientations, where the highest growth speed with minimum defects formation is observed for the c-direction. This requires the growth of polar GaN to take place on foreigner substrates. The common

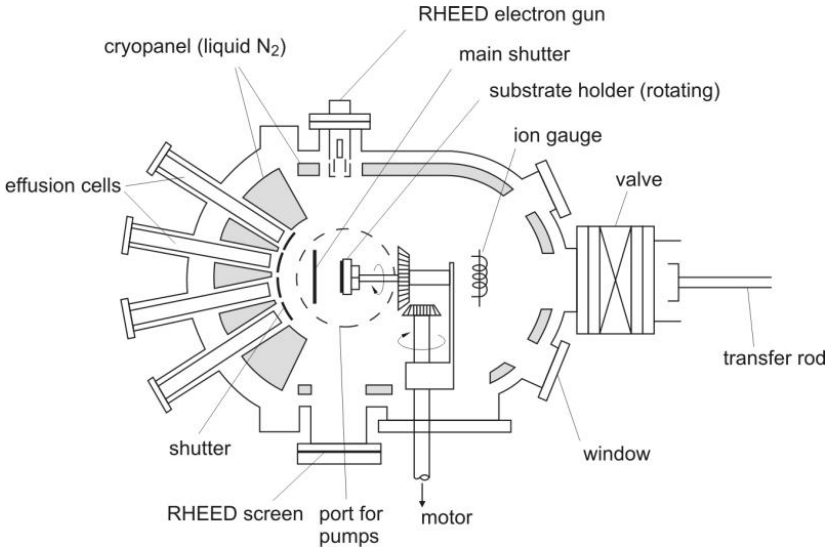

Figure 12: Schematic view of a MBE system from [35].

substrate for III-nitride growth is (0001) sapphire, which leads to epitaxial layer growth rotated by 30° with respect to sapphire [34].

Among all the techniques available for the epitaxial growth of III-nitrides, mainly metal-organic vapour phase epitaxy (MOVPE), hydride vapour phase epitaxy (HVPE) and molecular beam epitaxy (MBE) are used. These growth techniques will be discussed in greater detail below.

2.2.2 Molecular beam epitaxy

The molecular beam epitaxy (MBE) is ultrahigh vacuum (UHV) ($\sim 10^{-8}$ Pa) evaporation growth technique. In the MBE the elements of III-nitrides (Ga, Al, In and N) are heated in furnaces (effusion cells) and directed beams of atoms or molecules are condensed onto a heated single-crystal substrate where they react. The MBE growth is usually performed at relatively low temperatures of 650−800 °C. The growth of materials is operated by opening and closing effusion cells. During growth, reflection high energy electron diffraction (RHEED) is often used for monitoring the growth of the crystal layers. The RHEED use the high energy electrons diffraction and requires high vacuum. The view of typical MBE system is shown in the fig.12.

Typically, the growth rate employed is approximately $0.3-1\mu m/h$, although much higher growth rates can be obtained [3]. Under optimal conditions, the growth rates (in the order of 1 monolayer per second) are low enough to allow surface migration of the impinging species and smooth surfaces. The homogeneity of the deposited layers along the wafer can be improved adjusting the growth rate and the substrate holder rotation.

Growth of III-nitrides by MBE is a process capable for producing uniform epitaxy of diverse structures with abrupt interfaces and allows in-situ monitoring. However, the main disadvantage of MBE is a high cost and the limiting throughput of the process. Moreover, the MBE has the low growth rate which is not acceptable for the industrial production.

2.2.3 Metal organic vapour phase epitaxy

In this section, the growth of III-nitrides by metal organic vapour phase epitaxy (MOVPE) is shortly explained. To avoid confusion, it should be noted that the epitaxial technique MOVPE is also known by the acronyms MOCVD (metal-organic chemical vapour deposition) and OMVPE (organometallic vapour-phase epitaxy) [36].

The MOVPE is a process of an epitaxial deposition from gases on a hot substrate surface. The standard group III-precursors used in the MOVPE growth are: trimethylgallium (TMG) (C_3H_9Ga), trimethylaluminium (TMA) (C_3H_9Al), trimethylindium (TMI) (C_3H_9In), and ammonia (NH_3) is used as group V precursor. MOVPE growth of III-nitrides films performs at atmospheric pressure or low pressure of some ten Torrs. The precursors react at a substrate heated to roughly $1000°C$. To transport III-group precursors from bubblers to the substrate carrier gas N_2 or H_2 is used. The group III and V precursors are mixed up and injected to the substrate in the shower head. The unused reactants are transported out from the reactor. A typical MOVPE system (reactor) is presented in the

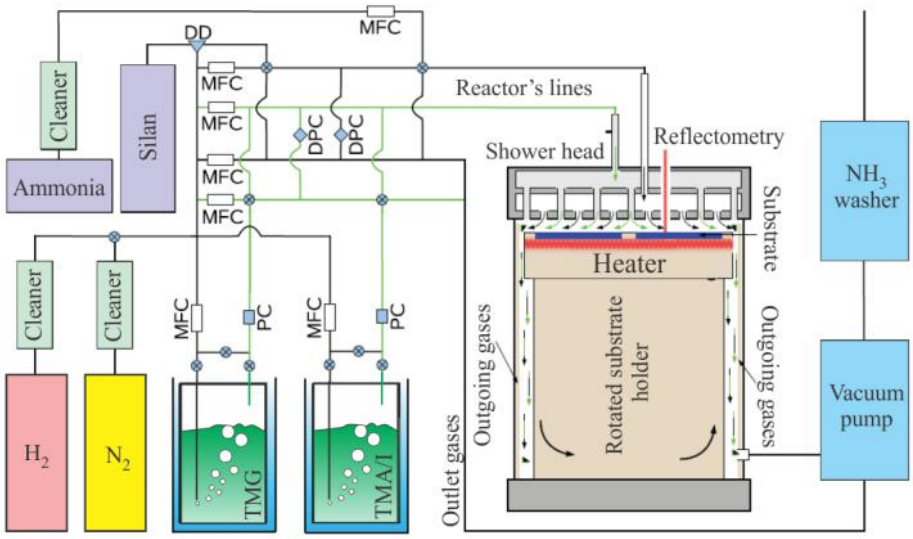

Figure 13: Scheme of a typical MOVPE reactor.

fig.13. There are different chemical processes are running in the reactor with certain probabilities, but nevertheless most important for III-nitrides growth are:

$$(CH_3)_3Ga + NH_3 \rightarrow GaN(s) \downarrow +3CH_4(g) \uparrow, \tag{4}$$

$$(CH_3)_3Al + NH_3 \rightarrow AlN(s) \downarrow +3CH_4(g) \uparrow, \tag{5}$$

$$(CH_3)_3In + NH_3 \rightarrow InN(s) \downarrow +3CH_4(g) \uparrow . \tag{6}$$

The growth process could be controlled by changing the pressure in reactor, temperature or ratio between III and V precursors (III/V ratio). Unlike the MBE system, RHEED is not suitable for in-situ monitoring of the growth rate in the high-pressure environment like MOVPE. RHEED requires a high electron mean free path, which can be achieved only in ultra high vacuum conditions. And growth rate is determined by normalized reflectometry.

The MOVPE is characterized by large-area growth capability, high surface mobility of the precursor gaseous molecules, good layer uniformity and precise control of the epitaxial deposition. Moreover, high purity, simple growth reactor, large scale production, possibility of selective growth, in-situ monitoring. These reasons together with the higher growth rate about tenth of $\mu m/h$ and even about $60\,\mu m/h$ [37], made the MOVPE to be the favorite growth method for industrial purposes and mass production.

Most of the samples studied in this work were grown by MOVPE.

2.2.4 Hydride vapour-phase epitaxy

Hydride vapour phase epitaxy (HVPE) is an epitaxial growth technique similar to MOVPE method, but with a number of basic differences. The growth of III-nitrides in HVPE is performed by chemical reaction between metallic sources of group III (Ga, Al, and In), HCl and ammonia at temperatures of 1000 - 1100°C and atmospheric pressure. The walls of reactor are heated to keep the constant temperature inside the growing chamber.

For III-nitrides HVPE growth $GaCl$, $AlCl$ and $InCl$ are typically used as III-group precursors, ammonia or nitrogen halide (NCl_3) as nitrogen sources and HCl, N_2 or H_2 as carrier gases [38]. The common chemical reactions in HVPE reactor lead to growth of III-nitrides are:

$$GaCl + NH_3 \rightarrow GaN(s) \downarrow +HCl(g) \uparrow +H_2(g) \uparrow, \tag{7}$$

$$AlCl + NH_3 \rightarrow AlN(s) \downarrow +HCl(g) \uparrow +H_2(g) \uparrow, \tag{8}$$

$$InCl + NH_3 \rightarrow InN(s) \downarrow + HCl(g) \uparrow + H_2(g) \uparrow . \quad (9)$$

The HVPE process is usually hold close to thermodynamic equilibrium whereas MOVPE growth is non-equilibrium. It yield higher efficiency of grown material usage. The high growth rate (about $1\,\mu m/min$) in HVPE does not allow to control the growth process [39].

Some difficulties during the growth process are related to strong thermodynamic propensity for GaN to form undesirable gas phase reactions and wall deposition due to their high temperature. Additionally, the HVPE reactor is destructing during the growth by highly corrosive HCl gas.

Thus, HVPE provides a simple, effective and large scale crystallization way to grow group III-nitrides, which is difficult to control during the growth. However, high growth rate leads decrease of material cracking grown on foreign substrates. It makes possible to grow low- defect and low-cost thick films of GaN or its compounds [39]. HVPE technique is often combined with epitaxial overgrowth by MBE and MOVPE. The layers grown in such way are shown comparatively low defect densities.

2.3 Defects in III-nitride crystals

2.3.1 Introduction

Crystalline solids are characterized by periodic crystal structures. In the ideal crystals, the atoms, ions or molecules (later in the work only atoms) form the periodic crystal lattice with fixed unit cell parameters. However, real crystals contain imperfections, known as crystallographic defects. Locally, these disturb the regular arrangement of atoms that break the perfect translational symmetry in the crystal. These imperfections can be classified according to their dimensional extension as point, line, planar or surface, bulk or volume defects. In turn, the presence of defects strongly affects the properties of crystalline solids.

2.3.2 Point defects

Point or zero-dimensional defects are defects that have the extension of a single atom and are formally limited to a single lattice site [40]. The point defects as native defects or intrinsic defects, are the most common defects occurring in semiconductors. They are important for the electrical and optical properties of nitrides semiconductors. For example they influence the carrier lifetime and consequently the radiative quantum efficiency and the longevity of GaN-based lasers and light-emitting diodes [2]. There are three basic types of native points defects: vacancies (atom missing from lattice sites), antisites (cations sitting on anion sites or vice versa) and interstitials (additional atoms in between the lattice sites).

There are two common types of point defects in the crystal lattice: Frenkel and Schottky defects, see fig.14.a. In case of Frenkel defect atoms of the same type as the crystal lattice occupy non-lattice sites in the crystal structure. Since ionic crystals are forced to be charged neutrally, it can not come to a single point defect in these structures. The same atom thus creates both vacancy and interstitial called a Frenkel defect. The mechanism of Frenkel defect formation is shown in the fig.14.b.

Another possible defect configuration arises when oppositely charged ions leave their lattice sites, creating vacancies, known as Schottky defect. The scheme of Schottky defect formation is shown in the fig.14.c.

The point defects occur during growth, heating, doping, plastic deformation, in the process of crystal growth and as a result of radiation exposure. GaN is commonly assumed to contain a large density of point defects ($10^{16} cm^{-3}$). The point defects could be arranged in a larger dimensional defects such as line or planar defects. In the next sections these kinds of defects in semiconductor crystals will be described.

2.3.3 Line defects

2.3.3.1 Dislocations Linear or one-dimensional defects are defects in crystals, which sizes in one direction are much larger than the sizes in the other two directions. The line defects are also called dislocations. They represent the border areas of unfinished shift in the crystal.

The quantitative description of the dislocation is given by Burgers vector. Its atomistic definition is derived from the Burgers loop in the deformed and ideal crystal lattices. This is an arbitrary closed clockwise circulation around a dislocation as a vector chain of the basis vectors of the lattice. The second Burgers loop, plotted in the similar crystal lattice without any dislocation, is compared with the first loop. The difference between the starting and ending points in the intact crystal is called the Burgers vector **b** that describes the magnitude and direction of lattice distortion.

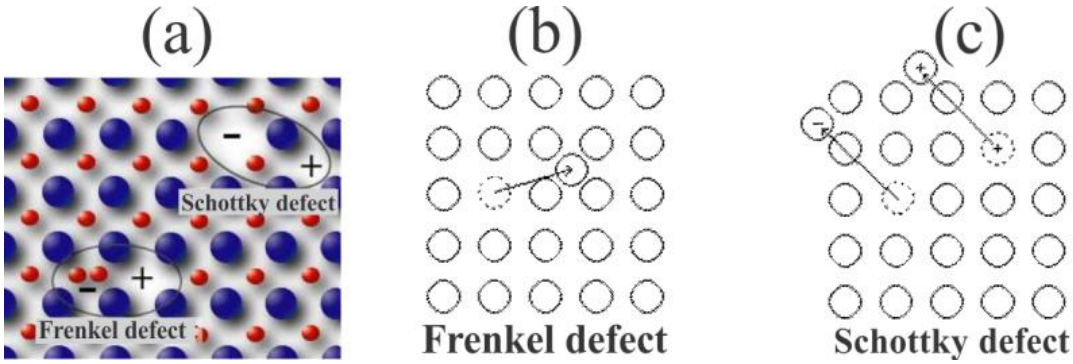

Figure 14: The Schottky and Frenkel defects in a crystal (a) and mechanisms of formation of Schottky (b) and Frenkel (c) defects.

Except the Burgers vector, every dislocation is characterized by the dislocation line, which is the line of the longest dimension, and the angle between the dislocation line and the Burger's vector, as it is illustrated in the fig.15.a. When $\varphi = 0°$ the defect is called a screw dislocation, and when $\varphi = 90°$ the defect is called edge dislocation, see fig.15.a. A schematic representation of an edge and a screw linear dislocations is illustrated in fig.15.b.

In case of $0° < \varphi < 90°$ the dislocation is called mixed and it can be decomposed into pure screw and pure edge components (see fig.15.a). The linear dislocations in real crystals are typically mixed [41].

An edge dislocation can be visualized as being caused by the termination of a plane of atoms in the middle of a crystal. In this case, the surrounding planes are not straight, but instead bend around the edge of the terminating plane so that the crystal structure is perfectly ordered on either side. In certain direction an extra half-plane could be introduced from two different directions. Thus, edge dislocations are conventionally divided into positive and negative. These two types of dislocations are distinguished only by turning by 180°. The atoms from one side of the dislocation line are squeezed together due to the extra half-plane that results in a compressive stress field. From the opposite side of the dislocation line the extra plane imposes a tensile stress on the lattice. The displacement field around pure an edge dislocation simulated by Holy et al. [42] is presented in the fig.16(right).

In order to visualize a screw dislocation, let us consider a cut of a crystal along a plane and a slip of one half across the other by a lattice vector, when the halves are fitted back together without leaving a defect. If the cut only goes part way through the crystal, and then slipped, the boundary of the cut is a screw dislocation. It comprises a structure in which a helical path is traced around the linear defect (dislocation line) by the atomic planes in the crystal lattice. Screw dislocations can be right-handed and left-handed, the direction of rotation plays the same role as the sign of the edge dislocation. The displacement field around pure a screw dislocation simulated by Holy et al. [42] is presented in the fig.16(left).

Thus, the screw and edge dislocation are the borders between the shifted and unmoved parts of the crystal, whereas the edge dislocation is perpendicular to the shear vector, and the screw one is parallel to this vector.

The dislocation in crystalline material can start to move under an applied stress. There are two types of dislocation movements:

• Glide or conservative motion, when the dislocation moves in the plane which contains both its line and its Burger's vector. A dislocation able to move in this way is termed glissile, one which can not is termed sessile.

• Dislocation motion by climb occurs when the dislocation moves out of the glide plane, and thus normal to the Burgers vector.

2.3.3.2 Threading dislocations in III-nitrides Threading dislocations (TDs) are linear dislocations with dislocations line perpendicular to the sample surface [8]. Usually the threading dislocations occur in [0001] direction grown III-nitrides, such as c-plane GaN [8]. In this case a dislocation line is elongated along c-axis of the unit cell of III-nitrides.

The GaN layers contain a high density of threading dislocations in the range of $10^8 - 10^{10} cm^{-2}$ [8]. The AlN and InN layers grown on foreigner substrates contain even higher threading dislocation density (TDD).

There are three kinds of treading dislocations: screw, edge and mixed. The screw type of dislocation has Burger's vector along c-axis and parallel to the dislocation line (see fig. 17.a). There are two kinds of screw dislocations with Burgers vector $\mathbf{b}_s = [0001]$ and $\mathbf{b}_s = [000\bar{1}]$ for both of them the magnitude of the $b_s = c$, where c is the unit cell lattice parameter in [0001] direction.

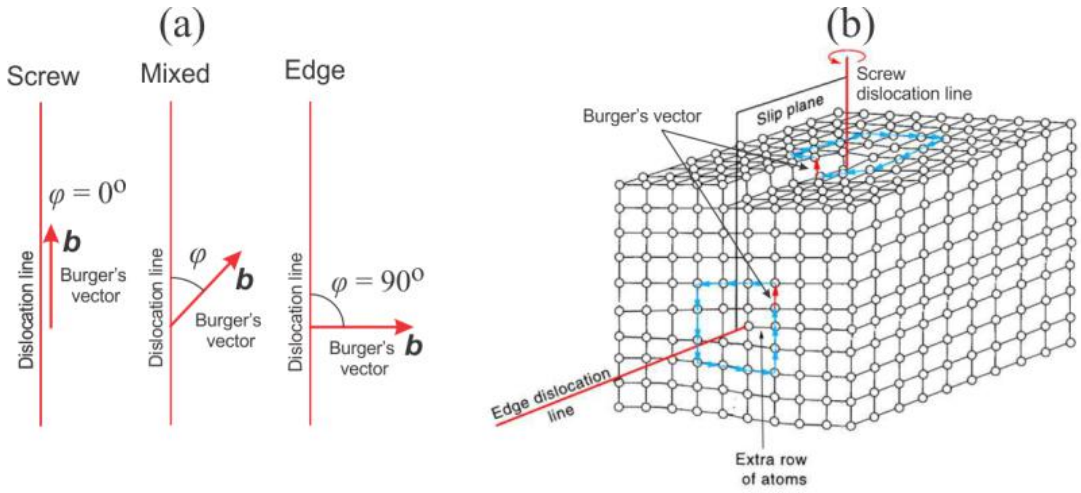

Figure 15: Burger's vector **b** position with respect to the dislocation line for screw, mixed and edge dislocations (a). The scheme of pure screw and edge line dislocations (b).

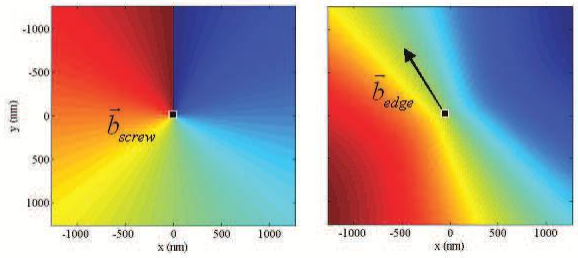

Figure 16: The displacement field distribution for single screw (left) and edge (right) dislocations from [42].

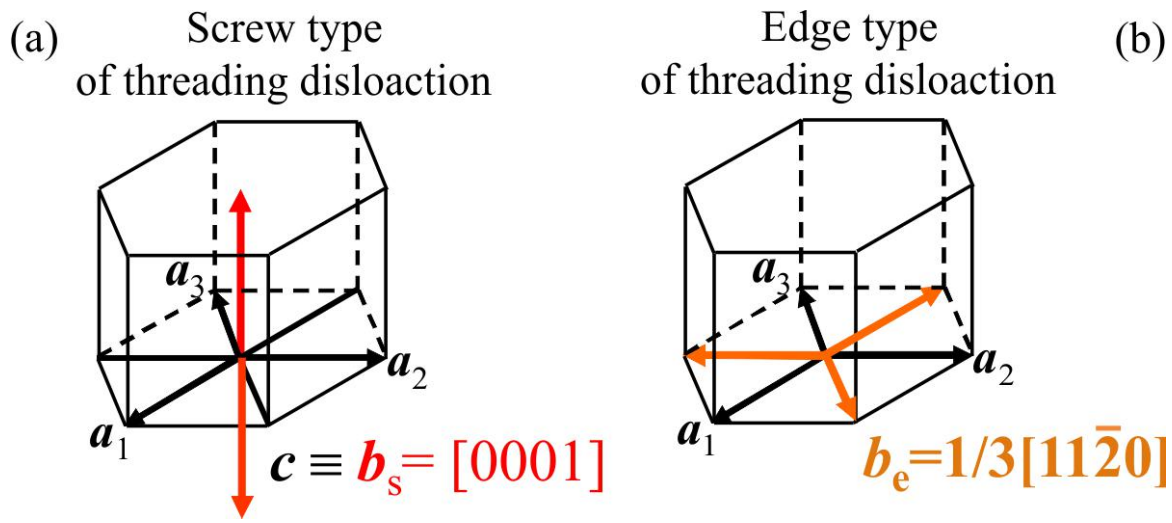

Figure 17: Screw (a) and edge (b) type of treading dislocations.

The edge type of dislocation has a Burger's vector in basal plane and perpendicular to the dislocation line (see fig. 17.b). There are three kinds of edge dislocations with Burgers vector $\mathbf{b}_e = 1/3 \cdot [11\bar{2}0]$, $\mathbf{b}_e = 1/3 \cdot [\bar{1}100]$ and $\mathbf{b}_e = 1/3 \cdot [1\bar{1}00]$ for all of them the magnitude of the $b_e = 1/3 \cdot a$, where a is the unit cell lattice parameter in $[11\bar{2}0]$ direction. Dislocations with opposite Burgers vectors can recombine each other.

The mixed type of dislocation has a Burger's vector inclined with respect to the dislocation line. The mixed dislocations could be performed as a summation of pure screw and edge TDs. Thus, there are six types of mixed TDs with Burger's vectors like $\mathbf{b}_m = 1/3 \cdot [11\bar{2}3]$, and magnitudes $b_m = \sqrt{(1/3 \cdot a)^2 + c^2}$. In this work the mixed TDs decomposed into pure screw and edge TDs, and therefore are not in the consideration.

Threading dislocations occur during crystal growth, with its plastic deformation, and in many other cases.

2.3.4 Misfit dislocations

The relative difference between in-plane lattice parameters of III-nitrides epitaxial layer a_L^{rel} and substrate crystals a_s^{rel} (see fig.18.a) calls lattice mismatch:

$$\frac{\triangle a^{rel}}{a_s^{rel}} = \frac{a_L^{rel} - a_s^{rel}}{a_s^{rel}}. \tag{10}$$

Lattice mismatch gives rise to elastic strains and change the lattice parameters of layer. The difference between strained in-plane lattice parameters of III-nitrides epitaxial layer a_L^{str} and substrate crystals a_s^{rel} (see fig.18.b) calls lattice misfit:

$$\frac{\triangle a^{str}}{a_s^{rel}} = \frac{a_L^{str} - a_s^{rel}}{a_s^{rel}}. \tag{11}$$

These can be relaxed by formation of surface undulations, of three-dimensional islands and of misfit dislocations (MDs) [2], which are sketched in the fig.18.c. The first two mechanisms take place during the initial stages of epitaxy, while the latter process is a dominant mechanism for comparatively thick layers.

To a first extent, misfit dislocations are not supposed to thread up into the layer and are very efficient in relieving strain. However, the threading dislocations can be interconnected to the misfit dislocation network [43].

2.3.5 Planar defects

2.3.5.1 Different kinds of planar defects Planar or two-dimensional defects are interfaces between homogeneous regions of the material. Planar defects include: external surfaces; internal surfaces; grain boundaries; twin boundaries; stacking faults.

A real crystal has a finite size and thus a surfaces. The external surfaces are surfaces of a crystal, which exist due to the final size of the crystal. Thus, the crystal surfaces can be considered as an interfaces between the homogeneous

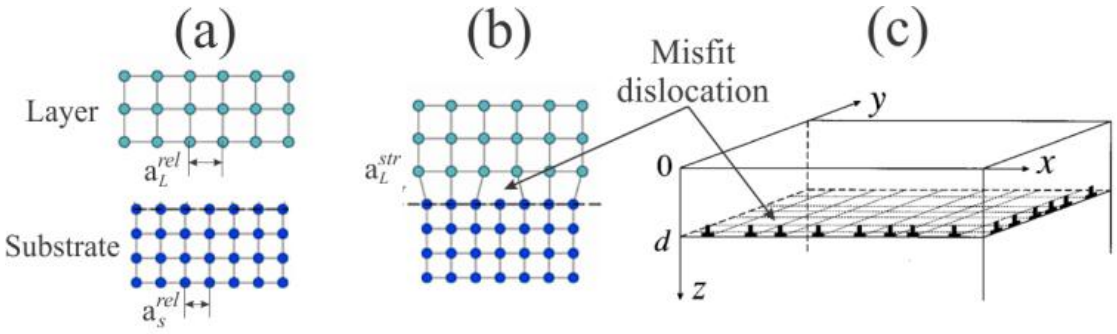

Figure 18: A layer and a substrate lateral lattice parameters (a). Heteroepitaxial system with misfit dislocation (b) and geometry of the network of the misfit dislocations in a layered heteroepitaxial system (c), taken from [44].

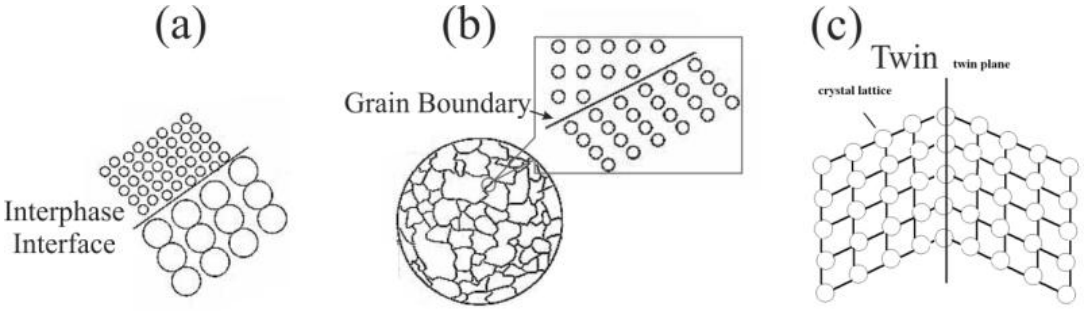

Figure 19: Planar defects: interphase (a), grain boundary (b), and twin (c).

crystal and another phase. External surface has a certain energy formation and, like in case of minimized energy in spherical liquid droplets, has certain strain component.

The internal surface or interphase could be between two different phases in the crystal, as it is shown in the fig.19.a.

In case of brains formation in the crystal, between grains planar defects - grain boundaries exist. The fig.19.b illustrates the sketch of the grains in a sample, and a grain boundary between two grains.

Twinning is a process in which a region of a crystal undergoes a homogeneous shear resulting in original crystal structure in a new orientation known as a twin. The twin can be considered as a mirror image of the original (parent) crystal in the composition plane. A twin boundary is the boundary surface between the two parts of a twin crystal, as it is sketched in the fig.19.c. Twinning usually occurs in the early stages of crystallization, during inter growth of two or more crystalline parts.

All of this planar defects listed above, are not common for standard grown III-nitrides. The last type of planar defects are stacking faults (SFs). They are mistakes in atomic layers packing, and quit common for III-nitrides. Thus, this kind of planar defects will be described in details in the next sections.

2.3.5.2 Stacking faults in III-nitrides The III-nitrides exist in wurtzite (2H, hexagonal) and zincblende (3C, cubic) structures (see Chapter 2.1.1). The wurtzite structure consists of two hexagonal close-packed sublattices Ga and N shifted by along [0001] direction. In both sublattices {0002} planes are close packed. Stacking these basal {0002} planes in the $\ldots A\alpha B\beta A\alpha B\beta A\alpha B\beta\ldots$ sequence forms the wurtzite structure, in which the atoms are tetrahedrally coordinated. Here capital letters correspond to Ga layers and the Greek letters to N layers. For simplicity the GaN molecule can be taken as a stacking unit. In this case the Greek letters can be omitted. Thus the hexagonal stacking sequence will further be named as $\ldots$ ABABAB$\ldots$, where capital letters represent Ga-N atomic bilayers. In the above notation the zincblende structure can be represented as an $\ldots$ ABCABCABC$\ldots$ stacking sequence along the [111] direction.

In the atomic layer sequences some mistakes are possible. Basal plane stacking faults (BSFs) in the wurtzite structure can be treated as planar defects forming locally the ABC cubic structure within the usual $\ldots$ ABABAB$\ldots$ stacking sequence [45]. Four types of basal plane stacking faults, three intrinsic faults ($I1$, $I2$, and $I3$) result from

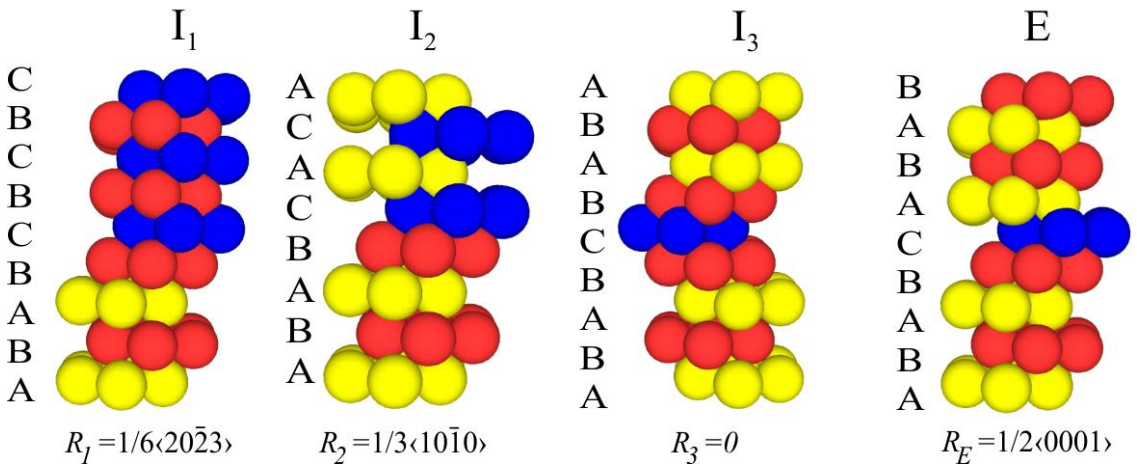

Figure 20: Basal plane stacking faults models and their stacking sequences.

errors in stacking and one extrinsic (E) results from an additional plane inserting, can be found in the wurtzite crystal structure [46] (see fig.20).2 re $I1$ type BSF is formed either by removal or insertion of a basal plane with further $\frac{1}{3}\langle 1\bar{1}00\rangle$ slip of one part of a crystal with respect to the other to decrease the fault energy. This changes the perfect stacking sequence of ...ABABABAB... to one with ...ABABABCBCBC..., as it is shown on the fig.20. The high resolution TEM of $I1$ BSF demonstrates the stacking fault in the fig.21.a. The $I2$ type fault having the ...ABABABCACACA... stacking sequence (see fig.20) can be formed by $\frac{1}{3}\langle 1\bar{1}00\rangle$ shear of one part of a crystal with respect to the other or by dissociation of a perfect edge dislocation ($\mathbf{b} = \frac{1}{3}\langle 11\bar{2}0\rangle$) into two Shockley partials with $\mathbf{b} = \frac{1}{3}\langle 1\bar{1}00\rangle$, and is result from joining two different stacking sequences (see fig.20). The $I3$ type with stacking sequence ...ABABCBABA... occurs from an isolated stacking error. And the extrinsic fault E with a stacking sequence ...ABABABCABABAB... appears due to insertion of an extra basal plane, as it is drawn in fig.20. The BSFs, their displacement vectors and their energy formation are summarized in the tab.6.

Formation energy of stacking fault proportional to the number of cubic bilayers in the particular fault. As described $I1$, $I2$, and E-type defects consist of one, two, and three cubic bilayers, respectively [20]. The type $I3$ consist of one cubic layer as $I1$, but has in two times higher energy formation. Therefore, the $I1$-type BSF has the lowest formation energy, and should mainly be formed during the growth process. This assumption is proved by TEM investigation of non- and semipolar GaN samples [47], where it was shown that density of $I1$-type $\rho_{BSF}(I1)$ is above or about 90% of all BSFs.

The BSFs can not propagate infinite, they should be stopped by some other defects, interfaces or by free surface (like surface of the sample) [45]. The most common way for BSF to be terminated is the partial dislocations, which bound a SF. So, $I1$, $I2$ and E types of BSFs are bounded by Frank– Shockley,Shockley and Frank partial dislocations, respectively. The $I3$ type has no bounded dislocation. The partial dislocations bounded the disc of BSFs and their Burgers vectors are also presented in the tab.6.

Not only dislocations can terminate the BSFs. An additional type of stacking fault common for wurtzite-structure compounds, such as AlN, InN and GaN, is prismatic stacking fault (PSF), which can terminate BSFs [48]. They occur in $\{\bar{1}2\bar{1}0\}$ planes (a-planes) with displacement vector $\mathbf{R} = \frac{1}{2}\langle 10\bar{1}1\rangle$. In the fig.21.b the scheme of two BSFs termination by PSF performed by Zakharov et al. [45], is shown in the fig.21.b. Both of these termination mechanisms were demonstrated by Liu et al. [49] in one TEM picture, and presented in the fig.21.c. The density of PSFs is one of the lowest and usually is about $\rho_{PSF} \sim 10^2 cm^{-1}$, meaning that PSFs are unlikely to contribute strongly to scattering in XRD [50, 21, 8, 51].

2.3.5.3 Mechanisms of the BSF formation

There are three main mechanisms of BSF formation:

- Classical mechanisms. Two formation mechanisms of BSFs are classically presented in the literature. According to the first mechanism the BSFs are result from growth errors [52]. And the second relate the BSF formation with condensation of vacancies [20].

SF type	R	e, (meV)	Stacking sequence	Bounded dislocation type	**b**
I_1	$\frac{1}{6}\langle 20\bar{2}3\rangle$	10	ABABCBCBC	Frank-Shockley partial	$\frac{1}{6}\langle 20\bar{2}3\rangle$
I_2	$\frac{1}{3}\langle 1\bar{1}00\rangle$	24	ABABCACAC	Shockley partial	$\frac{1}{3}\langle 1\bar{1}00\rangle$
I_3	none	19	ABABCBABA	none	none
E	$\frac{1}{2}\langle 0001\rangle$	38	ABABCABAB	Frank partial	$\frac{1}{2}\langle 0001\rangle$
Prismatic	$\frac{1}{2}\langle 10\bar{1}1\rangle$	-	occurs in $\{\bar{1}2\bar{1}0\}$planes	Stair rod	$\frac{1}{6}\langle 10\bar{1}0\rangle$, $\frac{1}{6}\langle \bar{3}\bar{2}50\rangle$

Table 6: Stacking faults (SF) types, displacement vector (R), SF energy formation per unit cell (e), stacking sequence, bounded dislocations and their Burgers vector **b**.

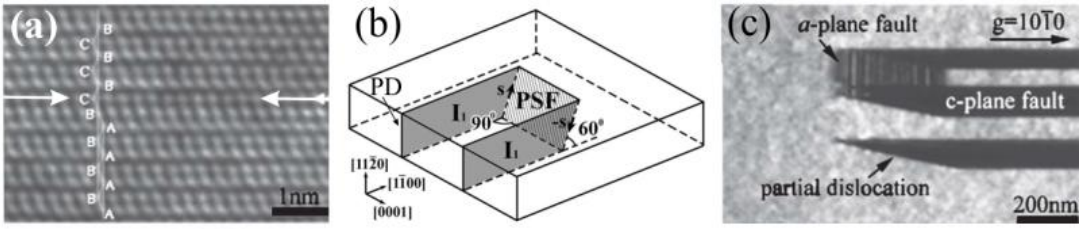

Figure 21: TEM images of stacking faults in the a-plane GaN epilayer (a), the scheme of PSF from [45] (b), and BSF intersecting a prismatic a-plane stacking fault (c) (from [49]).

- Mismatch relaxation. In heteroepitaxial growth, structural defects are often introduced to relax the stress due to the difference of lattice parameters between the deposited layer and the substrate. The termination of a BSF in an interface could influence on the misfit strain relaxation by helping the formation of misfit dislocations (MDs) [53]. In these cases, the PDs terminating the BSFs have their line and an edge component in the interfacial plane and are in fact MDs. And opposite, the MDs occurred to relax GaN material initiate the formation of the BSF. In any case, the BSFs are introduced for the lattice mismatch relaxation.
- Coalescence of nuclei. Another possible mechanism of BSFs formation consider growth of GaN start in in many nuclei positions on the substrate. In the next very early stage of the growth formed islands of the material coalescent with each other, but their borders form the BSFs [54].

2.3.6 Bulk defects

Bulk defects occur on a much bigger scale than the rest of the crystal defects discussed above. However, in semiconductors bulk defects are not common type of defects. A few of the more common bulk defects typical for metals are mentioned below.

Voids are regions where there are a large number of atoms missing from the lattice. In the fig.22 is a void in a piece of metal. Voids can occur for a number of reasons. When voids occur due to air bubbles becoming trapped when a material solidifies, it is commonly called porosity. When a void occurs due to the shrinkage of a material as it solidifies, it is called cavitation.

Another type of bulk defect occurs when impurity atoms cluster together to form small regions of a different phase. The term "phase" refers to that region of space occupied by a physically homogeneous material. These regions are often called precipitates.

In semiconductor III-nitrides usually don't have bulk defects and in this work bulk defects are not in consideration.

2.3.7 Influence of defects on properties of III-nitrides

As already mentioned defects may introduce strain in III-nitride films, which consequently leads to effects such as change in the lattice constant and band gap energy. Apart from that, defects form donor or acceptor levels in the band gap which are otherwise forbidden. Moreover, the defects influences the most important mechanical properties of the III-nitrides, such as: strength and plasticity..

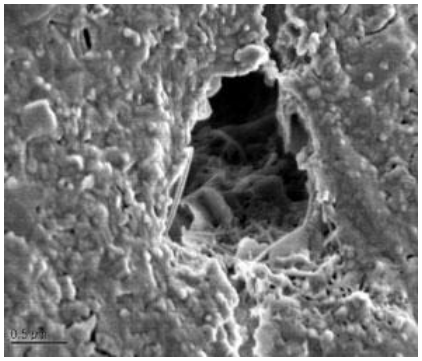

Figure 22: Void bulk defect in a piece of metal.

The defect-related levels in the band gap may be the source of radiative recombination centres in devices, leading to below gap optical emission. Such emission is usually broad and is generally dominant except in very pure material or in thin layer structures that exhibit quantum confinement [55]. A common defect-related emission in n-type GaN is the infamous yellow emission which occurs at energy about 2.2.eV. This emission is parasitic and decrease the quality of optical devices.

The TDs [56, 57] and planar defects [49] act as non-radiative recombination centers and affect the performance of GaN based light emitters . Moreover, the defects act also as strong scattering centers. Planar defects have larger square than other defects and therefore influence on larger crystal area. Additionally, they could split a single crystal into crystallites.

As all defects seriously impair the electrical and optical properties of of III-nitrides, it is of great importance to reduce the number of dislocations. In the next chapter the most common methods of dislocation density reduction are listed and investigated.

2.4 Defect reduction methods for III-nitride heteroepitaxial films

2.4.1 Introduction

Most III-nitride films contain a large quantity of TDs with a typical density of $10^8 - 10^{11} cm^{-2}$ for GaN [8], or BSFs in the order of $10^4 - 10^5 cm^{-1}$ for a-plane GaN [50], as well as many other defects [58]. As these defects seriously impair the electrical and optical properties of the material, it is important that the number of dislocations are reduced. In this chapter, the methods to reduce dislocation density will be discussed.

2.4.2 Nucleation layer

Usually III-nitrides are grown on foreigner substrates. The films of III-nitrides investigated in this work are grown on sapphire. The lattice mismatch between GaN and sapphire is about 13.8%. Such a large lattice mismatch should lead big number of defects in GaN grown directly on sapphire. The lattice mismatch between GaN and InN is about 11%, and between GaN and AlN is only 2.5%. Therefore, the lattice mismatch between GaN and AlN is the lowest one, and one can grow first AlN layer on sapphire and than GaN on this AlN layer. Hiramatsu et al. [59] developed a model for the MOVPE growth of GaN on a thin AlN nucleation layer (NL) with a thickness about 10-50 nm. The model is shown in the fig.23.a. The AlN nucleation layer is grown at $600°C$ on sapphire. At this temperature the nucleation layer is amorphous. Thus, one should write the nucleation layer as AlN_x, but for the simplicity here the index x is neglected and NL is marked as AlN. The NL crystallizes at the growth temperature ($\approx 1500°C$) in a columnar structure . The thin columnar crystallites of the nucleation layer have an extension in the growth direction of $\approx 10 - 50\,nm$ and a rough morphology. This morphology is reproduced in the layer grown directly on the nucleation layer. The column growth is selective, i.e. only the columns oriented in the direction of the growth (c-axis) are reproduced, see fig.23.a. This zone has a large defect density and it extends for some tenth nm. In the following zone, the lateral growth is enforced. The layer grows in crystallites of trapezoidal shape. The final layer is relatively poor of defects, see fig.23.a.

The experimentally determined critical thickness of GaN on c-plane sapphire with an AlN nucleation layer is about 3 nm. For films thinner than that, the lattice constant of the film is equal to that of AlN, i.e., the films are pseudomorphic with the AlN nucleation layer. As the thickness increases, the in-plane lattice constant increases

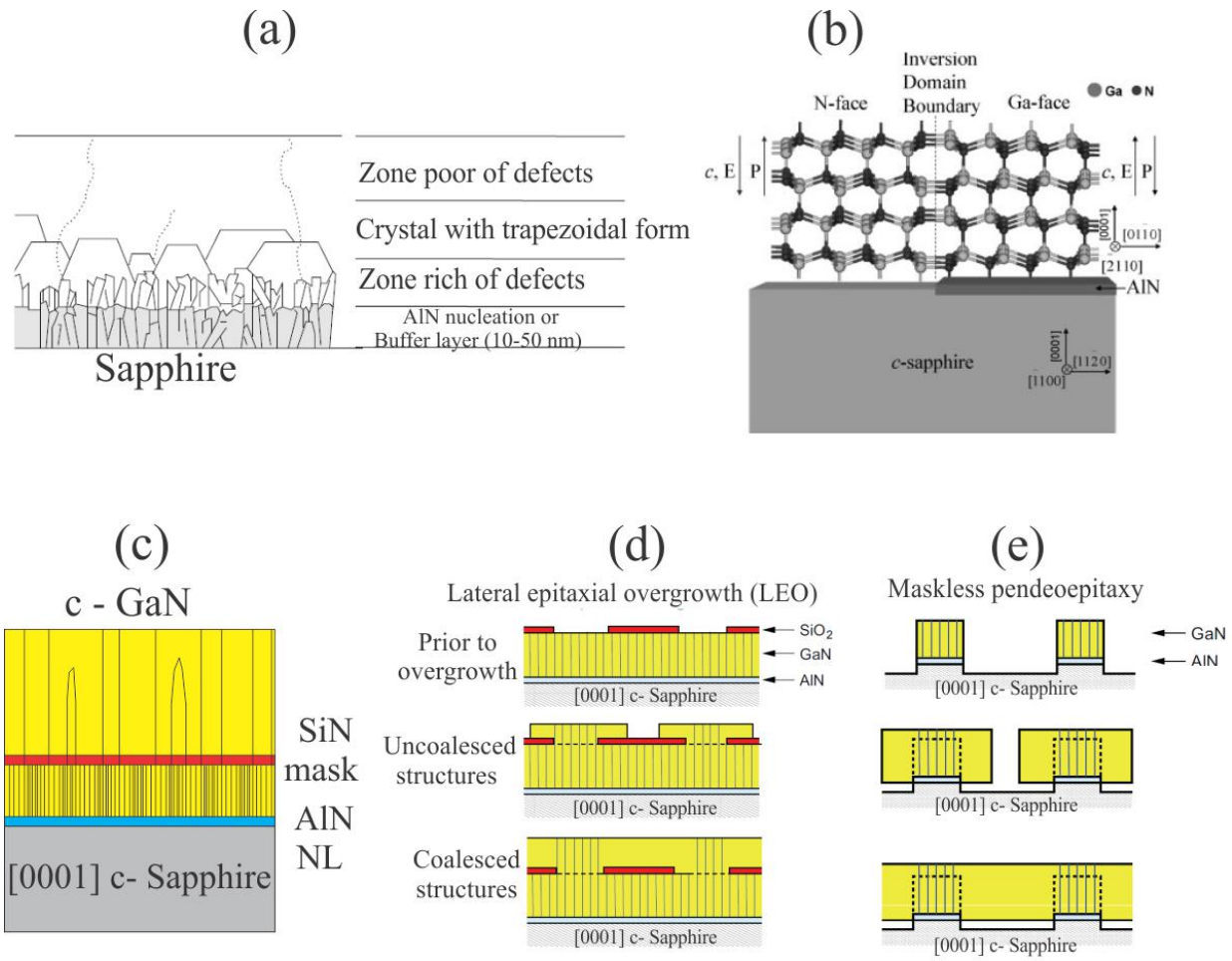

Figure 23: The AlN nucleation layer model from [59] (a), influence of AlN NL on face change taken from [60] (b), masking of the sample (c), lateral epitaxial overgrowth (LEO) (d), and pendeo-epitaxy (PE) (e).

due to the relaxation of strain by misfit dislocations. At a certain thickness, the relaxation is nearly complete and the lattice constant becomes the same as that of bulk GaN.

Liu et al. [60] shows that, the AlN NL changes the face of the GaN layer from N-face into Ga-face, as it is schematically shown in the fig.23.b. Therefore, in case of inhomogeneous growth of AlN NL formation of different domains with Ga-face and N-face is possible. The boundaries between them are called inversion-domain boundaries, and are plane defects.

Finally, one can conclude the AlN NL reduces the density of defects in the overgrowth GaN (or its alloys) layer.

2.4.3 Increase of overgrowth layer thickness

As it was mentioned in the Chapter 2.3.3.1 the dislocation in crystalline material can start to move under cause of stress, or some other reasons. Moreover, depending on circumstances they may cancel each other out, attract, repel or become entangled. When two dislocations with the same sign on the same slip plane meet the interaction of their compressive stress fields will cause them to repel each other. If they have opposite signs their tensile and compressive fields will attract. When they meet the two half-planes of atoms will join to become one whole plane and the dislocations will cancel each other. So, for screw dislocations: two right- or two left-handed screw dislocations repel each other, right and left - are compensated. And for edge dislocations is the same but for the signs of them.

Therefore, during the continuous overgrowth of a III-nitride layer due to forces between dislocations, the dislocations with opposite sign will meet each other and annihilate! The number of annihilated dislocations for a certain layer thickness dh is proportion to the number of dislocations, and therefore proportion to the layer thickness h.

Hence, the density of dislocations should decrease as $Ae^{-\mu h}$, where $e = 2.72$, A and μ are constants, and h is a layer thickness.

The number of dislocations decrease with the overgrowth layer thickness, but the time of layer growth and price of the final product increase. So, one should find a compromise between decreased number of defects in the layer and increased growth time of it, or some other methods of defects reduction should be established.

2.4.4 Masking of the layer

One growth technique which results in an improvement of crystal quality in MOVPE grown of III-nitrides is the use of an intermediate nitride-layer acting as a mask for selective area growth (SAG). Transition metal nitrides such as ScN [61], CrN [62], TiN [63] and SiN [64, 65] are examples of the nano-masking technique to reduce effectively the dislocation density in a layer. In this work SiN mask is used as a masking material of the samples. The SiN_x nano-mask can be deposited just in few minutes in-situ during the growth process by treating the film surface with silane and ammonia [66]. The thickness of such a mask is in order of one monolayer, and material of mask is in amorphous phase. So, the mask should be written as SiN_x, however for the simplicity the index x is neglected.

The model of SiN mask influence on the dislocations is shown in the fig.23.c. The SiN mask stops some of dislocations, bends the others increasing the probability of trier annihilation, but still some of the dislocations could grow though the mask. So, an in-situ deposited intermediate SiN layer in GaN films with a submonolayer thickness reduces the density of edge threading dislocations, while the density of screw threading dislocations remains almost unchanged [67].

2.4.5 Lateral epitaxial overgrowth

To reduce the threading dislocation density in c-plane III-nitrides the lateral epitaxial overgrowth (LEO) approach could be used. The LEO technique consists of coating a film (of III-nitrides) with a patterned mask (SiO2 or silicon nitride) so that dislocations under the mask are prevented from propagating into the overgrown parts of the layer during subsequent growth. Continuation of growth takes place only on the seeds (windows) left uncovered by the amorphous material, as it is shown in the fig.23.d. As soon as the growth front reaches the top of the mask, the GaN layer starts to grow not only vertically, along the c-axis, but also laterally, perpendicular to the c-axis, over the mask (see fig.23.d). The lateral growth can be several times faster than the growth along the c-axis. During this growth step, dislocations close to the edge of the seed areas tend to bend over and to follow the faster growth direction, such that their line directions differ between the laterally grown parts (wings) and the seed columns. Ideally there should be no dislocations grow along the c-axis in the wing regions, as it is illustrated in the fig.23.d. However, some segments extending in the c-direction will inevitably be formed in particular at the meeting front of overgrown material, as dislocation lines cannot terminate inside bulk material (unless they annihilate with dislocations having opposite sign of Burger's vector, i.e., forming a loop).

2.4.6 Pendeo-epitaxy

For pendeo-epitaxy (PE) stripes are etched through the film into the substrate, as it is depicted in the fig.23.e. Again GaN is grown laterally and vertically, the growth starts from the sidewalls of the GaN stripes and the wings hang free without being in contact with the substrate. The TD density in the laterally grown wings is reduced to $10^5 cm^{-2}$ relative to the initial $10^{10} cm^{-2}$ in GaN stripe [68]. Comparing PE and LEO, PE does not use a mask to initiate lateral growth but employs the substrate itself as a pseudomask.

2.5 Analysis of semiconductors using different methods

2.5.1 Introduction

Semiconductor materials can be investigated using different methods. For the purposes of this research, the X-ray methods used here, based on diffraction, are treated separately from all other techniques, presented in Chapter 3. In this chapter the range of different techniques that are not based on X-ray diffraction have been the subjects of investigation.

2.5.2 Optical microscopy

A specimen could be observed directly in visible light using optical systems [69]. However, theoretically the maximum resolution d, that one can obtain with a light microscope has been limited by the wavelength of the photons that are being used to probe the sample λ:

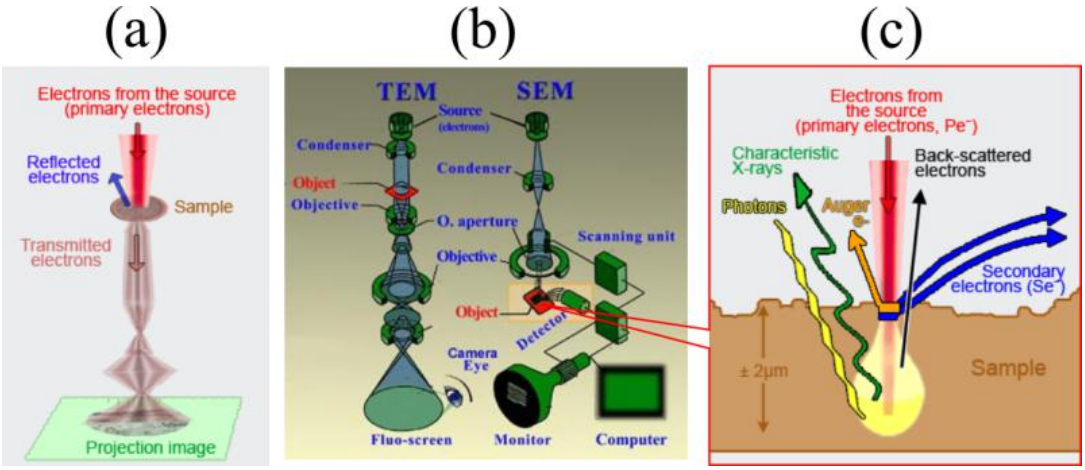

Figure 24: Scheme of TEM (a), realization of TEM (left) and SEM (right) (b), and scheme of SEM (c).

$$d = \frac{1.22\lambda}{2n \cdot \sin\alpha}, \tag{12}$$

where n is the index of refraction of the media surrounding the radiating points, and α is the half angle of the pencil of light that enters the objective.

The highest resolution in visible light could be estimated as:

$$d_{min} \approx \frac{\lambda_{min}}{2}. \tag{13}$$

Since the shortest wavelength of visible light is about $\lambda_{min} = 400\,nm$, hence the best achievable resolution in visible light is about $d_{min} = 200\,nm$. However, this resolution is not enough for the defect or structure analyze of the semiconductor materials, where resolution in nanometer range is needed.

In order to increase resolution, electron beam could be used for microscopy. Like all matter, electrons have both wave and particle properties (as theorized by Louis-Victor de Broglie), and their wave-like properties mean that a beam of electrons can be made to behave like a beam of electromagnetic radiation. The wavelength of electrons is related to their kinetic energy via the de Broglie equation. After taking into account relativistic effects wavelength of an electron could be written as:

$$\lambda_e \approx \frac{h}{\sqrt{2m_0E\left(1 + \frac{E}{2m_0c^2}\right)}}, \tag{14}$$

where, h is Planck's constant, m_0 is the rest mass of an electron and E is the energy of the accelerated electron. The maximum reachable resolution which was achieved using electrons is $50pm = 5 \cdot 10^{-11}m$ [70].

2.5.3 Semiconductor investigation using an electron beam

When an electron beam interacts with a material different radiations come out of it, e. g., X-rays, Auger electrons, secondary electrons, and cathodoluminescence, see fig.24.c. By detecting these radiations a lot of information about the irradiated sample can be obtained, including microstructure, surface morphology, composition, and optical properties. Moreover, an electron beam can transmit or diffract and then transmit a specimen if it is thin enough, see fig.24.a. These transmitted or diffracted electrons could also be recorded and an image of a specimen structure with high resolution can be formed. In this section methods based on electron beam interaction with materials will be described.

2.5.3.1 Transmission electron microscopy Transmission electron microscopy (TEM) is microscopy method based on the electron beam transmission or scattering and transmission. The electron beam should transmit a specimen, hence a specimen should be thin and usually is a thin slice of a sample. After transmission the beam is focused and unfocused several time to form the projection image with tunable magnification, as it is shown in the

fig.24.a. The realization of the TEM is shown in the fig.24.b(left). Using TEM a magnification allowing imaging with resolution on the atomic scale is achievable.

Two basic ways to form contrast in the TEM image are bright field (BF) imaging and dark field (DF) imaging.

Bright field TEM (BF).

In BF contrast regions that scatter the electrons most will appear dark, this means that, e.g. thicker regions or regions with high atomic number, or the parts of the samples that diffract the electron will appear darker and thin areas with small atomic number without diffracting the beam will appear brighter.

Dark field TEM (DF).

In DF, a selected part of the scattered or diffracted electrons are used in the imaging, making it possible to highlight certain structures in the sample. That means that one is able to image the defects with a certain Burgers vector and count the defect density!

Weak-Beam Dark-Field (WBDF) technique.

When analyzing dislocations in a crystal, it can be most important to determine the type of each dislocation visible in a TEM image. For this purpose it is necessary to determine the Burgers vector of a dislocation in order to decide if the dislocation is a pure screw, pure edge or a mixed dislocation. The imaging of dislocations in a TEM is predicated on the diffraction contrast by exploiting the DF method under special conditions. By using the WBDF method it is possible to image the dislocations and to determine the Burgers vector. In the following the WBDF technique is described.

High resolution transmission electron microscopy (HRTEM).

The electron beam could be focused to an area with size nanometer size that allows the imaging of the crystallographic structure of a sample at an atomic scale using HRTEM. At present, the highest realized resolution is $0.047\,nm$ at Tokyo Institute of Technology [71]. At these small scales, individual atoms and crystalline defects can be imaged.

Scanning transmission electron microscopy (STEM).

In STEM the electron beam is focused in the sample with spot size about nanometers and beam scanning the sample recording information with spatial resolution of about atomic distances. Usually in STEM the DF contrast by using high angle annular dark field (HAADF) detector is applied.

In the present work different techniques of TEM method will be used.

2.5.3.2 Scanning electron microscope

In a scanning electron microscope (SEM), a tiny electron beam is focused onto the sample. The types of signals produced by a SEM include secondary electrons (SE), back-scattered electrons (BSE), characteristic X-rays, light (cathodoluminescence) (CL), specimen current and transmitted electrons, as is schematically drawn in the fig.24.c. Secondary electron detectors are standard equipment in all SEMs, but some times SEM could have detectors for all possible signals. Simultaneous to scanning the beam across a selected sample area, generated signals are being recorded and thereby an image is formed pixel by pixel. In contrast to TEM methods needing very thin samples, compact samples can thus be investigated by SEM. Valuable information about morphology, surface topology and composition can be obtained. The SEM microscopes achieving resolution could be below 1nm, however typical resolutions are hundreds of nanometers, and under certain beam conditions less than 10 nm. The scheme of SEM is presented in the fig.24.b(right).

2.5.4 Investigation of III-nitrides using luminescence

Luminescence is emission of light by a substance not resulting from heat; it is thus a form of cold body radiation. It can be caused by chemical reactions, electrical energy, subatomic motions, or stress on a crystal and in fact it is transformation of diverse kinds of energy into visible light.. The different substances have different band gap and transmission of an electrons from conduction to valence shell causes an emission of electron with energy correspond to band gap of the material. Different imperfections of crystal, i.e. defects, dislocations, stacking faults, influence on the band gap and therefore luminescence could be used as an method for investigation of composition and quality of a specimen. Here we will use this phenomenon to investigate the quality of semiconductor crystals.

2.5.4.1 Photoluminescence

Photoluminescence (PL) is a luminescence caused by absorption of a substance photons and then re-radiation of photons. Quantum mechanically, this can be described as: if a photon has an energy greater than the band gap energy (usually ultraviolet light), then it can be absorbed and thereby raise an electron from the valence band up to the conduction band across the forbidden energy gap. In this process of photoexcitation, the electron generally has excess energy which it loses before coming to rest at the lowest energy in the conduction band. At this point the electron eventually falls back down to the valence band. As it falls down,

the energy it loses is converted back into a luminescent photon which is emitted from the material, see fig.25.a. Thus the energy of the emitted photon is a direct measure of the band gap energy (E_g).

The scheme of the photoluminescence measurement is shown at the fig.25.b. A laser usually uses to photo-excited electrons in a GaN semiconductor materials and the luminescence is analyzed with a spectrometer. The peaks in the spectra represent a direct measure of the energy levels in the semiconductor (fig.25.b).

2.5.4.2 Cathodoluminescence Cathodoluminescence (CL) is the electron-excited analogue to photoluminescence. The CL occurs because the impingement of a high energy electron beam onto a semiconductor, as it is realized in case of cathode rays of TV and PC's display. Electrons incident upon a sample result in the promotion of electrons from the valence band into the conduction band, leaving behind a hole. When an electron and a hole recombine, it is possible for a photon to be emitted. The energy of the photon, and the probability that a photon and not a phonon will be emitted, depends on the material, its purity, and its defect state.

Significant advantage of cathodoluminescence is the depth dependence of incident electrons as a function of beam energy. By tuning the electron beam energy from hundreds of electron volts to a few kilo electron volts, the electron-hole pair generation depth can be varied from tens of nanometers to about a micrometer, for practical beam energies.

Since high voltage electron beam is needed for the method realization cathodoluminescence devices can be installed in a SEM. Additional optical detection parts for the visible light is required, which incorporates a parabolic mirror mounted on the spectrometer port designed for high efficiency of light collection, see fig.25.c. This specially designed mirror is used for collecting the CL. Despite the high generation factors for the electron-hole pairs, the external photon yield is small. Furthermore, the intensity generated inside the specimen is considerably reduced by absorption in the specimen and by the total reflection at the specimen surface. From there, a fiber optic will transfer the light out of the microscope where it is separated into its component wavelengths by a monochromator and is then detected with a photomultiplier tube, these components schematically shown on the fig.25.c as filter, lens and detector. beamline is r, the luminescence of dislocated specimen is different from perfect crystal, and can be used for defects determination techniques.

- CL spectroscopy

Conventionally, there are several applications of CL in crystal quality analyze. One of them is a CL spectroscopy, where unfocused electron beam in stationary mode, illuminate an area on a specimen about $30\,\mu m$, and statistical information about this area is derived for different emitted energies of CL photons. Therefore, in order to carry out spectroscopy, the emitted radiation has to be spectral resolved by using a monochromator. The resolution of the method is an energy resolution of the monochromator. Finally intensity distribution against energy scan could be recorded from the selected area on the sample. Spectroscopy gives information about the real structure, and allows detection of trace elements, their valence and structural position.

- SEM CL

There is another application of CL, so called SEM CL or locally resolved CL, related to the imaging of the specimen area in certain wavelength, which requires spatial resolution of the position from which the emission originates. However, the spatial resolution of the CL is determined by the excitation source and not detection. For excitation, a focused electron beam of a SEM is used. The accelerating voltage of the beam is tunable between 1-30 keV. The emitted light is detected using a parabolic mirror which is placed a few millimeters above the sample in such a way that it's focal point coincides with the sample. The size of this focus is usually in tens of microns. The mirror is arranged to as to have a large acceptance angle. The light collected from the focal point is reflected as a parallel beam through a hollow waveguide tube and focused onto the entrance slits of a monochromator (fig.25.c).

By scanning the microscope's beam in an $X-Y$ (specimen surface) plane and measuring the light emitted with the beam at each point, a map of the optical activity of the specimen can be obtained. The primary advantages to the electron microscope based technique is the ability to resolve features down to 1 nanometer [72], the ability to measure an entire spectrum at each point if the photomultiplier tube is replaced with a CCD camera, and the ability to perform nanosecond- to picosecond-level time-resolved measurements if the electron beam can be "chopped" into nano- or picosecond pulses. Therefor, the optical properties of an object can be correlated to structural properties observed with the scanning electron microscope. The SEM CL allows record full map of the optical activity of the sample area and relate this activity to a certain object or defect of the sample, moreover contrasting of different phases visualization of defects and internal structures investigations are possible.

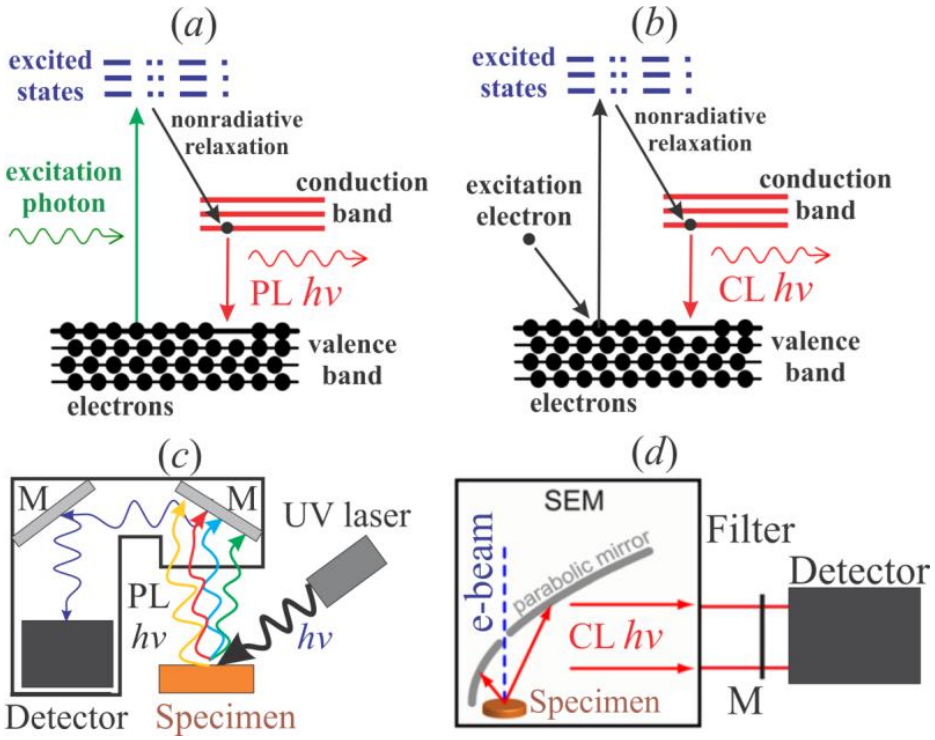

Figure 25: The PL photon emission scheme (a), CL photon emission scheme (b), photoluminescence measurement scheme (c), and cathodoluminescence experiment scheme (d).

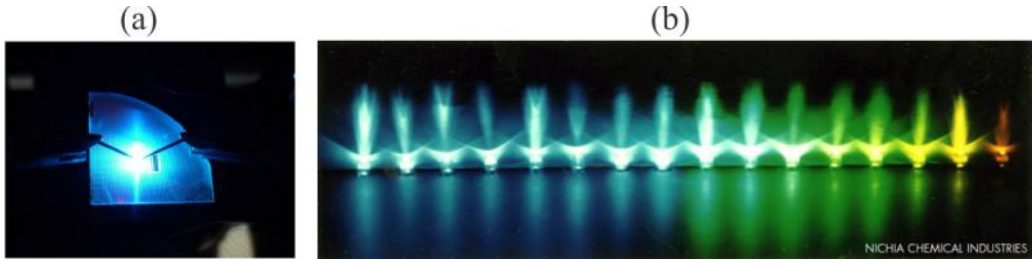

Figure 26: Light emission image of the bluish-green LED (a), and LEDs based on InGaN quantum wells (b), taken from [74].

2.5.4.3 Electroluminescence electrical injection The properties of the semipolar materials could be investigated by electrical injection electroluminescence, which results from injection of minority carriers into the region of a p-n junction where radiative transitions occur, as it was demonstrated by Okada [26], and presented in the fig.26.a.

In electroluminescence an electric field or current provides the excitation [73]. The wavelength (color) of the light emitted by an LED depends on the semiconductor material used, which is characterized by its own energy bandgap. and emitted light is depends on the material properties.

As an example the variation of the emitted wavelength for different InN content in InGaN quantum wells is given in the fig.26.b [74].

2.5.5 Atomic force microscopy

The surface morphology, morphology, surface texture and roughness could be investigated by atomic force microscopy (AFM). AFM provides a 3D profile of the surface on a nanoscale, by measuring forces between a sharp probe (<10 nm) and surface at very short distance (0.2-10 nm probe-sample separation). The probe is supported on a flexible cantilever. The AFM tip "gently" touches the surface and records the small force between the probe and the surface.

The probe is placed on the end of a cantilever (which one can think of as a spring). The amount of force between the probe and sample is dependent on the spring constant, and this force can be described using Hooke's Law. The spring constant of cantilever (typically ~ 0.1-1 N/m) is less than surface, and therefore the cantilever bends and the deflection is monitored.

The scanned area of AFM is typically small, and is about micrometer range. The cantilever is very sensitive and can measure only sample with surface roughness less than the probe-sample distance. Moreover, the method usually needs vacuum, antivibration system and takes some time.

In this work AFM measurements will be used for surface roughness measurement.

3 X-ray diffraction

3.1 Introduction

The methods described in the previous sections are destructive methods, and mostly used locally. The X-ray method is non-destructive, statistical or local (depending on focusing), and enables an investigation of crystalline materials to be carried out in-situ, i.e. during the process. X-ray scattering is one of the most important methods of characterizing semiconductor crystals.

The X-rays can interact differently with matter, in that they can be absorbed and both elastically or in-elastically scattered. By means of X-ray scattering, the structure of thin films, morphology, strain in the material, electron density and many other properties can be determined. In this chapter, we will focus on the basic principles of elastic X-ray scattering.

3.2 X-ray radiation

X-rays are electromagnetic waves with a wavelength in the region of $10^{-9} - 10^{-10}m$ that corresponds to dimensions of atomic plane interspacing in the crystals [75]. It gives an opportunity for investigation of the crystalline structures using of X-rays [75, 76]. For the purposes of this research, elastic scattering of X-rays from the solid structure has come under scrutiny, in that the wavelengths of incidence and outgoing beams are equal.

3.3 Interaction of X-rays with the crystalline material

The incoming X-ray beam can be absorbed by material resulting with the weaker outgoing beam. This process is described by exponential reduction of incident intensity I_0 while propagating through the sample with the thickness z:

$$I(z) = I_0 \exp(-\mu z), \tag{15}$$

where μ is absorption coefficient of the sample material at certain energy of x-rays.

Except being absorbed the incoming beam can be refracted or reflected. Every material has its own refractive index. For x-rays the complex refractive index is less then unity and it can be presented as follows:

$$n = 1 - \delta + i\beta. \tag{16}$$

The δ is related to the electron density through the expression:

$$\delta = \frac{2\pi\rho r_0}{k^2}, \tag{17}$$

where ρ is the electron density, $r_0 = 2.82 \cdot 10^{-15}m$ is the scattering length for each electron and $k = 2\pi/\lambda$ is the wave vector of the X-ray radiation which has the wavelength λ. And imaginary part of the refractive index β depends on the material absorption coefficient:

$$\beta = \frac{\mu}{2k}. \tag{18}$$

X-rays can undergo total external reflection if the incident angle is smaller than the critical one given as $\alpha_c = \sqrt{2\delta}$ that is often used in surface and near-surface regions investigation.

Finally, the incident X-ray beam can be diffracted from ordered crystalline structure. In general, diffraction of X-rays from a crystal lattice obeys the Bragg's Law:

$$n\lambda = 2d \sin\theta_B, \tag{19}$$

where λ is the wavelength, d is the lattice spacing, θ_B is the Bragg angle and n is an integer.

3.4 X-ray diffraction on crystal structure and reciprocal space

There are two general approaches to describe the X-ray diffraction, namely the dynamical and kinematic scattering theories [77]. Dynamical theory takes into account multiple scattering processes, and can be applied to highly prefect semi-infinite single crystal systems evolving the narrow Bragg peaks. The exact theoretical treatment of X-ray diffuse scattering from GaN epitaxial layers within the dynamical theory is practically impossible.

The kinematic approach known as the first Born approximation is successfully applied to describe the diffraction from rather imperfect systems and small scattering volumes. In the processes described by kinematic diffraction, scattering is supposed to be weak what implies that multiple scattering effects can be neglected.

In kinematic theory from all possible interaction of photons with matter only the elastic scattering process is considered, all processes that change the photon wavelength (Compton scattering, photo effect, etc.) are neglected (the wavelength should be far away from absorption edges). Principally photons interact with any charge inside the material (electrons and protons) however the atomic nuclei are screened by the electron cloud and one can assume that the radiation interact only with electrons.

The sample is thus pictured as an ensemble of many point like scattering centers which are the electrons. The general idea is now the following: first the scattering of the electromagnetic wave by one single electron (Thomson scattering) is considered. Afterward, coherently adding up the scattering response of all the electrons belonging to one atom delivers the scattering of the atom which is the atomic form factor. Coherent adding of the atomic form factors of all atoms inside a unit cell delivers the structure factor and finally the coherent adding of all Structure factors inside a sample leads to the desired scattering response of the complete objects, such as a film.

The X-ray detectors in an experiment record the scattered intensity $I_s = |E_s|^2$ which is the square amount of the scattering amplitude. Therefore, one needs to derive scattering amplitude of an electron, atom, unit cell and structure to calculate the intensity which will be recorded in the experiment.

In some cases the experimental problem cannot be solved neither dynamically nor kinematically, so other suitable approximation should be found. Within semi-kinematic approach the scattering from an undisturbed sample is assumed to be dynamical, while the contribution of the disturbance is calculated kinematically.

Scattering from the electron - Thomson scattering

The scattering process starts from the scattering by one scattering center, the electron. From a classical point of view, a charged free electron is accelerated by the incoming electromagnetic wave with the amplitude $E_o \exp(i\mathbf{k}_i\mathbf{r})$ [75, 78]. The resulting forced oscillation of the electron leads to re-emission of an electromagnetic spherical wave (Thomson scattering), which has the same frequency as the original incoming wave and exhibits a characteristic dipole-like angular distribution. At large distance R from the observer, the electric far field of the scattered wave is given by:

$$E(r,R) = r_0 C E_0 \exp(i\mathbf{k}_i\mathbf{r}) \frac{\exp(ikR)}{R}, \tag{20}$$

where r_0 is the classical electron radius, k_i is the incidence wave vector and C is the polarization factor having 1 or $|\cos 2\theta|$ (where 2θ is the angle between scattered and incidence waves) values for σ- (out of plane) and π-polarizations (in plane), respectively. The $k = |\boldsymbol{k_i}|$ is defined as a length of the wave vector that is constant for incidence and diffracted beams within the kinematic approximation.

Scattering from the atom - the atomic form factor

The total scattered amplitude from an atom is given by a coherent summation over all scattered partial waves:

$$E(\boldsymbol{R}) = r_0 C E_0 \int \rho(r) \exp(i\mathbf{k}_i\mathbf{r}) \frac{\exp(ik|\boldsymbol{r}-\boldsymbol{R}|)}{\boldsymbol{r}-\boldsymbol{R}} dV, \tag{21}$$

where $\rho(r)$ stands for the electron density in the atom. The expression in the integral of the eq.21 can be simplified, using kinematic approximation [76]: if the distance between the sample and detector is much larger than the diameter of the coherently illuminated sample area ($|\boldsymbol{R}| \gg |\boldsymbol{r}|$), the Fraunhofer approximation known as far-field diffraction is valid. By another words, the square of the size D of scattering object is much smaller then product of the X-rays wavelength λ and R ($D \ll \sqrt{\lambda R}$).

In this case eq.21 can be rewritten as:

$$E(\boldsymbol{Q}) = r_0 C E_0 \frac{\exp(ikR)}{R} \int \rho(\boldsymbol{r}) \exp(i\boldsymbol{Q}\cdot\boldsymbol{r}) dV = Const \cdot f_j(\mathbf{Q}), \tag{22}$$

Here, $\mathbf{Q}$ is the scattering vector defined as a difference between wave vectors of the diffracted $\mathbf{k}_f$ and incidence $\mathbf{k}_i$ beams:

$$\mathbf{Q} = \mathbf{k}_f - \mathbf{k}_i \tag{23}$$

From the eq.22 one can see that, the amplitude can be treated as the three-dimensional Fourier transform $f_i(\mathbf{Q})$ of the electron density $\rho(\boldsymbol{r})$ multiplied with a constant *Const*! The $f_i(\mathbf{Q})$ expresses the scattering response of one atom. It is called atomic form factor and listed in the international tables of crystallography for the different elements.

From the eq.22 additional and the most important conclusion of kinematic theory could be done if one generalize the result to any electron density: the scattering amplitude of an object with electron density $\rho(\mathbf{r})$ is proportional to the Fourier transform of this electron density! That means that one can recalculate the crystal structure from real space to so called reciprocal space (RS) and back by using Fourier transform.

Scattering from the unit cell - The structure factor

To obtain the scattering of the unit cell the analog process is continued: coherent adding of the atomic form factors of all atoms inside one unit cell delivers the scattering response of the unit cell:

$$F(\mathbf{Q}) = \sum_{j=1}^{S} f_j(\mathbf{Q}) \exp\left(-i\mathbf{Q}\mathbf{r}_j\right) \tag{24}$$

In case of an atom the electron positions were given by the presence probability density function which is a smooth varying function and thus the summation was done within an integral. In case of the atoms in the unit cell fixed and well known atomic positions are used. Therefore the summation is done via a simple sigma-summation sign instead of an integral. The result called structure factor is the scattering from the unit cell.

Scattering from the infinite crystal - the reciprocal lattice weighted with the structure factor

The next step is the coherent summation of the waves that were scattered by the unit cells inside the sample in order to obtain the scattering of the complete object. First the scattering of a (theoretical) infinite large sample that contains an infinite number of unite cells is assumed. The summation of the scattering of all unit cells (structure factors $F(\mathbf{Q})$) inside the infinitely extended crystal with the basis a_1, a_2, a_3 is

$$F_{crystal}(\mathbf{Q}) = F(\mathbf{Q}) \sum_{\mathbf{R}_n} \exp\left(-i\mathbf{Q}\mathbf{R}_n\right) \tag{25}$$

with $\mathbf{R}_n = n_1\mathbf{a}_1 + n_2\mathbf{a}_2 + n_3\mathbf{a}_3$ and $n_1, n_2, n_3 = integer$. The exponent term in equation 25 corresponds to a phase. In general case without some special conditions the infinite summation of arbitrary phases will lead to annihilation of $F_{crystal}(\mathbf{Q})$ and thus of the intensity which is proportional to its square. Only in case the argument of the exponential function is a multiple of 2π the sum not vanish but correspond to the number of unit cells in the sample.

$$\mathbf{Q} \cdot \mathbf{R}_n = 2\pi \cdot n \tag{26}$$

the scattering condition 26 is always fulfilled for the reciprocal lattice vector $\mathbf{G} = h\mathbf{a}_1^* + k\mathbf{a}_2^* + l\mathbf{a}_3^*$, with integers h, k, l called Miller indexes (or indexes of reflection), and:

$$\mathbf{a}_1^* = 2\pi\frac{\mathbf{a}_2 \times \mathbf{a}_3}{\mathbf{a}_1 \cdot \mathbf{a}_2 \times \mathbf{a}_3},\ \mathbf{a}_2^* = 2\pi\frac{\mathbf{a}_3 \times \mathbf{a}_1}{\mathbf{a}_1 \cdot \mathbf{a}_2 \times \mathbf{a}_3},\ \mathbf{a}_3^* = 2\pi\frac{\mathbf{a}_1 \times \mathbf{a}_2}{\mathbf{a}_1 \cdot \mathbf{a}_2 \times \mathbf{a}_3}. \tag{27}$$

Scattering is observed if the scattering vector corresponds to a reciprocal space vector (Laue Condition)

$$\mathbf{Q} = \mathbf{G}, \tag{28}$$

cause

$$\mathbf{G} \cdot \mathbf{R_n} = 2\pi\left(hn_1 + kn_2 + ln_3\right). \tag{29}$$

In summary the scattering amplitude of the sample corresponds to the Fourier transform of the electron density and constant factors. In case of a infinite large crystal the scattering amplitude can be presented by the concept of

reciprocal space (RS). The reciprocal lattice points (RLPs) or reflections (sometimes called "diffraction") indicate were the Laue condition eq.28 is fulfilled. The scattering amplitude in these points is proportional to the structure factor $E \propto F(\mathbf{Q})$. The experimentally obtained reflection intensity $I(\mathbf{Q})$ proportional to square of the structure factor $I(\mathbf{Q}) \propto F(\mathbf{Q})^2$, and thus can be used to determine the structure of the unit cell. Moreover, according to the formula in 25 the scattered intensity $I(\mathbf{Q})$ should also be proportional the square of the number of unit cells.

However, the structure factor $F(\mathbf{Q})$ depends on hkl and intensity of reflection could be "killed" if $F(\mathbf{Q}) = 0$. The reflections with zero structure factor called forbidden reflections, other reflections are allowed. The III-nitrides have hexagonal unit cell. The structure factor of a hexagonal (like GaN) unit cell according to the positions of atoms in the unit cell is:

$$F_{GaN} = f_{Ga}\left(1 + \exp\left(-2\pi i(\frac{2h}{3} + \frac{k}{3} + \frac{l}{2})\right)\right) + f_N\left(\exp\left(-2\pi i \cdot \frac{3l}{8}\right) + \exp\left(-2\pi i(\frac{2h}{3} + \frac{k}{3} + \frac{7l}{2})\right)\right) \tag{30}$$

where f_{Ga} and f_N are the atomic form factors of Ga and N atoms, respectively. Combination of Miller indices defines the intensity of reflection. The allowed reflections of diffraction from hexagonal crystal systems are for any even l and $h + 2k = 3n$, while forbidden are with $h + 2k = 3n$ and any with odd l, where n is an integer.

Scattering from a real object - shape function

In the previous section coherent adding the unit cell scattering of unit cells inside an infinite extended crystal delivered the reciprocal lattice. In this part the infinite extended crystal should be reduced to a realistic sample or object. The electron density of the infinite crystal can be written as real space lattice convoluted with the electron density inside the unit cell:

$$\rho_{inf.cryst.}(\mathbf{r}) = (\rho_{uc}(\mathbf{r}) \otimes \rho_{latt.}(\mathbf{r})) \tag{31}$$

to obtain now a realistic sample the expression for the infinite crystal is multiplied with the shape function $\Omega(\mathbf{r})$:

$$\Omega(\mathbf{r}) = \begin{cases} 1 & \text{inside the sample} \\ 0 & \text{outside} \end{cases} \tag{32}$$

that is cutting off a sample out of the infinite crystal:

$$\rho_{sample}(\mathbf{r}) = \Omega(\mathbf{r})(\rho_{uc}(\mathbf{r}) \otimes \rho_{latt.}(\mathbf{r})) \tag{33}$$

That means that scattering from a realistic sample could be obtained by multiplying the infinitely large crystal with a simple shape function that corresponds to 1 for all positions inside the sample and to 0 for all positions outside. As was shown above the scattering amplitude is proportional to the Fourier transformation (FT) of the electron density. The FT of 33 results in:

$$\rho^{FT}_{sample}(\mathbf{Q}) = \Omega^{FT}(\mathbf{Q}) \otimes (\rho^{FT}_{uc}(\mathbf{Q}) \cdot \rho^{FT}_{latt.}(\mathbf{Q})) \tag{34}$$

since a convolution transforms to a product and vice versa. The single terms can now be treated with the derived knowledge. The electron density in a crystal is periodically organized around real space lattice points. This results in reciprocal lattice points describing where in reciprocal space the scattering amplitude is unequal zero. The detailed structure around the real space lattice points, the unit cell, results in the structure factor indicating scattered intensity. The convolution of the infinite crystal with the shape function of a sample results to a distribution of the scattering amplitude around the reciprocal lattice points. By another words, the shape of a sample (shape function) influences on the shape of reflections in reciprocal space.

Scattering from strained and not perfect sample

Usually real structures are not perfect and have defects, or strain. Defects are also surrounded with stain field. Therefore, both stain and defects in crystal structure of a sample lead the small shift of atom positions from their theoretical positions in the crystal. This shift in periodic structure influences on electron density in the unit cells $\rho_{uc}(\mathbf{r})$ or on the periodicity of the electron density $\rho_{latt.}(\mathbf{r})$ in the specimen. The small change of the term in FT will not influence on the position of reflections, but will influence on their shape. Therefore from the shape of the reflections information about defects and strain in the sample could be derived. The methods and models allows dislocation density calculation from the shape of the reflection will be discussed later in the Chapter 4.

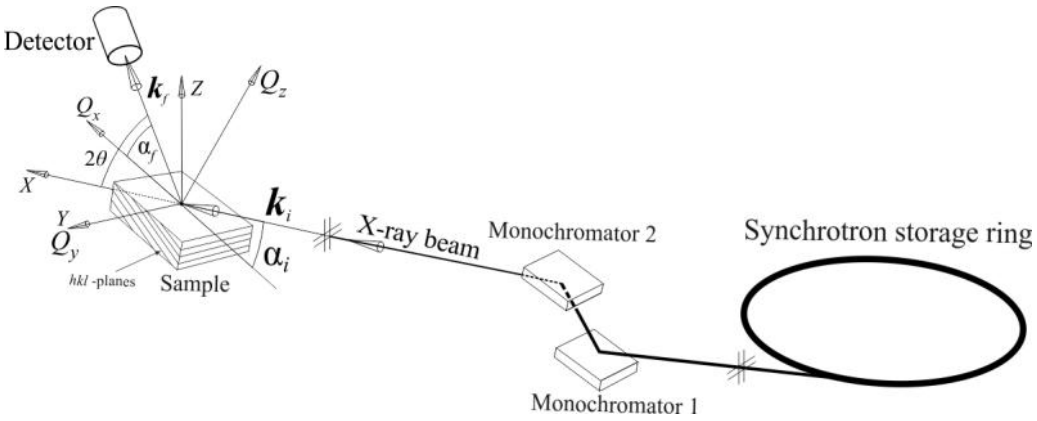

Figure 27: Laboratory and sample coordinate system definition.

3.5 Graphic representation of the reciprocal space

To explain more illustrative the reciprocal space graphical approach could be used. But first the laboratory and sample coordinate systems should be defined. The X-ray beam after the double crystal monochromator define the X axis direction of the laboratory system, see fig.27. Gravity vector $\mathbf{g}$ defines the Z axis of laboratory system as the axis opposite to the vector $\mathbf{g}$, and axis Y is predefined by right-hand rule. In the sample coordinate system the Q_z axis is defined as the axis perpendicular to the sample surface, thus the Q_x and Q_y related by right-hand rule are in sample plane. Finally, the plane XQ_z contain the axis Q_x, see fig.27.

Further, the incidence X-ray waves are described as a incidence wave vector $\mathbf{k}_i$ directed along the wave front propagation with the magnitude $|\mathbf{k}_i| = \frac{2\pi}{\lambda}$, and outgoing waves replaced with outgoing wave vector $\mathbf{k}_f$ with the same magnitude $|\mathbf{k}_f| = |\mathbf{k}_i| = \frac{2\pi}{\lambda}$. The vectors $\mathbf{k}_i$ and $\mathbf{k}_f$ are shown in the fig.27, and diffraction plane it is defined as the plane of vectors $\mathbf{k}_i\mathbf{k}_f$ in which diffraction occurs. The angles α_i and α_f are defined as the angles between the incident $\mathbf{k}_i$ and the outgoing $\mathbf{k}_f$ beams and the sample surface, respectively, and the angle between $\mathbf{k}_i$ and $\mathbf{k}_f$ is equal to 2θ.

Further the scattering diffraction processes are considered in Q_xQ_z diffraction plane. Addition and the most important vector, which should be defined is the diffraction or scattering wave vector $\mathbf{Q} = \mathbf{k}_f - \mathbf{k}_i$, introduced in the eq.23. The $\mathbf{Q}$ vector is shown in the fig.28.a, and its magnitude is

$$|\mathbf{Q}| = Q = 2k\sin\theta = 2\frac{2\pi}{\lambda}\sin\theta. \tag{35}$$

For a certain position of $\mathbf{k}_i$ with an α_i all possible positions of the $\mathbf{k}_f$ define the sphere of possible values of $\mathbf{Q}$ vector, as it is shown in the fig.28.a. This geometric construction is Ewald's sphere named after Paul Peter Ewald, a German physicist and crystallographer. If the Laue condition 28 is fulfilled for the $\alpha_i = \alpha_f$, meaning the Bragg's law 19 $n\lambda = 2d\sin\theta_B$ (where d is the spacing between the diffraction planes) allows for diffraction maximum, see fig.28.a inset. The Bragg law 19 could be rewritten as:

$$n\frac{2\pi}{d} = 2\frac{2\pi}{\lambda}\sin\theta_B. \tag{36}$$

Substitution of 35 into 36 gives:

$$n\frac{2\pi}{d} = Q. \tag{37}$$

From the eq.37 one can conclude appearance of the diffraction maximums along the direction of $\mathbf{Q}$ vector with the period $\frac{2\pi}{d}$, as it is drawn in the fig.28.b. This periodicity reveals the periodicity of the crystal planes in the chosen direction along $\mathbf{Q}$ vector (in this case perpendicular to the surface). Therefore, same repetition of the diffraction maximums could be found for any direction with different periods $\frac{2\pi}{d}$, where d corresponds the period of diffraction planes in arbitrary direction. An example of the periodic reflections in inclined with respect to the surface direction is illustrated in the fig.28.b. Moreover, for Q_x and Q_z directions the spacing d corresponds to the a and c unit cell lateral and vertical lattice parameters, respectively. And positions of the diffraction maximums along Q_x and Q_z could be described as:

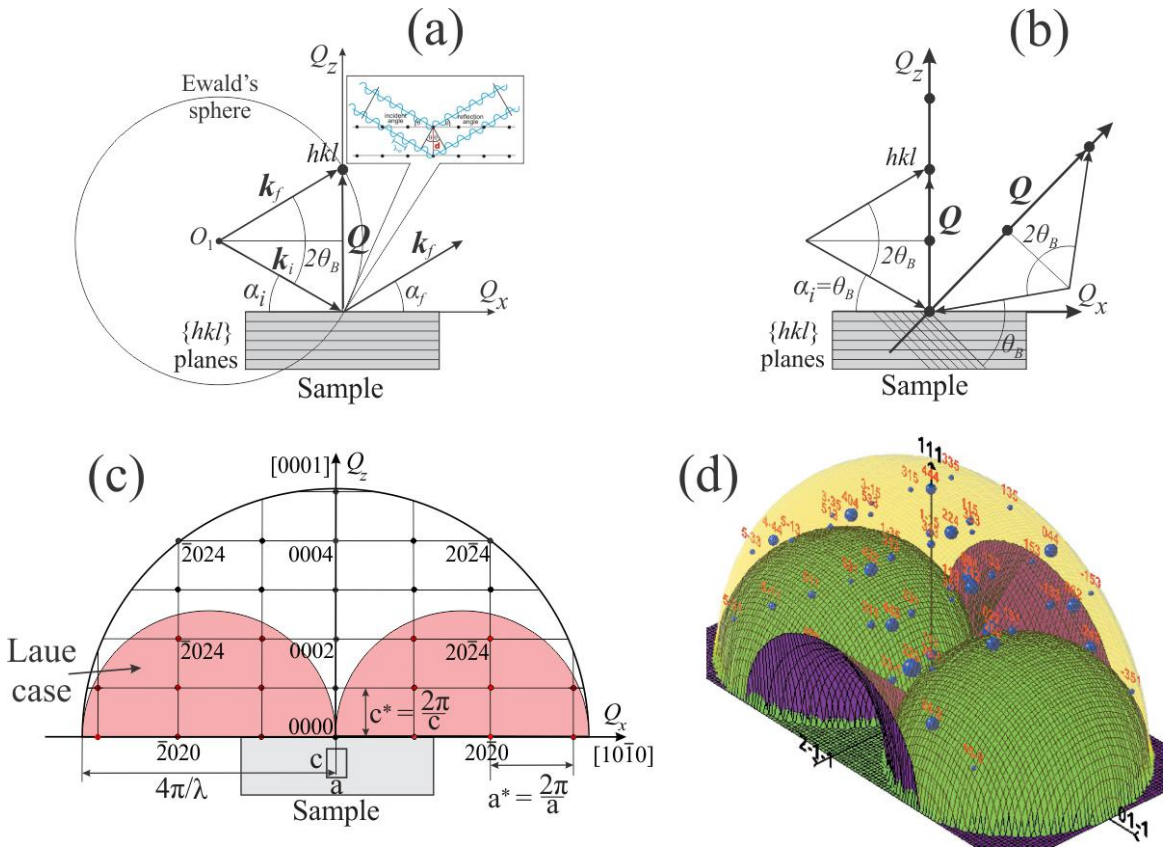

Figure 28: The Ewald's sphere (a), reflections in reciprocal space (b), available regions in reciprocal space (c), available regions in 3D reciprocal space for a certain azimuthal position of a crystal (d).

$$Q_x = h\frac{2\pi}{a},\ Q_z = l\frac{2\pi}{c}, \tag{38}$$

where h and l are the Miller or Miller-Bravais indexes of a reflection hkl or $hk.l$.

These periodicity of the diffraction maximums in Q-space (space of the vector $\mathbf{Q}$) demonstrates the reciprocal space of a crystal, shown in the fig.28.c. The period of the maximums correspond to the reciprocal space units $a^* = \frac{2\pi}{a}$ and $c^* = \frac{2\pi}{c}$ introduced in 27, see fig.28.c.

The magnitude of the vector $\mathbf{Q}$ is limited by the wavelength λ (or energy $E = \frac{hc}{\lambda}$) and can not exceed the Q_{max}=$2k = \frac{4\pi}{\lambda}$. Therefore, available region of the reciprocal space is limited by the sphere with radius Q_{max}=$2k = \frac{4\pi}{\lambda}$, as it is drawn in the fig.28.c. Moreover, if the incidence $\mathbf{k}_i$ or outgoing $\mathbf{k}_f$ beams is under the sample surface the diffraction calls Laue diffraction. In this work Laue geometry will not be used. Due to the limitations of the Laue case inside of the sphere Q_{max}, two additional not available regions corresponding to the negative α_i and α_f should be considered. The regions are colored in the fig.28.c in red color.

Finally, the reciprocal space could be considered in 3D. The accessible regions in 3D reciprocal space of a crystal were studied by Yefanov in [79, 80], and the accessible regions for a certain azimuthal position of a crystal are illustrated in the fig.28.d. Thus, the illustrative representation of the reciprocal space is given, and detailed investigation of the individual reflection could be performed.

3.6 Scans in reciprocal space and reciprocal space mapping

Graphical representation of the reciprocal space allows understand how and where in reciprocal space one can find intensity maximums. After the reflection is found the intensity from the area of reciprocal space around reflection could be recorded. The measurement could be performed by changing the $\mathbf{Q}$ vector position or magnitude in RS and recording intensity, in this section the point detector is considered. Such a "movement" in reciprocal space with the detector could be organized by changing the α_i and α_f, and is called scan in reciprocal space. In

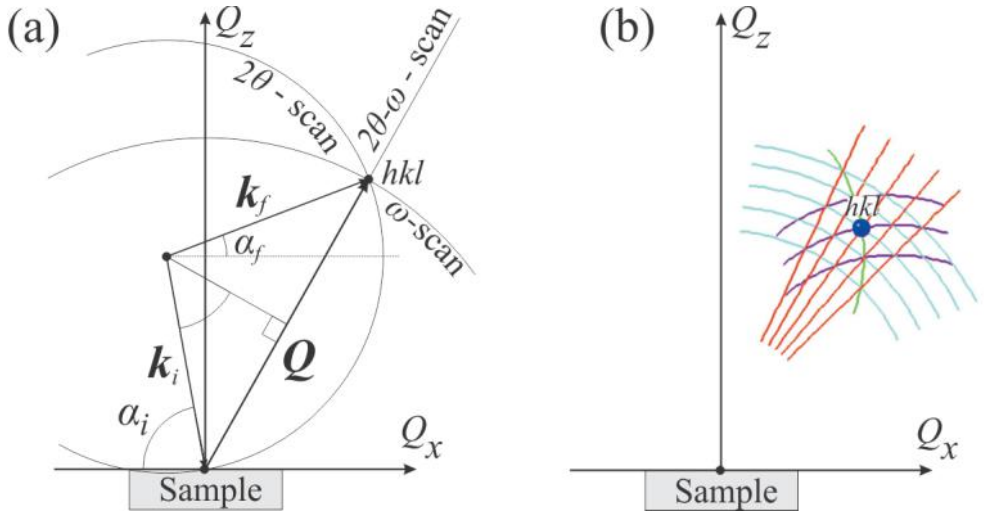

Figure 29: Scans in reciprocal space (a), and reciprocal space map (b).

the experiments at synchrotron α_i and 2θ could be changed and $\alpha_f = 2\theta - \alpha_i$, so the variation of α_i and 2θ is used to perform different scans in RS.

There are three main scans in reciprocal space, see fig.29.a. If the angle 2θ between $\mathbf{k}_i$ and $\mathbf{k}_f$ is constant, than variation of the α_i leads the rotation of the $\mathbf{Q}$ around origin of the RS, without changing Q. This scan is named as ω-scan or rocking curve scan (cause of rocking only sample during the scan), see fig.29.a. If the incidence angle $\alpha_i = constant$ and 2θ is varying the scan is 2θ-scan, and detector moves along the circle with radius k and center in the beginning of the $\mathbf{k}_i$, see fig.29.a. The last scan is $2\theta - \omega$ - scan, with changing α_i and 2θ in proportion $\triangle(2\theta) = 2\triangle(\omega)$. The scan changes the magnitude of the $\mathbf{Q}$ without changing the vector direction, as it is shown in the fig.29.a. The same scan could be achieved by changing the energy (λ) of X-ray, this scan is energy scan.

Combination of the scans allows to introduce grid of detector positions around the reflection and to record reciprocal space map (RSM) [81], as it is illustrated in the fig.29.b. The scans and RSM were introduced for the 2D RS and point detector. However, in the same manner 3D RSM could be recorded even with point detector. The linear detector for each α_i and 2θ records series of RS points corresponding the detector's channels, along the Ewald's sphere. In case of 2D detector the part of the Ewald's sphere in 3D RS is recorded for each α_i and 2θ. Therefore, the linear and 2D detectors do not change the bases of the scans and only increase the number of recorded points during the scan.

3.7 Reciprocal lattice point in reciprocal space

After the reflection is found and RSM of the reflection is recorded the shape of RLP should be studied. Mathematically is shown that the scattering amplitude in any RLP is proportional to the Fourier transform of the electron density of the sample, and shape of the reflection is defined by the shape of the sample (or an object).

Let us consider a reflection hkl of an infinite crystal (bulk crystal), as it is shown in the fig.30.a. The FT of the electron density of an infinite crystal reveals the point in reciprocal space. Hence, the RLPs of a bulk crystal are just a simple points in 3D RS, see fig.30.a. If an infinite crystal is truncated the Fourier transform of the electron density gives the rod of intensity through the reflection perpendicular to the surface of truncation, see fig.30.b. This rod of intensity in reciprocal space is a crystal truncation rod (CTR). Usually in the experiments the X-ray beam illuminates a part of the sample and sample could be assumed as a infinite truncated crystal. In this case the surface of truncation is the surface of the sample. And in the reciprocal space maps of a sample with the flat surface (not very rough) CTR should exist and should be perpendicular to the surface. Moreover, any free surface of the sample leads the formation of the streaks (rods) in RS due to FT of the electron density!

In general case if the illuminated by X-ray object has more complicated shape the shape of the reflection changes according to the FT of its electron density. However, usually for dislocation rich materials such as GaN the sample could be performed as a collection of an objects with the average lateral L and vertical V sizes. If the with the sizes are $L \ll \sqrt{\lambda R}$ and $V \ll \sqrt{\lambda R}$, than each scattered amplitude is a three-dimensional Fourier transform of an object. After the averaging of the Fourier transforms of the electron density of the objects the distribution of intensity around hkl could be received, see fig.30.c. The cuts of the "cloud" of intensity could be performed in RS

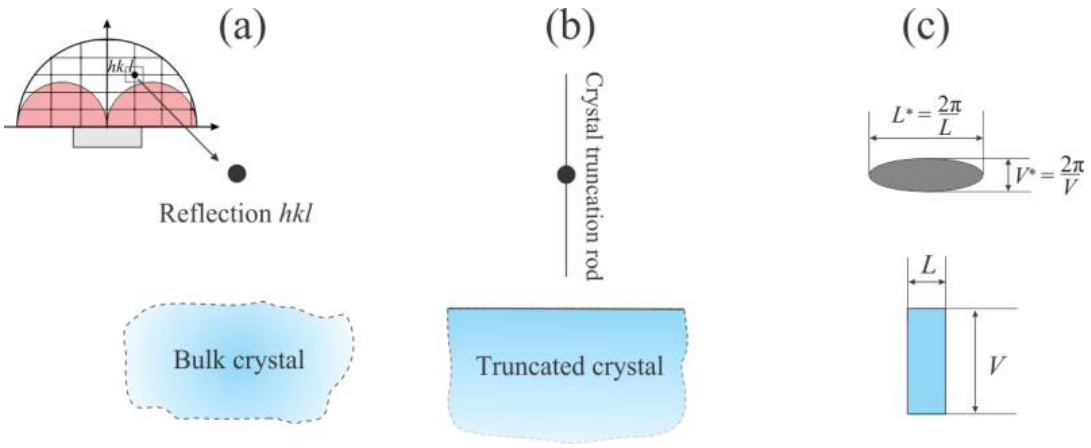

Figure 30: The RLP of a bulk crystal (a), RLP of a truncated crystal (b), and RLP of a distribution of the objects with mean sizes L and V (c).

in lateral and vertical directions and corresponding full width at half maximums (FWHMs) L^* and V^* could be derived. There is a very important relation between real space L and V and reciprocal space L^* and V^*sizes:

$$L^* = \frac{2\pi}{L},\ V^* = \frac{2\pi}{V}, \tag{39}$$

which means that L^* and $V^*$are reciprocal with respect to the L and V . That is very important property of the RS: than smaller object in some direction in real space than broader it in this direction in reciprocal space. Derived rules will be used to understand the diffraction patterns of the GaN layers.

3.8 The resolution element in reciprocal space

The divergences of the incidence and the scattered beam yield the certain distribution of different scattering signals that are summed up to the total intensity. In order to describe this effect properly the scattering intensity has to be averaged over the resolution element. The resolution element is called an area in reciprocal space that is illuminated by the incident beam and at the same moment accepted by the detector under geometrical and spectral conditions of the scattering experiment [76]. Its shape depends on the geometrical conditions of the X-ray experiment. For coplanar diffraction in the Q_xQ_z- plane the resolution element can be expressed as

$$A_{coplanar} = \Delta Q_z \Delta Q_x, \tag{40}$$

where ΔQ_z and ΔQ_x depend on the wave vector amplitude k, incidence α_i and outgoing α_f angles and the divergences of the incident and diffracted beams $\Delta_{i,f}$

$$\begin{aligned} \Delta Q_x &\approx k\sqrt{(\Delta\alpha_i \sin\alpha_i)^2 + (\Delta\alpha_f \sin\alpha_f)^2}, \\ \Delta Q_z &\approx k\sqrt{(\Delta\alpha_i \cos\alpha_i)^2 + (\Delta\alpha_f \cos\alpha_f)^2}, \end{aligned} \tag{41}$$

In grazing-incidence diffraction with $Q_{ang}Q_{rad}$ plane of diffraction the resolution element is introduced as

$$A_{GID} = \Delta Q_{ang} \Delta Q_{rad}, \tag{42}$$

where

$$\begin{aligned} \Delta Q_{ang} &\approx k\sqrt{\sin^2\theta_B \left[\alpha_f^2(\Delta\alpha_f)^2 + \alpha_i^2(\Delta\alpha_i)^2\right] + \cos^2\theta_B \left[(\Delta\theta_f)^2 + (\Delta\theta_i)^2\right]}, \\ \Delta Q_{rad} &\approx k\sqrt{(\Delta\alpha_f)^2 + (\Delta\alpha_i)^2}, \end{aligned} \tag{43}$$

where $\Delta\theta_{i,f}$ are the in-plane Bragg angles between the lateral projection of the incident and the scattered beam and the diffraction plane.

Measured in the experiments RSMs are convoluted with resolution element. Therefore, in any numerical simulation of the intensity distribution of a reflection hkl the simulated RSM should also be convoluted with the appropriate resolution function to be able to compare the intensity distributions from X-ray experiment and calculations.

3.9 Streaks in reciprocal space

Due to imperfection of the X-ray beam, experiment conditions and detection system addition distribution of intensity in reciprocal space could be observed. These intensity distributions usually elongated in predictable directions and called steaks. There are three common streaks in reciprocal space, and in this section the nature of them will be discussed.

The incidence beam has divergence, meaning a_i has certain variation $\triangle\alpha_i$ and instead of one single $\mathbf{k_i}$ vector there is a variation of $\mathbf{k_i}$, as it is illustrated in the fig.31.a. Therefore, the Bragg conditions will be satisfied for the series of incidence beams with $\alpha - \triangle\alpha_i/2 < \alpha_i^j < \alpha + \triangle\alpha_i/2$ if the detector will make angle $2\theta_B$ with respect to α_i^j. In the reciprocal space a locus of this condition is a segment in the hkl RLP parallel to the $\triangle\mathbf{k}_i$ vector and named as monochromator streak. From the geometric construction in the fig.31.a is visible that the monochromator streak is inclined with respect to the CTR in angle α_i. The presence of the streak in reciprocal space is an indicator of convergence (divergence) and from the length of the streak L_M the convergence (divergence) could be derived directly in radians:

$$\triangle\alpha_i = \frac{L_M}{k_i}. \tag{44}$$

In the fig.31.a the 2D case in shown in 3D real space the beam has convergence (divergence) in all directions and a locus is a part of the sphere boarded with an ellipse (monochromator disk).

Addition streak appears in the Bragg position due to divergence of the outgoing beam. In the Bragg condition, out of the crystal usually scatter a lot of intensity. If between a sample and detector is only air, than scattering on the air molecules occurs. If there is a flight tube, than X-ray scatter on the inlet and outlet coverage of it. So, due to the scattering the divergence of the outgoing beam $\triangle\alpha_f$ possible. If measurement is performed with point detector and an analyzer crystal, the streak is predefined by the acceptance angle of the analyzer and called analyzer streak (see fig.31.b). In case of a detector (point, linear or 2D) without analyzer the length of the streak L_A will depends on the divergence of the outgoing beam $\triangle\alpha_f$, which could be calculated in radians as:

$$\triangle\alpha_f = \frac{L_A}{k_f}. \tag{45}$$

The analyzer streak is inclined with respect to the CTR in the angle a_f, as it is seen from the fig.31.b. In 3D reciprocal space the analyzer streak is also a part of the sphere boarded with an ellipse, as the monochromator disk.

Addition problem with linear and 2D detectors could exist, due to their saturation in the Bragg peak. For some of non point detectors (linear and 2D) in case of saturation of some detector's area, electronic saturation of whole detector could happen. In this case a disk (for 2D detector) or a stripe (for linear detector) of intensity corresponding to the size of the detector will be produced in the Ewald sphere of the reflection. For 2D detector analyzer disk coincide with the disk of saturation and the streak (disk) could be called not an analyzer streak, but air scattering streak (see fig.31.b).

Usually the X-ray beam is monochromatized with a double crystal Si(111) monochromator which has high energy resolution about$\triangle E/E \approx 10^{-4}$. However, certain deviation of energy E exist. This deviation leads the deviation of the k_i, k_f and as a result $\triangle\mathbf{Q}$, as it is shown in the fig.31.c. Therefore, due to the deviation of the energy $\triangle E$ streak of the intensity along $\mathbf{Q}$ vector named as energy streak could be observed. The energy streak is inclined with respect to the CTR in the angle $\alpha_i - \theta_B$, as one can find from the fig.31.c. The length of the energy streak is $\triangle Q = 2\triangle k \sin\theta_B$. Taking into account that $k = \frac{2\pi}{\lambda}$ and $\lambda = \frac{hc}{E}$, one can calculate the energy variation as:

$$\triangle E = \frac{\triangle Q hc}{4\pi \sin\theta_B}. \tag{46}$$

Thereby, in a reflection except the CTR monochromator, detector and energy streaks inclined in a_i, a_f and $\alpha_i - \theta_B$ angles with respect to the CTR could be observed. The streaks are shown in the fig.31.d. Due to their certain inclination the streaks will not be mixed up with the other diffraction features, and moreover from the lengths of the streaks one can calculate the X-ray beam parameters.

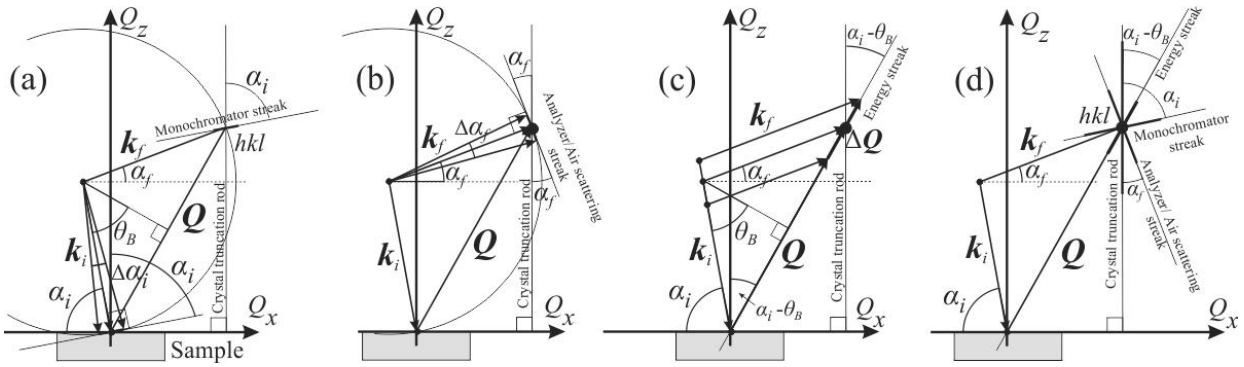

Figure 31: Streaks in reciprocal space: monochromator streak (a), analyser/air scattering streak (b), energy streak (c), all streaks in the reflection hkl (d).

3.10 X-ray diffraction geometries

Depending on the required information about a specimen different techniques realized by different diffraction geometries could be used. Structure determining methods based on precise measurement of absolute position and integral intensity of several reciprocal lattice points. The content and strain of an alloy could be derived from the position of a certain RLP. For shape, strain field or dislocation density determination scattered intensity around one reciprocal lattice point has to be measured since it contains the square of the FT of the shape function and strain information. To have clear overview different diffraction geometries and their application will be studied.

If the incident $\mathbf{k}_i$ and outgoing $\mathbf{k}_f$ wave vectors are lying in the same plane with the sample normal (by another words, if the diffraction plane is perpendicular to the sample surface), than diffraction geometry called coplanar diffraction geometry or just X-ray diffraction (XRD) geometry. If in coplanar diffraction geometry the incidence angle α_i is equal to the outgoing angle α_f the diffraction geometry has a name symmetric X-ray diffraction (SXRD) geometry, otherwise ($\alpha_i \neq \alpha_f$) the geometry is asymmetric X-ray diffraction (AXRD) geometry. In case of SXRD the diffraction planes are parallel to the surface and reflections are lying in the Q_z axis, and called symmetric reflections and reflections with Miller indexes $00l$, see fig.32.a. All other coplanar reflections are asymmetric with indexes hkl, and their diffraction planes $\{hkl\}$ are inclined with respect to the surface of the sample, as it is shown in the fig.32.b.

For the properties of the sample surface and interface investigation the X-ray reflectivity (XRR) coplanar diffraction geometry could be performed, see fig.32.c. In XRR the incidence and outgoing angles are small and in reciprocal space geometry study an area near to the origin or reflection 000.

If the plane of $\mathbf{k}_i$ and $\mathbf{k}_f$ doesn't contain the sample's normal diffraction geometry called non-coplanar diffraction geometry. There are three common non-coplanar diffraction geometries: GID, GISAXS and skew diffraction geometry. If the diffraction plane is inclined with respect to the sample surface, as it is shown in the fig.32.d, the geometry called skew diffraction geometry. The skew diffraction geometry study hkl reflections, and could be used to record some diffraction features, as it will be shown in the Chapter 7.3. However, the most frequently used example of non-coplanar diffraction geometry is the grazing-incidence diffraction (GID) geometry. The GID is the critical case of skew geometry, when the inclination of the diffraction plane with respect to the sample surface is about critical angle, and is almost zero, as it is illustrated in the fig.32.e. Therefore, in GID the incidence angle $\alpha_i \approx \alpha_c$ and outgoing $\alpha_f \approx \alpha_c$, and the angles θ_i and θ_f are the angles between the incident beam and the outgoing beam with the diffracting planes respectively. The major application of GID is study of the diffraction planes $\{hk0\}$ perpendicular to the sample surface, to measure strain relaxation in thin layers and investigation of nano-objects.

The last non-coplanar diffraction geometry is grazing incidence small angle X-ray scattering (GISAXS) geometry, shown in the fig.32.f. In GISAXS the incidence and outgoing angles are very small and area of investigation in reciprocal space corresponds to the origin 000, as it was for XRR. But in GISAXS the scattering intensity out of diffraction plane is recorded. The GISAXS geometry could be used for the investigation of the surface properties as well as XRR, but could be also performed for the nano-objects shape study.

In this work more often XRD (SXRD and AXRD) and GID geometries will be used.

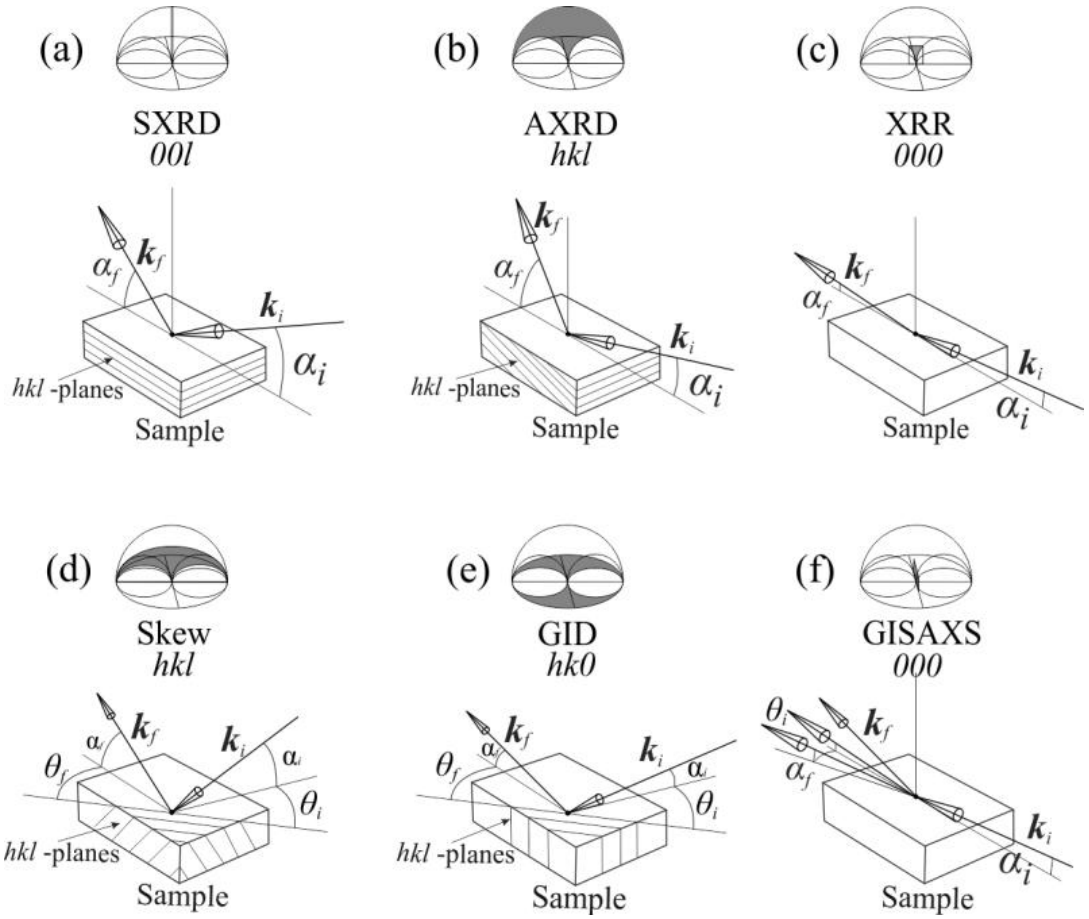

Figure 32: X-ray diffraction coplanar (up) and non-coplanar (down) geometries with accessible regions of reciprocal space: SXRD (a), AXRD (b), XRR (c), Skew (d), GID (e), and GISAXS (f).

3.11 Calculation of coordinates in reciprocal space

The coordinates of the diffraction vector **Q** could be calculated in general case as a dot products of the unit vectors of corresponding coordinate system. Usually coordinate system of the sample is used to find the components of the **Q**. In case of coplanar diffraction geometry in Q_xQ_z diffraction plane the coordinates of **Q** depend on α_i, α_f, and their relation with Q_x, Q_z is visible from the geometry of $\mathbf{k}_i$, $\mathbf{k}_f$ and **Q** in the fig.28. Thus, one can calculate the components of the **Q** using formulas:

$$Q_x = \frac{2\pi}{\lambda}(\sin\alpha_f + \sin\alpha_i), \tag{47}$$

$$Q_z = \frac{2\pi}{\lambda}(\cos\alpha_f - \cos\alpha_i), \tag{48}$$

In case of Skew or GID geometries the coordinates of **Q** depend on the four angles α_i, α_f, θ_i, and θ_f see fig.32. And **Q** coordinates in GID (or skew) geometry could be performed in $Q_xQ_yQ_z$ coordinate system as [76]:

$$Q_x = \frac{2\pi}{\lambda}(\cos\alpha_f \sin\theta_f + \cos\alpha_i \sin\theta_i), \tag{49}$$

$$Q_y = \frac{2\pi}{\lambda}(\cos\alpha_f \cos\theta_f - \cos\alpha_i \cos\theta_i), \tag{50}$$

$$Q_z = \frac{2\pi}{\lambda}(\sin\alpha_f + \sin\alpha_i). \tag{51}$$

However usually in GID the incident angle α_i and the outgoing angle α_f are relatively small and close to the critical angle, and could be neglected in the calculation of the components of scattering wave vector. And diffraction vector's **Q** components in GID could be calculated as:

$$Q_x = \frac{2\pi}{\lambda}(\sin\theta_f + \sin\theta_i), \tag{52}$$

$$Q_y = \frac{2\pi}{\lambda}(\cos\theta_f - \cos\theta_i), \tag{53}$$

To overcome the difference between indexation in GID and coplanar geometries angular coordinate system in diffraction plane could be used. In this case the components Q_{ang}, Q_{rad} are given in diffraction plane and depend only on angles β_i, β_f between diffraction planes and $\mathbf{k}_i$, $\mathbf{k}_f$, respectively. And components in diffraction plane could be calculated as:

$$Q_{ang} = \frac{2\pi}{\lambda}(\sin\beta_f + \sin\beta_i), \tag{54}$$

$$Q_{rad} = \frac{2\pi}{\lambda}(\cos\beta_f - \cos\beta_i), \tag{55}$$

Sometimes coordinates of **Q** are performed in the coordinate system related to the crystallographic orientations. In this case components could be written as $Q_{10\bar{1}0}$ and Q_{0001}, for example.

4 Dislocation density determination from diffuse intensity distribution in reciprocal space

4.1 The mosaic model of GaN materials

4.1.1 Mosaic model in 3D reciprocal space

The GaN material is dislocation rich material with dislocation density in order $10^{10} cm^{-2}$ [8, 82]. The treading dislocations leads the disordering of the diffraction planes. The screw type of TD disturb the ordering of the planes parallel to the sample surface and leads their tilt (fig. 33a.), in total for a some angle α. The edge type of TD interrupt sequences of the planes perpendicular to the sample surface and leads their twist (see fig.33b.), in total for a some angle β. To explain the broadening of the reflections in reciprocal space mosaic model was introduced[83, 84, 8, 85] . In the model the sample is presented as ensemble of the mosaic blocks, which are tilted (fig.33.c.) and twisted (fig.33.d.) with respect to each other, and dislocations are located at grain boundaries. The height of the blocks $L_{\perp}^{z}$ called vertical correlation length, usually corresponds to the layer thickness. The lateral parameters $L_{\parallel}^{x}$, $L_{\parallel}^{y}$ called lateral correlation length, correspond to mean distance between dislocations, and usually are much smaller than vertical correlation length ($L_{\parallel}^{x} \ll L_{\perp}^{z}$, $L_{\parallel}^{y} \ll L_{\perp}^{z}$)[8].

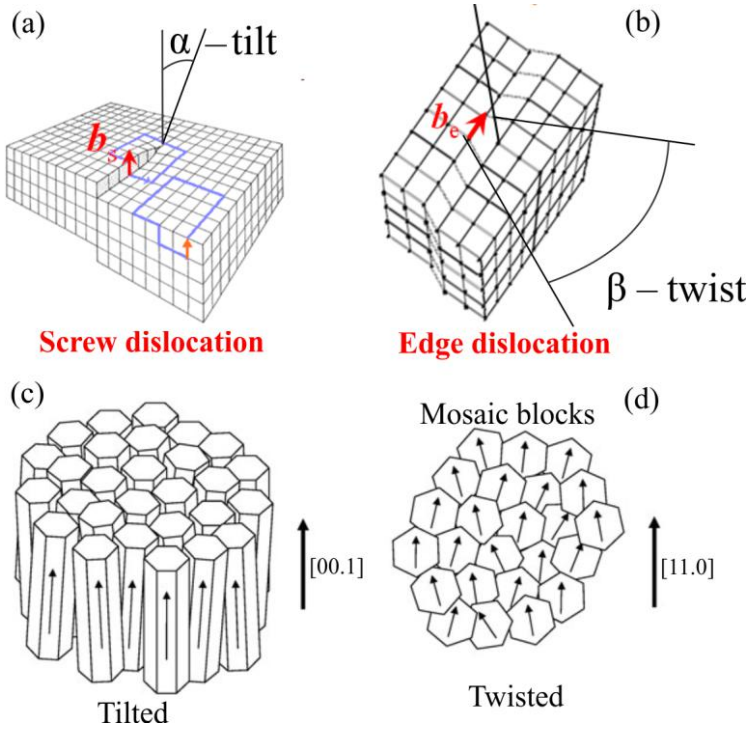

Figure 33: Screw dislocation with tilt of the crystallographic planes parallel to the sample surface (a), edge dislocation and twist of the crystallographic planes perpendicular to the sample surface (b), mosaic model blocks tilted (c) and twisted (d).

As it was shown in the Chapter 3.4, in far field the diffraction pattern in reciprocal space of an object is basically its Fourier transform. In case of a bulk (infinite) crystal in reciprocal space after Fourier transform one can receive certain point in all SXRD, AXRD and GID geometries, as it is shown in the fig.34.a. In order to understand the influence of the mosaicity on the diffraction processes and finally on the view of the reciprocal space reflections, it is necessary to start from one single block and understand the shape of the RLP of it. An average block has different finite sizes in different directions. A dimension finite size a will lead the broadening with reciprocal value $S = 2\pi/L$, of the reflection in RS in the same direction. In the fig.34.b. the broadening of the reflections in different directions are shown. That means that reflection of one single block should be broad due to finite size of the block. The next step should be the averaging over the mosaic blocks. Due to the fact that blocks have slightly different dimensions (some distribution of $L_{\parallel}^{x}, L_{\parallel}^{y}, L_{\perp}^{z}$) the reflections will be smoothed, but will be identical in different reflections (fig.34.c)! The blocks have larger size in the direction [0001], therefore the reflections will be compressed

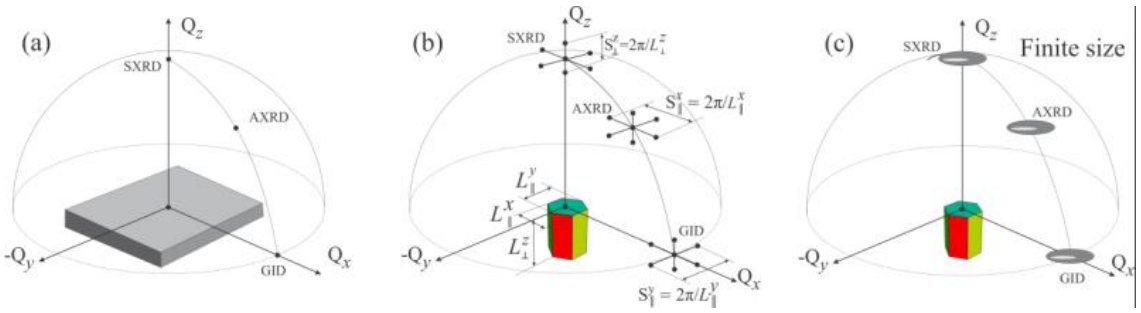

Figure 34: The view in 3D reciprocal space of the SXRD, AXRD and GID reflections in case of bulk crystal (a), broadening in different directions due to the finite size of the blocks (b), reflections view affected only by finite size (c).

in [0001] direction and will be broader in angular (perpendicular to [0001] direction). Usually, due to homogenous distribution the reflections are symmetric as it is shown on the fig.34.c.

The next question is the influence of the tilt α and twist β of the blocks on the reflections. To make our thought experiment easier let us neglect the finite size influence on the reflections and take a look only on one single point of the reflections in RS, as it was in case of infinite crystal (fig.34.a). Than the twist of the mosaic blocks in angle β , will rotate reflections about Q_z axis (about [0001] direction), as it is shown on the fig 35.a. It is visible that twist β directly influence on the GID reflection, partially on the AXRD and almost has no influence on the SXRD. The tilt α of the blocks will tilt reflections in reciprocal space around [0001] direction. It will spread SXRD in all directions on the sphere with radius equal diffraction vector of the reflection (fig.35.b). The influence on the GID reflection will be mostly represented in Q_zQ_x plane and almost no influence will be in the direction out of the Q_zQ_x diffraction plane. The AXRD will be spread in all directions, but mostly in Q_zQ_x plane.

Coming closer to the real influence of the tilt and twist, it is possible to combine the influence both of them on the reflections (fig.35.c). Now all of the reflections will be spread in all directions, nevertheless, the influence on GID reflection out of Q_zQ_x diffraction plane will be only due to twist β and on the SXRD in all directions only due to tilt α (fig.35.c). The AXRD reflection will be spread in all directions on its own sphere partially by tilt α and partially by twist β. And the dominant role between tilt and twist will play this factor to which geometry reflection position is closer, to SXRD or to GID. Than closer AXRD to SXRD (angle φ of inclination of the diffraction planes $\{hkl\}$ closer to zero), than more influence of tilt and less of twist and opposite, than closer AXRD to GID (angle φ closer to 90 degree), than higher influence of twist and lower of tilt (fig.35.c).

Finally taking into account finite size, tilt α and twist β of the blocks one can plot the view of the reflections in 3D reciprocal space (fig. 35.d). Some of the drawing related to the mosaic model reflections in 3D was done by Sirkant et al. [86], and R.S. Lee [87] has illustrated the influence of the tilt on all reflections in 2D, but with our thought experiment we understood influence of all this parameters deeper, especially for AXRD, which was a question for the Sirkant.

Using mosaic model one is able to answer on the question how it is possible to measure tilt α and twist β. As we already know, direct measurement of tilt α can be done by scanning SXRD in any angular (perpendicular to [0001]) direction, for example along AB in Q_zQ_x diffraction plane, introducing rocking curve scan (fig.35.d). The direct measurement of twist β can be realized by scanning GID reflection in out of Q_zQ_x diffraction plane along CD (perpendicular Q_zQ_x plane) direction, introducing rocking curve scan in GID geometry (fig.35.d).

4.1.2 Mosaic model in 2D reciprocal space

Now we can go deeper into details of mosaic model in 2D reciprocal space and have a good look at diffraction plane Q_zQ_x and angle of the tilt α . As that was shown by Chierchia et al. [88] in 2D reciprocal space, in case of only tilt α, without finite size effect, the broadening of a reflection should be always in angular (perpendicular to a diffraction vector $\mathbf{Q}$) direction and FWHM (in radian) should be equal to α (in radian) (see fig. 36.a.top):

$$FWHM(radian)=\alpha\,(radian) \quad or \quad FWHM(nm^{-1})=\alpha\,(radian)\cdot Q(nm^{-1}) \tag{56}$$

In another case, the broadening due to only finite size without tilt at all, leads the permanent broadening $S=\frac{2\pi}{L_{\|}}$, where $L_{\|}$ is the lateral coherence length of the mean mosaic block in diffraction plane (see fig. 36.a.bottom).

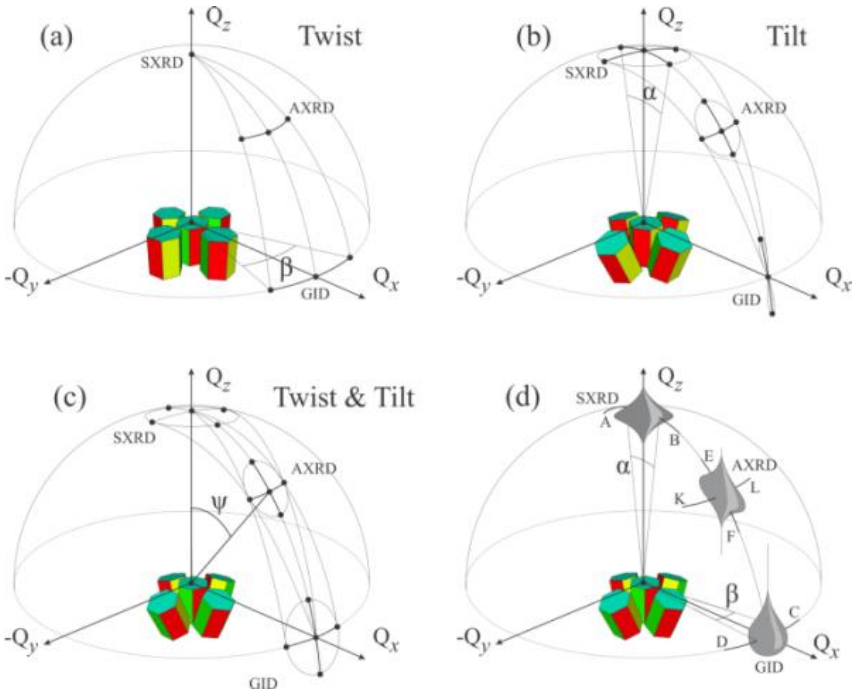

Figure 35: The 3D view of the SXRD, AXRD and GID reflections of mosaic blocks which are twisted (a), tilted (b), twisted and tilted (c) and 3D view of the reflections affected by finite size of the blocks, tilt and twist (d).

In case of simultaneous influence of tilt and finite size on the reflections, the broadening doesn't come to zero in the origin of the RS (fig. 36.b), but comes to $S = \frac{2\pi}{L_{\parallel}}$. And the FWHM (in nm^{-1}) is not proportional to the tilt α (in radian), however they are in linear dependence, as it is possible to see from fig. 36.b. From the fig.36.b. it is possible to write the dependence of FWHM (in nm^{-1}), as:

$$FWHM(nm^{-1}) = \alpha\,(radian) \cdot Q(nm^{-1}) + S_{\parallel}. \tag{57}$$

It is visible from the sketch that $FWHM(nm^{-1}) = FWHM(radian) \cdot Q(nm^{-1})$ and it is possible to rewrite 57 as:

$$FWHM(radian) \cdot Q(nm^{-1}) = \alpha\,(radian) \cdot Q(nm^{-1}) + S_{\parallel}. \tag{58}$$

Additionally, it is possible to derive from fig. 36.a.bottom that $Q = 2 \cdot k \cdot sin\theta$, where $k = \frac{2\pi}{\lambda}$. Then, one can substitute $Q = 2 \cdot \frac{2\pi}{\lambda} \cdot sin\theta$ and $S = \frac{2\pi}{L_{\parallel}}$ in the formula:

$$FWHM(radian) \cdot 2 \cdot \frac{2\pi}{\lambda} \cdot sin\theta = \alpha\,(radian) \cdot 2 \cdot \frac{2\pi}{\lambda} \cdot sin\theta + \frac{2\pi}{L_{\parallel}}, \tag{59}$$

and finally after all simplifications:

$$FWHM(radian) \cdot \frac{sin\theta}{\lambda} = \alpha\,(radian) \cdot \frac{sin\theta}{\lambda} + \frac{1}{2L_{\parallel}}. \tag{60}$$

The same logic could be applied for the twist angle β calculation, and all derived equations are valid for the twist β as well. The equation 60 first time was derived by Willamson and Hall and named after them [84, 83]. According to the equation of Williamson and Hall, the $FWHM(radian) \cdot \frac{sin\theta}{\lambda}$ linearly depends on the parameter $\frac{sin\theta}{\lambda}$, and it is possible to plot this dependence for the series of symmetric reflections. This plot has a name Williamson-Hall (WH) plot [8] and it is shown on the fig. 36.c. The slope of the plot is exactly tilt α of the mosaic blocks. And intersection of the line with ordinate axis equal to $\frac{1}{2L_{\parallel}}$. The Williamson-Hall plot is widely used method to determine twist α and tilt β of the mosaicity of III-V nitrides.

However, for the direct measurements of twist, GID geometry is needed [89]. The GID measurement is high flux, long exposition and experience required experiment. It is not so technically easy to perform GID measurement at standard laboratory X-ray source. For the twist angle β determination, series of asymmetric reflections could be

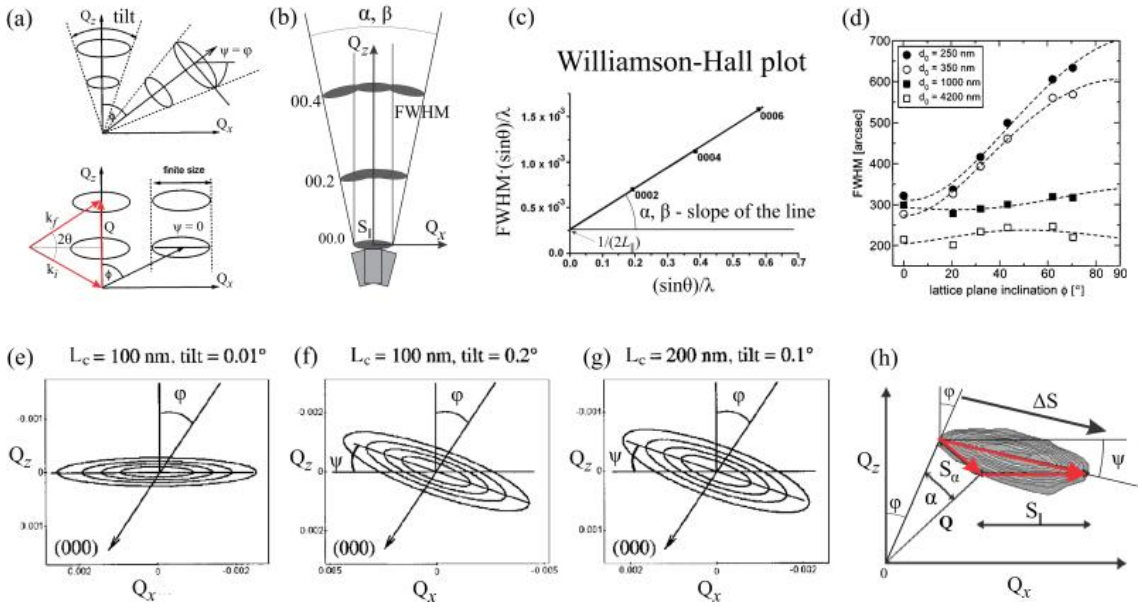

Figure 36: Reflections affected only by finite size or tilt shape (a), general case of tilt and finite size influence on the reflections (b), Williamson-Hall plot (c) and dependence of FWHM on diffraction plane inclination φ (d). In the bottom part of the figure, simulation results of asymmetric $10\bar{1}5$ RSMs of GaN are presented, taken from [91]. Dominant lateral coherence length (e); dominant tilt (f) and (g) (parameters are given on top of the figure) and representation of the inclination ψ of the AXRD reflection as influence of tilt α and lateral coherence length $L_{\parallel}$. Decomposition of α and $L_{\parallel}$components from AXRD RSM (h), taken from [8].

measured with different angles of inclination of diffraction planes φ. Here it is very important to choose correct scan of the reflection according to our knowledge about broadening of the AXRD reflections due to tilt and twist. The influence of twist β on AXRD should be measured only out of Q_zQ_x diffraction plane along KL. And not along EF using usual rocking curve scan in the Q_zQ_x diffraction plane (see fig.35.d). The measurement of the AXRD reflection broadening along KL direction in RS is possible to realize by simple rotation of the sample around its normal or using rocking curve scan in skew symmetric geometry (introduced in the Chapter 3.10). Then, FWHM of the AXRD reflections could be plotted against φ, and broadening of the GID reflection could be determined as a limit of the FWHM of AXRD reflections when φ is going to 90 degree (corresponds to GID). An example of the plot of AXRD FWHM against φ is shown on the fig.36.d, which was performed by Huang et al. in [90].

Measurements of asymmetric reflections may bring an additional problems in understanding. Therefore, it is better to take a look at some details of the AXRD reflections view. In Q_zQ_x diffraction plane tilt α and finite sizes $L_{\parallel}$ and $L_{\perp}$ of mosaic blocks will play the most important role. As we already know $L_{\parallel} \ll L_{\perp}$, that means that in reciprocal space the relation between parameters will be opposite $S_{\parallel} \gg S_{\perp}$,and we can neglect on parameter $L_{\perp}$. According to Chierchia [88], in case of only tilt, asymmetric reflections should be broad in angular direction (perpendicular to $\mathbf{Q}$), and therefore should be inclined in angle $\psi = \varphi$ with respect to Q_x direction. (fig.36.a.top). Oppositely, the same reflections should have no inclination $\psi = 0$ in case of only finite size effect (fig.36.a.top). Therefore, it is possible to conclude that in general case, where tilt α and broadening due to finite size $L_{\parallel}$ will influence simultaneously, AXRD reflection will be inclined and angle of inclination will ψ be $0 \leq \psi \leq \varphi$. The R. Chierchia had investigated the inclination of the AXRD reflections in [85], using the model of V. Holy developed in [91]. In this investigation he showed how ratio between α and $L_{\parallel}$ could influence ψ. If finite size $L_{\parallel}$ is dominated by α, the inclination ψ will be almost zero (fig.36.e.). And even more interesting that the same inclination ψ of the diffuse cloud could be achieved by different relations between α and $L_{\parallel}$. In the paper R. Chierchia gave an example of two reflections with parameters $\alpha = 0.2$, $L_{\parallel} = 100nm$ and $\alpha = 0.1$, $L_{\parallel} = 200nm$, which have the same angle of inclination ψ (see fig.36.f. and g.). From the first sight it seems like inclination of the reflection cloud possible to derive using only numerical simulation, but there is alternative simple method to estimate was introduced by Moram et al. [8]. In this simple model tilt α and finite size $L_{\parallel}$ components are presented as a vectors $S_{\alpha} = \alpha \cdot Q$, perpendicular to $\mathbf{Q}$ and $S_{\parallel} = \frac{2\pi}{L_{\parallel}}$, parallel to $\mathbf{Q}_x$ vector , and vector of inclination of the reflection $\triangle S = S_{\alpha} + S_{\parallel}$

(.see fig.36.h.). Using this model one can determine any of the vector if the other two are known. For example, if α and $L_{\parallel}$were derived from WH plot, then inclination of the AXRD reflection ψ could be found as [8]:

$$\psi = \arccos\left(\frac{(\mathbf{S}_{\alpha} + \mathbf{S}_{\parallel}) \cdot \mathbf{Q}_x}{|\mathbf{S}_{\alpha} + \mathbf{S}_{\parallel}| \cdot Q_x}\right). \tag{61}$$

To complete the discussion about mosaic model application one needs to answer on the question how to estimate density of dislocations, using derived parameters from WH plot. As we already know, $L_{\parallel}^x$ and $L_{\parallel}^y$ are correspond to mean distance between dislocations in lateral directions. And in principle, dislocation densities can be already obtained from lateral correlation lengths $L_{\parallel}^x$ and $L_{\parallel}^y$ measurement (usually $L_{\parallel}^x \approx L_{\parallel}^y = L_{\parallel}$). For a random dislocation distribution, dislocation densities D are given by Lee et al. [87]:

$$D = \frac{1}{L_{\parallel}^x L_{\parallel}^y} = \frac{1}{L_{\parallel}^2}, \tag{62}$$

However, $L_{\parallel}$ values often couldn't be measured precise enough, so tilt α and twist β measurements should be used dislocation density calculation. Gay et al. first related dislocation densities D to rocking curve ω-FWHM β [82]. Assuming a mosaic structure where dislocations are located at grain boundaries. The first approximate formula of dislocation density D is:

$$D \approx \frac{\beta}{3bt}, \tag{63}$$

where b is the length of the Burgers vector, β is the ω-FWHM and t is the mean grain size. A related, but more accurate formula was provided by Metzger et al. [92]:

$$D = \frac{\beta}{2.1bd_0}, \tag{64}$$

where d_0 is essentially the lateral correlation length.

Chierchia et al. [88] combined this for edge dislocations with an equation describing finite size effects

$$D_e = \frac{1}{2.1b_e d_0}\sqrt{\beta_e^2 - \left(\frac{0.9\lambda}{d_0 \cos\theta_B}\right)}, \tag{65}$$

where β_e is the twist value, affected by both tilt and by limited correlation lengths and θ_B is Bragg angle.

Kaganer et al. [93] showed that equation 64 must be modified for a random dislocation distribution in the case of correlation as:

$$D_e = \frac{18\beta_e^2 \cos^2\theta_B}{(2.8 + \ln M)^2 b_e^2}, \quad D_s = \frac{36\beta_s^2}{(2.4 + \ln M)^2 b_s^2}, \tag{66}$$

where M describes the degree of correlation and $M = L\sqrt{D_B}$, $D_B = \frac{\alpha}{2.1bd_0}$ for screw and $D_B = \frac{\beta}{2.1bd_0}$ for edge dislocations, and L is the area over which the Burgers vector averages to zero (note that no crystal analyzer is used). Parameter M can vary from $M \approx 1$ (highly correlated) to $M \gg 1$ (uncorrelated). When correlation is taken into account, dislocation density values can increase by up to a factor of 10 [93]. However, if d_0 is not known accurately (for example, in low dislocation density films), it may be simpler to separate the two effects beforehand and use equation 64 instead, as appropriate.

Formula for a random distribution of dislocations have been proposed by Kurtz et al. [94] for screw D_s and edge D_e dislocation densities:

$$D_s = \frac{\alpha^2}{9 \cdot |\mathbf{b}_{screw}|^2}, \quad D_e = \frac{\beta^2}{9 \cdot |\mathbf{b}_{edge}|^2}, \tag{67}$$

where α is tilt, β twist, $\mathbf{b}_{edge}$ - edge dislocation Burgers vector and $\mathbf{b}_{screw}$ - screw dislocation Burgers vector.

modified by Dunn and Koch [95]:

$$D_s = \frac{\alpha^2}{4.35 \cdot |\mathbf{b}_{screw}|^2}, \quad D_e = \frac{\beta^2}{4.35 \cdot |\mathbf{b}_{edge}|^2}. \tag{68}$$

Equations 64 and 68 show that the dislocation density is proportional to β for a mosaic film structure, but proportional to β^2 for a random dislocation distribution. Furthermore, equations 65 and 68 are appropriate for

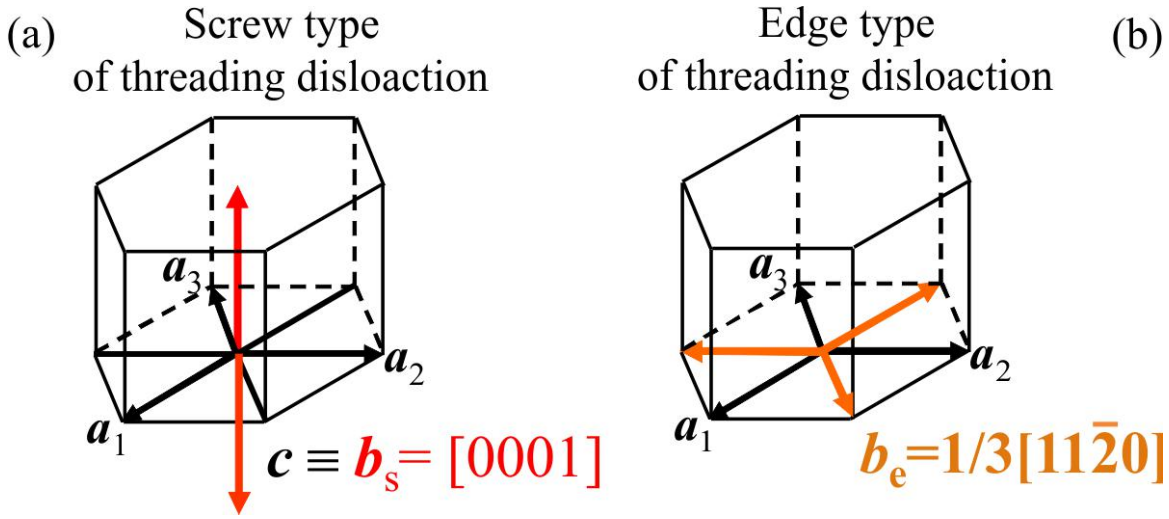

Figure 37: Screw (a) and edge (b) dislocations Burger's vectors.

high dislocation density films (broad ω-FWHM), whereas equation 64 may be sufficient for low dislocation density films (narrow ω-FWHM). In this work samples with high dislocation density is investigated, random distribution of TDs is assumed, and equation 68 will be used for screw D_s and edge D_e TD densities calculation using tilt α and twist β derived from WH plot.

In addition, one can think about mixed dislocations. One mixed dislocation combines the displacement of one screw plus one edge dislocation, and unfortunately, mosaic model with presented formulas are not able to distinguish between pure TDs and components of mixed dislocation. Therefore, mixed dislocations will partially contribute to tilt α and partially to twist β, and their density will be distributed between screw D_s and edge D_e dislocation densities.

4.2 Numerical Monte Carlo calculation of diffuse scattering from TDs.

Recently, Barchuk, Holy et al. [67] have developed the model based on numerical Monte Carlo (MC) calculation to simulate the diffuse scattering of the defects in [0001] oriented c-GaN materials. The model allows determine dislocation density with an error less than 10%. In this work the model of the V. Holy will be used for the TDD calculation and will be discussed in details in this section.

As we already know from the Chapter 2.3, that c-plane GaN materials have a hexagonal symmetry and contains in the majority cases of two basic types of defects, i.e., edge and screw threading dislocations, see fig.37. For convenience two types of screw dislocations with the Burgers vectors toward the surface $b_s = +[0001]$ and in opposite direction $b_s = -[0001]$ are distinguished (see fig.37.a). Edge dislocations can be divided into three types with the Burger's vectors $b_e = \frac{1}{3}[11\bar{2}0]$. The Burgers vectors b_e of different types of edge dislocations include an angle of 120°, and lie in the horizontal xy-plane parallel to the sample surface (see fig.37.b). In addition to these dislocation types, mixed threading dislocations occur frequently, however they can be decomposed into pure screw and edge components as it was discussed in the Chapter 4.1: $b_m = b_s + b_e$ and we do not consider these dislocations separately.

The simulation depends on a specimen properties and on the beam parameters i.e. convergence, coherence... The synchrotron X-ray beam has limited coherence in beam and transverse directions. Due to this reason it is possible to define the coherent element of the incoming radiation, as an area with the same phase of X-ray. Therefore, different areas of a specimen surface will be irradiated by different coherent elements of the incoming radiation. And specimen could be presented as an ensemble of coherently irradiated areas (S_{coh}), sample with a coherently irradiated area is shown in the fig.38.a. For each S_{coh} coordinate system x, y, z was define that xy plane is parallel to the sample surface, as it is shown in the fig.38.b.

The algorithm of the calculation in the model consists of several steps:

- In a coherently irradiated area (S_{coh}) the positions $\left(x_j^{(\alpha)}, y_j^{(\alpha)}\right)$ and types α of the TDs using a random generator are distributed, see fig.38.c.

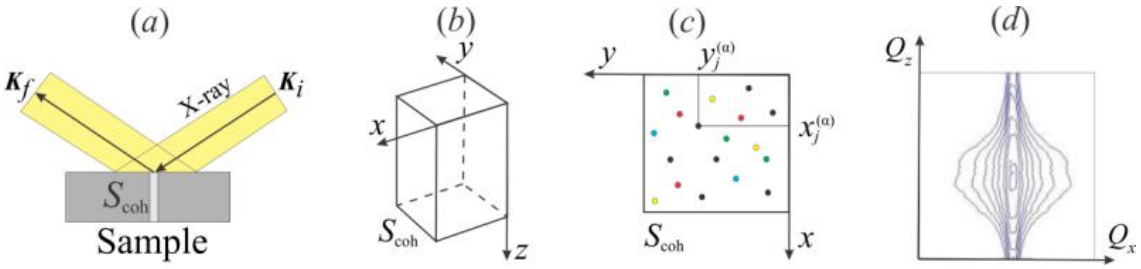

Figure 38: A sample with a coherently irradiated area (S_{coh}) (a), S_{coh} with coordinate system (b), random distribution of the dislocations on the xy plane of S_{coh} (c), and simulated RSM based on Monte Carlo simulation (d).

- From the positions of individual dislocation types in S_{coh} obtained in the previous step the total displacement field of all dislocations in S_{coh} assuming a linear superposition is calculated:

$$\mathbf{u}(\mathbf{r}) = \mathbf{u}(x,y,z) = \sum_{\alpha=1}^{5}\sum_{j=1}^{N}\mathbf{u}^{(\alpha)}\left(x - x_j^{(\alpha)}, y - y_j^{(\alpha)}, z\right), \tag{69}$$

where $u^{(\alpha)}(x,y,z)$ is the displacement vector in point (x,y,z) due to a dislocation of type α ending at the sample surface in point $(x,y) = (0,0)$, and $\left(x_j^{(\alpha)}, y_j^{(\alpha)}\right)$ is the intersection point of the j-th dislocation of type α with the sample surface. In the expressions for $\mathbf{u}^{(\alpha)} \times (\mathbf{r})$ surface relaxation of internal stresses was taken into account, explicit formulas can be found in [96]. The scattered intensity depends only on the component of the total displacement field parallel to the diffraction vector $\mathbf{Q}$, therefore, in symmetrical diffraction, only the vertical component $u_z(\mathbf{r})$ matters. The expressions for $u_z^{(s,e)}(r)$ are rather simple:

$$u_z^{(s)}(r) = \frac{b_z^{(s)}}{2\pi}\arctan\left(\frac{y}{x}\right), \tag{70}$$

$$u_z^{(e)}(\mathbf{r}) = \frac{\nu}{1-\nu}\cdot\frac{\mathbf{r}\cdot\mathbf{b}^{(e)}}{2\pi}\cdot\frac{z + 2r(\nu-1)}{r(r-z)}, \tag{71}$$

where ν is the Poisson ratio (for simplicity, isotropic elasticity is assumed).

- Knowing the total displacement field of all dislocations present in S_{coh} the amplitudes $E_j(\mathbf{q})$ and the intensity $I_j(\mathbf{q}) = |E_j(\mathbf{q})|^2$ of the X-ray wave scattered by this part of the sample using the far-field limit and kinematic approximation were calculated:

$$I_j(\mathbf{q}) = \left| A \int_{S_{coh}} \int dx dz \int_{-T}^{0} dz\, e^{-i\mathbf{h}\cdot\mathbf{u}(\mathbf{r})} e^{-i\mathbf{q}\cdot\mathbf{r}} \right|^2, \tag{72}$$

where A is a constant containing among other parameters the amplitude of the primary wave and the polarizability coefficient χ_h, $\mathbf{q} = \mathbf{K}_f - \mathbf{K}_i - \mathbf{Q}$ is the reduced scattering vector, and $\mathbf{K}_{i,f}$ are the wave vectors of the primary and scattered waves, respectively.

- The simulations of the scattered intensity from S_{coh} (first three steps) were repeated $M \approx 10^4$ times and obtained intensities I_j for $j = 1, ..., M$. Each intensity $I_j(q)$ corresponds to the intensity scattered from a single coherently irradiated area, M is the number of these areas in the totally irradiated sample area.

The average intensity distribution in diffraction plane:

$$I(\mathbf{r}) = \frac{1}{M}\sum_{j-1}^{M} I_j(\mathbf{r}). \tag{73}$$

- After that the intensity distribution in diffraction plane Q_xQ_z from the eq.73 ($I(\mathbf{r}) = I(Q_xQ_z)$) was convoluted with the resolution function of the experimental setup. And received simulated RSM was compared with experimental map.

The model can be applied if the measured intensity is averaged over a statistical ensemble of all configurations of the dislocations and the distance sample-detector is large so that the far-field limit can be used. The validity of the first assumption depends on the density of dislocations, on the S_{coh} and on the total size of the irradiated sample surface, and in our case is satisfied as it was discussed in [97]. The far-field approximation is valid if the diameter of S_{coh} (d_{coh}) is much smaller than the diameter of the first Fresnel zone, which can be approximated by the expression $\sqrt{R\lambda}$, where R is the sample-detector distance and λ is the wavelength. In our case energy was $12keV$ or $\lambda = 0.1033\,nm$, distance $R = 0.7m$, therefore $\sqrt{R\lambda} \approx 10^4 nm$, and the diameter $d_{coh} \approx 10^2 nm$, therefore this condition is fulfilled as well.

4.3 Mosaic model of BSF density calculation

4.3.1 Mosaic model of a crystal with BSFs

Often the microstructure of epitaxial films may be represented by the mosaic block model, where the film is comprised of a number of disoriented and relatively defect-free domains (as we already discussed in the Chapter 2.3). The BSFs split the perfect crystal into blocks with finite sizes in close packed direction [0001]. The sizes of the blocks in basal plane is usually equal to the thickness of the layer (in case of nonpolar material) or even large (in case of semipolar). The model could be applied for any crystallographic orientation of the structure with respect to the sample surface: for nonpolar, where blocks are perpendicular to the sample surface; semipolar, where blocks are inclined with respect to the sample surface; and even for polar material with blocks parallel to the surface. In the fig.39.a an example of the BSF mosaic blocks for an semipolar sample is shown.

The size of the blocks in [0001] direction, which is correspond to the mean distances between BSFs, is much smaller and depends on the BSF density (see fig.39.a). And Fourier transform of a block will reveal in the reciprocal space a distribution of intensity along the direction perpendicular to the basal plane (along [0001]), see fig.39.b. Therefore, the blocks lead appearance of the streak in [0001] direction. The streak of BSFs is quite narrow due to large dimensions in basal plane. The $FWHM$ of a reflection in [0001] direction corresponds to the average thickness of the blocks in this direction, which means to the average distance between BSFs L. From the measured reflection broadening $FWHM$ (in RS units) in BSF influenced [0001] direction one can calculate the mean distance between BSFs L, as:

$$L(nm) = \frac{2\pi}{FWHM(nm^{-1})}. \tag{74}$$

And the density of basal plane stacking faults ρ_{SF} could be derived as an reciprocal to the mean distance L:

$$\rho_{SF}(nm^{-1}) = 1/L(nm) = \frac{FWHM(nm^{-1})}{2\pi}. \tag{75}$$

Usually from experiment $FWHM$ is measured in angular units (radian or degree), and one can transfer $FWHM(radian)$ into $FWHM(nm^{-1}) = FWHM(radian) \cdot Q_{hkl}(nm^{-1})$. From the Chapter 3.11 one can derive $Q_{hkl}(nm^{-1}) = 2K\sin\theta_{hkl} = 2\frac{2\pi}{\lambda}\sin\theta_{hkl}$, and substitution of the $Q_{hkl}(nm^{-1})$ gives equality $FWHM(nm-1) = FWHM(radian) \cdot 2\frac{2\pi}{\lambda}\sin\theta_{hkl}$, and expression for L could be written as:

$$L = \frac{2\pi}{FWHM(radian) \cdot 2\frac{2\pi}{\lambda}\sin\theta_{hkl}} = \frac{\lambda}{2 \cdot FWHM(radian) \cdot \sin\theta_{hkl}}. \tag{76}$$

The relation between $FWHM$ in angular units and L could be presented as:

$$FWHM(radian) = \frac{\lambda}{2 \cdot L \cdot \sin\theta_{hkl}}, \quad FWHM(degree) = \frac{180^\circ \cdot \lambda}{2\pi \cdot L \cdot \sin\theta_{hkl}}. \tag{77}$$

And BSF density ρ_{SF} could be calculated using following formulas:

$$\rho_{SF}(nm^{-1}) = 1/L(nm) = \frac{2 \cdot FWHM(radian) \cdot \sin\theta_{hkl}}{\lambda} = \frac{2\pi \cdot FWHM(degree) \cdot \sin\theta_{hkl}}{180^\circ \cdot \lambda}. \tag{78}$$

In this simple model the contributions of tilt α and twist β from the mosaic block model of (0001) GaN (see Chapter 4.1) were not taking into consideration, however their influence is still possible.

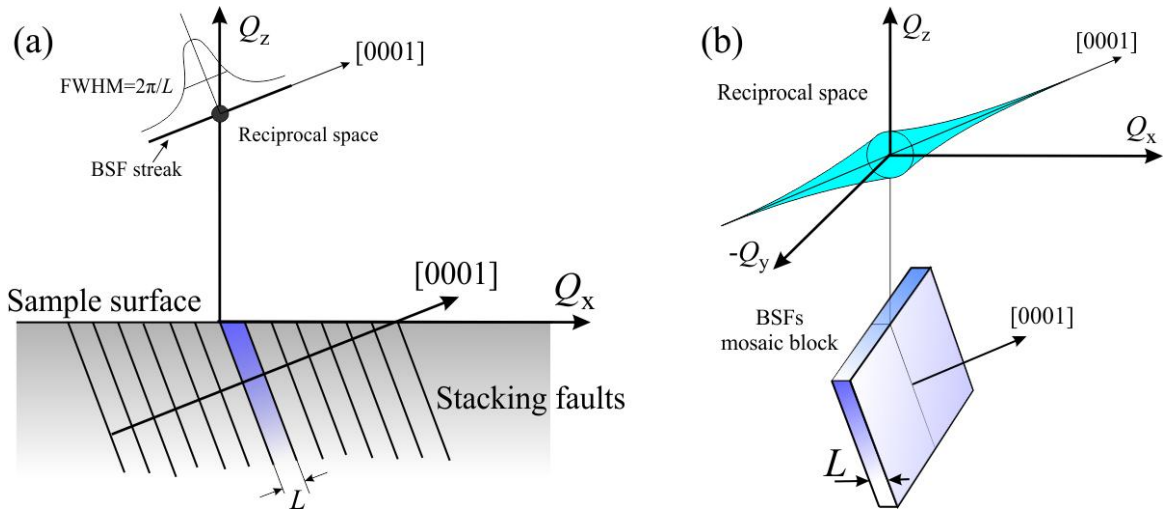

Figure 39: Sketch of a semipolar sample split into BSF mosaic blocks (a), and RSM of a BSF mosaic block (b).

4.3.2 Calculation of BSF density using mosaic model

In case of nonpolar sample the close packed [0001] direction of *hcc* structure is parallel to the surface of the sample and the streak of BSF is oriented "horizontally" in RS. If the influence of other dislocations will be taken in consideration than the symmetric reflections will be broad in angular (ω-scan) direction not only due to BSFs, but also due to tilt α of the sample domains caused by screw and other types of dislocations. In the work of McLaurin et al. [46] broadening due to tilt (see fig.40.a.left) and finite lateral coherence length (see fig.40.a.right) were separated using standard WH plot (see Chapter 4.1). For that the series of symmetric reflections were measured and the slope $\Delta\omega_{mosaic}$ of the fitted line was derived from WH plot (see fig.40.b).

This slope $\Delta\omega_{mosaic}$ is a component of measured $\Delta\omega_{measured}$ FWHM (in radian) of rocking curve of a reciprocal lattice point hkl, which correspond to the screw and other types of dislocations. Finally, the broadening of the reflections could be written as:

$$\Delta\omega_{measured} = \Delta\omega_{mosaic} + \frac{\lambda}{2L\sin(\theta_{hkl})}, \tag{79}$$

where λ is the X-ray wavelength, θ_{hkl} is the Bragg angle of the reflection and L is the lateral crystal domain size. The second component in the sum is correspond to the broadening of the reflection due to BSFs. The lateral crystal domain size is the mean distance between BSFs and could be used for the estimation of the BSF density ρ_{SF}:

$$\rho_{SF} = 1/L = \frac{2\sin(\theta_{hkl})}{\lambda} \cdot (\Delta\omega_{measured} - \Delta\omega_{mosaic}). \tag{80}$$

In the investigation of McLaurin, good agreement between BSF density derived by X-ray method and TEM was shown [46].

S. Paduano had applied more precise method in 2010 [98] to determine BSF density from series of AXRD reflections. In his calculations the influence of tilt, twist, strain, and BSFs on the hkl reflection ω-scan peak width Γ_{hkl} were taking into account using formula:

$$\Gamma_{hkl}^n = (\Gamma_\perp \cos\chi)^n + (\Gamma_\parallel \sin\chi)^n + (\xi \tan\theta_{hkl})^n + \left(\frac{2\pi}{LK_{hkl}}\right)^n, \tag{81}$$

where χ is the inclination angle between the $\{hkl\}$ plane and the surface normal K_{hkl} is the magnitude of the reciprocal lattice vector, L is the average value of the lateral coherence length (mean distance between BSF), $\Gamma_\perp$ is the broadening resulting from lattice plane tilt, $\Gamma_\parallel$ is the broadening resulting from in-plane twist, and $\xi \tan\theta_{hkl}$ represents the inhomogeneous strain contribution which depends on Bragg angle θ_{hkl}. For better precision the exponent n was introduced in the eq.81. Depending on how the contribution from each broadening element is convolved to produce an overall peak profile the n has a value between 1 and 2 (1 for Lorentzian distribution and 2 for Gaussian distribution).

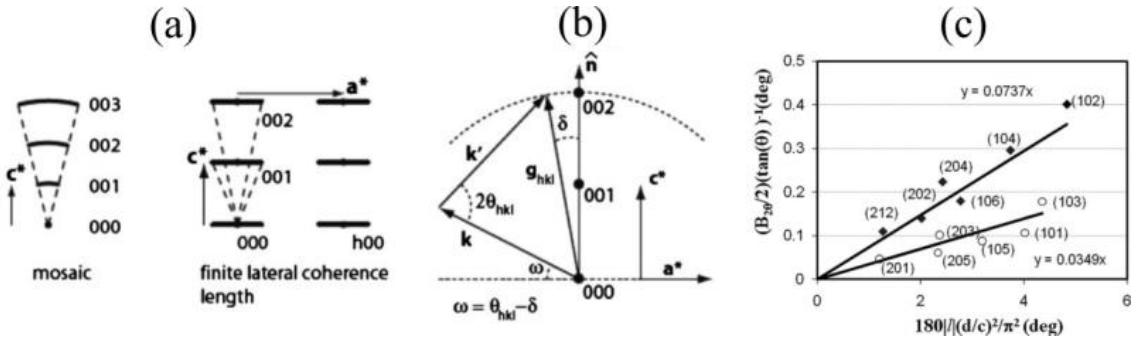

Figure 40: Schematic representation of the effects of mosaic tilt (a) and reduced lateral coherence length on the shape of the reciprocal lattice. schematic representation of the XRD measurement of the SXRD reflections (b), and WH-like plot of the AXRD reflections with even and odd index l (c).

In addition, Paduano had calculated the probabilities of stacking faults of types I_2 and I_2 using formulas of Warren [78] for the broadening of the reflections with $h-k=3n\pm1$:

$$\begin{cases} l\ even: & B_{2\theta}=\left(\frac{360}{\pi^2}\right)\tan\left(\theta_{hkl}\right)|l|\left(\frac{d}{c}\right)^2(3\alpha+3\beta), \\ l\ odd: & B_{2\theta}=\left(\frac{360}{\pi^2}\right)\tan\left(\theta_{hkl}\right)|l|\left(\frac{d}{c}\right)^2(3\alpha+\beta), \end{cases} \tag{82}$$

where $B_{2\theta}$ is the broadening, d is the lattice spacing for the planes $\{hkl\}$, c is the lattice constant, $|l|$ is the absolute value of the index l, θ_{hkl} is the Bragg angle, and α and β are probabilities of stacking faults of types I_2 and I_2, respectively. For the series of reflections with even and odd index l is possible to plot WH-like plots and derive two different slopes, which depend on the probabilities α and β of I_2 and I_2, respectively. The plot of Paduano is shown on the fig.40.c.

However, even with all modifications of Paduano the meaning of the eq.81 is quit similar to the equation of McLaurin eq.79. To prove this fact one can rewrite eq.81 using the equality $\Gamma_{hkl}=\Delta\omega_{measured}$, $\left(\Gamma_{\perp}\cos\chi\right)^n+\left(\Gamma_{\parallel}\sin\chi\right)^n+\left(\xi\tan\theta_{hkl}\right)^n=\left(\Delta\omega_{mosaic}\right)^n$, and $\frac{2\pi}{LK_{hkl}}=\frac{\lambda}{2L\sin(\theta_{hkl})}$, as:

$$\left(\Delta\omega_{measured}\right)^n=\left(\Delta\omega_{mosaic}\right)^n+\left(\frac{\lambda}{2L\sin\left(\theta_{hkl}\right)}\right)^n. \tag{83}$$

And eq.83 is different from the eq.79 only in term of exponent n.

As a conclusion we can say that BSF density calculation from $FWHM$ of the reflections is based on mosaic model taking into account influence of some other factors such as other type of dislocations.

4.4 Monte Carlo simulation of BSF diffuse intensity in reciprocal space

4.4.1 Model of BSFs diffuse scattering based on Monte Carlo method

Besides simple calculations presented in the previous section 4.3, almost no other alternative methods of BSF densities determination in non- and semipolar GaN based on X-ray diffraction technique are developed. However, recently the model of the scattered intensity distribution from BSFs in RS along [0001] direction based on Monte Carlo method was developed by V. Holy and M. Barchuk for the nonpolar GaN material [51]. This model with some modifications will be used for the BSF density determination in semipolar GaN material. Let us take a look on the main steps in the algorithm of the model.

The hexagonal basis vectors are $\mathbf{a}_{1,2,3}$, the vectors $\mathbf{a}_{1,2}$ and $\mathbf{a}_3=-\left(\mathbf{a}_1+\mathbf{a}_2\right)$ lie in the basal plane (0001) and $\mathbf{a}_4$ is orthogonal to them, as it is illustrated in the fig.41.a.

In case of a perfect layer without any structural defects, the amplitude of the wave $E(\mathbf{Q})$ diffracted from the layer is a function of the scattering vector $\mathbf{Q}=\mathbf{K}_f-\mathbf{K}_i$, where $\mathbf{K}_f$ and $\mathbf{K}_i$ are the wave vectors of the diffracted and primary beams, respectively. Using the kinematic approximation and the far-field limit (see Chapter 3.4), this amplitude can be written as:

$$E(\mathbf{Q})=A\left[f_{Ga}(Q)+f_N(Q)e^{-i\mathbf{Q}\cdot\mathbf{d}}\right]\sum_{\mathbf{n}}e^{-i\mathbf{Q}\cdot\mathbf{R_n}}. \tag{84}$$

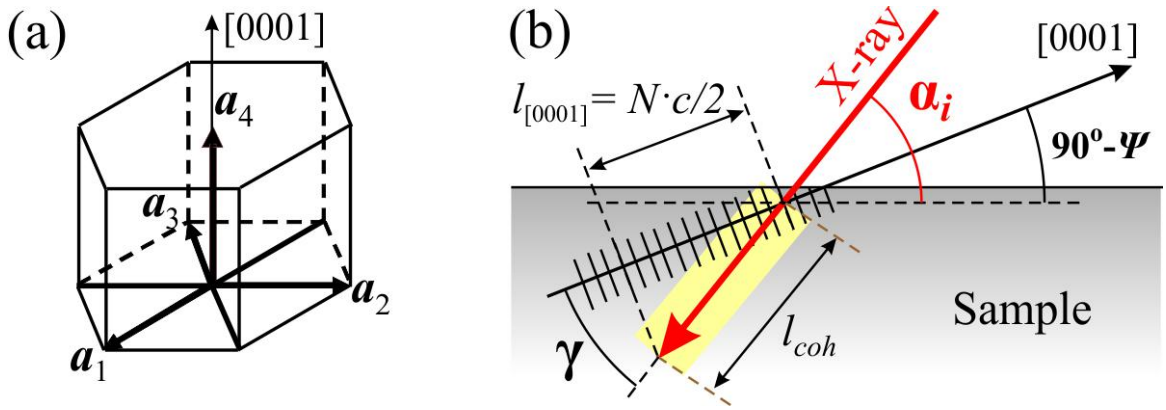

Figure 41: The sketch of the elementary unit cell of wurtzite GaN (a) and explanation of coherently illuminated area in GaN sample (b).

Where $f_{Ga,N}(Q)$ the form-factor of atoms Ga and N, and $\mathbf{d} = 3a_4/8$ is the position vector of the N atom with respect to Ga in GaN molecule. The $\mathbf{R}_n$ is position vector of the GaN molecule, $\mathbf{n} \equiv (\mathbf{n_1}, \mathbf{n_2}, \mathbf{n_3})$ and A is a constant, which contains of the amplitude of the primary beam, the classical electron radius and the polarization factor.

The position vector $\mathbf{R}_n$ cold be written as:

$$\mathbf{R_n} = n_1\mathbf{a_1} + n_2\mathbf{a_2} + n_3\mathbf{a_4}/2 + \sigma_{n_3}\mathbf{p},$$

where $\mathbf{p} = \frac{2}{3}\mathbf{a_1} + \frac{1}{3}\mathbf{a_2}$ is the lateral shift of the second Ga-N bilayer in the elementary unit cell with respect to the first one.

$$E(\mathbf{Q}) = \Phi(\mathbf{Q}) \sum_{\mathbf{n_3}=\mathbf{0}}^{N} \xi^{n_3}\kappa^{\sigma_{n_3}}, \tag{85}$$

where $\xi = e^{-i\mathbf{Q}\cdot\mathbf{a}_4/2}$, $\kappa = e^{-i\mathbf{Q}\cdot\mathbf{p}}$ are responsible for the stacking of the Ga-N layers. In the model the presence of BSFs is organized by random generation of the different sequences using σ_{n_3} parameter. The N is the number of coherently irradiated (0001) basal planes (see fig.41.b), and function $\Phi(\mathbf{Q})$ is:

$$\Phi(\mathbf{Q}) = A\left[f_{Ga}(Q) + f_N(Q)e^{-i\mathbf{Q}\cdot\mathbf{d}}\right] \sum_{\mathbf{n_1},\mathbf{n_2}} e^{-iQ\cdot(n_1\mathbf{a_1}+n_2\mathbf{a_2})}.$$

The range of the double sum $\sum_{\mathbf{n_1},\mathbf{n_2}}$ corresponds to the lateral size S of the stacking faults and in the model it is assumed that this size is comparable to the layer thickness or even larger, taking into account inclination of the {0001} planes with respect to the sample surface, in case of semipolar GaN. Therefore, the function $\Phi(\mathbf{Q})$ leads to the narrow streak in RS. The width of the cross-section of this streak can be estimated to $2\pi/S$ and it is usually comparable to the resolution limit of the experimental setup. Therefore it is enough to deal with the intensity distribution along $Q_{[0001]}$ direction in reciprocal space (along the BSFs-streak).

To overcome difficulties in calculations related to the experimental resolution function, broadening of the reflection curve not only due to a limited coherence of the primary beam but also due to other effects such as limited angular resolution of the detector and diffuse scattering from other dislocations (like treading dislocations), the function $\Psi(x)$ is introduced in the

$$E(\mathbf{Q}) = \Phi(\mathbf{Q}) \sum_{\mathbf{n_3}=\mathbf{0}}^{N} \xi^{n_3}\kappa^{\sigma_{n_3}}\Psi\left(n_3\left|a_4\right|/2\right). \tag{86}$$

The form of the $\Psi(x)$ function can be determined from the diffraction curve measured in [0001] direction through the reflection, where BSFs do not produce any diffuse scattering. In the simulations the function $\Psi(x)$ is described by well-known PearsonVII distribution function [99]:

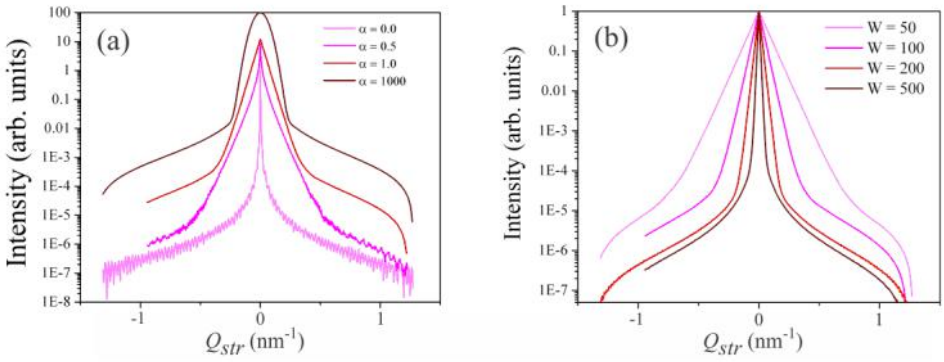

Figure 42: Dependence of the $I(Q_{[0001]})$ intensity distribution on the PearsonVII parameter α for $W = 100$ (a) and on the parameter W for $\alpha = 1$ (b).

$$\Psi(x) = \left[1 + 4\left(2^{1/\alpha} - 1\right)\left(\frac{2x}{W}\right)^2\right]^{-\alpha},$$

where W is the FWHM of the function and α is the shape parameter. Dependence of the intensity distribution $I(Q_{[0001]})$ along direction [0001] on the α shape parameter of the function $\Psi(x)$ is shown on the fig.42.a. For $\alpha \to \infty$ this function approaches the Gauss function, in the case of $\alpha = 1$, the $\Psi(x)$ corresponds to the Lorentz function.

The influence of the parameter W variation on the intensity distribution $I(Q_{[0001]})$ in reciprocal space for $\alpha = 1$ is shown on the fig.42.b. The case $W \to \infty$ represents an ideally coherent and plane primary wave and no diffuse scattering from other defects (dislocations). Decreasing W, resulting diffraction curve changes its form and its FWHM increases. To discriminate the influence of all listed factors from true intensity profile it is necessary to measure the intensity distribution along the [0001] direction of the reflection without BSF streak (in the best case from the same direction of Q vector). Therefore, the parameters W and α could be derived from fitting of the$\Psi(x)$ function to the experimental curve of the reflection not affected by the BSFs at all. These values can be used for the analysis of the diffraction curves in other reflections. Taking into account that, both the effect of transverse coherence and diffuse scattering from the dislocations scale with the length of the diffraction vector Q, the $FWHM$ $W(SFeffected)$ of the reflection with diffraction vector $Q(SFeffected)$, which is affected by BSFs could be calculated as:

$$W(SFeffected) = W(SFnot) \cdot \frac{Q(SFeffected)}{Q(SFnot)}, \tag{87}$$

where $Q(SFnot)$ and $W(SFnot)$ are diffraction vector and $FWHM$ of the reflection not affected by BSFs, respectively. The shape parameter α does not depend on the reflection order.

Finally the intensity distribution along the streak of BSFs (along [0001] direction) can be rewritten as follows:

$$I(Q_{[0001]}) = \left|E(Q_{[0001]})\right|^2. \tag{88}$$

4.4.2 Algorithm of the intensity distribution along [0001] direction calculation

In the program algorithm, the irradiated sample volume is much larger than the coherence volume of the primary beam. Therefore, the measured diffracted intensity is an incoherent superposition of the intensities originated from different coherently irradiated volumes. In a coherently irradiated volume consisting of N (0001) Ga-N bilayers, positions and types of the BSFs are defined using random generator. In the model the sequence of the BSFs of the same type creates a homogeneous Markov chain [100], to definite random positions of the latest. It is assumed that the mutual positions of the BSFs of different types are statistically uncorrelated and that the total diffracted intensity is a sum of contributions of the Markov chains of various defect types. The amplitude of the diffracted wave and the diffracted intensity are calculated according to eq.86 and eq.88 , respectively. The generation of BSFs and subsequent computation of the diffracted intensity I_j are repeated M times. Each intensity distribution I_j corresponds to the intensity scattered from a single coherently irradiated volume, M is the number of these volumes

in the irradiated sample volume. The number of the configurations M is large integer number and chosen so that maximum of standard deviation not exceed 10%. Finally, the average intensity profile is calculated as:

$$I\left(Q_{[0001]}\right) = \frac{1}{M}\sum_{j=1}^{M} I_j(Q_{[0001]}). \tag{89}$$

The root-mean-square (rms) deviation σ_I of the average intensity:

$$\sigma_I^2 = \frac{1}{M}\left(\frac{1}{M}\sum_{j=1}^{M} I_j^2(Q_{[0001]}) - \left(\frac{1}{M}\sum_{j=1}^{M} I_j(Q_{[0001]})\right)^2\right). \tag{90}$$

Increasing the number M of coherently irradiated volumes, the rms deviation σ_I decreases. The simulation procedure is quite time consuming so that we were not able to use the actual number M given by the experimental conditions. Instead, M was chosen so that the maximum of $\sigma_I(Q_{[0001]})$ did not exceed 5%; the resulting computation time was few minutes for a scan of about 10^3 values of $Q_{[0001]}$.

The mean distance between uncorrelated BSFs D_0 is an input parameter of the model. The D_0 is introduced as dimensionless integer number of Ga-N bilayers. The density of BSF ρ possible to determine using equation:

$$\rho = \frac{2}{cD_0}. \tag{91}$$

And for GaN with parameter $c = 0.5186\,nm$ the density of BSF could be calculated in cm^{-1}:

$$\rho = \frac{3.86}{D_0} \cdot 10^7 cm^{-1}. \tag{92}$$

In the work the BSFs density will be calculated from the MC simulation of the diffuse intensity along [0001] direction using eq.92.

5 Investigation of threading dislocations in GaN epilayers

5.1 Introduction

The growth of c-oriented [0001] GaN on c-oriented [0001] sapphire is a well-established method (see Chapter 2.2). However, due to a lattice mismatch of 16% between sapphire and GaN, the GaN epilayers still contain a high density of edge and screw TDs [8, 61]. In Chapter 2.4.4 the introduction of a SiN mask was presented as a method of dislocation density reduction. In this section, the influence of the length of time the SiN mask is deposited on the TDD in GaN epilayers will be discussed.

5.2 Sample description

In the investigation of Barchuk et al. [67] a series of four c-oriented [0001] GaN epilayers denoted G1-G4 with different dislocation densities were grown by MOVPE in an AIXTRON 200/RF-S horizontal flow reactor. All layers were grown on c-plane (0001) sapphire (Al_2O_3) wafers slightly miscut by about 0.3° toward the a-plane ($11\bar{2}2$). On top of the substrate, an oxygen doped AlN nucleation layer with the thickness of about 20 nm was deposited. On the AlN nucleation layer the GaN epilayer with the thickness 300 nm was grown. The GaN growth was then interrupted for the in-situ deposition of a submonolayer thick Si_xN_y mask (later just SiN). The deposition time of the mask was 0, 120, 150 and 180 seconds for the samples G1, G2, G3 and G4, respectively. For the samples G1-G3, GaN was overgrown on the top of SiN mask till total thickness of about 1800 nm. For the sample G4 the total overgrowth layer thickness of 2400 nm was achieved by HVPE overgrowth. The sketches of the samples are presented in the fig.43.

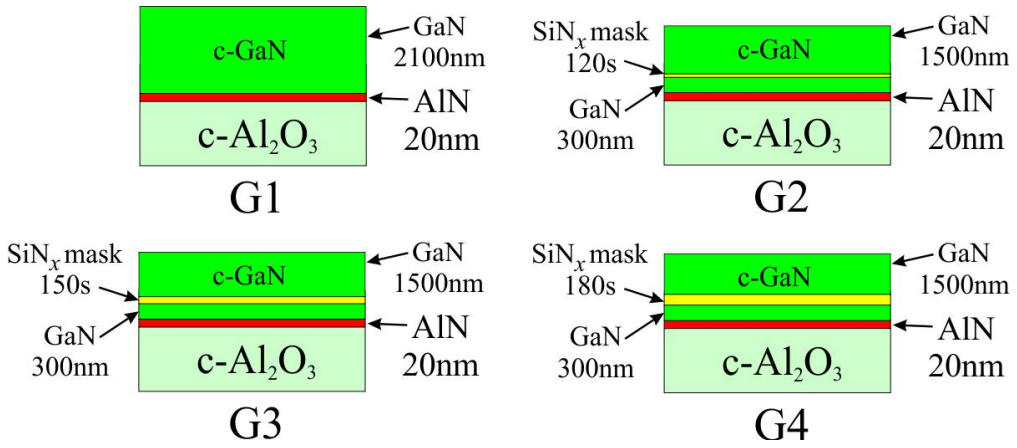

Figure 43: GaN samples sketches.

5.3 Threading dislocation density in GaN epilayers with and without SiN interlayer

Barchuk et al. [67] have investigated the influence of the SiN mask on the TDD in c-oriented [0001] GaN epilayers (samples G1-G4) using X-ray diffraction method. The TDDs in GaN epilayers were derived using numerical Monte Carlo simulation method (see Chapter 4.2) applied for the measured RSMs. For the determination of screw TDD, the SXRD 0004 reflections, while for the calculation of the edge TDD the AXRD $10\bar{1}4$ reflections were employed. The TDDs were calculated with accuracy of about 10% [67] and values are summarized in the tab.7. However, the asymmetric reflections only partially influenced by edge TDs (see section 4.1). In order to perform precise determination of edge type TDDs, RSMs of non-coplanar GID reflections affected mostly by edge TDs were measured and simulated by Barchuk et al. [101]. The result of the edge TDD calculation and total TDD from [101] is shown in the tab.8.

From the TDD comparison, the influence of the SiN mask on the edge TDD reduction was demonstrated, while screw TDD remains almost unchanged [67]. However, due to high penetration depth in SXRD and AXRD diffraction geometries, the dislocation rich GaN layer below the SiN mask should contribute to the diffuse scattering of the reflections. In this work the signal of the layer below SiN mask, which is much broader in angular direction due to high TDD was not taken into consideration. Therefore, in the future X-ray experiments the influence of the layer below the SiN mask should be considered.

Sample	SiN_x deposition time, (s)	TDD (EPD), ($10^8 cm^{-2}$)	Screw TDD (SXRD simulations), ($10^8 cm^{-2}$)	Edge TDD (AXRD simulations), ($10^8 cm^{-2}$)	Total TDD from simulations, ($10^8 cm^{-2}$)
G1	0	20	2.1	20.6	22.7
G2	120	7.6	1.6	6.9	8.5
G3	150	4.8	1.3	4	5.3
G4	180	2.6	1.1	1.7	2.9

Table 7: Densities of screw and edge threading dislocations determined from the measured intensity distributions and from the densities of etch pits, taken from [67].

Sample	SiN_x deposition time, (s)	Screw TDD (SXRD simulations), ($10^8 cm^{-2}$)	Edge TDD (GID simulations), ($10^8 cm^{-2}$)	Total TDD from simulations, ($10^8 cm^{-2}$)
G1	0	2.1	20.6±1.9	22.7
G2	120	1.6	7.0±0.6	8.6
G3	150	1.3	4.1±0.4	5.4
G4	180	1.1	2.1±0.2	3.2

Table 8: Densities of the threading dislocations determined from the scattered intensity distributions in the coplanar symmetric and grazing-incidence geometries, taken from [101].

6 Study of threading dislocation density reduction in AlGaN epilayers

6.1 Introduction

The $Al_xGa_{1-x}N$ alloys are attractive candidates that have been grown mainly on sapphire and SiC substrates for a range of ultra violet (UV) system applications (i.e. detectors, emitters etc.), which includes ultraviolet light emitting diodes (UV LEDs), flame and heat sensors, missile plume detection equipment [102, 103], secure-ground to earth inter-satellite communication equipment, and UV calibration and monitoring devices for medical and biological applications. Furthermore, nitride-based ultraviolet light emitting diodes have also been investigated for their application in high density optical storage media, biotechnology, air/water purification and curing resins. By changing the Al composition, the cut-off wavelength of AlGaN photo-active devices can cover the spectrum from 200 nm to 360 nm at room temperature. See fig.44.

It should be emphasized that in comparison with GaN epilayers, AlGaN layers that are grown directly on sapphire, typically exhibit a larger number of TDs, and form mainly edge-type TDs [104]. The reduction in the number of threading dislocations, which act as non-radiative recombination centers [56], is essential [56, 57] for the improvement of the UV performance of LEDs. Recently, research has been carried out on the optimization of $Al_{0.2}Ga_{0.8}N$ epilayers, emitting wavelengths of about 322 nm (see fig.44) and directly grown on sapphire by MOVPE has been researched [66]. TEM investigation has led to a comprehensive understanding of mechanisms for growth and defect reduction that occurs during the formation of dislocation half loops on the SiN interface. A qualitative estimation of the dislocation densities was based on the observation of TEM images [105]. Improvements have been achieved by applying in-situ nano-masking technology with ultra-thin SiN interlayers. The edge type dislocation density could be significantly reduced by optimizing the growth parameters and depositing the SiN interlayer on a 150 nm $Al_{0.2}Ga_{0.8}N$ interlayer grown on an AlN nucleation layer.

In this chapter, the possibility of using a Monte-Carlo method in the modeling of reciprocal space maps of $Al_{0.2}Ga_{0.8}N$ epilayer structures has been examined. Furthermore, the scaling law of TD density reduction with overgrowth thickness will be established. Moreover, TD densities of AlGaN layers below and above the SiN nano-mask have been derived from the Monte-Carlo simulation, with the aim of estimating the SiN nano-mask efficiency in reducing the defects in AlGaN epilayers.

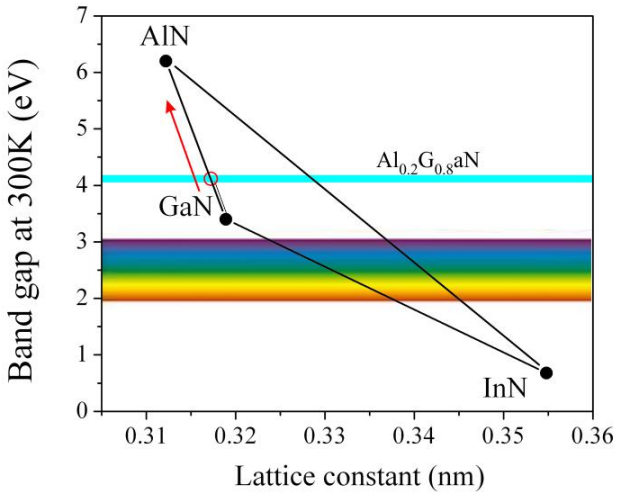

Figure 44: Band gap energy and wavelength of $Al_{0.2}Ga_{0.8}N$.

6.2 Growth of c-plane AlGaN epilayers on sapphire substrate

The growth of $Al_xGa_{1-x}N$ films on high quality GaN or AlN substrates is advantageous, because of the minimum lattice mismatch between film and substrate. As a result, high quality $Al_xGa_{1-x}N$ epilayers with low dislocation densities could be achieved [106, 107].

Nevertheless, the efficiency of $Al_xGa_{1-x}N$ based UV-LEDs grown on GaN templates is still not satisfying for application as it has been argued by Kamiyama et al. [108]. Besides the high cost of the GaN substrates [109, 58],

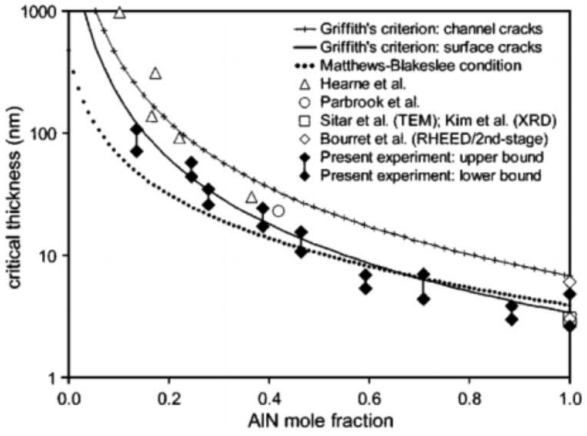

Figure 45: Dependence of the critical thickness of the $Al_xGa_{1-x}N$ layer on the Al content x, taken from [115].

templates are not well suited for the growth of UV-LEDs since the shorter band gap of GaN causes the reabsorption of the generated photons in the $Al_xGa_{1-x}N$ active region.

Alternatively $Al_xGa_{1-x}N$ film with low dislocation density has been grown on AlN templates having similar problematic of the $Al_xGa_{1-x}N$ films grown on the GaN substrates mentioned above.

The convenient price of sapphire substrate encourages the direct growth of $Al_xGa_{1-x}N$ epilayers on sapphire. The large lattice mismatch between the sapphire substrate and the epilayers, being 16% and 14% for the case of GaN and AlN, respectively, causes large TDD in the order of $10^9 cm^{-2}$ [110, 111] and even higher ($10^{10} cm^{-2}$) for the AlN epilayers [112, 113].

In order to reduce the TDD, AlN nucleation layer (NL) was introduced to form a virtual substrate of relaxed AlN acting as intermediate layer between sapphire and $Al_xGa_{1-x}N$ epilayer [114]. In this case the AlN layer plays the role of substrate for $Al_xGa_{1-x}N$ epilayer. As a consequence, by decreasing the Al content x the lattice mismatch between $Al_xGa_{1-x}N$ and AlN virtual substrate increases up to:

$$\varepsilon(AlN\,on\,GaN) \leq \frac{a(GaN) - a(AlN)}{a(GaN)} \approx 2.3\% \tag{93}$$

Furthermore, the increase of the Al content lead to an exponential decrease of the critical thickness for crack formation in the $Al_xGa_{1-x}N$ films, as it was demonstrated by Lee et al.[115] and shown in the fig.45.

Due to the decrease of TDD to $10^9 - 10^{10} cm^{-2}$ by intercalating the AlN nucleation layer, the growth procedure became as a standard recipe for the growth of AlGaN epilayer on the foreigner substrate like sapphire.

Further reduction of the TDD in a GaN film up to $10^6 cm^{-2}$ could be achieved by increasing the layer thickness to tens-hundreds micrometers [116, 117, 118]. The growth of thick GaN films could not be performed by MOVPE and it requires rather HVPE growth process. An alternative method of TDD reduction in GaN epilayers is to introduce the SiN masking with atomic coverage (thickness) of less than one monolayer acting as an anti-surfactant for GaN [65]. Engl et al. [119] has investigated GaN and $Al_{0.07}Ga_{0.93}N$ epilayers with the in-situ deposited SiN nanomask. Accordingly, they reported no effective reduction in the TDDs for $Al_{0.07}Ga_{0.93}N$ in comparisons with GaN sample. Recently the group of Prof. Dr. Ferdinand Scholz from university Ulm [66, 120] has demonstrated significant reduction of the TDD in $Al_{0.2}Ga_{0.8}N$ epilayers due to intercalation of SiN nanomask. According to his method, first the 20 nm thick AlN:O NL was deposited on sapphire substrate , the SiN nanomask was deposited in-situ after growing 150 nm treading dislocation rich $Al_{0.2}Ga_{0.8}N$ layer corresponding approximately the critical thickness of the $Al_{0.2}Ga_{0.8}N$ with 20% of Al, see fig.45. Then SiN nanomask was overgrown by desired $Al_{0.2}Ga_{0.8}N$ epilayer of about several micrometer grown with the same growth parameters as the layer below the SiN mask and having fewer TDD. The key factor in this method is the selective area growth (SAG) of the deposited $Al_{0.2}Ga_{0.8}N$ epilayer on the SiN mask.

Kamran et al. [66, 120] has investigated the influence of the SiN nanomask deposition time on the crystal quality using the X-ray diffraction on the $Al_{0.2}Ga_{0.8}N$ epilayers with SiN mask. The broadening of the rocking curve peak of the symmetric reflections (SXRD) was attributed to the screw TDs and the broadening of the asymmetric reflections (AXRD) to edge. Since the dominant type of the TDs in the AlGaN film is the edge TD the broadening of the AXRD was chosen as a criteria for the sample quality qualification. The series of samples with different SiN

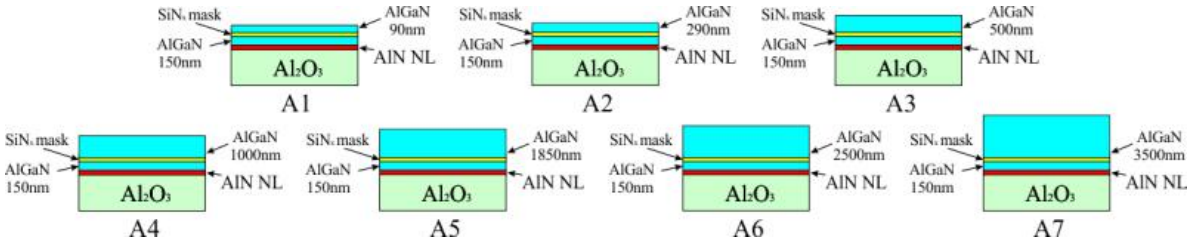

Figure 46: The AlGaN sample sketches with overgrowth layer thicknesses of 90, 290, 500, 1000, 1850, 2500 and 3500 nm corresponding to the samples A1, A2, A3, A4, A5, A6 and A7, respectively.

deposition time between 3 and 8 minutes were grown. The lowest broadening of an AXRD reflection was obtained for a deposition time of 6 minutes and this time was selected for the SiN nanomask deposition.

Intercalation of the second SiN nanomask after 300 nm AlGaN growth with total sample thickness of $1.4\mu m$ revealed the narrowest AXRD peak reflecting the best achieved sample quality [120]. However, the surface of the sample was extremely rough. Moreover, higher inhomogeneity in Ga/Al distribution is expected being susceptible of absorption of light generated by the active region of a UV-LED.

6.3 $Al_{0.2}Ga_{0.8}N$ sample description

In order to investigate the influence of the overgrowth layer thickness on the TDD reduction, seven samples of c-plane epitaxial $Al_{0.2}Ga_{0.8}N$ structures were grown on sapphire (0001) substrates with a miscut of 0.3° towards the a-plane. Growth was carried out in a low-pressure horizontal MOVPE reactor (Aixtron AIX-200/4 RF-S) using the standard trimethylgallium (C_3H_9Ga), trimethylaluminium (C_3H_9Al), and ammonia (NH_3), as group III and group V precursors, respectively. The growth temperature was set to 1120°C. The Al content of 20% for the AlGaN samples was estimated from growth parameters and was measured by photoluminescence [121]. The growth was initiated by an oxygen doped AlN nucleation layer (about 20 nm). A SiN nano-mask layer was deposited in-situ by briefly flowing SiH_4 and ammonia into the reactor after growing about 150 nm of AlGaN, for approximately 5 minutes. On the top of this layer, the AlGaN layer was deposited with thicknesses of 90, 290, 500, 1000, 1850, 2500 and 3500 nm corresponding to the samples A1, A2, A3, A4, A5, A6 and A7, respectively. The sketches of the samples are presented in the fig.46. In the following the layer above the SiN mask is termed as overgrowth layer while the layer below the mask is named as 150 nm AlGaN interlayer.

6.4 TEM investigation of AlGaN epilayers and growth model

To figure out the dislocation type and to understand the dislocation propagation mechanism in $Al_{0.2}Ga_{0.8}N$ epilayers with SiN nanomask, TEM investigations on the sample were performed by our cooperation partner Klein et al. [105] as complimentary characterization to our X-ray diffraction measurement.

In the following we propose to give a summary about the results derived from TEM investigation of Klein et al. [105] regarding to this dislocation propagation mechanism. In the fig.47.a the cross sectional BF TEM micrograph of a sample edge is given. The system consist of few layers from bottom to top: sapphire (Al_2O_3), Al:O NL, 150 nm AlGaN interlayer, SiN mask and overgrowth layer. Darker parts of the sample correspond to the TDD rich areas. From fig.47.a, it is visible that the SiN nanomask stops TDs from propagating through the mask, and therefore, the area above the SiN mask is dislocation free.

Fig.47.b and fig.47.c correspond to the TEM micrographs of the same sample area recorded with diffraction vectors along edge and screw TDs. From the comparison of TEM micrographs, one can conclude that edge TDD is higher than screw TDD. The edge-type TDs are generally stopped by the SiN nanomask. From fig.47.b one can see in some regions TDs are merged or bent, creating bundles of dislocations reaching the surface.

Klein et al. [105] have developed a model for the $Al_{0.2}Ga_{0.8}N$ overgrowth layer describing the TDs propagation mechanism based on TEM investigation (see fig48 and fig.49). In his model, it was taken into account that SiN nanomask has submonolayer thickness, meaning doesn't cover completely the surface of the $Al_{0.2}Ga_{0.8}N$ as a film (even in one monolayer), but has open areas with nanometer range diameter, as it is sketched in the fig48.a. The Al and Ga atoms have different growth behavior on the top of the SiN mask. The GaN doesn't grow on the SiN masked areas whereas AlN doesn't show such growth selectivity and nucleates on the SiN masked areas. This results in a diffusion of Ga ad-atoms to the window (open) area of the SiN mask at the very beginning of the AlGaN overgrowth

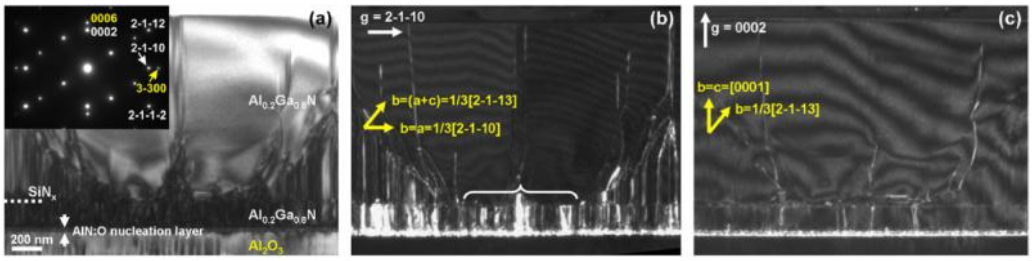

Figure 47: Cross-section TEM images of the $Al_{0.2}Ga_{0.8}N$ sample. The BF image (a) from the $[01\bar{1}0]$ zone axis shows the AlGaN heterostructure on c-plane sapphire. The BF image as well as the WBDF images (b) and (c) were taken from the same sample area. The yellow arrows in (b) and (c) mark the Burger's vectors of the TDs visible for the respective g reflection, taken from [105].

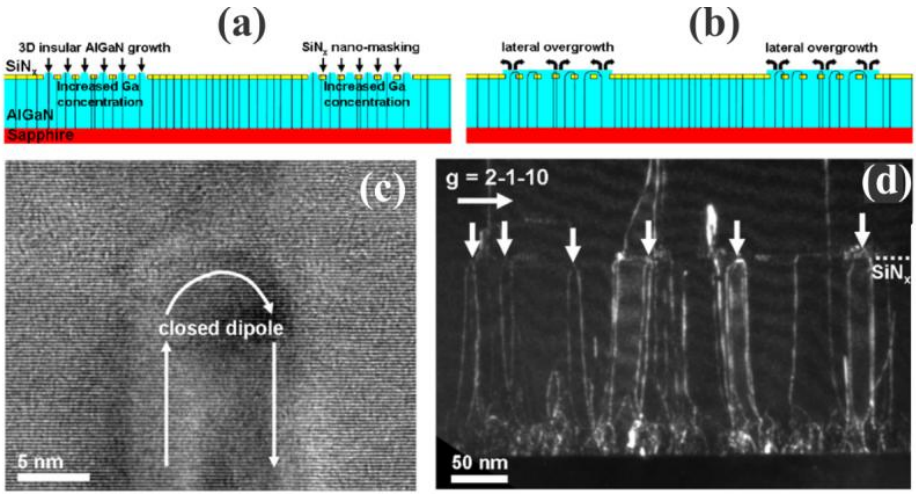

Figure 48: The SiN nanomask coverage model (a), overgrowth of the SiN mask (b), HRTEM of a TD closed dipole (c), and TEM of the near to SiN area (d) taken from [105].

while this is not the case for Al ad-atoms. This has influenced the Al and Ga distribution (at least) above the SiN nanomask.

The growth behavior of the AlN and GaN forms 3D selective area growth (SAG) above the SiN mask. Above the "open areas" of SiN mask Ga rich islands start to form, being surrounded by Al rich areas. The Si atoms precipitate around the dislocation core. As a result of such Si-clouds around the edge dislocations, the hydrostatic pressure around the dislocation line becomes unbalanced. Therefore, the presence of high concentrations of Si atoms due to SiN deposition promotes the edge dislocations to bend. So, the TDs start to band in the SiN film, and in the "open areas" going through the mask. And the TDs with opposite Burgers vectors have higher probability to meet each other and annihilate. The scheme of this process is shown in the fig.48.b. The closed dipole of the annihilated TDs recorded in HRTEM is shown in the fig.48.c, and fig.48.d shows the TEM picture of the closed loops formation in the SiN mask.

The bended TDs in the window areas annihilate and in the borders bend out from the center of the window area. Therefore, the SAG reveal the change in the growth mode from layer by layer (2D) growth mode to hexagonal nano-islands (3D) growth mode. The sudden change of growth mode after the deposition of the SiN (from 2D before the SiN to 3D above the SiN) compels the dislocation line to bend towards the faster growing direction and hence increases the probability for dislocation-dislocation interaction.

The formation of AlGaN pyramidal nano-islands above the SiN nanomask was demonstrated by TEM investigation of thin AlGaN overgrowth layer about 290 nm. TEM micrographs of two close formed and distant islands are shown in the fig.49.a and fig.49.b, respectively. It is clearly visible that the grown AlGaN epilayers between the nano-islands are full of dislocations, contrary to the pyramidal nano-islands being dislocation free on the window of the mask.

For further overgrowth of the islands two scenarios are possible: the first scenario fig.49.a shows the formation of close islands. In this case the dislocation free pyramidal islands grow laterally in size and then dominate the

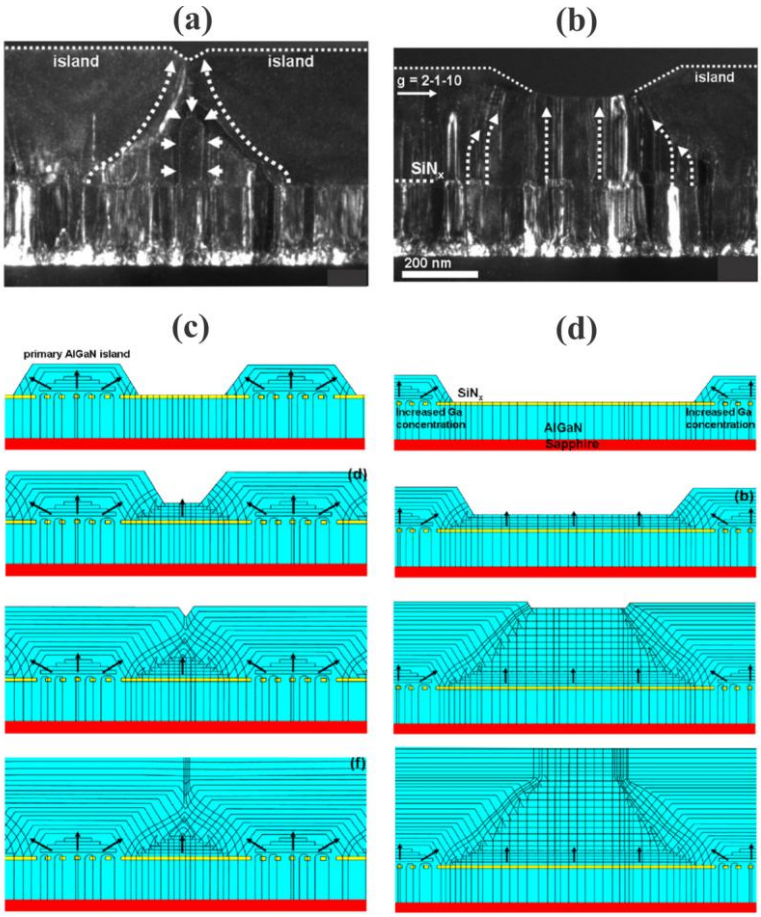

Figure 49: The TEM pictures of two close (a) and distant (b) AlGaN islands. The model of the overgrowth layer formation from the close (c) and distant AlGaN islands (d), taken from [105].

dislocation-rich AlGaN areas between them on the wing area. Furthermore, as the islands become larger the dislocations located between the islands and the dislocation rich areas are forced to interact with other dislocations to form dislocation loops. Finally, the islands coalesce and further growth continue as a single layer. The scheme of the AlGaN overgrowth by islands coalescence is demonstrated in the fig.49.c.

The second scenario treats the situation where islands are located very far from each other (see fig.49.b), and therefore the dislocations which don't interact, form bundle-like dislocation lines reaching the surface. As a consequence, the dislocation rich area between the islands is not affected by SiN mask, and further overgrowth of these areas will continue as separated layers. The scheme of this scenario is presented in the fig.49.d.

Therefore, there is formation of three distinguishable regions above the SiN mask: one region without AlGaN islands and the SiN nanomask doesn't affect the dislocation line motion (see fig.49.d); second region above the islands, where dislocations have been terminated at the AlGaN-SiN interface (see fig.49.c); and third region between islands, where the dislocation lines bent towards each other forming a dislocation bundle above the SiN interlayer.

The bending of the TDs in the borders of the AlGaN nano-islands is accompanied with the basal plane stacking fault formation. The TEM micrograph and the scheme of the BSF formation as an inset are presented in the fig.50.

6.5 Locally resolved cathodoluminescence of AlGaN epilayers with SiN mask

To investigate the Al and Ga incorporation in the AlGaN overgrowth layer, cross sectional SEM (fig.51.a) and locally resolved cathodoluminescence (CL) recorded at temperature of 10 K and an electron energy of 2 kV (fig.51.b) were performed on an AlGaN epilayer with SiN nanomask at the same area. Fig.51.a made in evidence the existence of several layers: sapphire (Al_2O_3) and AlGaN. In the CL map several colored regions could be recognized: blue color region (i.e. 315 nm), turkeys color (i.e. 322 nm), green (i.e. 327 nm), yellow (i.e. 345 nm) and red (i.e. 340 nm). Al and Ga rich areas correspond to blue and red colored regions, respectively. It should be

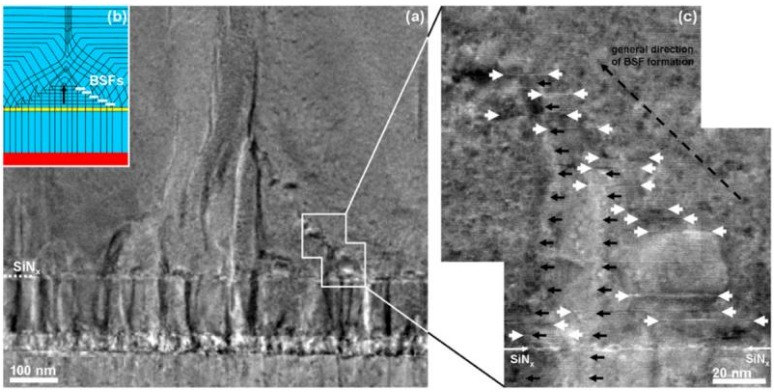

Figure 50: The TEM picture of the islands coalescence area shows the BSF formation on their borders, taken from [105].

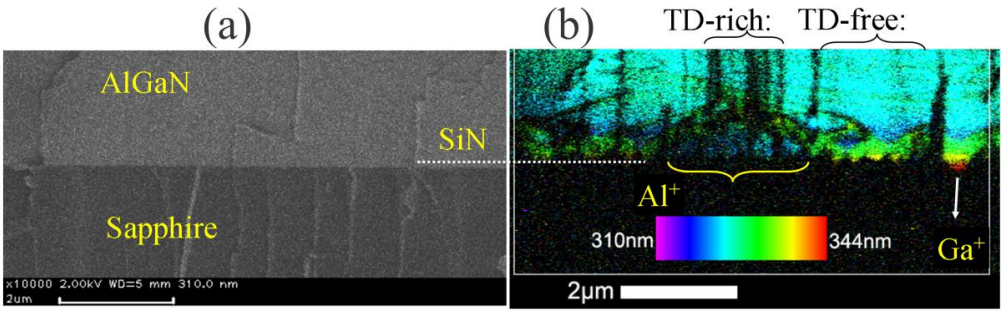

Figure 51: Cross sectional SEM micrograph of a high quality AlGaN sample with the SiN nanomask deposited at 150 nm above the NL (a) and corresponding color coded CL distribution recorded at a temperature of 10 K and an electron energy of 2 kV (b). The (Al+) and (Ga+) denotes the regions with higher than average AlN or GaN contents, respectively.

emphasized that dislocations appear as vertical dark lines in the CL map and their density is higher in the blue region corresponding to higher Al content. Oppositely, Ga-rich areas (red region) has been found to be TD-free. It should be reminded that Al-rich areas which are located above the uniform SiN mask are TD-rich whereas the Ga-rich areas corresponding to the pyramidal nano-islands promote the TD-free areas, see fig.51.b. The upper overgrowth layer (turkeys) is almost homogenous and corresponds to the Al content of 20%. According to the TEM investigation of Klein et al. [105] reported in the Chapter 6.4, the TD are localized above the uniform parts of SiN mask while and TD-free areas correspond to the mask openings. On the other side locally resolved CL data show that TD-rich areas correspond to Al-rich areas. This confirms the assumption of Klein et al. [105] that uniform parts of SiN mask are Al-rich areas while mask opening regions are Ga-rich areas.

The influence of the $Al_{0.2}Ga_{0.8}N$ overgrowth layer thickness on the TDD reduction will be investigated by X-ray diffraction in the next chapters.

6.6 AFM investigation of AlGaN sample surfaces

The surfaces of four A4, A5, A6 and A7 samples were investigated by Forghani et al. [120] using atomic force microscopy (AFM) with the scanning area of $10\mu m$ x $10\mu m$ (see fig.52). From the fig.52 hexagonal shape domains (see sample A4) are observed. These domains could be originated from the "defect free" areas above the SiN mask opening introduced in the Chapter 6.2. From AFM roughness (RMS) evaluation of Forghani et al. [120] and Neuschel et al. [121] is evident that samples surface becomes smoother with increasing the overgrowth layer thickness (see fig.52). Roughness values derived from AFM investigation are presented in the tab.9 showing that for an overgrowth layer thickness above 2.5 μm the roughness is in the range of subnanometer. The AFM pictures were recorded only for the samples A4-A7 with roughness less than 40 nm. Due to the high roughness of the samples A1-A3, AFM measurements were difficult to be performed.

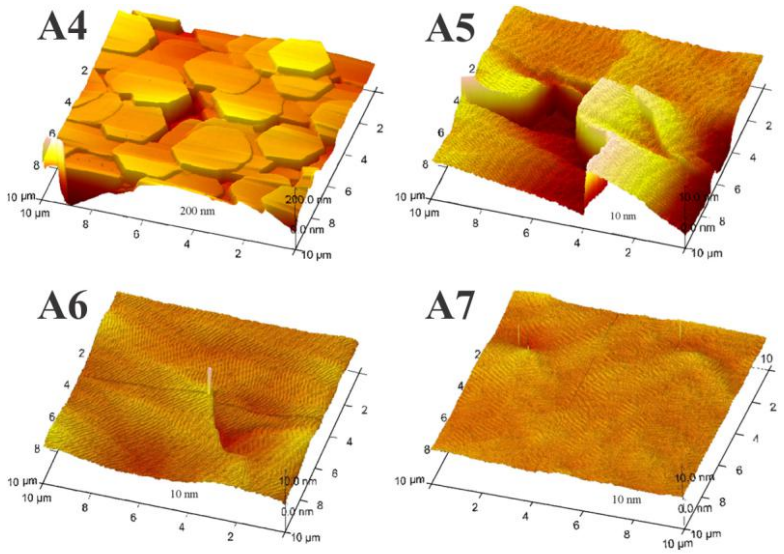

Figure 52: The AFM pictures of the samples A4, A5, A6 and A7 surfaces.

Sample name	RMS, nm
A1	300
A2	200
A3	95
A4	25
A5	3
A6	0.8
A7	0.3

Table 9: The roughness of the samples A1-A7 derived from AFM measurements.

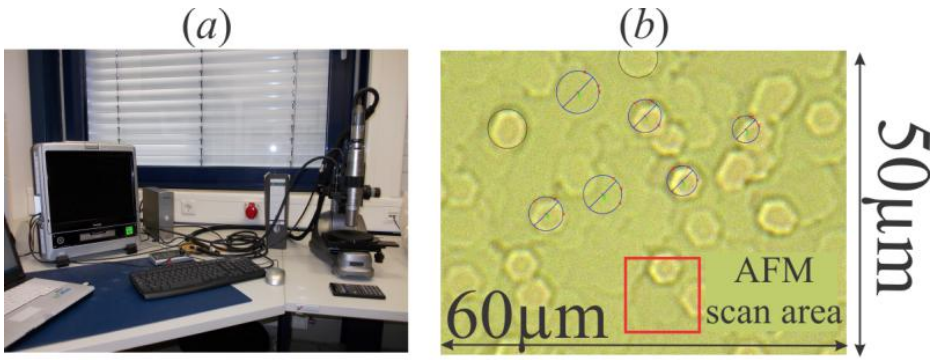

Figure 53: High resolution optical microscope (OM) at NANO beamline at ANKA (a). The sample A4 measured with highest resolution surface (b). Additionally, size of the AFM scanned are (see fig.52) sketched as a red square and measured domains diameters are drown.

Sample	Grain mean size, μm
A1	0.8
A2	1.6
A3	4.1
A4	7.2
A5	14.3
A6	15.8
A7	23.8

Table 10: Mean grain size of AlGaN samples.

6.7 Optical microscopy of AlGaN sample surfaces

Beside the AFM investigation, optical microscope study of the samples surface was performed using optical light microscope (OM) with resolution up to 0.5 μm at NANO beamline at ANKA. The view of the OM is shown in the fig.53.a.

OM pictures of all AlGaN samples surfaces were recorded with the highest zoom of 5000 times with field of view of 50 μm x 60 μm. The OM micrographs of the sample A4 is shown in the fig.53.b. Similar hexagonal shape domains on the surface of the sample A4 could be detected by the OM (fig.53.b) and AFM (fig.52). It should be mentioned that the area of AFM investigation was in 5-6 times smaller as it is illustrated by red square on the OM picture fig.53.b.

The OM micrographs of all AlGaN samples surfaces are compared in the fig.54, showing the evolution of the hexagonal domains with the overgrowth. For the sample A1, the surface is covered by islands with relatively small lateral size of about 0.8μm whereas for sample A2, the domains have larger diameters and start to coalescent. For the samples A3-A7, an increase of the overgrowth layer leads to the coalescence of islands forming consequently hexagonal large domains extended to flat surface (see fig.54). Due to the large field of view of OM in comparison to AFM it was possible to detect hexagonal shape islands for all samples even when the diameter exceed AFM field of view (10μm). Mean sizes of the hexagonal shape domains summarized in the tab.10 reveal diameter increase from 0.8μm to 23.8μm for samples from A1 to A7. The formation of hexagonal shape domains in good agreement with the GaN-rich "defect free" islands growth above the SiN mask opening introduced in the Chapter 6.2.

For the samples A5-A7, the scanning range of AFM maps was smaller than mean size of the hexagonal shape domains observed in OM investigation. This allow us to conclude that AFM performed by Forghani et al. [120] provide the roughness correspond to one single domain rather than the mean roughness of the sample's surface.

6.8 X-ray investigation of AlGaN epilayers with SiN interlayers

By combining TEM and CL, it was possible to understand the interrelation between TDs formation and Al content distribution. Furthermore, TEM has strongly contributed in deep understanding in TDs propagation mechanism during the growth which is influenced by SiN interlayer. Regarding to the surface morphology, AFM

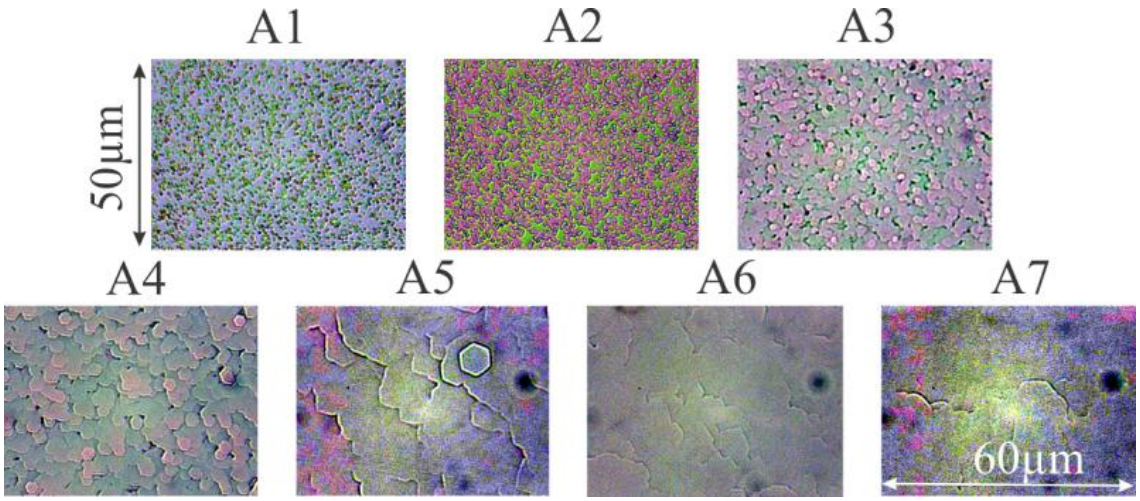

Figure 54: Optical microscope pictures of the surface of the AlGaN samples.

and OM micrographs recorded for different overgrowth layer thickness have explained the layer formation as a result of island coalescence.

It is fairly known, that determination of TDD from TEM is challenging to be performed accurately besides to the lack of statistics. X-ray diffraction (XRD) has proven to be advantageous as a non destructive and sensitive to the structure method allowing quantification of different types of TDDs.

In this chapter, high resolution X-ray diffraction (HRXRD) study of AlGaN epilayers will include recording and analyzing complete RSM of 000l RLPs with higher order of indexes l. Furthermore, determination of screw and edge type dislocation densities below and above the SiN nanomask from symmetric and grazing incidence diffraction geometries will be performed using Monte Carlo simulation. Moreover, the scaling law of screw and edge TDD reduction with overgrowth layer thickness will be discussed.

6.8.1 Experimental set-up

The HRXRD measurements have been performed at the bending magnet single crystal diffraction (SCD) beamline at the synchrotron facility ANKA. The SCD beamline offers the energy range from 4 keV to 20 keV. This covers the K-edges from Ti to Mo, and L-edges from I to U. The beam could be focused or collimated at the sample using sagittally bent second crystal monochromator.

All X-ray data were recorded with a monochromatic beam using Si (111) double crystal monochromator. The energy resolution of the Si (111) crystal monochromator used in our investigation is $\delta E/E \approx 0.0001$. The X-ray beam was focused on the sample, with the beam size of 0.3 mm x 0.3 mm. As detection system, a fast read-out microstrip solid-state linear detector Mythen 1K, manufactured by the company DECTRIS Ltd. [122]. The Mythen 1K has 1280 channels with a channel size of 50μm x 8mm (full length of the detector is 64 mm) and a point-spread function of one channel. The sample-detector distance was 700 mm, which delivers an angular resolution of about 0.004° per pixel.

In the experiment coplanar SXRD, AXRD and non-coplanar GID diffraction geometries were used, see fig.55. The coplanar diffraction geometry was performed to record RSMs of the symmetric 0002, 0004, 0006, 0008, and $10\bar{1}6$, $10\bar{1}8$, $30\bar{3}8$, asymmetric reflections, at an energy of 12 keV for all samples. Fig.55.a gives a schematic presentation of coplanar diffraction geometry used in the experiment. The sample was placed in horizontal position and the Mythen linear detector in vertical position, as it is shown in the fig.55.a. In order to reduce the integration area out of diffraction plane slits with the gap of 0.5 mm were mounted on the detector. In this geometry the incident and the outgoing beams lie in the plane perpendicular to the sample surface (see Chapter 3.10). In this case the distance between the crystalline planes $\{hkl\}$ parallel and inclined with respect to the surface, here later referred to as "d-spacing" has been determined. As is illustrated in fig.55.a, α_i and α_f are defined as the angles between the incident and the outgoing beams and the sample surface respectively. The total angular range of the scattering angle α_f and the angular resolution (0.004°) are given by the effective detector length (64 mm), the sample-detector distance and the number of detector channels, as it is shown in the fig.55.a. The components Q_{rad} and Q_{ang} of the scattering wave vector $\mathbf{Q}$ will be given as following:

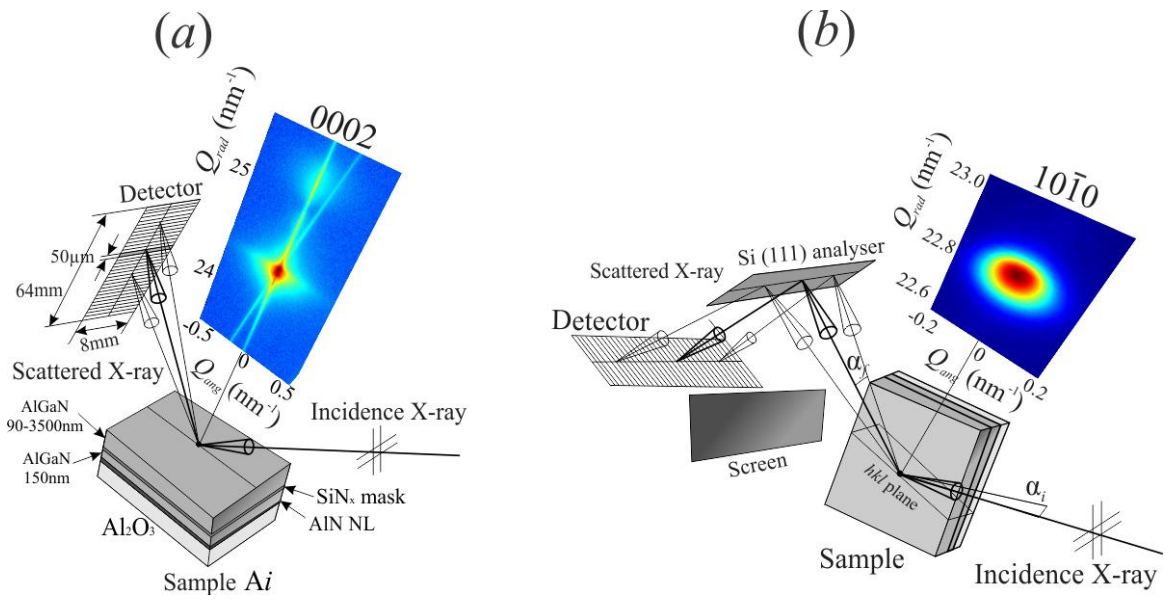

Figure 55: Schematic representations of the coplanar geometry used for symmetric high-resolution X-ray diffraction (a) and for the non-coplanar GID geometry (b) .

$$Q_{rad} = \frac{2\pi}{\lambda}(\sin\alpha_f + \sin\alpha_i), \tag{94}$$

$$Q_{ang} = \frac{2\pi}{\lambda}(\cos\alpha_f - \cos\alpha_i), \tag{95}$$

where λ is the wavelength, Q_{rad} corresponds to the component of $\mathbf{Q}$ along the surface normal and Q_{ang} represents the in-plane component of $\mathbf{Q}$. The variation of α_i at the Bragg reflection was performed by rocking the sample with respect to the incoming beam, and recording the coplanar RSMs. The resolution function (δQ_{rad}, δQ_{ang}) depends on the angular divergence of the incident and diffracted beams as well as on the monochromaticity of the X-ray beam. Since the scattering plane corresponds to the vertical plane, the resolution function in reciprocal space depends on the vertical divergence of the incident beam which was defined by the vertical opening of the slit (0.3 mm) situated before the sample. The angular resolution (0.004 degrees) of the diffracted beam was predefined by the channel size of 50 μm and the distance between sample and the detector of 700 mm.

Fig.55.b illustrates a schematic presentation of non-coplanar diffraction geometry used for GID measurements, which were performed at an energy of 12 keV using the Mythen 1K linear detector in combination with a Si (111) crystal analyzer. In this case the resolution function (δQ_{rad}, δQ_{ang}) was defined by the crystal analyzer angular resolution of 0.003° and the energy resolution of the Si (111) crystal monochromator. In the GID geometry the diffracted intensity originates from the crystalline planes (hkl) perpendicular to the sample surface. In non-coplanar geometry the incident as well as the outgoing wave vectors are defined by two angles (α_i, θ_i) and (α_f, θ_f) respectively (see figure55.b). However the incident angle α_i and the outgoing angle α_f are relatively small and close to the critical angle of 0.336 degrees, and will be neglected in the calculation of the components of scattering wave vector.

The angles θ_i and θ_f are the angles between the incident beam and the outgoing beam with the diffracting planes respectively. For GID reflections the components of the scattering wave vector $\mathbf{Q}$ in radial and angular directions Q_{rad} and Q_{ang} given by the following equations respectively:

$$Q_{rad} = \frac{2\pi}{\lambda}(\sin\theta_f + \sin\theta_i), \tag{96}$$

$$Q_{ang} = \frac{2\pi}{\lambda}(\cos\theta_f - \cos\theta_i), \tag{97}$$

For each sample, the RSMs of the $10\bar{1}0$, $20\bar{2}0$ and $30\bar{3}0$ GID reflections were recorded.

Fig.56 shows the six-circle diffractometer at SCD beamline used to bring the sample into the Bragg condition and to measure coplanar and GID reflections. The diffractometer has 4 degrees of freedom for the sample and

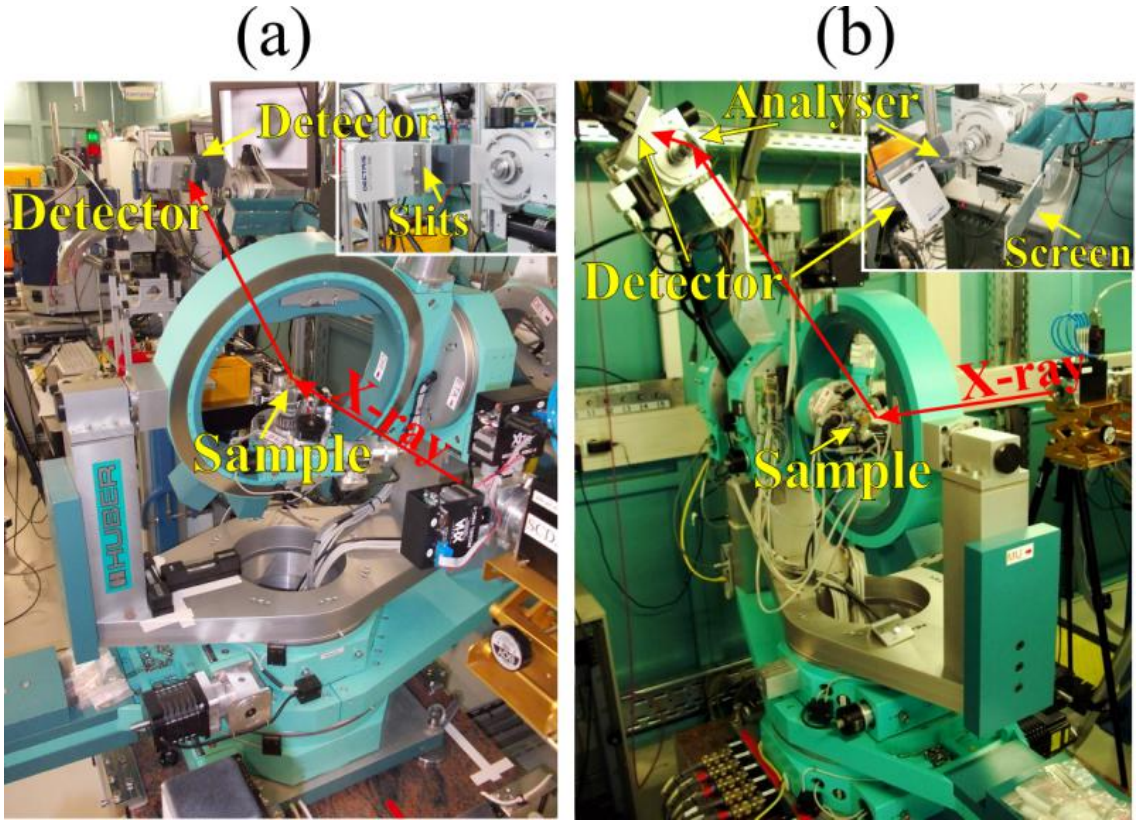

Figure 56: The six-circle diffractometer at the SCD bending magnet beamline at ANKA in coplanar (a), and non-coplanar GID geometries (b), showing linear detector, crystal analyzer and a sample mounted on the Euler cradle stage. The insets show position of the detector in the experiment.

2 degrees of freedom for the detector. Fig.56.a and fig.56.b correspond to the six-circle diffractometer in coplanar and in non-coplanar GID diffraction geometries, respectively. The Mythen 1K linear detector equipped with the 0.5 mm slits and the Si (111) crystal analyzer is presented in the fig.56.a and fig.56.b, respectively as an inset.

The available regions of reciprocal space at 12 keV of the $Al_{0.2}Ga_{0.8}N$ alloy are shown in the fig.57, where the forbidden reflections are not sketched. The available reflections are colored in black while the non-reachable in red and the measured one in blue.

6.8.2 Symmetric X-ray diffraction of AlGaN epilayers with an SiN mask

In this section symmetric reflections 0002, 0004, 0006 and 0008 are measured at the X-ray energy of 12 keV (see fig.57). In coplanar diffraction geometry, the penetration depth is calculated to be about 5000 nm. Therefore, both AlGaN epilayers should contribute to the diffraction pattern. Moreover, a comparison of AlGaN and GaN RSMs will be discussed.

6.8.2.1 Comparison of the X-ray diffraction of GaN and AlGaN epilayers with SiN interlayers

In order to understand the diffraction particularity of the $Al_{0.2}Ga_{0.8}N$ heterostructure the GaN sample was used as a reference to show the changes due to the incorporation of 20 % of Al. For that purpose, a GaN sample and the $Al_{0.2}Ga_{0.8}N$ A6 sample with similar overgrowth layer thicknesses of 2400 and 2500 nm, respectively, were investigated by Lazarev et al. [123]. A schematic presentation of the GaN and AlGaN samples having nearly the same growth layout is given in fig.58.up.

First the lowest symmetric reflection 0002 of the GaN and AlGaN samples were measured. Their RSMs are presented in the fig.58. All graphics placed left correspond to the AlGaN sample while the ones located at the right side of the figure belong to the GaN sample.

In the RSMs two main peaks , and two streaks are distinguishable. The first one along Q_{rad} direction at $Q_{ang} = 0$ corresponds to the crystal truncation rod (CTR) where $\alpha_i = \alpha_f$. An additional inclined with respect to CTR streak

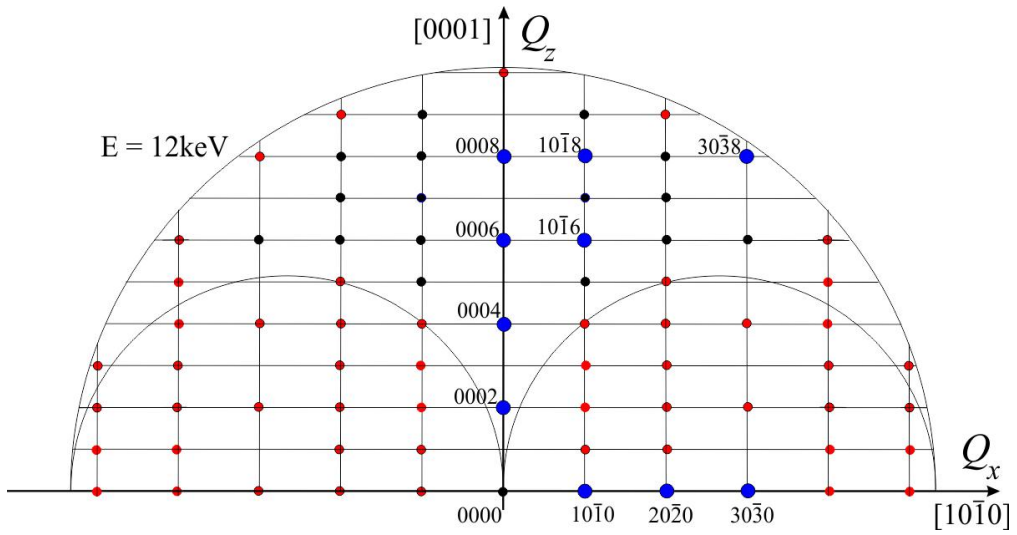

Figure 57: Reciprocal space of the $Al_{0.2}Ga_{0.8}N$ at 12 keV. In the scheme the forbidden reflections are not drawn, not reachable colored in red, available in black, and measured in blue.

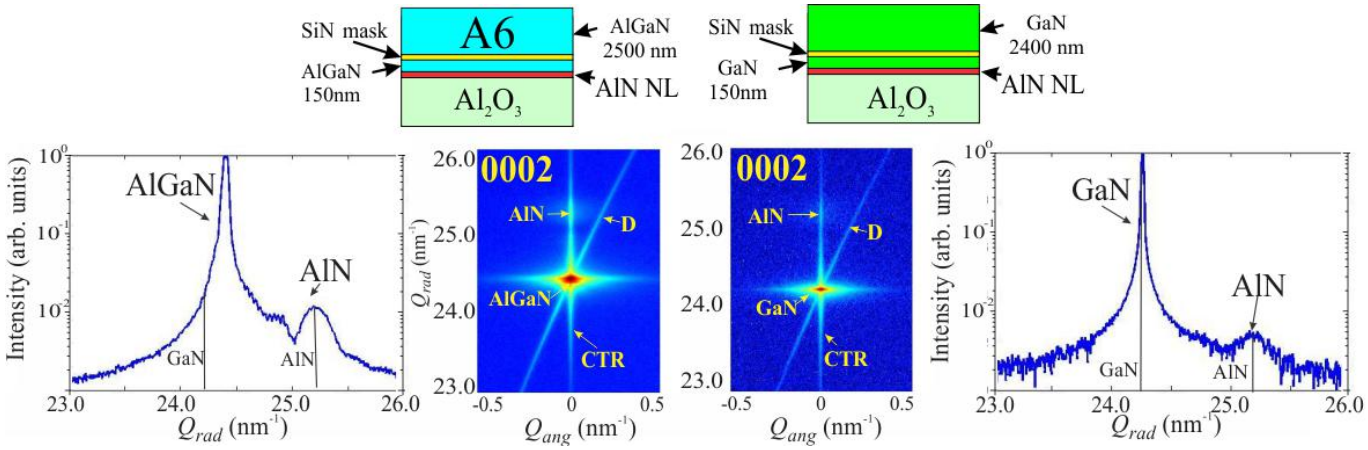

Figure 58: Comparison of the RSMs and cuts along the CTR which correspond to the vertical scans at $Q_{ang} = 0$ in the RSMs through the diffraction peaks maximum of the GaN (right) and AlGaN (A6) (left) samples of the reflection 0002.

(D) corresponds to the air scattering streak. Besides the RSMs vertical scans along the crystal truncation rod are displayed at the left side for $Al_{0.2}Ga_{0.8}N$ and at the right side for the GaN sample. The unit cells parameters of GaN and AlN are given as $a\,(GaN) = 0.3186nm$, $c\,(GaN) = 0.5178nm$ and $a\,(AlN) = 0.3110\,nm$, $c\,(AlN) = 0.4980\,nm$, respectively. The corresponding reciprocal space coordinates of the symmetric reflections 0002 and 0008 hence are given by the following:

$$Q_{rad}^{0002}(GaN) = 2 \cdot \frac{2\pi}{c\,(GaN)} = 24.27nm^{-1},\ Q_z^{0002}(AlN) = 2 \cdot \frac{2\pi}{c\,(AlN)} = 25.23nm^{-1}. \tag{98}$$

The RSMs as well as the CTRs of the reflection 0002 for both samples show scattering peak originating from the AlN nucleation layer at $Q_{rad} = 25.23\,nm^{-1}$ corresponding to the theoretically expected value. As it is shown at the CTR cuts of GaN and AlGaN, the peak position of the reflection 0002 appearing at $Q_{rad} = 24.27nm^{-1}$ in the case of the GaN sample, and is shifted toward higher $Q_{rad} = 24.41nm^{-1}$ for $Al_{0.2}Ga_{0.8}N$ sample. The diffuse scattering in the transversal direction of the main GaN peak at $Q_{rad} = 24.27nm^{-1}$ and AlGaN peak at $Q_{rad} = 24.41nm^{-1}$ is due to the dislocations.

In comparison to the GaN-CTR profile of the 0002 reflection, the AlGaN-CTR profile shows a shoulder appearing at the position $Q_{rad} = 24.8nm^{-1}$. To understand the origin of the shoulder, higher order reflections 0004, 0006 and 0008 were measured (see fig.57). Such high order reflections, are advantageous for resolving diffraction peaks

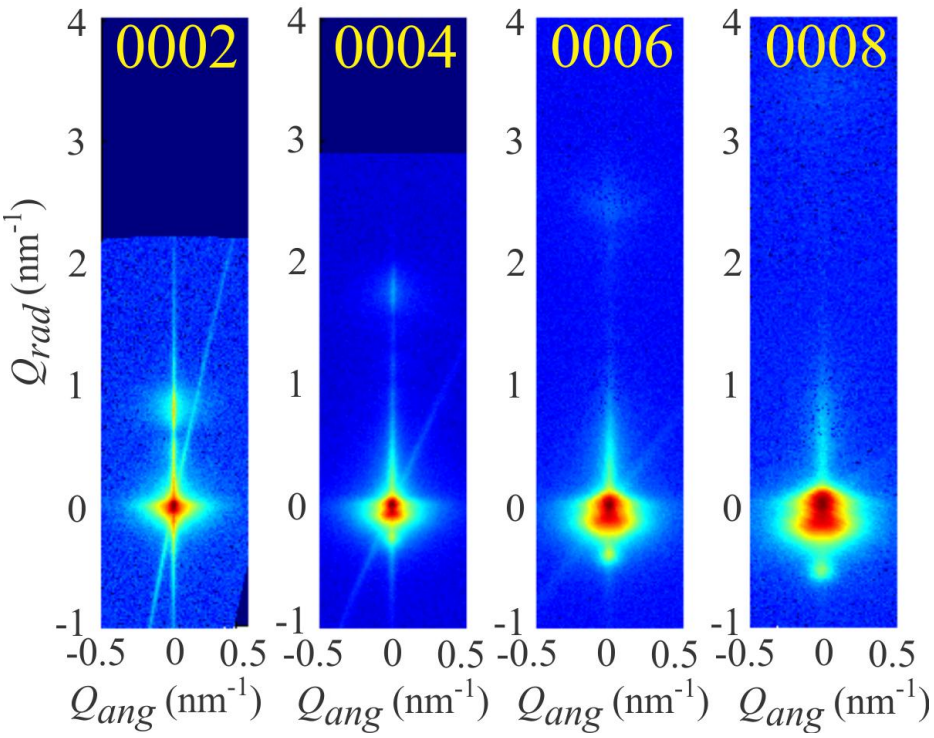

Figure 59: Symmetric reflections 0002, 0004, 0006 and 0008 of the AlGaN sample A6.

originating from only small differences in "d-spacing" in the growth direction. The RSMs of the reflections are shown in the fig.59. From the comparison of the reflections one can see that main peak of the AlGaN in the reflection 0002 start to split into several peaks by measuring higher reflections till 0008.

For the comprehension of the origin of AlGaN peaks, 0008 reflection RSMs and CTR profiles of GaN and AlGaN epilayers are compared in the fig.60, as it was performed for the reflection 0002. The coordinates Q_{rad} of pure GaN and AlN in the reflection 0008 could be found as:

$$Q_{rad}^{0008}(GaN) = 8 \cdot \frac{2\pi}{c\,(GaN)} = 97.08nm^{-1},\ Q_{rad}^{0008}(AlN) = 8 \cdot \frac{2\pi}{c\,(AlN)} = 100.93nm^{-1}. \tag{99}$$

In the GaN RSM only one diffraction peak at $Q_{rad} = 97.08nm^{-1}$corresponding to the theoretically expected value of GaN is found (see fig.60.right). In contrast to GaN RSM, the AlGaN RSM reveal the presence of several AlGaN peaks, named as GaN rich peak, AlGaN bottom peak, AlGaN main peak and AlN rich peak (see fig.60). These peaks refer to several crystalline regions owing to different crystalline parameters in the growth [0001] direction. The position of the GaN rich peak of the 0008 reflection corresponds to $Q_{rad} = 97.09nm^{-1}$ which is very close to the position of a pure GaN 0008 reflection. Bottom peak of the AlGaN is detected at $Q_{rad} = 97.3nm^{-1}$, and the main peak at $Q_{rad} = 97.6nm^{-1}$. On the opposite side of the AlGaN main peak, the AlN rich peak at $Q_{rad} = 98.5nm^{-1}$ was detected, which is closer to the 0008 reflection coordinates of AlN. The origin of the AlGaN reflections will be discussed in details in the next chapter.

6.8.2.2 Symmetric X-ray diffraction from the AlGaN epilayer system Measurement of 0008 symmetric reflection of the AlGaN samples reveal the presence of several AlGaN diffraction peaks [123]. One of the aims of this chapter is to identify the origin of the Bragg reflections detected in the RSMs of the AlGaN structure with respect to the individual layers or area of the sample.

The evolution of X-ray diffraction pattern as a function of the overgrowth thickness was examined by recording the RSMs of the 0008 reflection for all samples. The intensity distribution along the CTR was derived for the samples A1-A7, and is displayed in the fig.61.a. For better representation each profile in fig.61.a has been multiplied by a factor of five relative to the previous one.

In order to identify the origin of the different peaks and to demonstrate accurately the resulting changes in peak position and broadening as function of the overgrowth thickness, a decomposition procedure was systematically applied to all samples. Figures fig.61.b and fig.61.c contain the intensity distribution along the CTR as well as the

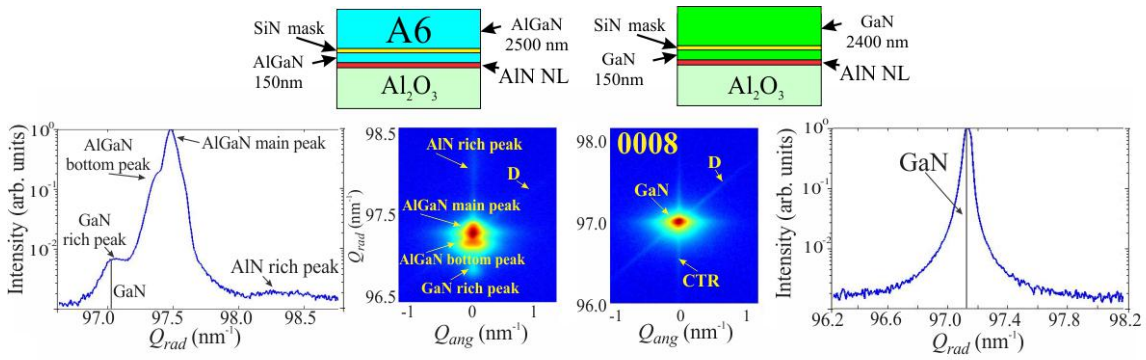

Figure 60: Comparison of the RSMs and cuts along the CTR which correspond to the vertical scans at $Q_{ang} = 0$ in the RSMs through the diffraction peaks maximum of the GaN (right) and AlGaN (A6) (left) samples of the reflection 0002.

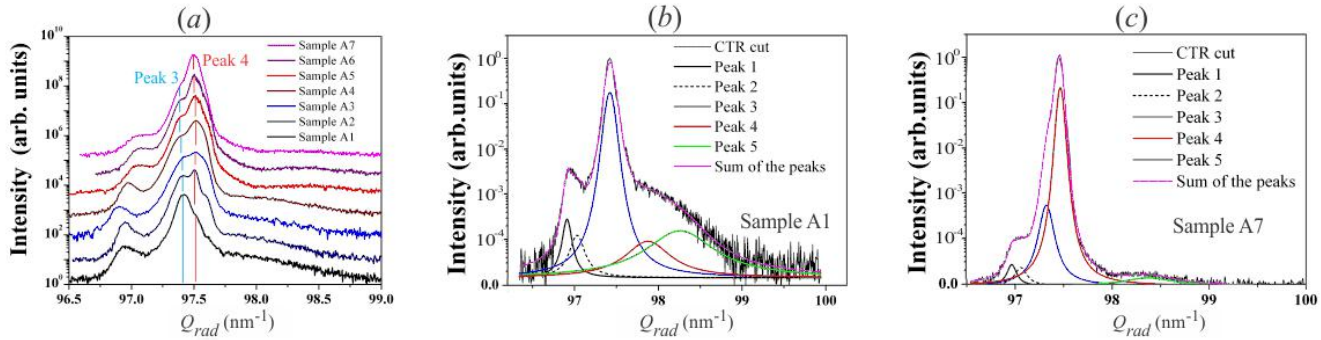

Figure 61: The CTR profiles of samples A1–A7 derived from RSMs of the 0008 reflections (a). The profiles were shifted vertically in order to make the changes in peak positions and intensities visible as a function of the overgrowth thicknesses. It is observed that the intensity of peak 3 decreases while that of peak 4 increases. The CTR profile of the 0008 reflection and the corresponding decomposed peaks for sample A1 (b), where the overgrowth layer is 90 nm, i.e. lower than the thickness of the 150 nm AlGaN interlayer. The intensity of peak 3 is higher than that of peak 4. The CTR profile of the 0008 reflection and the corresponding decomposed peaks for sample A7 (c), where the overgrowth layer is 3500 nm, i.e. higher than the thickness of the 150 nm AlGaN interlayer. Peak 4 is dominant because of the increase of the diffracting volume coming from the overgrowth layer.

contributing profiles for the sample A1 and A7, respectively. It should be emphasized that A1 and A7 correspond to the lowest and to the highest overgrowth layer thicknesses, respectively. The choice of Lorentzians as a fitting function for the individual peaks enables us to achieve a good fit for the CTR profiles of the samples. We propose to follow the change in the peak intensities when the thickness of overgrowth layer increases. For this purpose the $h_1 = 150nm$ was defined as the thickness of the AlGaN layer below the SiN interlayer and h as the thickness of the overgrowth layer, varying from 90 nm up to 3500 nm (see Chapter 6.3). As is shown in fig.61.b for sample A1, where $h = 90nm$ is less than h_1, the intensity of peak 3 is higher than peak 4, while in the case of sample A7 (see fig.61.c), where $h = 3500nm$ is greater than h_1, the intensity of peak 4 is dominating, due to the increase of the diffracting volume coming from the overgrowth layer. As a consequence, the increase of the overgrowth layer thickness h leads to a continuous increase in the peak 4 intensity (see fig.61.a).

In conclusion, peak 3 could be attributed to the 150 nm AlGaN interlayer and peak 4 to the overgrowth layer. The decomposition procedure applied systematically to all the samples does not reveal any change in the position of the peaks 3 and 4. Since peak 3 and peak 4 have different positions in the CTR cut, one can conclude that the corresponding vertical lattice parameters of the structure below and above the SiN mask are different.

A previous study using spatially resolved scanning electron microscope cathodoluminescence [121] and TEM [105] revealed the growth of GaN-rich islands in the openings of the SiN interlayer, surrounded by AlN-rich areas (see Chapter 6.2). These islands coalesce to a fairly uniform AlGaN layer, corresponding to the overgrowth AlGaN layer. The observed diffraction peaks 1 and 2 occur close to the values of a pure GaN crystalline structure (at

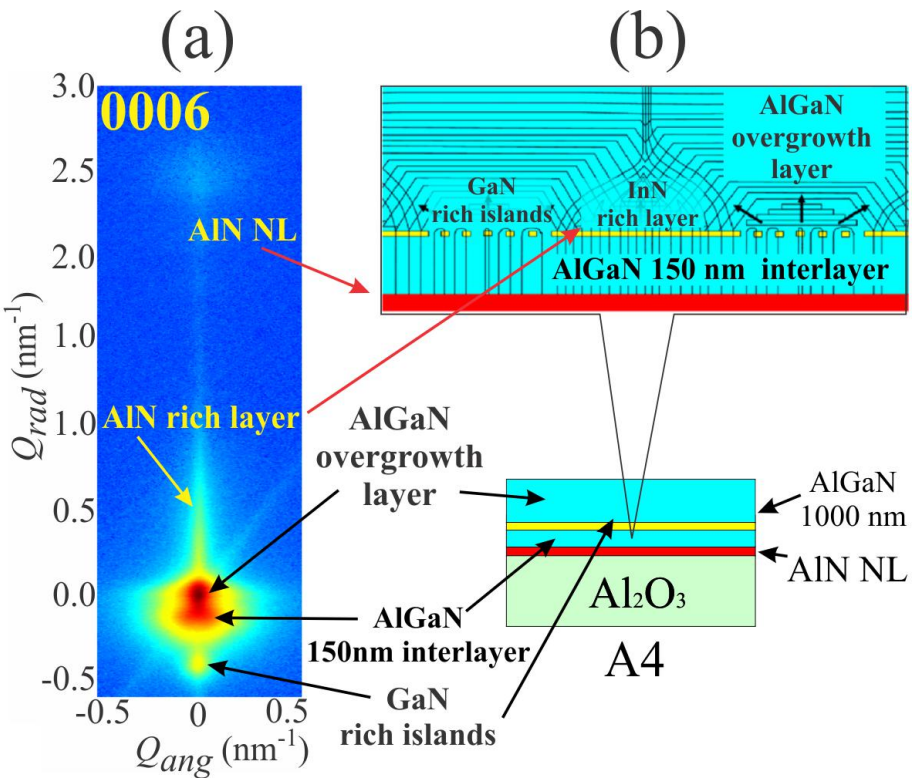

Figure 62: The RSM of the reflection 0006 of the sample A4 with depicted diffraction peaks (a), and sketch of the sample A4 with growth model scheme (b).

$Q_{rad}(GaN) = 97.08 nm^{-1}$), while peak 5 is closer to the peak of a pure AlN (at $Q_{rad}(AlN) = 100.93\, nm^{-1}$), and therefore presumably attributed to the GaN and AlN-rich areas, respectively.

In order to clarify the relation between all diffraction peaks and the growth parts of sample the RSM of the reflection 0006 of the sample A4 is presented with growth scheme of the sample in the fig.62. The RSM of the reflection 0006 (see fig.62.a), and not 0008, is chosen to show additionally the AlN NL peak which is invisible in the RSM of the reflection 0008. In the RSM (see fig.62.a) from lower Q_{rad} value to higher: the peak denoted as GaN rich islands corresponds to the "defect free" GaN rich islands in the openings of the SiN mask (see fig.62.b); the AlGaN 150 nm interlayer peak has origin from the AlGaN 150 nm interlayer below the SiN mask; peak AlGaN overgrowth layer is the peak of intensity from fairly uniform AlGaN layer above the SiN mask (see fig.62.b); the intensity distribution above the AlGaN overgrowth layer (AlN rich layer in the fig.62.a) is attributed to the InN rich layer above the uniform SiN film; and the AlN NL peak is attributed to the AlN nucleation layer before the 150 nm AlGaN interlayer (see fig.62.b).

6.8.3 Asymmetric X-ray diffraction of AlGaN epilayers with SiN mask

As it was discussed in the Chapter 4.1 asymmetric reflections are affected by screw (tilt α) and by edge (twist β) threading dislocations. Additionally, the lateral $L_{\parallel}$ and vertical $L_{\perp}$correlation lengths of the mosaic blocks influence the diffuse intensity of asymmetric reflections. Moreover, inhomogeneity of Al distribution in the epilayers has affected asymmetric reflections. In the following, the influence of threading dislocations and Al distribution inhomogeneity will be discussed in details separately.

6.8.3.1 Influence of TDs on the asymmetric reflections of AlGaN epilayers The fig.63 compares asymmetric reflections $10\bar{1}6$, $10\bar{1}8$ and $30\bar{3}8$ of the GaN (right) and AlGaN A6 (left) samples. In order to understand the impact of dislocations on asymmetric reflections of GaN and AlGaN, the mosaic model (see Chapter 4.1) illustrated at the fig.63.a should be considered. The mosaic model is characterized by a set of four parameters [88]: tilt α, lateral correlation length $L_{\parallel}$, twist β and vertical coherence length $L_{\perp}$. The RSM of asymmetric reflections of GaN (right) shows a disorientation of the main axis of the reflection's ellipse with respect to Q_{ang} which is sensitive to the product of tilt α and lateral correlation length $L_{\parallel}$. The estimation of the inclination angle ψ for the GaN

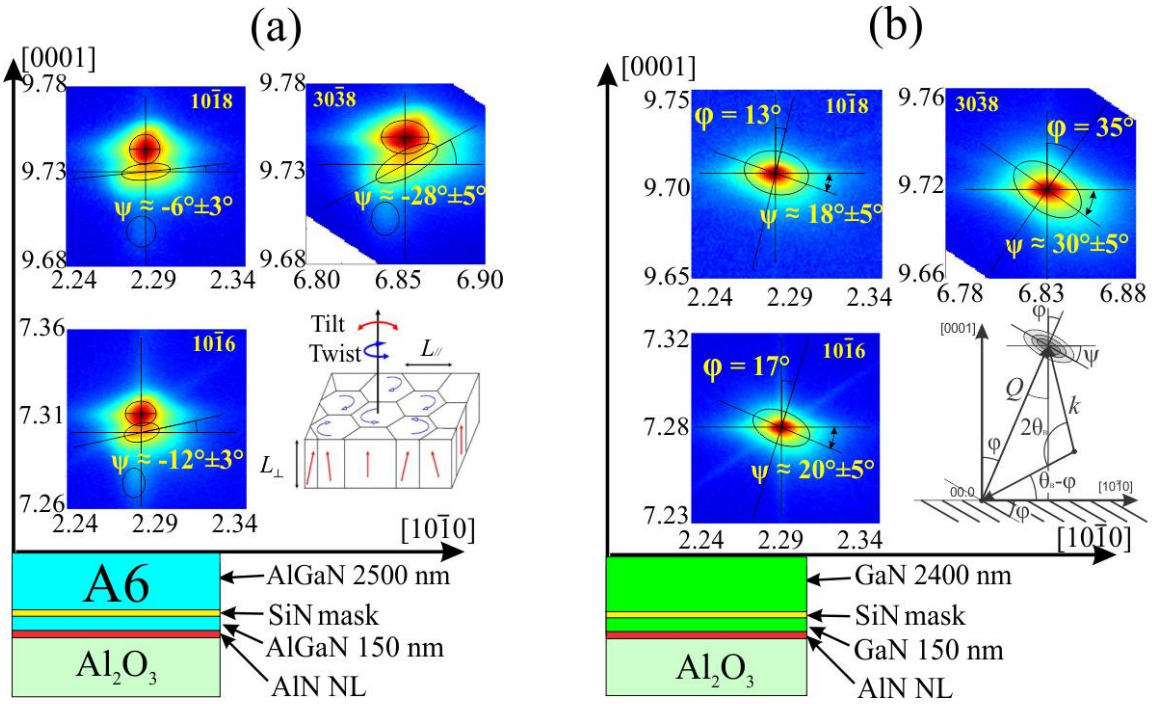

Figure 63: The asymmetric reflections of $Al_{0.2}Ga_{0.8}N$ A6 (a) and the GaN (b) samples with overgrowth thicknesses of about 2500 nm.

sample give the values $\psi = 20 \pm 5°$, $\psi = 18 \pm 5°$, $\psi = 30 \pm 5°$ for the asymmetric reflections 10$\bar{1}$6, 10$\bar{1}$8 and 30$\bar{3}$8, respectively. In the fig.63, the angles $\phi = 17°$, $\phi = 13°$ and $\phi = 35°$ correspond to an inclination of the diffracting {10$\bar{1}$6}, {10$\bar{1}$8} and {30$\bar{3}$8} crystalline planes with respect to the sample surface, respectively. The simulation of RSMs of asymmetric reflections according to the model developed by V. Holy [91] has shown that ψ should be equal to ϕ in the absence of the lateral correlation length $L_{||}$ effect. By comparing ψ and ϕ for the GaN sample, we conclude that the broadening of the asymmetrical RLP is strongly dominated by the tilt α.

Contrary to GaN, AlGaN RSMs display a different behavior. The RSMs of asymmetric reflections show the same diffraction peaks. The AlGaN overgrowth peak is oriented almost horizontally while the 150 nm interlayer peak is inclined with an angle ψ (see fig.63.b). The measured inclination of the 150 nm interlayer peak corresponding to the reflections 10$\bar{1}$6, 10$\bar{1}$8 and 30$\bar{3}$8 of AlGaN are $\psi = -12 \pm 3°$, $\psi = -6 \pm 5°$, $\psi = -28 \pm 5°$, respectively. The measurement of peak inclinations were not performed for the GaN and AlN rich peaks since the first has round shape and the second is invisible due to the low scattered intensity (see fig.63.a). This behavior was found for all of the samples.

Negative inclination of the 150 nm AlGaN interlayer peak could be attributed to the inhomogeneity of Al distribution measured by locally resolved CL measurements (see Chapter 6.2).

6.8.4 Non-coplanar GID study of AlGaN epilayers

From our coplanar diffraction study, we conclude that AlGaN epilayers grown on sapphire substrate contain two phases having different crystalline structure parameter. GID method is sensitive for the lateral in-plane "d-spacing" of the overgrowth layer upper part due to the penetration depth which is limited to 150 nm as it is estimated using the approach of Dosch et al. [124]. One of the main gals of using GID is to investigate whether phase segregation phenomena take a place at the sample surface. In this case several diffraction peaks in GID geometry are expected to appear between theoretical positions of relaxed GaN (GaN^{rel}) and AlN (AlN^{rel}). For this purpose GID reflections 10$\bar{1}$0 and 11$\bar{2}$0 corresponding to two different crystallographic directions [10$\bar{1}$0] and [11$\bar{2}$0] were recorded and analyzed. The positions of GaN^{rel} and AlN^{rel} could be calculated from their lateral unit cell lattice parameters: $a(AlN^{rel}) = 0.311nm$, and $a(GalN^{rel}) = 0.319nm$. The radial reciprocal coordinates Q_{rad} of completely relaxed GaN and AlN for 10$\bar{1}$0 and 11$\bar{2}$0 reflections are:

$$Q_{rad}^{10\bar{1}0}(GaN^{rel}) = \frac{2\pi}{a(GalN^{rel}) \cdot \cos 30°} = 22.74nm^{-1}, \quad (100)$$

Sample	Grain mean size, μm	Dislocation density, D $10^6 cm^{-2}$
A1	0.8	156.3
A2	1.6	39.1
A3	4.1	5.9
A4	7.2	1.9
A5	14.3	0.5
A6	15.8	0.4
A7	23.8	0.2

Table 11: Mean grain size and dislocation density of AlGaN samples A1-A7.

$$Q_{rad}^{10\bar{1}0}(AlN^{rel}) = \frac{2\pi}{a(AllN^{rel}) \cdot \cos 30^{\circ}} = 23.33nm^{-1}, \tag{101}$$

$$Q_{rad}^{11\bar{1}0}(GaN^{rel}) = \frac{2\pi}{a(GalN^{rel})/2} = 39.39nm^{-1}, \tag{102}$$

$$Q_{rad}^{11\bar{1}0}(AlN^{rel}) = \frac{2\pi}{a(AlN^{rel})/2} = 40.41nm^{-1}. \tag{103}$$

The measured RSMs of sample A4 (overgrowth layer thickness 1000 nm) of the reflections $10\bar{1}0$ and $11\bar{2}0$ with depicted positions of GaN^{rel} and AlN^{rel} are presented in the fig.64.a and fig.64.b, respectively. Both of the reflections reveal only one AlGaN peak between GaN^{rel} and AlN^{rel} at $Q_{rad}^{10\bar{1}0}(AlGaN) = 22.78nm^{-1}$ and $Q_{rad}^{11\bar{2}0}(AlGaN) = 39.45nm^{-1}$. This phenomena demonstrates presence of only one AlGaN phase at the surface samples. The same behavior is found for all of the samples except the thinnest sample A1 which will be discussed in details in the Chapter 6.11.2.

However, an asymmetry of the AlGaN peaks in radial direction Q_{rad} is visible (see fig.64). This latter indicates the presence of a local difference in the in-plane lattice parameters, meaning minor inhomogeneity of the Al incorporation in the AlGaN sample surface.

The broadening of the reflections in angular direction Q_{ang} is related to the twist β of mosaic blocks meaning edge TDD. The $FWHM$ of the reflection cut in angular direction (in reciprocal units) proportional to the $\mathbf{Q}$ vector length. Since $Q_{rad}^{11\bar{2}0}(AlGaN)/Q_{rad}^{10\bar{1}0}(AlGaN) \approx 1.7$, the broadening of the reflection $11\bar{2}0$ should be in 1.7 times larger than for the reflection $10\bar{1}0$. Edge TDD could be calculated from the GID reflection $FWHM$ in angular direction as it was discussed in the Chapter 4.1.

6.9 Estimation of dislocation density of AlGaN epilayers from the average hexagonal domain size

The optical microscopy in combination with TEM and AFM studies allowed us to conclude that the hexagonal shape domains are "dislocation free" (see Chapter 6.7). These domains could be well described by mosaic model blocks introduced in the Chapter 4.1 and therefore total dislocation density could be estimated from the mean grain size $L_{\parallel}$ using simple equation introduced by Lee et al. eq.62:

$$D = \frac{1}{L_{\parallel}^2}. \tag{104}$$

The $L_{\parallel}$ could be derived either from the WH plot or from OM micrographs. The mean grain size $L_{\parallel}$ for samples A1-A7 and the corresponding dislocation densities are summarized in the tab.11. where the estimated dislocation density represent the summation of screw and edge TDD: $D = D_s + D_e$. Alternatively, more accurate method based on XRD will be devoted to determine precisely the TDDs.

6.10 Calculation of TDD using the mosaic model

The mosaic model and its application for the determination of the TDD has been introduced in details in the Chapter 4.1. In the RSMs of AlGaN samples, two distinguishable peaks were originated from AlGaN overgrowth and 150 nm AlGaN layers due to difference in Al content. This permits us the determination of the density of dislocations for the AlGaN overgrowth and 150 nm AlGaN layers separately.

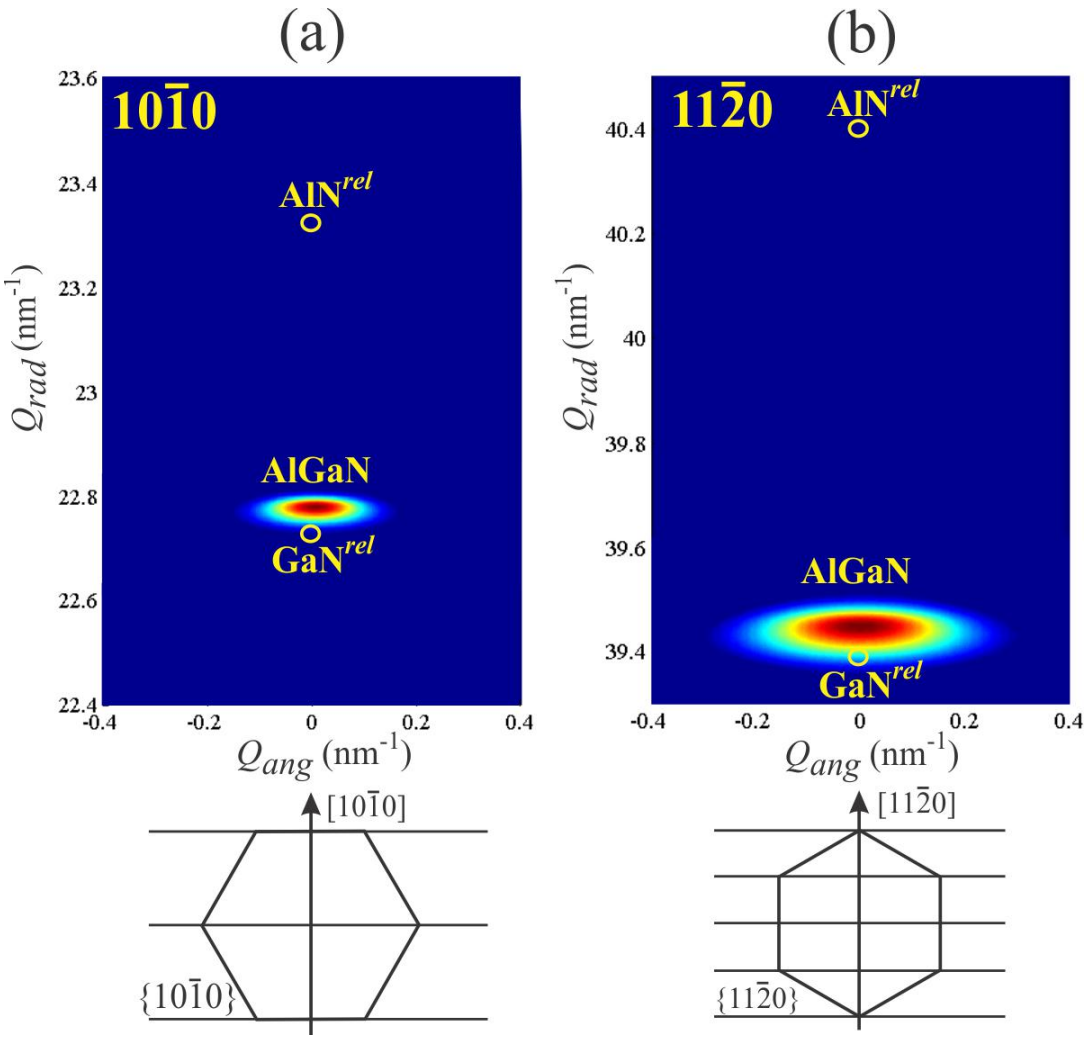

Figure 64: GID RSMs of the $10\bar{1}0$ (a) and $11\bar{2}0$ (b) reflections of the sample A4, with crystallographic directions shown below.

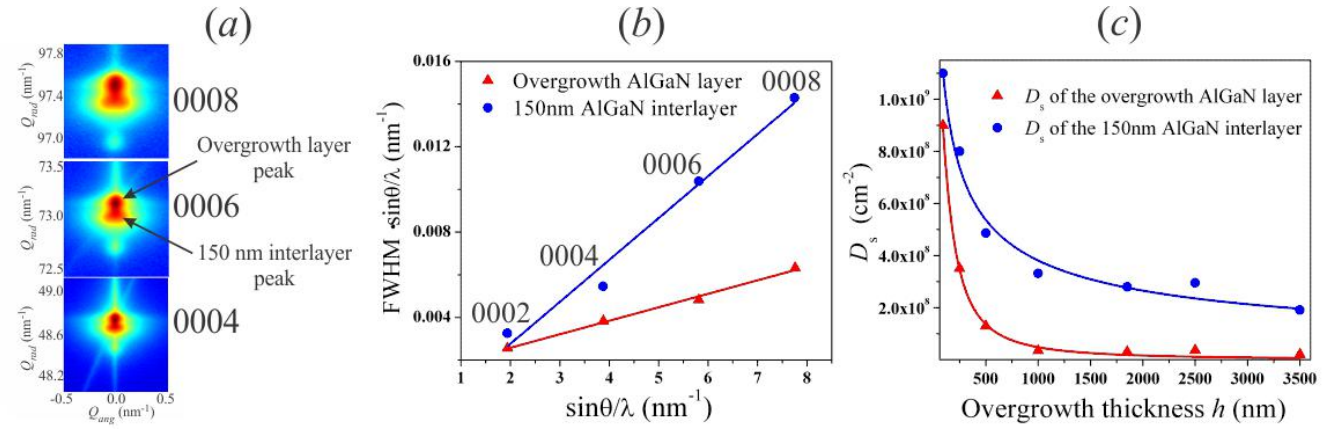

Figure 65: The RSMs of symmetric reflections of the sample $Al_{0.2}Ga_{0.8}N$ with thickness 1000 nm with overgrowth layer and 150 nm interlayer shown (a), WH plot of the same sample's symmetric reflections (b), and variation of screw dislocation densities D_s derived from two peaks calculated using WH plot (c).

In this section the screw (D_s) and edge (D_e) TDDs will be calculated using equations derived from mosaic model introduced in the Chapter 4.1.

6.10.1 Screw type TDDs calculation using the mosaic blocks model

According to the mosaic model, the average absolute values of the tilt α and twist β are directly related with the full width half of maximum (FWHM) of the corresponding distributions of the crystallographic orientations. Therefore, the dislocation densities are correlated to the FWHM values of rocking curve scans and are calculated from the tilt α and twist β angles [92]. The tilt of the mosaic blocks (screw TDD) causes the broadening of the symmetric reflections in angular Q_{ang} direction, while the twist almost doesn't influence on them. The WH plot is a plot of the FWHM of the rocking curve as a function of the reflection order of symmetric reflections (see Chapter 4.1). The density of screw dislocations has been calculated using the eq.68:

$$D_s = \frac{\alpha^2}{4.35 \cdot |\mathbf{b}_{screw}|^2},$$

where $|\mathbf{b}_{screw}| = |\langle 0001 \rangle| = c$ is the length of the Burgers vector of the screw dislocation and the tilt α represents the slope of the WH plot. In case of the alloy $Al_{0.2}Ga_{0.8}N$, one can derive the value of the Burgers vector $|\mathbf{b}_{screw}| = c(Al_{0.2}Ga_{0.8}N) = 0.2 \cdot c(AlN) + 0.8 \cdot c(GaN) = 0.514nm$.

The WH plot was applied for the overgrowth layer and 150 nm interlayer detected peaks of symmetric reflections (shown in the fig.65.a for the sample A4) for all $Al_{0.2}Ga_{0.8}N$ samples having different overgrowth thicknesses h. The fig.65.b presents an example of the WH plot for the sample A4 with 1000 nm AlGaN layer thickness. The derived densities D_s of screw dislocations for the150 nm interlayer and overgrowth layer of RSMs are drawn against the overgrowth thickness h, and their fit with h^{-n} function is shown in the fig.65.c. Both densities decrease with the overgrowth thickness. A remarkable decrease in the overgrowth peak's D_s from $9 \cdot 10^8$ to $3 \cdot 10^7 cm^{-2}$ has been found by increasing the overgrowth thickness from 90 nm to 1000 nm. Moreover, the D_s values determined from the 150 nm interlayer peak are larger than those calculated from the overgrowth peak due to the larger broadening of the reflection. This result enables us to conclude that in the AlGaN epilayers besides to the phase formation due to the occurrence of local variations in the AlN content, the sample contains local differences in D_s.

6.10.2 Edge type TDDs calculation using the mosaic blocks model

Edge dislocations cause distortions of lattice planes perpendicular to the surface but do not disturb the position of these planes along the layer normal. The highest sensitivity to edge dislocation is obtained by diffraction from lattice planes perpendicular to the surface. Lattice planes inclined with respect to the surface and measured by asymmetric reflections are partially affected by the edge TDD. However, a precise determination of the D_e requires obligatory GID measurement, especially in our case with many other factors influence on asymmetric reflections. The GID reflections $10\bar{1}0$, $20\bar{2}0$ and $30\bar{3}0$ were measured to determine D_e. Their RSMs are shown in the fig.66.a

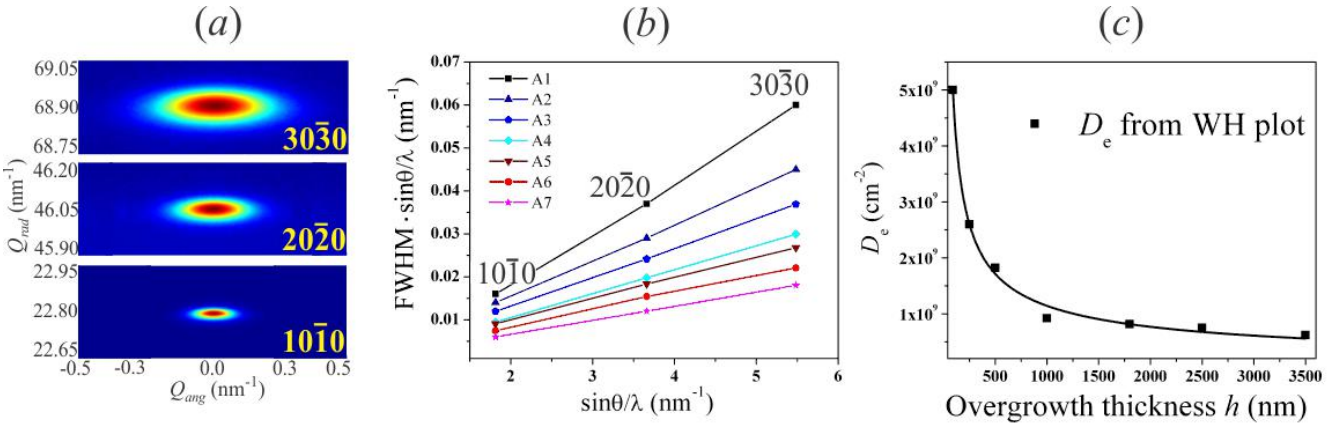

Figure 66: The GID reflections of the AlGaN sample A4 (a), GID reflections WH plots of samples with different overgrowth thicknesses (b), edge dislocation density as a function of overgrowth layer thickness h (c).

for the sample A4 as an example. The impact of the edge type threading dislocations on the width of the X-ray reflections in the case of planes perpendicular to the surface is commonly referred as twist β in the model of disoriented blocks (see Chapter 4.1). Similar to the symmetric reflections, the WH method has been applied to the GID reflections and the edge type dislocation densities could be derived using the following formula68:

$$D_e = \frac{\beta^2}{4.35 \cdot |\mathbf{b}_{edge}|^2},$$

where β is the slope of the linear function $FWHM \cdot \sin\theta/\lambda$ plotted against $\sin\theta/\lambda$ and $|\mathbf{b}_{edge}| = \left|\frac{1}{3}\langle 11\bar{2}0\rangle\right|$ is the length of the edge dislocation Burgers vector (for the alloy $Al_{0.2}Ga_{0.8}N$ $|\mathbf{b}_{edge}| = a(Al_{0.2}Ga_{0.8}N) = 0.2 \cdot a(AlN) + 0.8 \cdot a(GaN) = 0.317nm$). The WH plots corresponding to the different samples are shown in fig.66.b. The derived densities of edge dislocations for all AlGaN samples are shown in fig.66.c. The density of edge TD D_e decreases with the overgrowth layer thickness h. By increasing the overgrowth thickness h from 90 nm until 1000 nm D_e varies from $5 \cdot 10^9$ to $0.9 \cdot 10^9 cm^{-2}$. However, by further increasing the thickness h, only a weak decay is noted.

6.10.3 Scaling law of the TDD reduction derived from the mosaic model

As mentioned in chapter, the X-ray diffraction of high reflections showing two peaks reveals the presence of two phases having nearly similar structure in the growth direction (0001). Furthermore, these two peaks are found to have different screw treading dislocation density.

The derived D_s of the overgrowth layer, 150 nm interlayer and D_e are plotted in log-log scale as function of overgrowth thickness h in the fig.67. The fitting of the calculated TDDs with a scaling law h^{-n} shows a good agreement, and fitted curves are lines in log-log scale (see fig.67). For the screw TDD D_s corresponding exponents n for the overgrowth AlGaN layer and the 150 nm interlayer are $n = 1.05$ and $n = 0.43$, respectively. The decay of D_s derived from the overgrowth layer peak is faster than in the case of the 150 nm interlayer peak. Therefore, the dependency of D_s densities on the overgrowth thickness h is different for the two peaks. Theoretically the TDD of the 150 nm interlayer should be independent from the h, since the layer is always almost the same. However, small decay is observed probably due to the overlapping of AlGaN overgrowth and 150 nm interlayer peaks, which omit to determine the TDDs accurately. By fitting the edge TDD D_e dependence with the scaling law h^{-n}, the exponent n is found to be equal to 0.62.

6.11 Calculation of TDD using the Monte Carlo numerical method

6.11.1 Application of the Monte-Carlo simulation to a two layer system

Numerical Monte-Carlo simulation was applied successfully for the determination of the edge (D_e) and screw (D_s) dislocation densities from the diffuse scattering of GaN samples having nearly the same growth structure as the AlGaN samples [67, 101]. The simulation of RSMs of GaN samples was carried out with the assumption that the diffracted intensity distribution is originating only from the GaN layer above the SiN mask. An attempt to

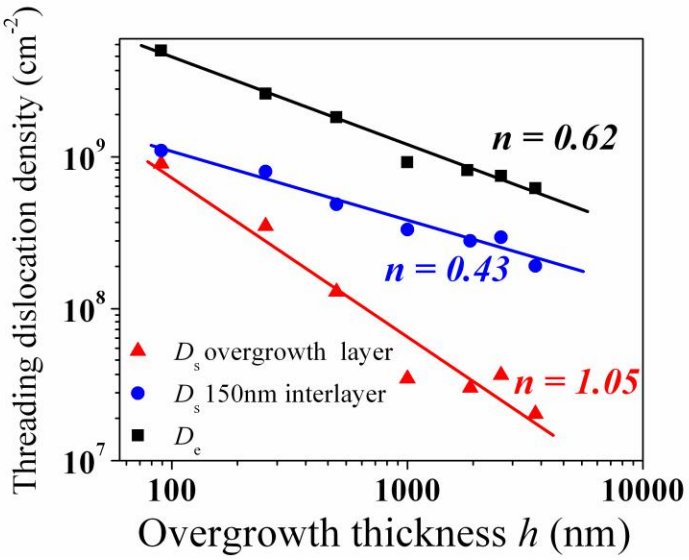

Figure 67: Comparison of edge D_e and screw D_s TDD reduction with h derived from WH plot.

apply the Monte-Carlo method to simulate the RSM by considering only the AlGaN overgrowth layer was not successful in achieving a good fit with the measured RSM. For this reason a further development was implemented into the model to calculate the RSM of a more complex system consisting of two AlGaN layers, in order to derive independently and accurately the density of edge and screw threading dislocations of each individual AlGaN layer. Because of their relatively low density the presence of screw dislocations in the calculation of the RSMs in GID for either the 150 nm interlayer or for the overgrowth layer was not taken into account. Nevertheless, the simulation of the RSMs of the symmetric reflection of the overgrowth layer and the 150 nm interlayer are slightly different due to different types of interfaces: the 150 nm interlayer AlGaN does not have a free surface and hence does not reveal any surface stress relaxation since it forms a top interface with the AlGaN overgrowth layer and a lower interface with the AlN nucleation layer. In contrast, the overgrowth layer possesses a discontinuity at the surface which gives rise to an additional non-zero vertical component parallel to the diffraction vector of the symmetric reflections, resulting from the displacement field created by edge dislocations [96]. Since in the case of the overgrowth layer the edge dislocations play an important role in the general intensity distribution in the RSMs of symmetric reflections, D_e serves as an input parameter in the simulations of these RSMs. Therefore, first GID RSMs should be simulated to derive the edge TDD D_e. In contrast, these symmetric reflections are not affected by D_e in the case of the 150 nm AlGaN interlayer.

In the experiment the penetration depth in GID was estimated to be less than 150 nm which enables to probe solely the upper part of the overgrown AlGaN layer for the samples A2 through A7 with $h > h_1$. Hence, the densities of edge TDs for this thickness could be determined. This statement does not apply to the sample A1, where the overgrowth layer was only 90 nm, i.e. smaller than the penetration depth. The study of this sample will be presented in the following Chapter 6.11.2. A detailed description of the different steps involved in the application of Monte-Carlo simulation to the RSMs was introduced in the Chapter 4.2. To derive the TDD the RSMs of the GID reflections $10\bar{1}0$ and $11\bar{2}0$ were simulated. The simulation of the reflections from different crystallographic orientations are required for better accuracy.

The simulated RSMs were then convoluted with a resolution function to achieve a finite experimental resolution. The resolution function was chosen as a two-dimensional Gaussian with a width corresponding to the coherently irradiated area of the sample surface estimated for the experimental setup to be 300 x 600 nm^2. A similar procedure for GaN films is described in [101]. The comparison of experimental and simulated RSMs for the sample A4 is shown in fig.68.b and fig.68.c.

In the experimental $11\bar{2}0$ RSM (fig.68.c) one can see some asymmetry in the radial direction, which indicates the presence of a local difference in the in-plane lattice parameters and was discussed in Chapter 6.8.4. However, for the TDD determination it is more important to fit the tails of the peaks, and therefore this asymmetry does not affect the accuracy or reliability of the values determined by the simulation.

Subsequently the D_s was determined by considering a system with two AlGaN layers as described above.

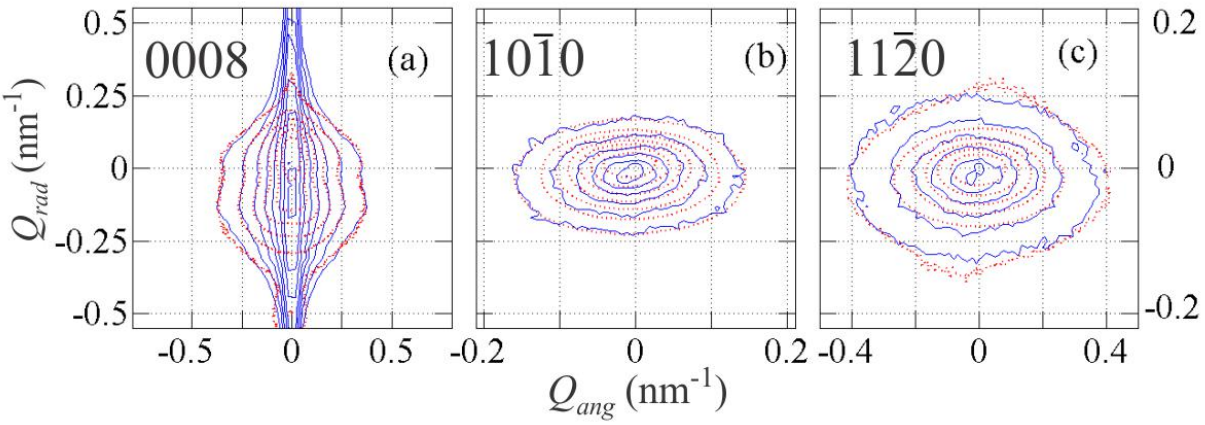

Figure 68: Measured (red, dots) and simulated (blue, solid) reciprocal-space maps for the reflections 0008 (a), 10$\bar{1}$0 (b) and 11$\bar{2}$0 (c) for sample A4. The intensity steps are in logarithmic scale: $10^{0.5}$ (a) and $10^{0.25}$ (b), (c).

Contrary to the GID method, the penetration depth in coplanar diffraction geometry was about 5000 nm for the 0008 reflection, so all layers deposited on the sapphire substrate contribute to the RSM.

In the Chapter 6.8.2.2 two diffraction peaks appearing in the RSM of 0008 symmetric reflections were attributed to the AlGaN overgrowth layer and to the 150 nm AlGaN interlayer. Consequently, the intensity distribution of the RSMs represents the overlap of these two peaks. The RSMs from these two layers were simulated independently and then the intensity distributions were superposed. The densities of screw dislocations in both layers were derived after achievement of the best agreement between experimental and simulated RSMs (see fig.68.a). The Q_{ang} axis is chosen as the [10$\bar{1}$0] direction and Q_{rad} axis as the [0001]. One can observe some disagreement between the experimental and simulated RSMs of the 0008 reflection in the lower Q_{rad} values due to the fact that the GaN rich peak was not taken into consideration in our simulation model. In addition to comparing the shapes of intensity distributions in the RSMs we analyzed their cuts along the angular directions as has been introduced by Kaganer et al. [93]. For the symmetric 0008 reflection we compared the cuts through both peaks. The experimental and simulated profiles in log-log representation are in good agreement, especially in the diffuse part of the intensity distributions, which confirms that our model was applied successfully and could be used for accurate determination of TD densities. The cuts through the main peak of symmetric reflections are depicted in fig.69.a.

The asymptotic behavior of the tails seems to follow a law Q_{ang}^{-n} , with n between 2 and 3, which indicates the presence of screw TDs as the prevailing type of dislocation, as is proposed by Holý et al. [42]. In a similar way, the cuts through the maximum of intensity of the GID reflections are displayed in fig.69b and fig.69c. In contrast to the symmetric reflections, the asymptotic behavior of GID reflection cuts is mainly influenced by the edge type of TDs. The tails of the curves lie between Q_{ang}^{-1} and Q_{ang}^{-2} rather than Q_{ang}^{-2} and Q_{ang}^{-3}, as might be expected from the universal law [93]. One possible explanation is the excess of the edge TD density with respect to the screw TD density.

6.11.2 Determination of the edge TDD below and above the SiN nanomask

The TEM investigation has led to a comprehensive understanding of growth and defect reduction mechanisms occurring by the formation of dislocation half loops at the SiN interface (see Chapter 6.4). A qualitative estimation of the dislocation densities was based on the observation of TEM images [105, 125]. In fact, a homogenous edge type dislocation density has been observed in the layer below SiN while defect-free and defect-rich areas have been detected side by side on a several 100 nm scale above the SiN nano-mask. In order to determine quantitatively the efficiency of the SiN nano-mask in the reduction of threading dislocation densities, it is very important to probe simultaneously with X-rays the AlGaN layer below and above the SiN nano-mask. For all samples, the GID 11$\bar{2}$0 reflection was measured with a maximum achievable penetration depth of 150 nm, calculated using an approach described by Dosch et al. [124]. For the samples A2 to A7 the overgrowth thickness h was greater than the penetration depth of 150 nm and only for sample A1, was it possible to measure simultaneously the signals from the overgrowth layer completely and partially (60 nm) from the 150 nm AlGaN interlayer. Consequently the RSM of the 11$\bar{2}$0 GID reflection of sample A1 shows different features in comparison to the remaining samples. The RSM of the 11$\bar{2}$0 reflection presented in fig.70(left) shows the presence of two overlapped signals shifted along the Q_{rad}

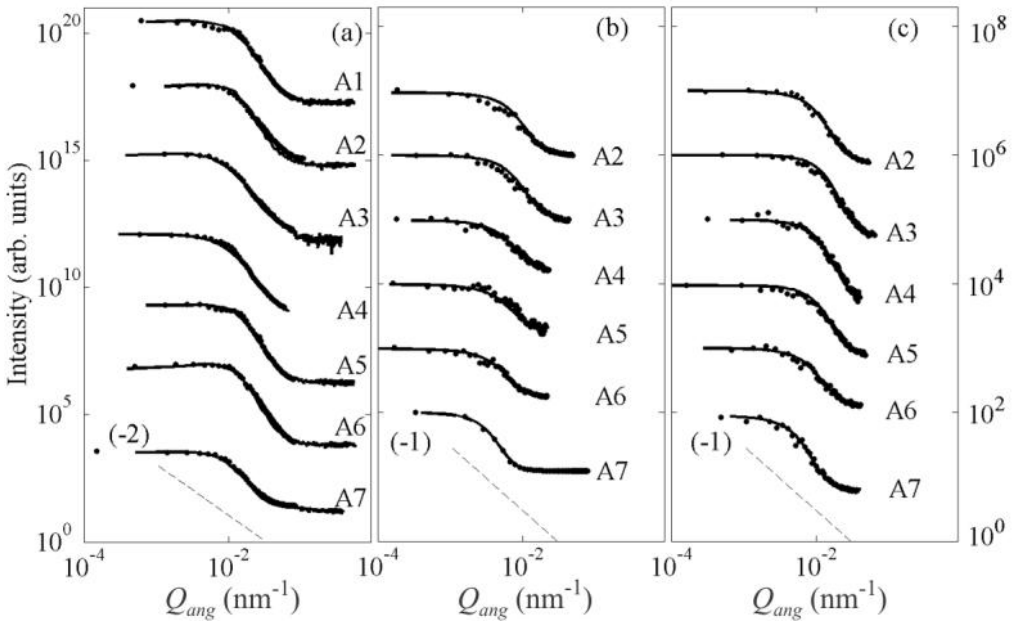

Figure 69: The cuts through the main peak of symmetric reflection 0008 along the angular direction Q_{ang}; the asymptotic behavior of cuts obeys $Q_{ang}^{-2} - Q_{ang}^{-3}$ (a). The cuts through the maximum of intensity of the $10\bar{1}0$ GID reflection (b) and the $11\bar{2}0$ reflection (c). For all the samples, the experimental curves are depicted by dots and the theoretical curves by solid lines.

direction and originating from the overgrowth layer and the 150 nm interlayer. In order to derive the TD densities from the overlapped signals, fig.70(middle) illustrates the decomposition procedure applied to the RSM into two-dimensional Lorentzians. The parameters of the Lorentzians were determined from the decomposition of the radial and angular scans through the maxima of the signals indicated in the RSM in fig.70(left). The two derived RSMs were simulated separately by considering two separated layers having 90 nm and 150 nm thicknesses. The RSMs simulated by the Monte-Carlo method for the two layers are compared to the decomposed RSMs in fig.70(right). The edge dislocation densities were consequently determined from the best fit and are found to be $6.4 \cdot 10^{10} cm^{-2}$ for the 90 nm AlGaN overgrowth layer and $9.8 \cdot 10^{10} cm^{-2}$ for the 150 nm AlGaN interlayer. This method allows to quantify the efficiency of the SiN nano-mask discussed in the next section.

6.11.3 Scaling law of the TDD reduction derived from Monte Carlo method

The D_e and D_s data derived from the Monte Carlo simulation are plotted in log-log scale as a function of the overgrowth thickness h (fig.71.a). The density of edge TD decrease with overgrowth from $6.4 \cdot 10^{10} cm^{-2}$ for the 90 nm to $1.9 \cdot 10^{9} cm^{-2}$ for 3500 nm. The fitting of the D_e variation with a scaling law h^{-n} gives an exponent $n = 0.95$. Additionally, the efficiency factor of the SiN nano-mask as the ratio between $D_e = 9.8 \cdot 10^{10} cm^{-2}$ of the 150 nm AlGaN interlayer and D_e of the overgrowth layer thickness h is defined (fig.71.b). The increase of the overgrowth layer thickness improves conspicuously the efficiency of the SiN nano-mask. In fact, this factor increases up to 52 for the overgrowth thickness of 3500 nm.

As described by Klein et al. [105], the dislocation bending leads to the annihilation of TDs by the formation of dislocation loops. From the growth model proposed by Klein (see Chapter 6.4) the overgrowth favours the coalescence of two nearby islands leading to small areas with TDs at the surface. This dislocation reduction mechanism proposed by the model leads to the enhancement of the efficiency factor with the overgrowth thickness h.

The values of D_s are found to be lower than D_e for all overgrowth thicknesses h, and follows a scaling law h^{-n}, with an exponent $n = 0.18$ for the overgrowth layer and $n = 0.33$ for the 150 nm AlGaN interlayer. A similar result was derived by high resolution TEM investigation [105, 125]. Furthermore, the D_s of the overgrowth layer is about a factor 2 lower than the D_s of the 150 nm AlGaN interlayer. This demonstrates that the SiN nano-mask plays a role in the reduction of D_s as well as of D_e. Some variation of the 150 nm interlayer D_s with h could be explained by influence of the overgrowth AlGaN layer diffuse intensity, as it was described in Chapter 6.10.3.

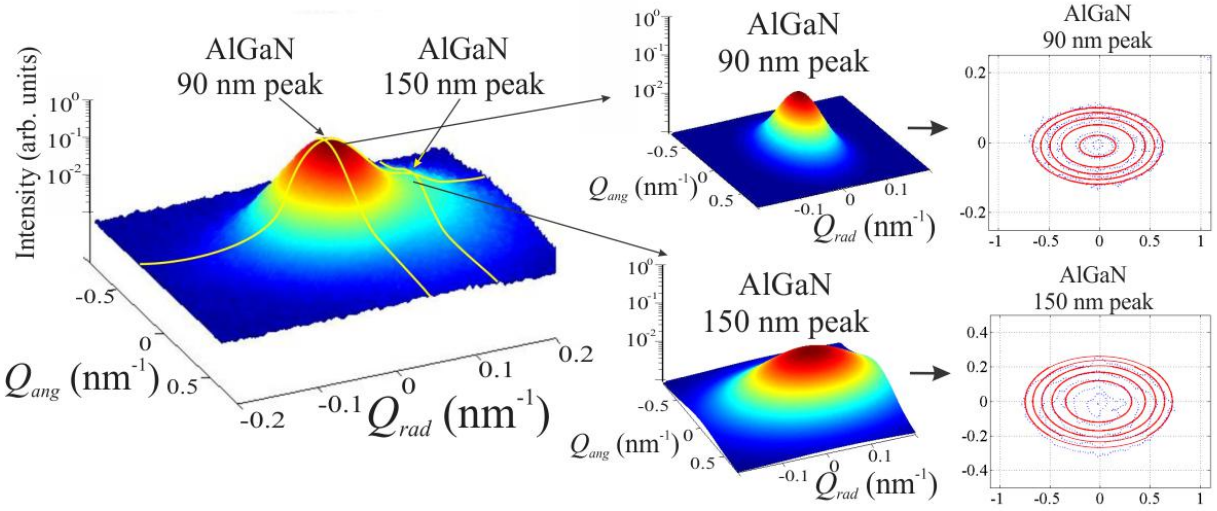

Figure 70: The $11\bar{2}0$ GID reflection of sample A1 (left), decomposition of the overlapped signals from the 150 nm AlGaN interlayer and the 90 nm overgrowth layer (middle), and Monte Carlo simulations of the peaks (right).

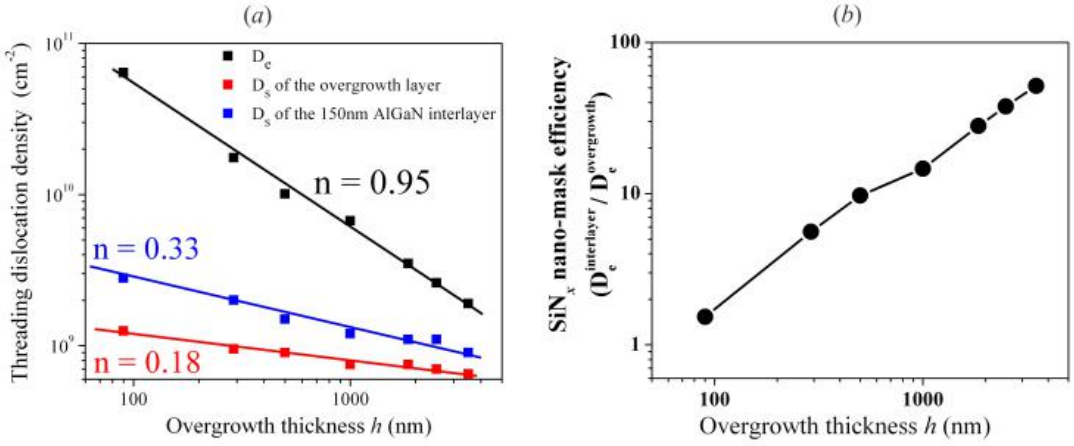

Figure 71: The variation of D_s determined from coplanar high-resolution X-ray diffraction and D_e determined from GID measurement as a function of the overgrowth thickness h (a). The variation of the efficiency of the SiN nano-mask in dislocation reduction with overgrowth thickness h (b).

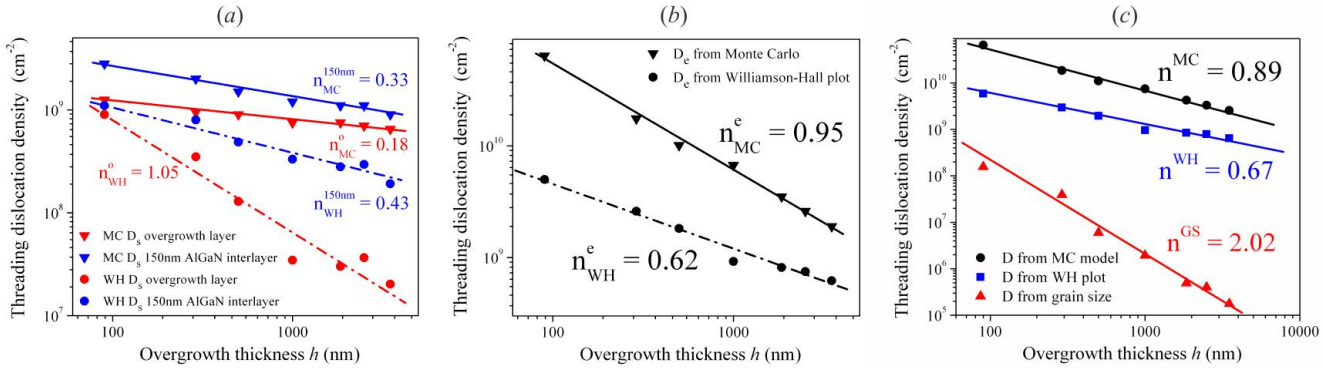

Figure 72: Comparison of the screw dislocation densities of the overgrowth and 150 nm AlGaN layers (a), and edge calculated using MC method and WH plot (b). Comparison of the total TDD of the AlGaN overgrowth layer derived from WH plot, MC simulation and domain mean size (c).

6.12 Comparison of TDDs derived from different methods

The modeling of TDs reduction as function of the GaN film thickness was developed by Mathis et al. [110] who has demonstrated that the dependency of the TDs for GaN does not follow the inverse proportional law of the film thickness $\sim 1/h$ as it is known from the work of Romanov et al. and other [126, 127] in the case of fcc semiconductors. The fitting of the experimental data of GaN films as function of the buffer layer thickness gives a dependency on $h^{-2/3}$[110]. In this chapter the TDDs derived using WH plot, MC model and direct measurement of grain size will be compared between them self and with h^{-1}, $h^{-2/3}$ scaling laws.

6.12.1 Comparison of TDDs

Comparison of the screw TDD derived from the WH plot and MC simulations is presented in log-log scale in the fig.72.a. The scaling laws for 150 nm AlGaN interlayer derived from WH and MC models has been found to be comparable ($n_{MC}^{150} = 0.33$, $n_{WH}^{150} = 0.43$) indicating slightly variation of the TDDs with the overgrowth AlGaN layer thickness, which is not expected since the thickness of the AlGaN interlayer remains constant. This variation could be caused by the uncertainties in determining the broadening of the overlapped peaks of the overgrowth AlGaN and 150 nm AlGaN interlayers.

Behavior of the overgrowth layer screw TDD reduction is found to be more different. The screw TDD of the overgrowth layer of WH and MC models are rather different. The exponent of MC model TDD scaling law is $n_{MC}^{0} = 0.18$ while the exponent of WH is $n_{WH}^{0} = 1.05$.

The edge dislocation densities from WH and MC models are presented in the fig.72.b. In case of MC model the exponent of the scaling law is $n_{MC}^{e} = 0.95$ and for the WH plot $n_{WH}^{e} = 0.62$.

The total TDDs $D^{GS} = D_s + D_e$ of the AlGaN overgrowth layer are derived in the Chapter 6.9 from simple equation using the mean domain size. Comparison of the total TDDs D^{WH} determined from WH plot and D^{MC} from MC simulation of the AlGaN overgrowth layer with D^{GS} is presented in the fig.72.c. The highest value of TDD gave MC simulation, one order lower WH plot and from two up to four orders lower mean grain size approach. The exponent $n^{MC} = 0.89$ of MC simulation is close to h^{-1} law while $n^{WH} = 0.67$ of WH plot correspond to $h^{-2/3}$, contrary $n^{GS} = 2.02$ of grain mean size is close to h^{-2}.

Different behaviors for the TDDs reduction are found for the scaling law exponents of WH, MC and mean grain size based models. The determination of the TDDs using WH plot considers that peak broadening is mainly due to dislocations and ignore the influence of dislocations on the diffuse parts of the reflections. Contrary, MC model takes into account the influence of the TDs on the broadening as well as on the tail of the diffraction profile which lead to a good agreement between the measured and calculated diffraction profiles in the coherent and the diffuse parts [67].

Our study has emphasized that MC simulation is a reliable method to determine TDD in comparisons with WH plot and mean grain size methods, which could give an acceptable and fast estimation for TDD. Unfortunately, obtainment of reliable values of TDD using MC simulation is a time consuming process.

6.13 Conclusions

Understanding of the influence of Al on the structure of GaN alloys, such as AlGaN epilayers with 20% Al content, requires high-resolution X-ray diffraction data, which is obtained by measuring the RSMs in coplanar (SXRD, ASXRD) and non-coplanar (GID) geometries. Furthermore, if we had restricted our investigation to simple rocking-curve measurements of symmetric and asymmetric reflections, without recording complete RSMs, we would not have been able to detect any local variations of the lattice constants. The presence of several peaks in the RSMs demonstrates the existence of different crystalline structures within several phases, due to an inhomogeneous distribution of the Al content.

Through a systematic study of the intensity distribution along the CTR of the 0008 symmetric reflection it was possible to attribute the different peaks to the different individual layers that comprise the AlGaN epilayer system. Our investigation enabled us to conclude that the main upper and lower peaks of the symmetric reflection originate from the 150 nm AlGaN interlayer and in the overgrowth layer respectively. The intensity of the GaN-rich peak is attributed to the GaN-rich so-called "defect free" islands on the opening of the SiN mask, while the AlN-rich intensity distribution is attributed to the areas above solid SiN layer. For all the samples, the decomposition of the CTR profile into several peaks shows a change in the peak intensities but no change in the peak positions. This would indicate that the local difference in the "d-spacing" is not influenced by the overgrowth thickness.

By using the WH plot, the screw and the edge type dislocation densities were examined for overgrowth, while the 150 nm layers were examined as a function of the overgrowth thickness from a series of symmetric and GID reflections. The values of screw TDD D_s are found to be lower than the edge TDD D_e for all overgrowth thicknesses h. The variation of the screw and edge type dislocation densities with the overgrowth thickness can be determined by applying the scaling law h^{-n} where n is equal to 1.05, 0.43 and 0.62 for the D_s of the overgrowth layer, 150 nm interlayer peaks of symmetric reflections and D_e of GID peaks respectively. For the thickest AlGaN layers investigated, a very low edge type dislocation density of the order $5 \cdot 10^8 cm^{-2}$ was found.

By comparing the threading dislocation density determined by Barchuk et al. [67, 101] for GaN to the values calculated for the $Al_{0.2}Ga_{0.8}N$ samples grown in a similar way, it can be concluded that the AlGaN epilayers contain higher threading dislocation densities.

The Monte Carlo method has proven to be reliable in modelling the RSMs in coplanar and non-coplanar geometries within a two-layered system. The experimental and the Monte Carlo simulated RSMs concur, enabling screw and edge type threading dislocation densities with an error less than 15% to be derived. Furthermore, the reduction of D_s and D_e follows the scaling law h^{-n} with regards the overgrowth thickness, with $n = 0.18$ for D_s of the overgrowth layer, $n = 0.33$ for D_s of 150 nm interlayer, and $n = 0.95$ for the D_e. The asymptotic behavior of the tails of the symmetric reflections adhere to the law of $2 < n < 3$, while the tails of the diffraction peaks in the GID adhere to the law of $1 < n < 2$. The deviation of asymptotic decay from the universal law, particularly with regards to GID, is due to the large edge type TD densities.

One of the aims of the study was to demonstrate that the analysis of diffuse scattering using the simulation of decomposed RSMs of GID reflections, is a powerful and effective method for determining the TDs in a two-layer system separately, e.g. below and above a SiN nanomask. The objective here would be in order to qualify the SiN mask efficiency by reducing the TDs as a function of the overgrowth layer thickness h.

In the future, it would be worthwhile considering investigating TDs during the growth process, something which is currently under discussion and planned to be performed at the NANO beamline at ANKA synchrotron.

7 X-ray investigation of nonpolar GaN epilayers

7.1 Introduction

Optoelectronic devices are generally based on [0001]-oriented III-nitride films, but their efficiencies can be limited by the quantum-confined Stark effect (QCSE) [128, 129]. The wurtzite crystal structure is non-centrosymmetric and has a polar axis along [0001] direction, along which spontaneous polarization fields occur. In case of [0001]-oriented films the spontaneous polarization fields lead to separation of the electrons and holes spatially and hence reducing their recombination probability. In order to avoid the influence of the polarization field on the carrier movement direction perpendicular to the sample surface, Horino et al. [130, 131] in 1996 began to grow GaN epitaxial layers in the m orientation on m-oriented SiC, with [0001] orientation parallel to the sample surface.

The influence of the lattice mismatch between the substrate and GaN layer on closed packed [0001] growth direction leads to the formation of the basal plane stacking faults (BSFs). This latter act as non-radiative recombination centers and drop the efficiency of optoelectronic devices. In this chapter the influence of different growth techniques on the BSFs density reduction will be investigated.

7.2 Description of nonpolar GaN samples

In order to investigate the density of BSF in nonpolar GaN epilayers, four a-plane ($11\bar{2}0$) GaN samples, denoted as N1-N4 (see fig.73), were grown heteroepitaxially on r-oriented sapphire substrates by MOVPE in an AIXTRON 200/RF-S horizontal flow reactor. TMGa, TMAl and ammonia (NH_3) have been used as Ga, Al, and N precursors as described in detail by Schwaiger et al. [132]. Before starting the growth of all samples, the substrate was heated up to $1200°C$ for a desorption of surface impurities. Then, the growth of all samples was initiated with an about 20-nm-thick high-temperature AlN nucleation layer (NL).

For the sample N1, the growth temperature of $1120°C$ and a NH_3 to TMGa molar flow ratio (V/III ratio) about 1100 were chosen to deposit a-GaN film with thickness of approximately 2.2 μm . In order to optimize the GaN layer quality for the sample N2, the SiN mask deposition technique was used as it is described in [64]. First 1 μm thick GaN layer was grown with a temperature of $1120°C$ and the molar flow ratio V/III of about 2200, then on the top of GaN layer the SiN mask of 300 nm was deposited in-situ. Further GaN layer at the same temperature, but with V/III ratio of about 540 is overgrown until the total thickness of the system reach about 2.3 μm.

For the sample N3 an alternative two-steps mode technique of defect-reduction was used. Firstly, 1 μm GaN layer was epitaxially grown with increased V/III ratio about 2200, owing to achieve best bulk crystal quality. Then, the top layer of GaN was grown with reduced V/III parameter to 540 up to total GaN film thickness of 2.3 μm, in order to minimize the surface roughness.

For the sample N4, the same growth procedure as for sample N3 was applied and additionally the sample was overgrown by hydride vapour phase epitaxy to a total thickness of approximately 9 μm (see [132] for more details). The sketches of the samples are shown in the fig.73.

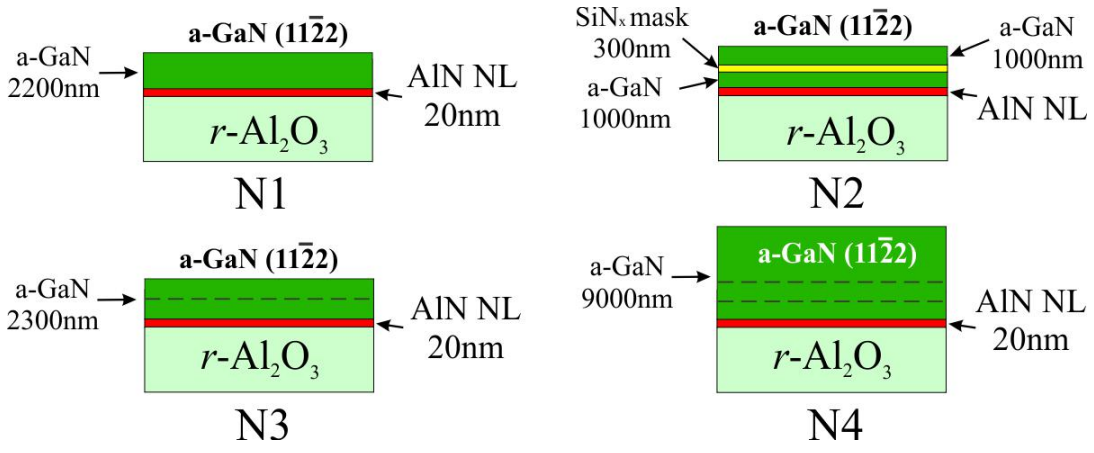

Figure 73: Non-polar a-GaN ($11\bar{2}2$) samples sketches.

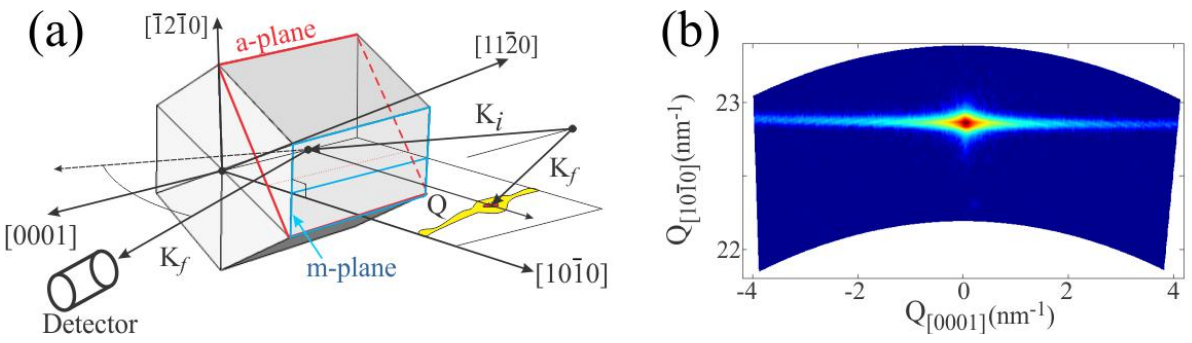

Figure 74: Scheme of skew diffraction geometry experiment (a) and the first measured RSM at NANO beamline of $10\bar{1}0$ reflection of a-GaN sample (b).

7.3 Investigation of nonpolar GaN epilayers

The X-ray investigation of a-GaN ($11\bar{2}0$) samples by Moram et al. [50, 21, 8], reveals no influence of the BSFs on the coplanar reflections, and argues the importance of measuring the reflections $10\bar{1}0$, $20\bar{2}0$ and $30\bar{3}0$. The BSF streaks of the reflections $h0\bar{h}0$ are located in $Q_{0001}Q_{10\bar{1}0}$ diffraction plane, which is inclined with respect to the sample surface in angle 30°. This measurements could be performed in non-coplanar skew symmetric geometry (see Chapter 3.10) at a 6-circle diffractometer. The fig.74.a demonstrates the scheme of this geometry for a sample with *hcc* unit cell. The a-plane ($11\bar{2}2$) which is the sample surface is marked as a red contour and diffraction planes are parallel to m-plane ($10\bar{1}0$) of GaN (see fig.74.a). The diffraction plane $Q_{0001}Q_{10\bar{1}0}$ is defined by incident K_i and diffracted K_f vectors and was horizontal in the experiment. The sample surface is inclined with respect to the diffraction plane $Q_{0001}Q_{10\bar{1}0}$ in angle of 30° (see fig.74.a).

The RSMs of nonpolar ($11\bar{2}0$) GaN samples in skew symmetric geometry were measured at NANO beamline at ANKA synchrotron in Karlsruhe, Germany. That was the first experiment at this heavy duty high precision diffractometer situated at excellent established beamline supported by Dr. Sondes Bauer (see Chapter 8.10.3). The first reciprocal space map of the sample N4 reflection $10\bar{1}0$, presented in the fig.74.b was measured using avalanche photodiode (APD) equipped with double slit system. The monochromatic X-ray beam with energy 8 keV was focused on the sample with the size 0.2 mm x 0.2 mm, the slits were closed horizontally and vertically up to 0.5 mm, and the sample/detector distance was about 1.2 meters.

The crystal truncation rod (CTR) is not visible in the RSM cause it is parallel to $11\bar{2}0$ direction and out of diffraction plane, as one can see in the fig.74.a. However, some diffuse intensity from the CTR is visible along $10\bar{1}0$ direction. The BSF streak is parallel to (0001) direction in RS (fig.74.b), as it was predicted by mosaic model (see Chapter 95), while, the RSM was recorded as series of ω-scans, which are segments of the circles with the centers in origin of the RS. It is possible to see these circles in the upper and bottom edges of the RSM in the fig.74.b. Thus, one should be careful with the definition of the measured intensity distribution in reciprocal space from BSF, cause of two possible scans, as it is demonstrated in the fig.75.a. The first one is ω-scan through the reflection's maximum of intensity, which is shown in the fig.75.a as a segment of a circle, and the second is Q_{str}-scan along the (0001) direction in reciprocal space (along the BSF streak, see fig.75.a).

The comparison of the intensity distribution of the two scans, shown in the fig.75.b, demonstrates clearly significant difference. In fact, in the case of ω-scan it is not possible to scan along the BSF streak, therefore the intensity of the tails is lost, while the central part of the peak is comparable with Q_{str}-scan.

For the BSF density calculation using simple mosaic model, the $FWHM$s of the BSF intensities distribution could be derived. The $FWHM$s of ω- and Q_{str}-scans are comparable and the ω-scan can be used for this calculations, as it was performed by McLaurin et al. [46].

The MC model of V. Holy simulates the BSF intensity distribution along the [0001] direction, including the central parts and the tails of intensity distributions [51]. Since the tails of the ω- and Q_{str}-scans are significantly different (see fig.75.b), only Q_{str}-scan could be used for the BSF density calculation using MC model. As a conclusion, for the Q_{str}-scan it is convenient to determine the BSF density either by mosaic model or by MC simulation. This Q_{str}-scan could be realized using *hkl* mode of the diffractometer or by recording RSM and extracting the intensity distribution along [0001] direction.

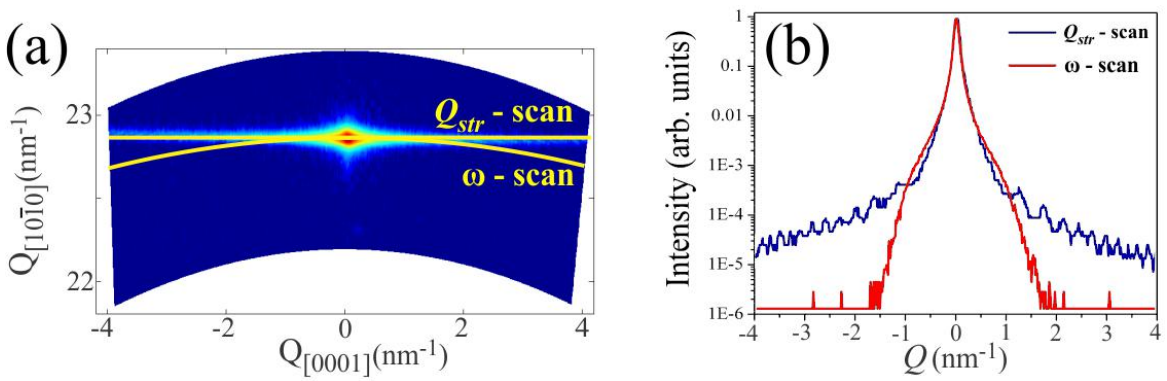

Figure 75: The Q_{str}- and ω - scans through the a-GaN reflection peak (a) and intensity distribution in the corresponding scans (b).

7.4 Calculation of BSFs density using Monte Carlo simulation

In order to derive the BSF densities ρ_{BSF}, intensity distributions $I(Q_{str})$ of the BSF streaks were performed for all nonpolar samples using Q_{str}-scan. The comparison of the distributions $I(Q_{str})$ is presented in the fig.76.a in logarithmic scale. Since, higher intensity of reflection's tails means higher value of ρ_{BSF}, from comparison of the tails in the fig.76.a, it is possible to conclude, that $\rho_{BSF}(N1) > \rho_{BSF}(N3) > \rho_{BSF}(N2) > \rho_{BSF}(N4)$. The numerical data of the BSF densities ρ_{BSF} calculated using simple mosaic model and sophisticated MC simulation are summarized in the tab.12.

The simulation of the BSF streaks intensity distribution was organized by M. Barckuk et al. [51]. Average BSF density ρ_{BSF}^{MC} of the samples N1-N4 derived from MC simulations are presented in the second column of the tab.12. The calculated values of BSF densities are in the same relation with tails intensities comparison: $\rho_{BSF}^{MC}(N1) > \rho_{BSF}^{MC}(N3) > \rho_{BSF}^{MC}(N2) > \rho_{BSF}^{MC}(N4)$.

For the mosaic model ρ_{BSF}^{FWHM} determination, first the $FWHM$s of the $I(Q_{str})$ were derived. The $FWHM$s data is given in the third column of the tab.12, and $FWHM(N1) > FWHM(N3) > FWHM(N2) > FWHM(N4)$. The BSF densities ρ_{BSF}^{FWHM} calculated using mosaic model are presented in the fourth column of the tab.12. It is necessary to emphasize that for the derived densities ρ_{BSF}^{FWHM} and ρ_{BSF}^{MC}, the values are in good agreement (see tab.12).

The tails of the intensity distributions $I(Q_{str})$ are presented in the fig.76.b in log-log scale. The slopes of the tails are in good agreement with exponential law $I(Q_{str}) = I_0 e^{-n}$. The values of n are summarized in the last column of the tab.12, and exponents n are $2 < n < 3$.

From the X-ray investigation of nonpolar a-GaN samples we can conclude that the highest stacking faults density was found for the sample N1. The two-step growth mode of the sample N3 reveal reduction of the BSFs density in comparison with the sample N1. However, the in-situ deposited SiN masking technique (N2) and HVPE overgrowth (N4) demonstrated the lowest density of BSF. Despite of ρ_{BSF} reduction in nonpolar GaN epilayers introducing different techniques, the ρ_{BSF} values are still quit high ($10^5 cm^{-1}$) for the production of optoelectronic systems with high efficiency. Therefore, an alternative growth methods of GaN epilayers with reduced QCSE are required.

Sample	ρ_{BSF}^{MC} from MC model, (10^5 cm^{-1})	$FWHM$, (nm^{-1})	ρ_{BSF}^{FWHM} from FWHM, (10^5 cm^{-1})	Exponent, n
N1	4.10	0.2397	3.81	2.46
N2	3.30	0.1271	2.02	2.35
N3	3.50	0.1729	2.75	2.42
N4	2.65	0.1051	1.67	2.32

Table 12: Nonpolar a-GaN ($11\bar{2}2$) samples BSFs density calculated from $FWHM$ and MC model comparison.

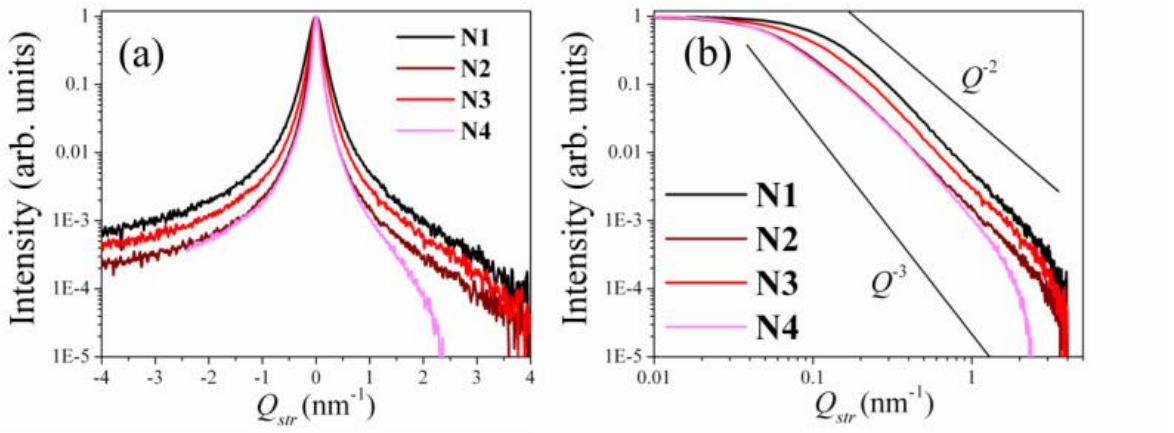

Figure 76: The a-GaN nonpolar sample's intensity distribution along the BSF streak of the reflection $10\bar{1}0$ in log scale (a) and their tails in log-log scale (b) comparison.

8 X-ray investigation of semipolar GaN grown on patterned sapphire substrate

8.1 Introduction

In the previous chapter, the X-ray investigation of nonpolar GaN samples reveal high density of the BSF in order of $10^5\,cm^{-1}$. Considering, the BSFs are planar defects and cover large area of the sample this high BSFs density droop the intensity of emitted photons almost to the value of polar GaN. In order to overcome the problem of BSFs high density in nonpolar GaN, the crystallographic surface orientations different from polar and nonpolar materials, called semipolar could be tried [133].

By changing the main epitaxial growth direction from the polar c-direction into less polar crystallographic directions, the internal fields can be strongly reduced and the BSFs density is expected to be lower than in nonpolar epilayers [9]. Furthermore, the growth of the semipolar GaN on flat foreign substrates of accurate orientation different from c-plane typically result in highly defective layers[9].

The growth in the polar c-direction leads to lowest defect densities. Therefore, a heteroepitaxial approach where the epitaxial process starts from c-plane-like sidewalls of trenches etched into sapphire wafers and the stripes nucleating on these side facets later coalesce to a closed surface with semipolar orientation is the best known method to grow the BSFs free semipolar layers. The influence of the crystallographic surface orientation and in-situ deposited defect-blocking SiN nanomask layer on the defects in semipolar GaN layers will be investigated in this chapter.

8.2 Description of semipolar GaN samples

Four semipolar GaN samples named S1-S4 investigated in the present work were grown using patterned sapphire substrate with trenches having a c-plane-like side facet. First, a 200 nm thick layer of SiO_2, which later acts as a mask for selective area growth, is deposited, followed by an about 500 nm thick nickel layer structured via standard optical lithography with a stripe mask (3 μm opening, 6 μm period). The pattern is transferred into the sapphire by reactive ion etching (RIE). The resulting grooves have a width at the bottom of about 1.5 μm, a depth of about 1.2 μm and possess a c-plane-like facet on one side. The subsequent epitaxial growth was performed in low-pressure horizontal MOVPE reactor (Aixtron) using standard precursors. The growth starts with an oxygen doped AlN nucleation layer at low temperature, followed by a GaN buffer layer at higher temperature [134]. To achieve coalescence of the single stripes nucleating at the c-plane side facets of the trenches, a thick GaN layer is grown at low temperature of about $1030°C$. The sketches of the samples are presented in the fig.77. The GaN samples S1 and S2 are grown with $(10\bar{1}1)$ surface orientation on $(10\bar{1}2)$ n-PSS substrate, see fig.77. The samples S3 and S4 are grown with $[11\bar{2}2]$ surface orientation on $(11\bar{2}3)$ r-PSS substrate, see fig.77.

As already known from common c-plane GaN [64], an in-situ deposited thin SiN interlayer can reduce the defect density considerably. The SiN interlayer was deposited in-situ after growing an about 300 nm thick GaN buffer layer for samples S2 and S4, see fig.77.

The area 50 μm x 60 μm of the sample S1 surface observed by optical microscope at NANO beamline (see Chapter 6.7) is presented in the fig.78.a. The view of the surface and partially the edge of the sample S3 performed by SEM measurement is shown in the fig.78.b. In the edge of the sample S3 the inverted pyramid-like structures are already visible. From the top view of the samples S1 and S3 the average width of the upper part of the inverted GaN pyramids could be measured, and is about 5.5 μm for the samples S1 and 6.5 μm for the samples S3 (see fig.78.a and fig.78.b).

At the fig.78.c and fig.78.d the SEM pictures of the edges of the samples S1$(10\bar{1}1)$ and S3$(11\bar{2}2)$ are presented, respectively. In these SEM pictures well resolved sapphire substrate trenches (TR), bridged GaN blocks and air gaps (AG) limited by "+c" and "-c" facets and substrate are visible.

For the sample S1 with surface orientation $[10\bar{1}1]$ the average width of GaN blocks is about 5.4 μm, and for the sample S3 with surface orientation $[11\bar{2}2]$ is about 6 μm (see fig.78.c and fig.78.d). The semipolar GaN blocks coalesce and further growths to form a single layer with thickness of 2.26 μm and 5.5 μm, of the samples S1 and S3, respectively (see fig.78.c and fig.78.d). The geometric parameters of the GaN layers blocks of the samples S2 and S4 are the same with samples S1 and S3, respectively.

8.3 Experiment description

The measurements of the semipolar PSS GaN samples was performed at bending magnet SCD beamline at energy 10 keV, at ANKA synchrotron in Karlsruhe, Germany. The X-ray beam was focused to the size of about

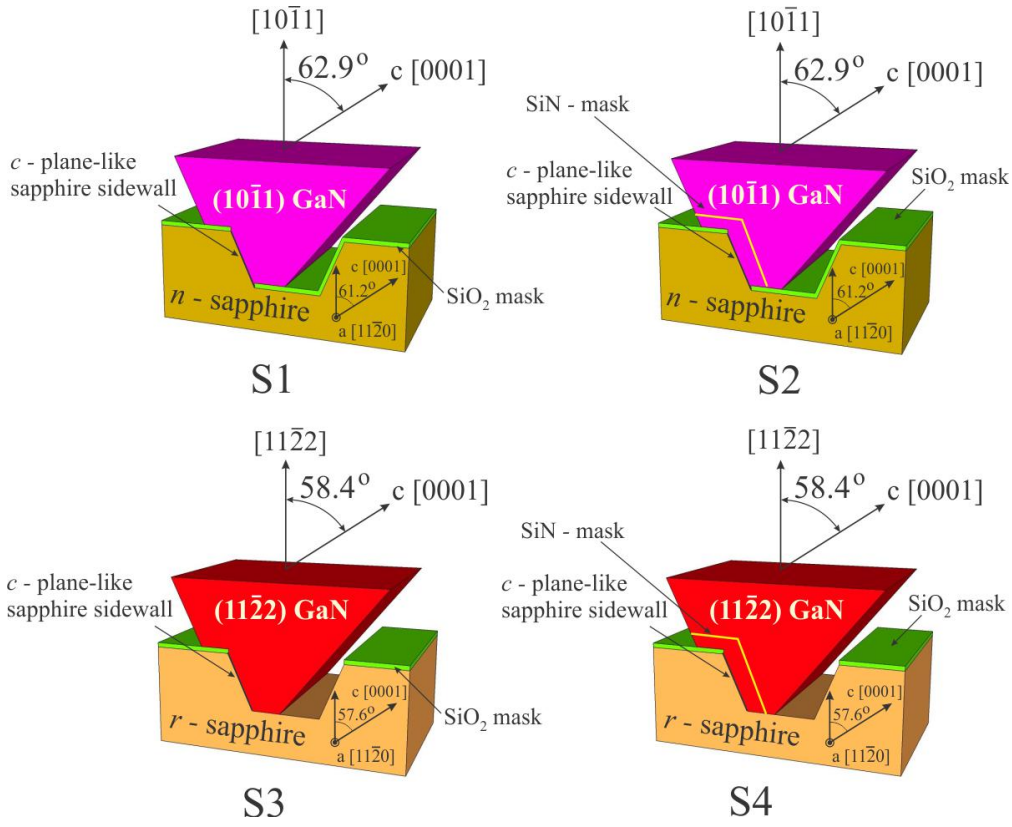

Figure 77: Sketches of the semipolar GaN samples.

0.3 mm x 0.3 mm at the center of rotation of the 6-circle diffractometer. The Mythen 1K linear detector, introduced in the Chapter 6.8.1, fixed in horizontal and vertical positions was used. The slits with variable gap were mounted on the detector in order to reduce the integration area in channel width direction. The sample/detector distance was about 700 mm.

In the experiment two diffraction geometries were used, and their sketches are presented in the fig.79. The first one is well known (see Chapter 3.10) coplanar diffraction geometry used to measure symmetric and asymmetric reflections in coplanar diffraction plane, see fig.79.a. In the coplanar XRD the detector with mounted slits was placed in vertical position and channels were in the diffraction plane. As a result of the rocking curve scan, the 2D RSMs were recorded.

The second diffraction geometry is non-coplanar diffraction geometry with the detector placed in horizontal position perpendicular to the diffraction plane, see fig.79.b. The 3D RSMs of GaN reflections were recorded in this geometry by performing the series of the ω (α_i) and $2\theta - \omega$ (($\alpha_f + \alpha_i$)-α_i) scans.

8.4 X-ray diffraction of semipolar GaN epilayers

8.4.1 BSFs streak in reciprocal space of semipolar GaN epilayers

The BSFs in GaN epilayers cause the formation of diffuse intensity in reciprocal space along [0001] direction (see Chapter 7.3). In case of nonpolar GaN epilayers the BSFs streak appears parallel to the sample surface and perpendicular to the CTR, as it is shown in the see fig.80.a.

In the case of polar c-oriented GaN epilayers, the BSFs streak should be parallel to CTR and perpendicular to the sample surface, as it is sketched in the fig.80.c. Hence, the diffuse intensity of BSFs should be distributed along the CTR and could not be observed as a separate streak in the RSMs. The BSFs density in polar GaN epilayers is usually very low [8], however depending on the growth process their formation is possible and is observed by TEM even in our AlGaN samples [105].

Since the semipolar GaN epilayers have inclined [0001] direction with respect to the sample surface, the BSFs streak should be inclined in the RS with respect to the CTR, as it is demonstrated for the semipolar (10$\bar{1}$1) GaN 10$\bar{1}$1 reflection in the fig.80.b.

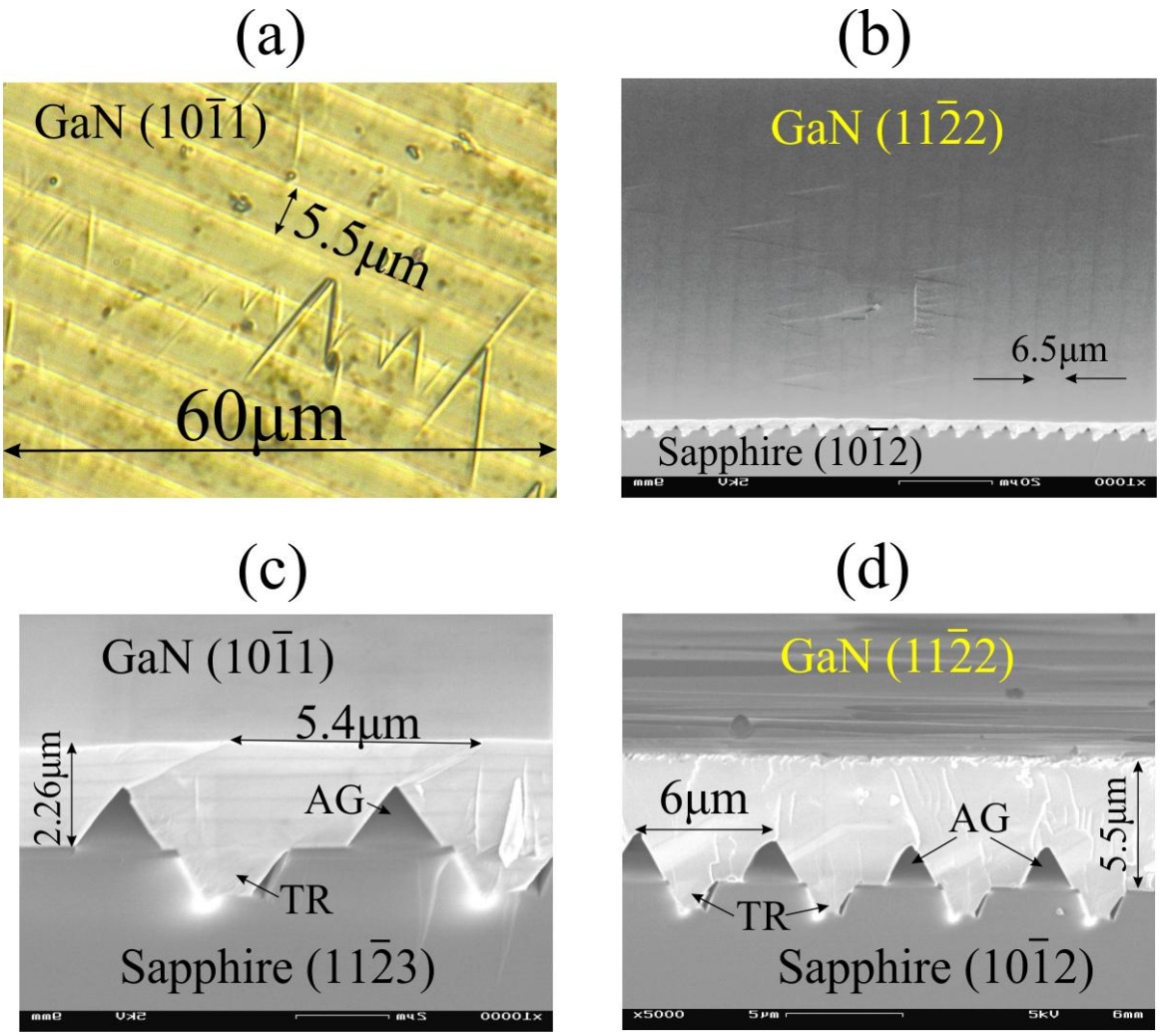

Figure 78: Optical microscope picture of the surface of the sample S1 (a), SEM picture of the sample S3 surface (b), edge SEM picture of the sample S1 (c), and SEM picture of the sample S3 edge (d).

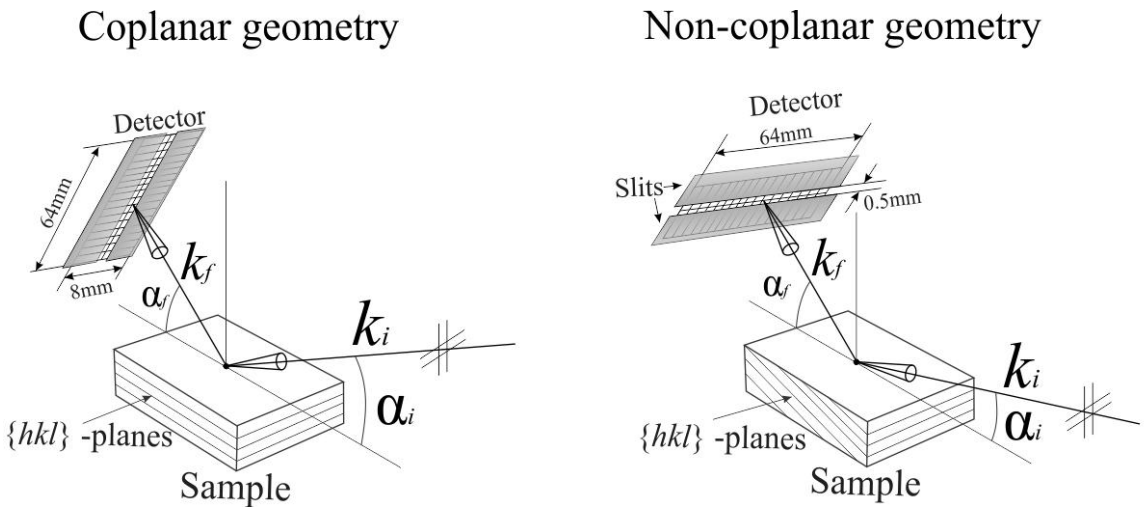

Figure 79: The coplanar XRD geometry (a) and non-coplanar diffraction geometry for 3D reciprocal space mapping (b).

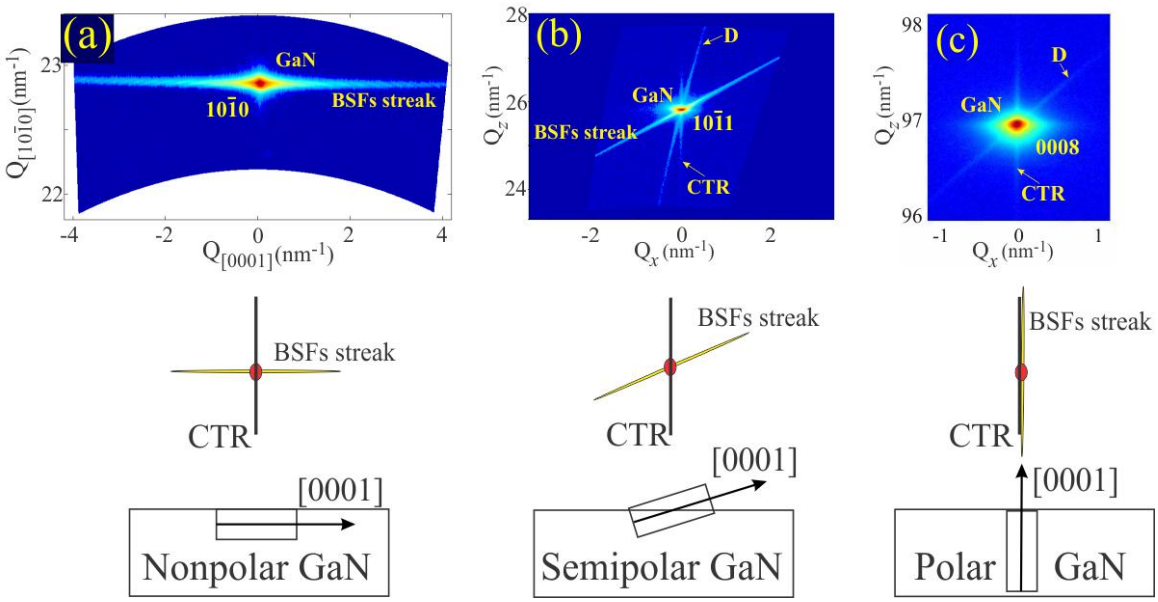

Figure 80: The RSMs of the nonpolar (a), semipolar (b) and polar (c) GaN crystals.

The semipolar samples S1-S4 have triangular shape air gaps, limited by "+c", "-c" facets and substrate (see fig.78). These "+c" and "-c" facets could cause the "+c" and "-c" streaks in reciprocal space inclined with respect to the CTR. Therefore, the "-c" streak should coincide with BSFs streak and "+c" streak should be symmetric to the BSF streak where the CTR is the symmetry axis. However, from the experimental RSMs the "+c" streak was detected only ones for the sample S1 in the most intense reflection 10$\bar{1}$1 (see Chapter 8.5.1). For all other samples and all other reflections of the sample S1, the "+c" streak was not registered. The streak absence could be explained due to high roughness and incoherent inclination of "+c" and "-c" facets. Since, the reflection 10$\bar{1}$1 is not used for the BSFs density calculation, the influence of the "+c", "-c" streaks could be neglected in the investigation.

8.4.2 Visibility criteria of BSFs streak

The BSFs don not influence all GaN reflections. From the literature, several BSFs streak visibility criteria are known.

The first visibility criteria is based on TEM investigation of nonpolar GaN films given by Moram [21, 8] and McLaurin et al. [46]. According to this criteria, the intensity distribution from BSFs along [0001] direction will be visible in the reciprocal lattice point, if the dot product of the diffraction vector $\mathbf{Q}$ and displacement vector $\mathbf{R}$ of a BSF is not an integer and if it is an integer the steak is not observed. Since dominant type of BSF is intrinsic I_1 type with $\mathbf{R}_1 = \frac{1}{6}\langle 20\bar{2}3\rangle$, the criteria could be written as:

$$\mathbf{R_1} \cdot \mathbf{Q} = 2\pi\left(\frac{2}{3}h + \frac{1}{3}k + \frac{1}{2}l\right), \tag{105}$$

$$\frac{2}{3}h + \frac{1}{3}k + \frac{1}{2}l \neq n, \tag{106}$$

where n is an integer.

The second visibility criterium was given by Barchuk et al. [51] for the reflections hkl using scattering factor $\kappa = e^{-i\mathbf{Q}\cdot\mathbf{p}}$ of BSFs diffuse intensity occurring in eq.85 for the scattered intensity. If factor $\kappa = 1$ ($e^{-i\mathbf{Q}\cdot\mathbf{p}} = 1$), than BSF does not influence on the reflection with diffraction vector $\mathbf{Q}$, and if $\kappa \neq 1$ ($e^{-i\mathbf{Q}\cdot\mathbf{p}} \neq 1$), than BSF create diffuse streak in the reflection. Therefore, the visibility criterium of the BSFs streak could be written as $e^{-i\mathbf{Q}\cdot\mathbf{p}} \neq 1$, which is equivalent to $\mathbf{Q}\cdot\mathbf{p} \neq 2\pi n$, where n is an integer. As it is know the vector $\mathbf{p} = \frac{2}{3}\mathbf{a} + \frac{1}{3}\mathbf{b} + 0\cdot\mathbf{c}$, and $\mathbf{Q} = \frac{2\pi}{a}\mathbf{h} + \frac{2\pi}{b}\mathbf{k} + \frac{2\pi}{c}\mathbf{l}$, therefore:

$$\mathbf{p}\cdot\mathbf{Q} = \frac{2\pi}{a}\frac{2}{3}ha + \frac{2\pi}{b}\frac{1}{3}kb + \frac{2\pi}{c}0lc = 2\pi\left(\frac{2}{3}h + \frac{1}{3}k\right). \tag{107}$$

Substitution of eq.107 into visibility criteria $\mathbf{Q}\cdot\mathbf{p} = 2\pi n$ gives:

$$2\pi\left(\frac{2}{3}h+\frac{1}{3}k\right)\neq 2\pi n. \tag{108}$$

And finally, visibility criterium could be written as:

$$\frac{2}{3}h+\frac{1}{3}k\neq n. \tag{109}$$

An another criterium is given by the model of Warren [78]. According to Warren, for lattice planes of the type $h-k=3n$ ($n=\{0,\pm1,\pm2\ldots\}$), such as {300} and {112}, the diffraction peaks will have no appreciable broadening due to stacking faults. For planes of the type $h-k=3n\pm1$, diffraction peaks will be broadened by faulting to an extent that depends on the third index l. Therefore, we can write the visibility criteria of Warren for all types of BSF as:

$$\frac{h-k}{3}\neq n. \tag{110}$$

It is should be emphasized that all of these criteria give the same result for BSFs type I_1 Barchuk et al. [51].

8.4.3 Visibility criteria for semipolar ($10\bar{1}1$) GaN

Coplanar reflections (in plane containing [0001] direction) of semipolar ($10\bar{1}1$) GaN samples S1 and S2 have diffraction indexes $h0\bar{h}l$. According to V. Holy visibility criteria [51], for the reflections $h0\bar{h}l$:

$$\mathbf{p}\cdot\mathbf{Q}=2\pi\left(\frac{2}{3}h+\frac{1}{3}\cdot 0+0\cdot l\right)=2\pi\cdot\frac{2}{3}h. \tag{111}$$

The streak will appear in all reflections except those where $h=3n$ (n is an integer): 0008, $30\bar{3}0$, $30\bar{3}2$. The criteria doesn't depend on the index l, that means that BSFs streak will be visible in all reflections in the series with variation of l: $10\bar{1}1$, $10\bar{1}7$, $20\bar{2}1$, $20\bar{2}2$, $20\bar{2}3$, $20\bar{2}4$, $20\bar{2}5$.

8.4.4 Visibility criteria for semipolar ($11\bar{2}2$) GaN

Coplanar reflections (in plane containing [0001] direction) of the semipolar ($11\bar{2}2$) GaN samples S3 and S4 have diffraction indexes $hh\overline{2h}l$. For the reflections $hh\overline{2h}l$, the visibility criterium of V. Holy is as follow:

$$\mathbf{p}\cdot\mathbf{Q}=2\pi\left(\frac{2}{3}h+\frac{1}{3}\cdot h+0\cdot l\right)=2\pi\cdot h. \tag{112}$$

As a consequence, the streak of BSFs is invisible in all coplanar reflections: 0008, $11\bar{2}2$, $22\bar{4}4$, $22\bar{4}2$, $22\bar{4}0$, $22\overline{42}$, $11\bar{2}4$, $11\bar{2}6$. Therefore, the BSFs streak could be observed only in the reflections series $h0\bar{h}l$ ($20\bar{2}0$, $20\bar{2}3$, $20\bar{2}5$, etc.) measured in the non-coplanar geometry.

8.5 X-ray investigation of semipolar GaN

8.5.1 X-ray investigation of semipolar ($10\bar{1}1$) GaN

For the ($10\bar{1}1$) GaN semipolar samples S1 and S2, reflections $hkil$ affected by BSFs are found using visibility criteria (see Chapter 8.4.2). The $10\bar{1}1$ reflection, affected by BSFs, is coplanar symmetric reflection. In three dimensional reciprocal space the reflection $10\bar{1}1$ (with BSFs streak) should have two rods: CTR parallel to [$10\bar{1}1$] direction and BSFs streak along [0001] direction, as it is sketched in the fig.81.a.

Since, any diffraction plane containing the sample normal is coplanar diffraction plane, the symmetric reflections could be recorded from different azimuthal angles. Nevertheless, by rotating the sample around its normal, there is only one coplanar diffraction plane -α containing the axis [0001] and therefore the BSFs streak (see fig.81.a). The RSM measured in coplanar diffraction plane-α is shown in the fig.81.b. There are three visible streaks: crystal truncation rod (CTR), air scattering streak (D), and BSFs streak. From another side, the measurement of the reflection in any other plane, for example in plane-β perpendicular to the plane-α (see fig.81.a) could reveal presence of only CTR and D, see fig.81.c. Therefore, in order to record the intensity $I(Q_{str})$ of BSFs streak it is necessary to find the azimuthal angle corresponding to [0001] direction by recording some of the reflections $000l$.

The coplanar reflections of the samples S1 and S2 have the Miller indexes $h0\bar{h}l$ (see Chapter 8.4.2). The reciprocal space of the semipolar ($10\bar{1}1$) GaN samples S1 and S2 limited by Ewald's sphere at energy 10 keV is

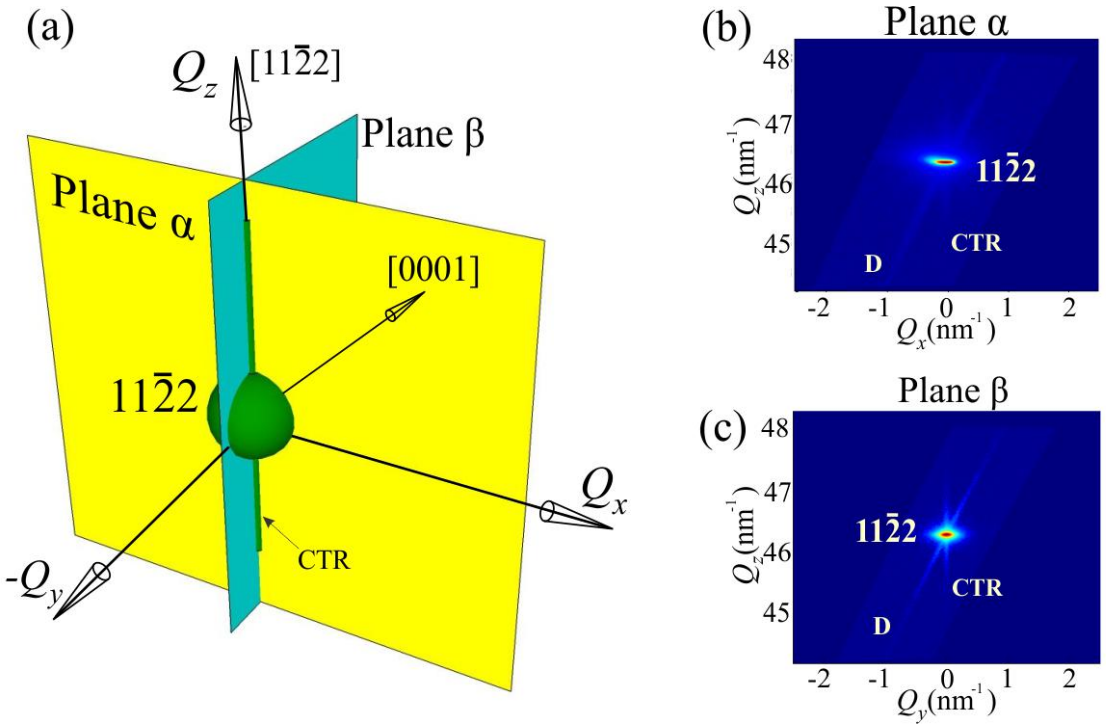

Figure 81: The sketch of the 10$\bar{1}$1 reflection of the samples S1 and S2 in 3D RS (a), and the reflection's cuts in α plane (b) and β plane (c).

sketched in the fig.82. The reflections affected by BSFs are drawn with the streaks. The forbidden reflections are not sketched. The available reflections are colored in black while the non-reachable in red and the measured one in blue. The angle of inclination of the [0001] crystallographic direction and BSFs streaks with respect to the surface normal Q_z (direction [10$\bar{1}$1]) is 62.9°. Due to this inclination, the number of available reflections is reduced and the measurement of 10$\bar{1}$0, 20$\bar{2}$0, 30$\bar{3}$0 reflections at one specific energy was not possible, as it was done for nonpolar GaN.

The resolution function depends on the parameters of the beamline optics. For this reason, the semipolar GaN reflections should be measured without changing the beamline parameters, including energy. Finally, the energy of 10 keV with maximum of available reflections was chosen.

The 10$\bar{1}$1 reflection RSMs of the samples S1 (without SiN mask) and S2 (with SiN mask) are presented at the fig.83.a and fig.83.b, respectively. Three common streaks marked as 1, 2, 3 are visible in the RSMs. The streak 1 one is the crystal truncation rod (CTR) parallel to [10$\bar{1}$1] direction and perpendicular to the samples surface.

In order to understand the origin of the other streaks, the angles between them and CTR are measured and shown for the samples S1 and S2 in the fig.83.c and fig.83.d, respectively. The inclination angle of the streak 2 is found to be $15° \pm 2°$, corresponding to the incidence angle $\alpha_i = \theta_B = 14.75°$ of the reflection 10$\bar{1}$1 at energy 10 keV. Since, the inclination of the air scattering streak (D) with respect to the CTR should be equal to the incidence angle (see Chapter 3.9), the streak 2 could be attributed to the D. The measured inclination of the streak 3 is $63° \pm 2°$. This latter corresponds to the theoretical inclination of [0001] crystallographic direction in angle of 62.9° (see fig.82). This allows us to attribute streaks 3 of the samples S1 and S2 to the BSFs streak.

By comparing the RSMs of the reflection 10$\bar{1}$1 of S1 and S2, it should be noted that RSM of the sample S1 reveals an additional streaks 4 inclined with an angle $54° \pm 2°$(see fig.78.a and fig.78.c). This latter shows that streak 4 and streak 3 are almost symmetric with respect to CTR. Since, no planar defects could lead to the formation of diffuse scattering streak 4, one could conclude that streak 4 is originated from the "+c" facets of air gaps between coalescent semipolar GaN blocks (see fig.78.c), as it was discussed in the Chapter 8.4. The other investigated reflections do not reveal the presence of the streak 4 and hence the influence of "-c" and "+c" facets diffuse intensity will be neglected in the discussion.

In the RSM of the sample S1, two additional curves 5 and 6 are visible (fig.83.a). The curves 5 and 6 are underlining on the segments of the circles with the centers in origin of the reciprocal space (see fig.83.c). These

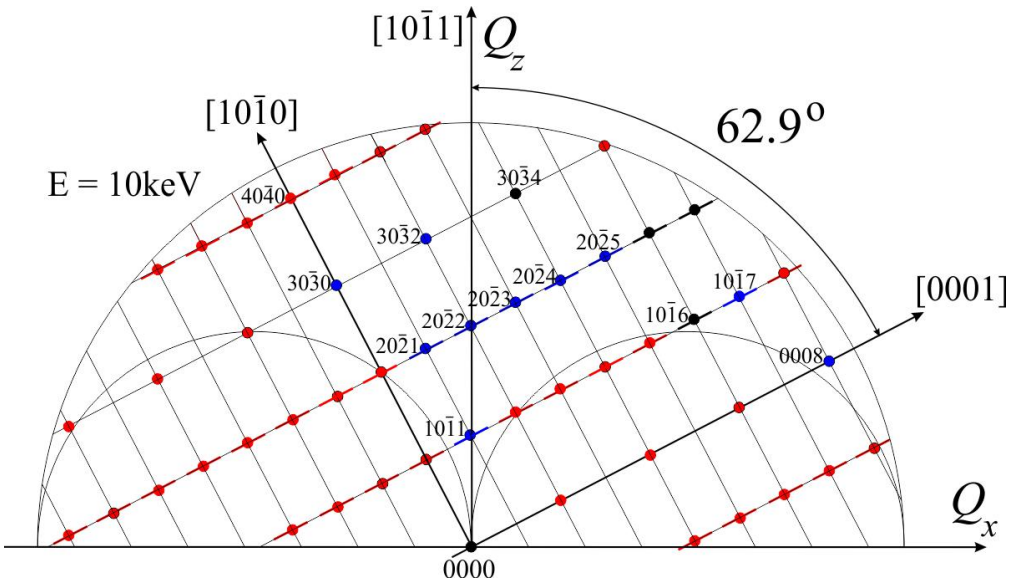

Figure 82: The reciprocal space of the semipolar GaN samples S1 and S2 with (10$\bar{1}$1) surface orientation limited by Ewald's sphere correspond to energy of 10 keV. The measured reflections are marked in blue color, available in black, not available in read and forbidden not shown.

curves are attributed to the powder diffraction rings or polycrystalline rings of GaN material. For all other samples the powder rings were not observed.

Finally, the streak 3 intensity distribution $I(Q_{str})$ from BSFs of the samples S1 without and S2 with SiN mask of the reflection 20$\bar{2}$3 are compared and presented in the fig.84. The comparison of the diffuse intensity at the tails demonstrates a decrease in the case of the sample S2. This enables us to conclude that in-situ deposited SiN mask reduces the density of the BSFs in sample S2 in comparison with sample S1.

8.5.2 X-ray investigation of semipolar (11$\bar{2}$2) GaN

The coplanar reflections $hh\overline{2h}l$ of the (11$\bar{2}$2) GaN samples S3 and S4 are not influenced by BSFs (see Chapter 8.4.4). The reciprocal space of semipolar (11$\bar{2}$2) GaN limited by Ewald's sphere at energy of 10 keV is sketched in the fig.85. The forbidden reflections are not sketched. The available reflections are colored in black while the non-reachable in red and the measured one in blue. The angle of inclination of the [0001] crystallographic direction with the surface normal is 58.4°. Since $hh\overline{2h}l$ reflections with odd index l are forbidden, the total number of available reflections is even lower than for $h0\overline{h}l$ diffraction plane (compare fig.85 and fig.82).

The $hh\overline{2h}l$ reflections of the samples S3 and S4 have no BSFs streaks and in three dimension reciprocal space only CTR perpendicular to the samples surface is expected, as it is shown in the fig.86.a. Therefore, neither RSM of symmetric reflection 11$\bar{2}$2 measured in diffraction plane-α containing direction [0001] (see fig.86.b) nor plane-β perpendicular to plane-α (see fig.86.c) reveal the presence of BSFs streak.

In order to detect the BSFs diffuse intensity $I(Q_{str})$, reflection with indices $h0\overline{h}l$ should be measured. Due to inclination of the diffraction plane $h0\overline{h}l$ with respect to $hh\overline{2h}l$ plane, most of the reflections measured for (10$\bar{1}$1) GaN (samples S1 and S2) are not reachable for the (11$\bar{2}$2) GaN (samples S3 and S4). The only common reflection, reachable at 10 keV and influenced by BSFs is the asymmetric reflection 20$\bar{2}$3. The schematic view of the reflections 11$\bar{2}$2 and 20$\bar{2}$3 and coplanar plane-β containing them are shown in the fig.87.a. The BSFs streak is not visible at the RSM of the reflection 20$\bar{2}$3 (fig.87.b) in coplanar diffraction plane-β, since the plane doesn't contain [0001] direction. The plane-γ containing the 20$\bar{2}$3 reflection and BSFs streak is in non-coplanar plane parallel to the coplanar diffraction plane-α shown in the fig.87.a. Therefore, the reflection 20$\bar{2}$3 should be measured in non-coplanar diffraction geometry either using hkl mode and recording intensity along [0001] direction or by recording complete intensity in 3D reciprocal space.

In order to investigate full diffuse intensity, the 3D RSMs of the reflection 20$\bar{2}$3 of the samples S3 and S4 were recorded. The 20$\bar{2}$3 reflection 3D RSM of the sample S3 is shown in the fig.88.a. In 3D RSM the rod of intensity along Q_z is the crystal truncation rod (CTR), the inclined disk of intensity is detector disk (D) and finally the streak elongated in [0001] direction is the BSFs streak. The cut of 3D reflection 20$\bar{2}$3 with plane-γ (see fig.87.a) is

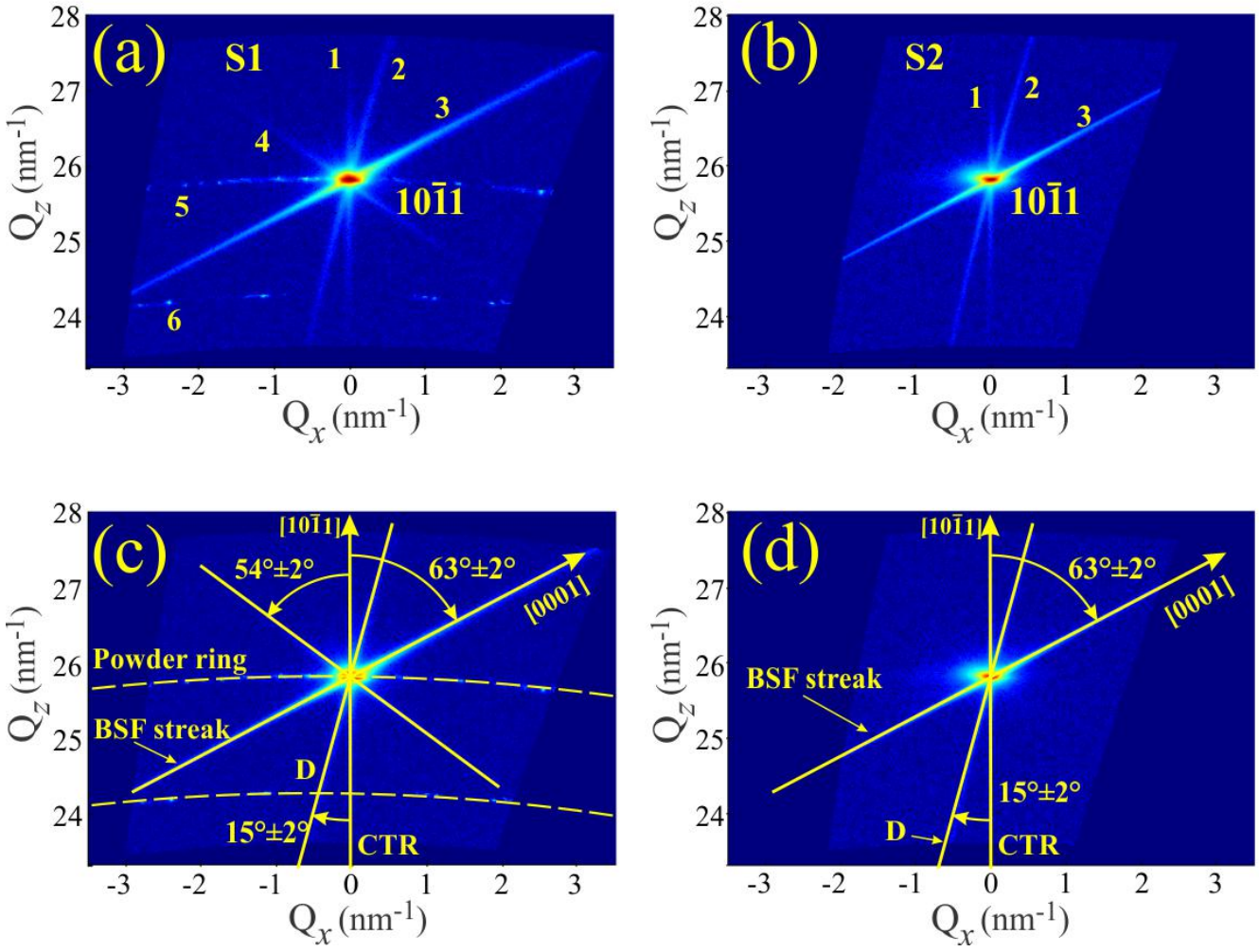

Figure 83: The S1 (left) and S2 (right) samples RSMs of the reflection 10$\bar{1}$1 (top), and they with marked RS directions (bottom).

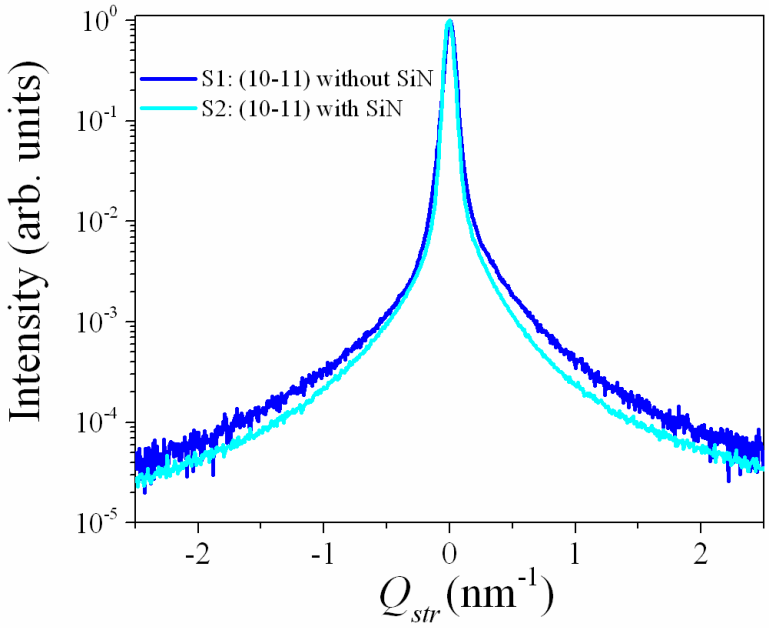

Figure 84: Comparison of the intensity distribution $I(Q_{str})$ of the BSF streaks of the samples S1 without and S2 with the SiN mask of the reflection $20\bar{2}3$.

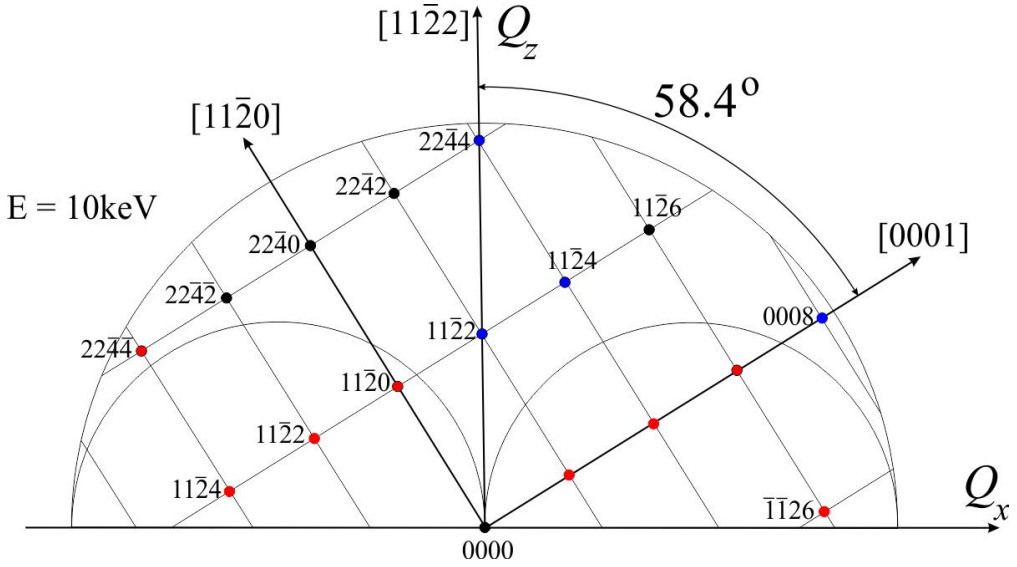

Figure 85: The reciprocal space of the semipolar GaN samples S3 and S4 with $(11\bar{2}2)$ surface orientation limited by Ewald's sphere correspond to energy of 10 keV. The measured reflections are marked in blue color, available in black, not available in read and forbidden not shown.

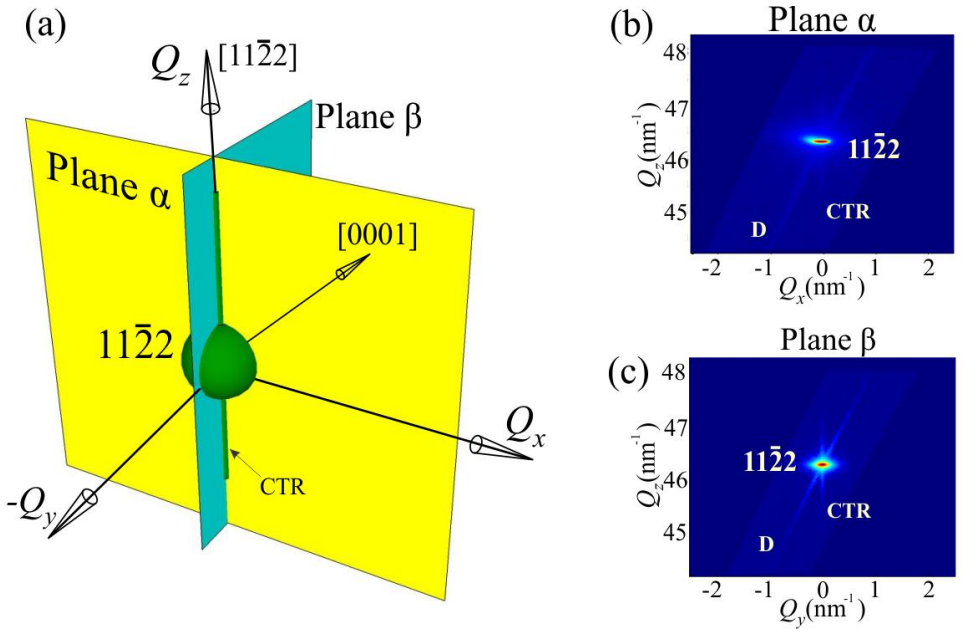

Figure 86: The sketch of the reflection 11$\bar{2}$2 of the samples S3 and S4 in 3D RS (a), and the reflection's cuts in α plane (b) and β plane (c).

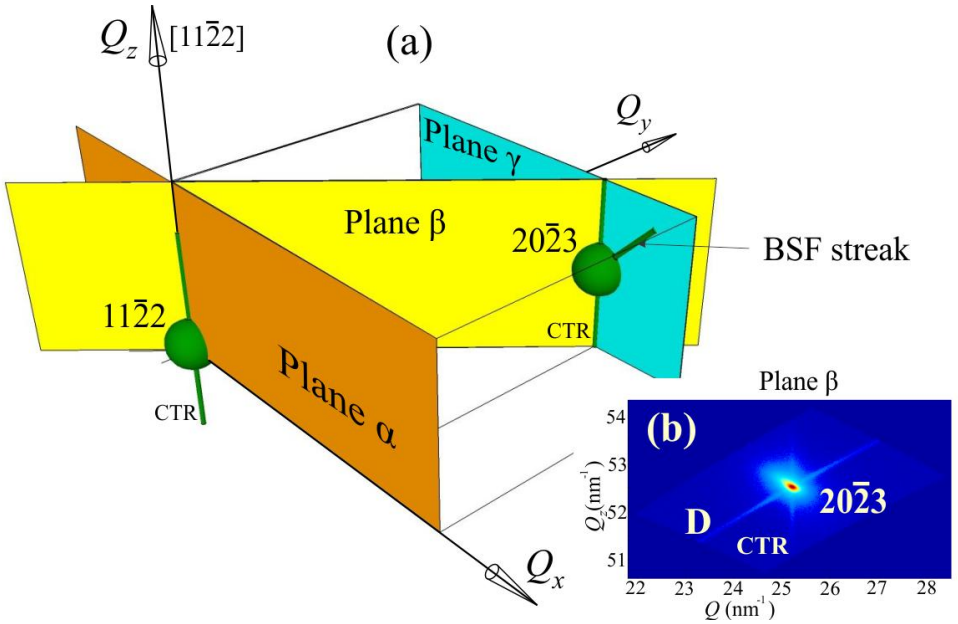

Figure 87: The sketch of the reflections 11$\bar{2}$2 without streak and 20$\bar{2}$3 with streak of BSF of the samples S3 and S4 in 3D RS (a) and coplanar geometry RSM of the reflection 20$\bar{2}$3 in plane-β (b).

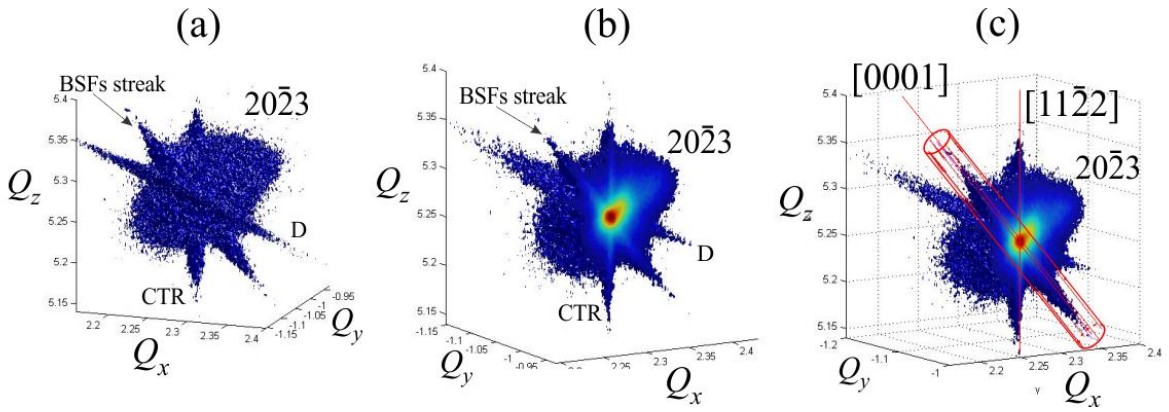

Figure 88: The reflection $20\bar{2}3$ of the sample S3 in 3D reciprocal space (a), the cut of the reflection in plane γ (in which streak of BSF is visible) (b), and region of integration around the [0001] direction (BSFs streak) (c).

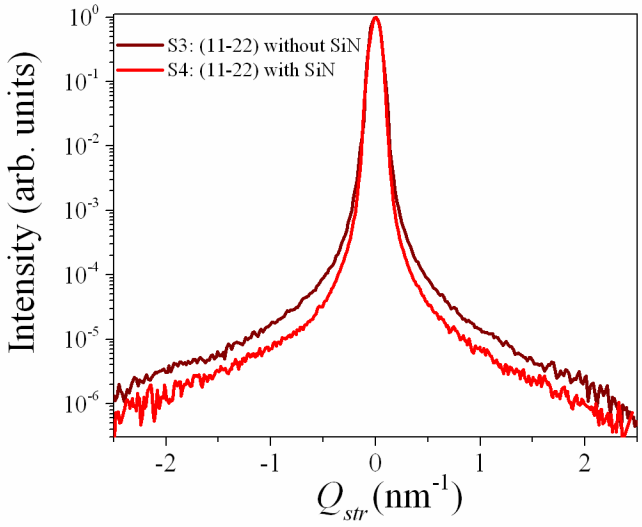

Figure 89: Comparison of the intensity distribution along the BSFs streak $I(Q_{str})$ of the samples S3 (without SiN mask) and S4 (with SiN mask) of the reflection $20\bar{2}3$.

shown in the fig.88.b. As it is expected, in the RSM recorded in the plane-γ the CTR, D, and BSFs streak inclined in angle 58.4° with respect to the CTR are visible. For better accuracy, the diffuse intensity $I(Q_{str})$ of BSFs was derived as an integration of intensity in cylindrical volume around BSFs streak, shown in the fig.88.c.

The comparison of derived $I(Q_{str})$ from the reflection $20\bar{2}3$ for the samples S3 and S4 is shown in the fig.89. The diffuse intensity $I(Q_{str})$ at the tails of the sample S4 with SiN mask is found to be lower than the one of sample S3 without SiN mask. One could conclude that in-situ deposited SiN mask play an important role in reducing the BSFs density in semipolar $(11\bar{2}2)$ GaN.

8.5.3 Comparison of BSFs streak intensity distributions

From X-ray investigation of semipolar $(10\bar{1}1)$ GaN (samples S1 and S2) and $(11\bar{2}2)$ GaN (samples S3 and S4), the BSFs streak intensity distributions $I(Q_{str})$ of the reflection $20\bar{2}3$ are compared in the fig.90.

The semipolar $(10\bar{1}1)$ GaN samples S1 and S2 have higher intensity $I(Q_{str})$ at the tails in comparison with semipolar $(11\bar{2}2)$ GaN samples S3 and S4. Therefore, the BSFs density should be higher for semipolar $(10\bar{1}1)$ GaN than for $(11\bar{2}2)$ GaN.

For both $(10\bar{1}1)$ and $(11\bar{2}2)$ semipolar GaN, reduction of the BSFs density by introducing in-situ deposited SiN mask is found. The BSFs intensity distributions $I(Q_{str})$ could be used for the numerical calculation of BSFs density

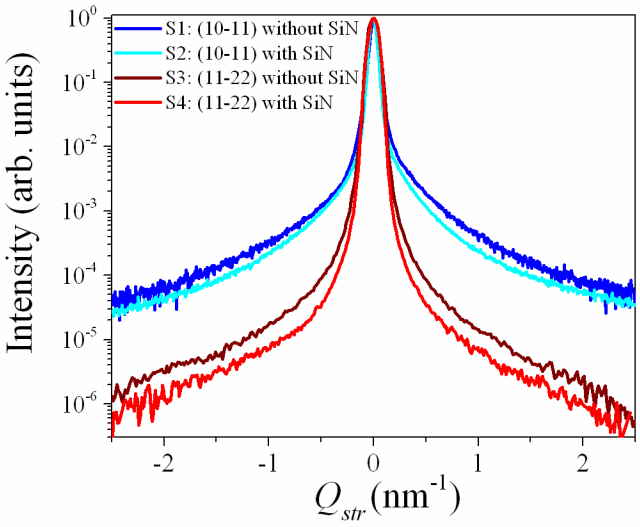

Figure 90: Comparison of the intensity distribution along the BSFs streak $I(Q_{str})$ of the reflection $20\bar{2}3$ of all semipolar GaN samples.

Sample	$FWHM$, (nm^{-1})	BSFs density ρ_{BSF}^{FWHM}, 10^4 (cm^{-1})
S1	0.0786	12.7
S2	0.0758	12.0
S3	0.0710	11.4
S4	0.0706	10.7

Table 13: BSFs density ρ_{BSF}^{FWHM} calculated using simple equation.

using simple mosaic and sophisticated MC models.

8.6 Calculation of BSFs density using the mosaic model

The average BSFs density could be calculated from the BSFs streak $FWHM$ using eq.75 based on simple mosaic model introduced in the Chapter 4.3. The $FWHM$s were derived in units of reciprocal space (and not in angular units) from Lorentzian fitting functions for the intensity distribution $I(Q_{str})$ of the BSFs streak. The densities of BSFs ρ_{BSF}^{FWHM} were calculated as:

$$\rho_{BSF}^{FWHM}(cm^{-1}) = 1/L = 10^7 \cdot FWHM(nm^{-1})/2\pi. \tag{113}$$

The $FWHM$s and calculated using eq.113 ρ_{BSF}^{FWHM} are presented in the tab.13. Comparison of calculated BSFs densities proves that ρ_{BSF}^{FWHM} is higher for $(10\bar{1}1)$ GaN than for $(11\bar{2}2)$ GaN, and that SiN mask reduces the ρ_{BSF}^{FWHM} for both $(10\bar{1}1)$ GaN and $(11\bar{2}2)$ GaN.

8.7 Calculation of BSFs density using Monte Carlo method

The mosaic model considers that peak broadening is mainly due to BSFs and ignore the influence of BSFs on the diffuse parts of the streak. Consequently, the mosaic model approach could be used only for rough estimation of the BSFs density.

Contrary, the MC model developed by Holy and introduced in the Chapter 4.4 takes into account the influence of the BSFs on the broadening of the streak as well as on the tails, and as a result a good agreement is performed between MC model simulated $I(Q_{str})$ and measured profiles in the coherent as well as in the diffuse parts.

The reflection $20\bar{2}3$ affected by the BSFs was used for the determination of BSFs average density using MC model, while by using the reflections $30\bar{3}2$ (S1 and S2) and $11\bar{2}2$ (S3 and S4) without BSFs steak, the parameters W

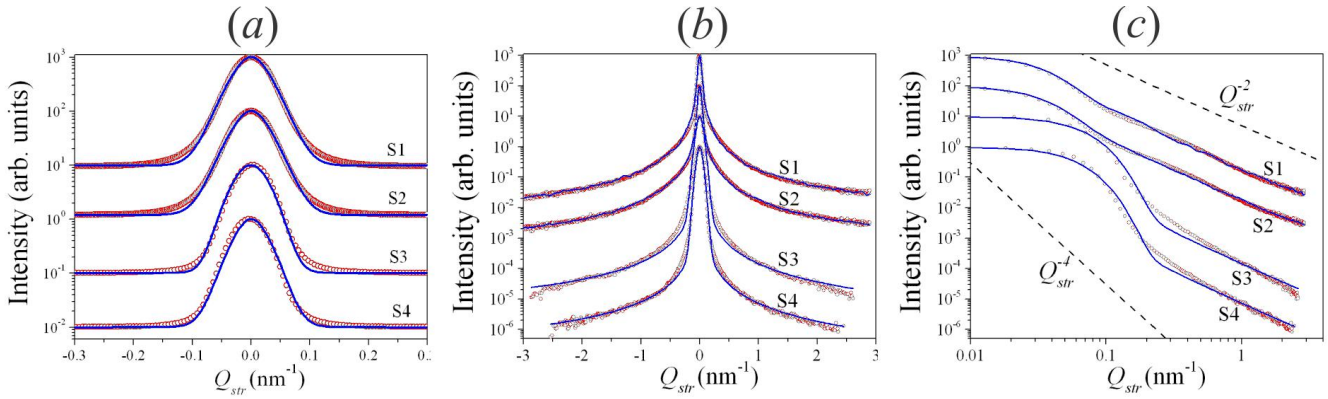

Figure 91: Comparison of the MC simulated (lines) with experimental (circles) intensity distributions of the reflections $30\bar{3}2$ (samples S1 and S2) and $11\bar{2}2$ (S3 and S4) without BSFs streak (a), reflection $20\bar{2}3$ with the BSFs streak for all of the samples (b) and tails of intensity of the reflection $20\bar{2}3$ in log-log scale for all of the samples (c).

(broadening of simulated profile) and α (shape of the simulated profile), defining our resolution function were derived by fitting the experimental intensity distribution along [0001] direction with the calculated one (see Chapter 4.4).

For the MC model calculation the number of coherently illuminated {0001} planes N should be estimated from the experimental parameters, as it was described in the Chapter 4.4 (see fig.41.b):

$$N = \frac{l_{0001}}{c/2}, \tag{114}$$

where l_{0001} is the coherence length of the incidence radiation in closed pack [0001] direction, and c is the unit cell lattice parameter in [0001] direction (see fig.41.b). From the right-angled triangle in the fig.41.b is visible that $l_{0001} = l_{coh}\cos(\gamma)$, and $\cos(\gamma) = \cos((90-\psi)-\alpha_i)$, where l_{coh} is the coherence length of the incidence X-ray in the beam propagation direction. The ψ is the angle of inclination of the {0001} planes with respect to the surface and α_i is the incidence angle of the X-ray beam. Substitution of the received expressions in eq.114 gives:

$$N = \frac{2l_{coh}cos((90-\psi)-\alpha_i)}{c} = \frac{2l_{coh}\sin(\psi+\alpha_i)}{c}. \tag{115}$$

The inclination of the planes {0001} with respect to the semipolar $(10\bar{1}1)$ GaN and $(11\bar{2}2)$ GaN samples surfaces are $\psi = 62.9°$ and $\psi = 58.4°$, respectively. For the reflection $20\bar{2}3$ at the energy 10 keV, the incidence angles were $\alpha_i = 30.6°$ and $\alpha_i = 24.5°$ for $(10\bar{1}1)$ GaN and $(11\bar{2}2)$ GaN samples, respectively. Therefore, the $\sin(\psi+\alpha_i)$ for all of the samples was about 0.99 and is the same for semipolar $(10\bar{1}1)$ GaN and $(11\bar{2}2)$ GaN. Taking into account that coherence length in the beam propagation direction of the SCD beamline is about $l_{coh} \approx \lambda^2/(2\cdot\triangle\lambda) \approx 0.6\mu m$, the number of coherently illuminated basal planes N could be estimated as:

$$N \approx \frac{2l_{coh}\cdot 0.99}{c} \approx 2.3\cdot 10^4 \tag{116}$$

The reflections $30\bar{3}2$ (samples S1 and S2) and $11\bar{2}2$ (S3 and S4) without BSFs steak were used to determine the parameters W and α and the number of coherently illuminated {0001} diffraction planes N is chosen to be the same with the number of coherently illuminated basal planes of the reflection $20\bar{2}3$.

The fits of the simulated intensity profiles with the experimental intensity distribution along [0001] direction of the reflections $30\bar{3}2$ (samples S1 and S2) and $11\bar{2}2$ (S3 and S4) are shown in the fig.91.a, and of the reflection $20\bar{2}3$ for all of the samples are illustrated in the fig.91.b. For better representation each profile in fig.91 has been multiplied by a factor of ten relative to the previous one.

By achieving best fitting the average BSFs densities ρ_{BSF}^{MC} were derived for all samples, and their values are summarized in the tab.14. The intensity distributions of the reflection $20\bar{2}3$ along the BSFs streak in log-log scale are shown in the fig.91.c. The slopes of the tails obey the exponential low $I(Q_{str}) = I_0 e^{-n}$ and their exponents n are summarized in the tab.14. The exponents n are in the range $2 < n < 4$ and the average slope for the $(10\bar{1}1)$ GaN (samples S1 and S2) is $n = 2.2$ and for the $(11\bar{2}2)$ GaN (samples S3 and S4) is $n = 3$.

Sample	Average BSFs density ρ_{BSF}^{MC}, $(10^3 cm^{-1})$	Exponent, n
S1	22.5	2.18
S2	11.3	2.19
S3	7.9	2.75
S4	4.4	3.72

Table 14: The BSFs density calculated using Monte Carlo simulations.

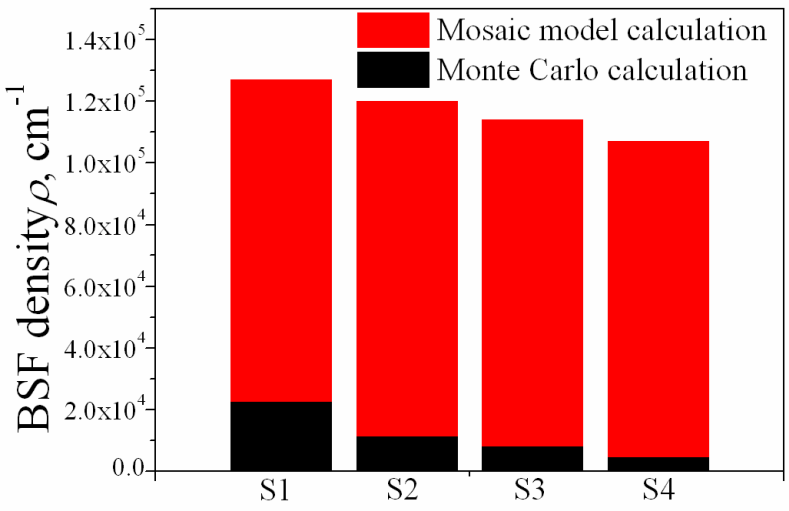

Figure 92: Comparison of the BSFs densities calculated using simple mosaic model and Monte Carlo simulation.

8.8 Comparison of the BSFs densities calculated using the mosaic model and MC calculation

The densities ρ_{BSF} of BSFs for samples S1-S4 calculated using mosaic model and Monte Carlo simulation are compared in the histogram form in the fig.92. Decay of the BSFs density from S1 to S4 is found for mosaic model and for MC simulation results. However, the mosaic model ρ_{BSF}^{FWHM} is one order of magnitude higher than ρ_{BSF}^{MC}. As it was discussed above, the mosaic model considers the influence of BSFs only on the peak broadening and ignore the influence on the diffuse parts of the streak, while the MC simulation takes into account the influence of the BSFs on the broadening of the streak as well as on the tails. Therefore, the MC simulation is more reliable method to derive the BSFs density in comparison with simple equation of mosaic model.

In order to quantify the SiN mask efficiency, the ratio ζ between difference of BSFs densities without and with SiN mask and BSFs density without mask calculated using Monte Carlo simulations are used. The SiN mask efficiency for the $(10\bar{1}1)$ GaN (samples S1 and S2) is $\zeta(10\bar{1}1) = (\rho(S1) - \rho(S2))/\rho(S1) = 0.50$, meaning 50% of BSFs density reduction. The SiN mask efficiency for the $(11\bar{2}2)$ GaN (samples S3 and S4) is $\zeta(11\bar{2}2) = (\rho(S3) - \rho(S4))/\rho(S3) = 0.44$, meaning 44% of BSFs density reduction. The comparisons of the $\zeta(10\bar{1}1)$ and $\zeta(11\bar{2}2)$ demonstrates almost the same amount of BSFs density reduction for both semipolar orientations.

8.9 Cathodoluminescence and photoluminescence of semipolar GaN with and without SiN mask

The X-ray investigation of semipolar $(10\bar{1}1)$ GaN and $(11\bar{2}2)$ GaN samples with and without SiN mask has shown the significant influence of the mask on the BSFs density reduction. To prove this result the complimentary photoluminescence (PL) and cathodoluminescence (CL) measurements were done for the samples S3 without and S4 with the SiN mask. The comparison of the PL/CL spectra of the samples with and without SiN mask could provide the information about BSFs density reduction.

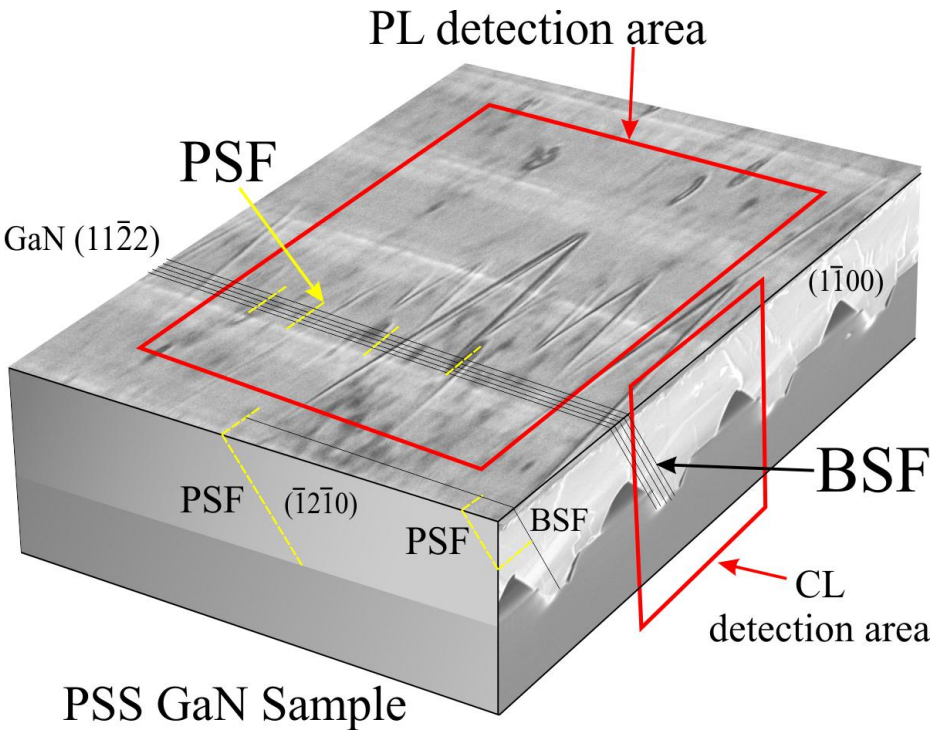

Figure 93: The sketch of the semipolar GaN sample with PL and CL detection areas shown.

The CL measurements of the samples S3 and S4 were performed at relatively small area of about 6 μm at the edge of the samples corresponding the cut of {1$\bar{1}$00} plane perpendicular to the semipolar GaN blocks, while the PL spectrum was measured from the area of about few millimeters at the samples surface. In the fig.93 the detection areas of the PL and CL data are shown in the sketch of the sample.

The BSFs are formed in the basal {0001} planes of "-c" wings and are planes parallel to the "-c" wings plane. These latter intersect the surface and the edge of the samples in the lines parallel to the intersection lines of "-c" wings, as it is shown in the fig.93. In contrast to the BSFs the PSFs accrue in {$\bar{1}$2$\bar{1}$0} planes inclined with respect to the sample surface, see fig.93. These planes intersect the surface and the edge of the samples in the linear segments perpendicular to the lines of BSFs (see fig.93), and usually bridges two of them [45, 49]. The density of PSFs is much lower than density of BSFs and consequently the PSFs luminescence signal should be lower than BSFs.

A Zeiss LEO DSM 982 field emitter type scanning electron microscope (SEM) equipped with a liquid helium cryostat to cover the temperature range between 7 K and 475 K was used to measure the CL. The light is collected by a 100 μm UV optimized glass fiber. Further the emitted photons are analyzed by a 90 cm focal length Spex 1702 monochromator together with a liquid nitrogen cooled charge coupled device (CCD) camera for highly resolved cathodoluminescence (CL) spectra. The CL spectra was recorded by collecting the intensity of the series of wavelength (monochromator) with the integration in time about 30 seconds. And the typical PL spectrum was recorded at T=15 K with laser beam exposition time about 1 minute.

The normalized PL and CL spectra measured for the samples S3 and S4 are shown in the fig.94.a and fig.94.b, respectively. There are several peaks of intensity for different wavelength on the PL and CL curves are visible. The PL and CL spectra reveal the peaks of the GaN near edge emission (NBE) marked as GaN NBE in the figures, at the energy close to the stain free theoretical value 3.4875 eV (λ=355.5 nm) [49, 16]. The CL GaN NBE peak of the sample without SiN mask is shifted more to the lower energy from the PL GaN peak, than in case of the sample with SiN mask.

Liu et al. [49] has shown through direct TEM/CL correlation that emission in the range 3.29–3.43eV is related to stacking faults in a-plane nonpolar GaN. As that was shown by Wu et al. [18] and Okada et al. [26] the peak at energy about 3.41 eV could be attributed to the basal plane stacking faults type $I1$, this assumption was proved by Liu et al. [49]. In our measurements the peak of BSFs was slightly shifted to higher energy and was at the energy 3.425 eV (λ=367 nm), see fig.94.a,b.

The PSFs should have the emission peak at lower energy than BSFs peak [18, 16, 49]. From the CL/TEM investigation of the same area Liu et al. [49] it is known that intensity peaks in energy range from 3.28 to 3.40 eV

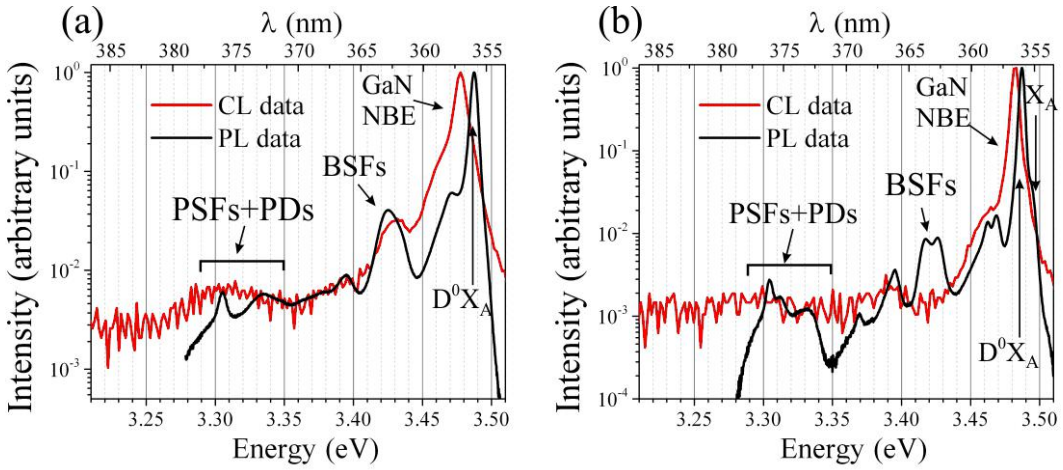

Figure 94: The PL and CL of the samples S3 without SiN mask (a) and S4 with SiN mask (b).

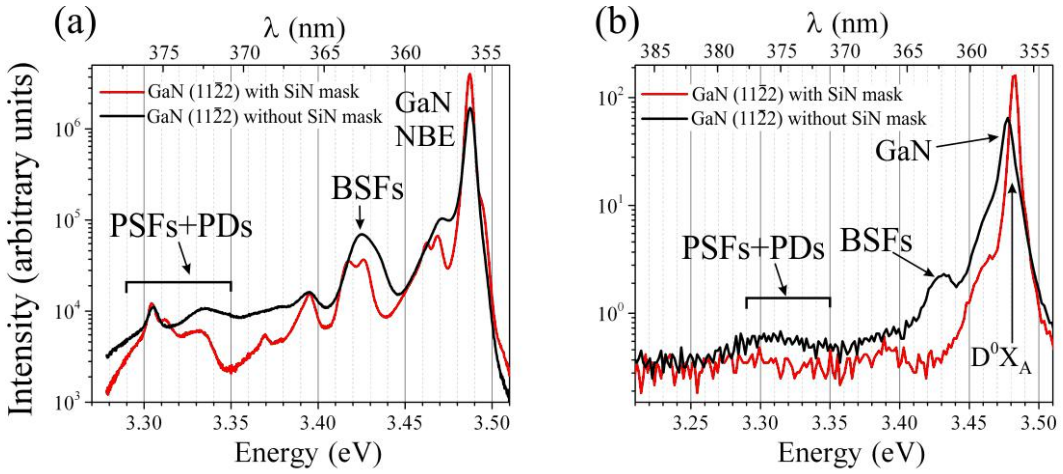

Figure 95: Photoluminescence (a) and cathodoluminescence (b) comparison of the samples S3 without SiN mask and S4 with SiN mask.

are correspond to the PSFs and partial dislocations bounded stacking faults. Usually, the peak of PSFs in nonpolar GaN material is observed at 3.32 eV [49, 16]. In our CL measurements the intensity was not high enough to resolve several peaks in the area from 3.28 to 3.35 eV. For the PL spectra several peaks in this range were found. Finally, the area 3.28 to 3.35 eV was attributed attributed mostly to PSFs and also to partial dislocations (see fig.94).

From the comparison of the PL and CL spectra one could find the differences in the peaks behavior. These differences could be explained by different crystallographic orientations of the spectra measurements. Additionally, in the PL measurements the illuminated area was large and could contain more types of defects and different variants of intersection of the defects with the surface which might influence on the emission spectrum.

To investigate the influence of the SiN mask comparison of the PL spectra for the samples S3 without and S4 with the SiN mask is presented in the fig.95.a, and CL data in the fig.95.b.

Comparison of the GaN NBE peaks of the samples with and without SiN mask allows to conclude that its intensity is higher in several times for the sample S4 with SiN mask, than for S3 without SiN mask. In contrast to the GaN NBE peak the peak of BSFs has much lower intensity for the sample with SiN mask in PL spectrum and disappeared in CL spectrum. The same behavior is observed for the peak of PSFs. The peak of PSFs is lower for the sample with SiN mask, see fig.95.a and fig.95.b.

Reverse behavior of the GaN emission and defects peaks allows to conclude the significant influence of the SiN mask on the stacking faults density reduction.

To allocate the BSFs and PSFs in the PSS GaN structure spatially resolved monochromatic CL distribution was measured. For this locally resolved CL samples investigation the SEM was equipped with a Jobin Yvon HR250

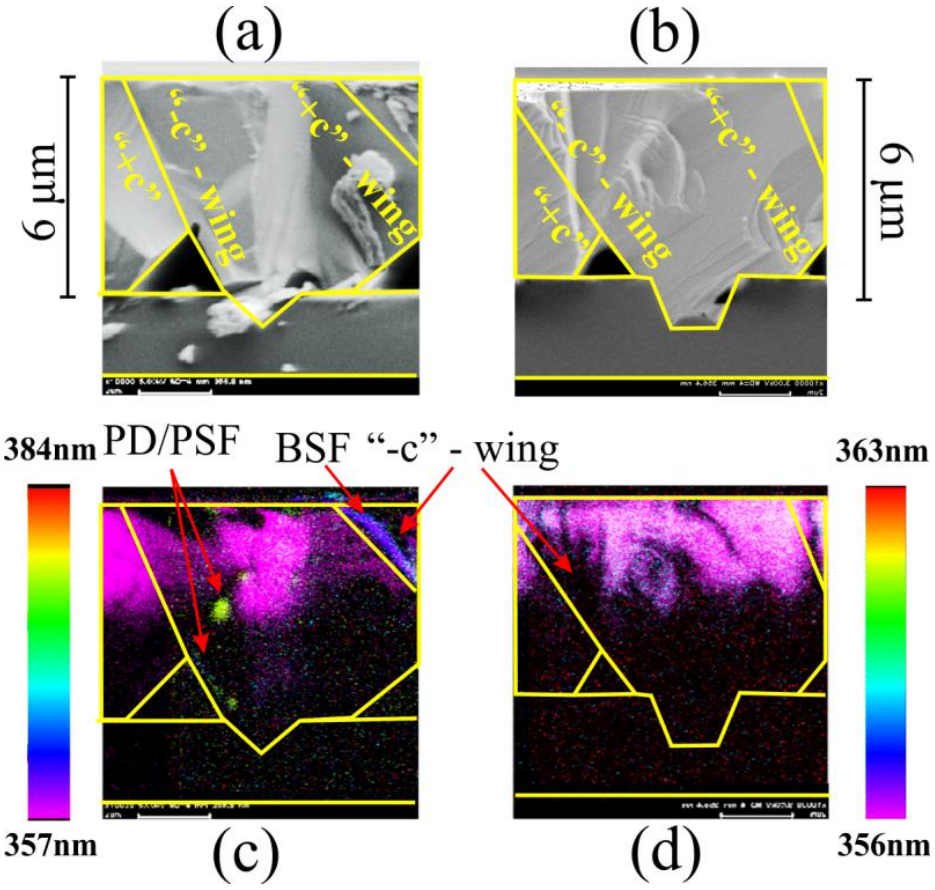

Figure 96: The SEM images of the edges of the samples S3 (a) and S4 (b). The locally resolved CL of the same regions of the samples S3 (c) and S4 (d).

25 cm focal length monochromator with a photomultiplier tube. These monochromatic CL maps were recorded simultaneously with the SEM pictures of the sample area allowing determining the exact position of any localized luminescence feature. The SEM pictures of the samples S3 and S4 are demonstrated in the fig.96.a and fig.96.b, respectively. For easier understanding of the locally resolved CL results in the SEM pictures the contours of the GaN inverted pyramid structures are drawn, also "+c" and "-c" wings are marked.

The spatially resolved monochromatic CL is presented in the fig.96.a for the sample S3 without SiN mask and in the fig.96.b for the sample S4 with SiN mask. The magenta color corresponds to the wavelength of NBE GaN about 355.5 nm, the violet to the BSFs emission ($\lambda \approx 367\,nm$), and green to the range of PSFs and partial dislocations ($371.0\,nm < \lambda < 377.5\,nm$).

From the comparison of the fig.96.c and fig.96.d one can see the direct evidence that the SiN mask reduce the BSFs and PSFs density.

The areas of "-c" wings of the sample without mask almost don't emit in the NBE GaN wavelength due to high amount of dislocations especially stacking faults. The BSFs and the PSFs intensity is visible in the "-c" wings of the sample S3. The BSFs intensity is presented as a line distribution parallel to the "-c" wing plane (fig.96.c), as it was shown in the fig.93. The PSFs and partial dislocations illuminate as a segments perpendicular to the "-c" wings plane, as it was discussed above (see fig.93).

In contrast to the sample without mask for the samples S4 with SiN mask almost homogenous intensity distribution of NBE GaN intensity was observed (fig.96.d). Moreover, the magenta area is larger meaning the total intensity of the GaN emission is higher for the sample with SiN mask (see fig.96).

As a conclusion, the CL/PL and X-ray investigation results are in good agreement and demonstrate reduction of BSFs density by introducing in-situ deposited SiN mask.

8.10 Micro focus X-ray investigation of stacking faults in semipolar GaN

8.10.1 Introduction

It is should be mentioned that calculated BSFs density ρ_{BSF} from mosaic and MC models are average densities over the illuminated with X-ray beam area of the sample. Since, the BSFs are formed in periodically repeating "-c" wings, the distribution of the BSFs should be inhomogeneous and periodic as well. In order to investigate locally the distribution of ρ_{BSF}, the illuminated area of the sample should be reduced and BSFs streaks intensity $I(Q_{str})$ should be measured for different positions on the sample surface. Calculation of the ρ_{BSF} using MC simulation for each position at the sample will lead to the mapping of the ρ_{BSF} and will allow us to determine local distribution of the ρ_{BSF}. Since, the measurement of a reflection in 3D RS with linear Mythen 1K detector takes about 9 hours, the measurement of ρ_{BSF} map was almost impossible. Using of two dimensional detector is found to be crucial method to investigate local distribution of the ρ_{BSF}.

8.10.2 Locally resolved determination of stacking faults using 2D detector

According to visibility criteria (see Chapter 8.4.2), the symmetric $h0\bar{h}h$ reflections of $(10\bar{1}1)$ GaN (samples S1 and S2) have BSFs streak. Recently, two dimensional (2D) X-ray detectors become available for the X-ray diffraction experiments [135]. The detection area of a 2D detector in reciprocal space is a part of Ewald's sphere. Therefore, in Bragg conditions for the symmetric reflections the detector's frame in RS will intersect the 3D diffuse intensity of reflection, as it is illustrated in the fig.97.a. By rotating the sample around its normal, the position of the detector with maximum of detected BSFs streak intensity $I(Q_{str})$ could be found. The maximum of the detected BSFs steak is achieved ones the inclination angle of detector frame with respect to the CTR is minimized. For symmetric reflections detector frame inclination is equal to the incidence angle $\alpha_i = \theta_B$ (see Chapter 3.9). Therefore, the reflection $h0\bar{h}h$ with lowest h index, and usually the most intense should be chosen and is $10\bar{1}1$ for semipolar $(10\bar{1}1)$ GaN (fig.97.a). The detector frame intensity recorded in the described position of 2D detector in the reflection $10\bar{1}1$ with line drawn along [0001] (BSFs) direction is shown in the fig.97.b.up. Moreover, the intensity distribution $I(Q_{str})$ along the BSFs streak could be measured, and fitted with Lorentzian, as it is shown in the fig.97.b.bottom. The $FWHM$ of the fitted Lorentzian is in the number of the detector's pixels $\triangle N_{ch}$. The number of the pixels $\triangle N_{ch}$ could be recalculated into the units of the reciprocal space $\triangle Q_{str}$ using formula:

$$\triangle Q_{str}(N_{ch}) = \frac{4\pi^2 \sin\theta_B}{180^\circ \lambda} \cdot \frac{\triangle N_{ch}}{N_{ch}^{deg}}, \tag{117}$$

where λ is the wavelength of the X-ray, θ_B is the Bragg angle, $\triangle N_{ch}$ is the number of the detector pixels to be recalculated into reciprocal space units, and N_{ch}^{deg} is the number of detector pixels correspond to one degree.

The N_{ch}^{deg} could be calculated from the size of the detector's pixel d_{ch}^0 and the detector sample distance L_{det}^{samp}:

$$N_{ch}^{deg} = \arctan^{-1}\left(\frac{d_{ch}^0}{L_{det}^{samp}}\right). \tag{118}$$

Since, the derived $FWHM$ of the Lorentzian and the BSFs density are interrelated, recording 2D diffraction pattern is found to be an efficient method for determining ρ_{BSF} without recording the RSM. By organizing a grid of positions on the sample surface, one could record the map of BSFs density distribution in the sample. In the fig.97.a an example of the scan area on the sample surface is shown.

The special resolution of the ρ_{BSF} map is depends on the size of illuminated area, hence on the footprint of the X-ray beam on the sample. The scan grid for investigation a sample with a ρ_{BSF} inhomogeneity should be chosen relay on the knowledge of approximate ρ_{BSF} inhomogeneity resolution. For the semipolar $(10\bar{1}1)$ GaN samples the BSFs are concentrated in the "-c" wings of semipolar GaN blocks. The width of the GaN blocks is about $5.4\,\mu m$ for the sample S1 and S2 (see Chapter 8.2). Therefore, the footprint should be at least in two times smaller, and should be less or equal to $2.5\,\mu m$.

In order to record the ρ_{BSF} map, the sample should be moved in two orthogonal directions x and y using translation stage of the diffractometer, as it is demonstrated in the fig.97.a. The step of the motors should be at least equal or smaller than the footprint of the X-ray beam. The streak of the BSFs in the experiment could be found by rotation of the sample around its normal at the angle δ, where the [0001] crystallographic direction of GaN sample aligned along the detector plane, and semipolar GaN structures are perpendicular to the detector plane (see fig.97.a). During rotation of the sample, scanning motors x and y are also rotated with the sample around its normal in the same angle δ and the borders of the scan are inclined with respect to the semipolar GaN structures in the angles δ. Hence, the inclination of the semipolar GaN structures in the scanned ρ_{BSF} map is known, and could

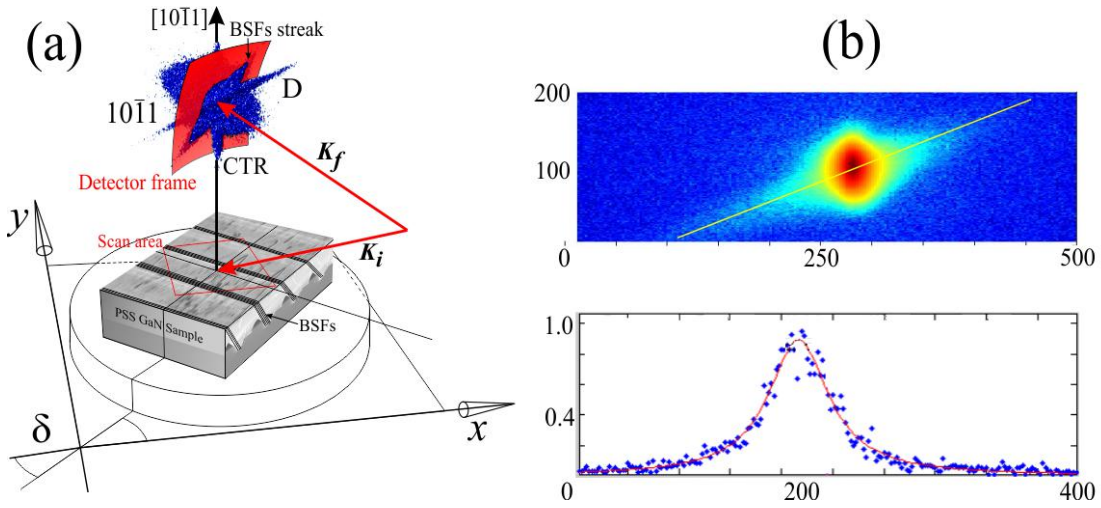

Figure 97: The sketch of the experiment with 2D detector (a), the single frame of the 10$\bar{1}$1 GaN reflection with BSFs streak in the plane of the detector and fit of the $I(Q_{str})$ (b).

be drawn, as a lines inclined with respect to the scan border in the angle δ, see fig.97.a. For the semipolar GaN the ρ_{BSF} is expected to be periodic in direction perpendicular to the GaN stripes with period of about 5.4μm, due to periodicity of "-c" wings rich of BSFs. Therefore, the knowledge of the semipolar GaN stripes orientation on the ρ_{BSF} map is very important to prove the .

The scan across the semipolar GaN stripes could be organized as a two motors x and y scan, using "d2scan" command in the software of the diffractometer. For the scan the coordinates of the beginning (x_1, y_1) and the end (x_2, y_2) of the scan should be known. One way to realize the scan is to choose the borders x_1 and x_2 of the sample in x direction for some y_1 (from the reflection disappearing from the detector) and from the calculated angle δ, the second border $y_2 = y_1 + (x_2 - x_1) \cdot \tan\delta$, corresponding the direction perpendicular to the GaN stripes is determined.

8.10.3 Locally resolved determination of BSFs density in semipolar GaN using microfocus X-ray diffraction at NANO beamline

For high spacial resolved ρ_{BSF} mapping, the focusing of the X-ray beam down to one micrometer is crucial, as it was demonstrated by Kachkanov et al. [136]. Therefore, the footprint of the X-ray beam should be decreased from 0.3 mm down to 1 μm. Realization of this experiment at SCD beamline was not possible, and the experiment should be held in more sophisticated and well established NANO beamline, presented in the Chapter 7.3.

The scheme of the diffraction experiment with microfocus X-ray beam at NANO beamline is shown in the fig.98.a. The double crystal Si(111) monochromator, depicted in the scheme as monochromators 1,2 were used. The collimated monochromatic beam was focused by the compound refractive lens (CRL), see the fig.98.a. In our experiment crossed CRL for focusing the X-ray beam in two directions was used, see fig.98.b. The crossed CRL was produced at the Institute for Microstructure Technology (IMT) at the synchrotron ANKA using LIGA technology by Vladimir Nazmov [137, 138, 139]. The lenses are structured in a SU-8 polymer on the Si(111) substrate. The crossed CRL in the SU-8 structures inclined in two opposite directions (shown in the fig.98.c) allows us to focus the beam in the horizontal and vertical directions. The number of the structures should be chosen according to the experiment parameters and required properties of the focused beam [137]. The X-ray beam could be focused down to the submicron focus (hundreds of nanometer) with a focus depth of the centimeter range.

The commissioning of the CRL required high precision set-up to align them with respect to the direct beam. For that purpose the hexapod was used and the cleaning slits were placed after the hexapod system to remove the diffuse part of the beam (fig.98.a). The inclination of the sample with respect to the direct beam in diffraction geometry limit our distance sample/CRL to 80 mm which restrict our focus capability of the beam to about 10 μm at the center of the diffractometer.

Further, in the reflection 10$\bar{1}$1 the streak of BSFs was found and the sample was successfully scanned with 2D Pilatus 100K detector, with the pixel size 172 μm and number of pixels 487 x 195 [140, 141].

However, the X-ray beam focusing decreases the intensity, due to absorption and the limited aperture of the CRL of one milliliter. For the diffuse scattering from the defects of the crystal intensity loses are critical. Moreover, the X-ray beam focusing increases the beam divergence. Therefore, by increasing spacial resolution in real space

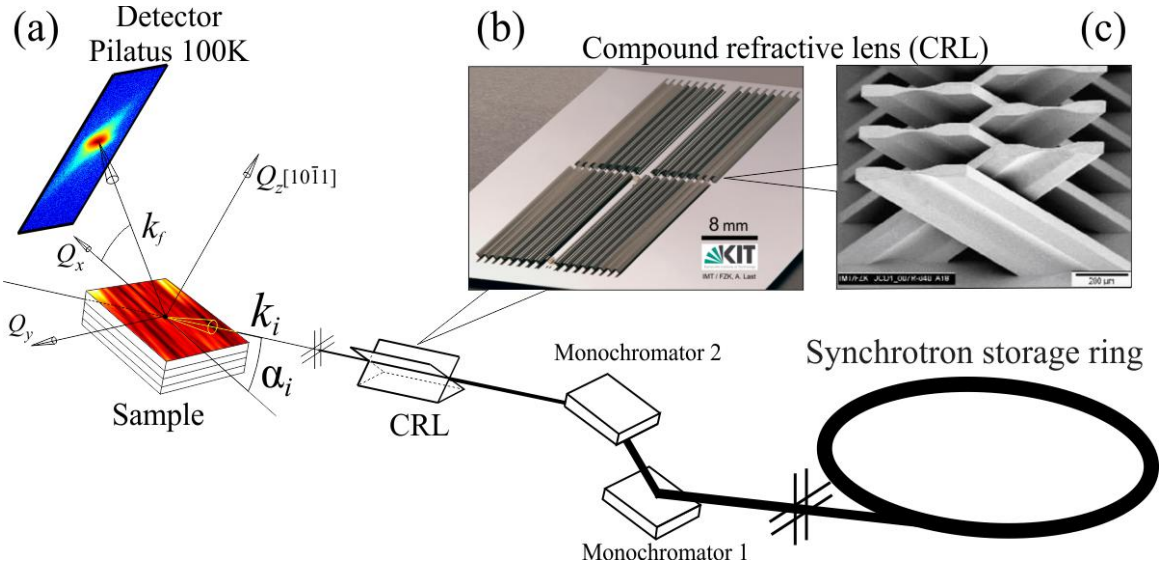

Figure 98: Scheme of the microfocus experiment with compound refractive lens (CRL) (a), the view of the compound refractive lens manufactured by LIGA (IMT) (b), and the CRL's structures (c).

(footprint) the resolution in reciprocal space is decreasing (see Chapter 3.8). The resulting the resolution was found to be enough for the investigation of the BSFs diffuse scattering.

The view of the 8-circle diffractometer with two detector arms at NANO beamline is shown in the fig.99.a. The Pilatus 100K detector was equipped with the 1000 mm length flight tube with low vacuum to minimize air diffuse scattering. The sample/detector distance was about 1150 mm.

The CRL was mounted on the hexapod (see fig.99.b) to align precisely of the SU-8 structures with respect to the direct beam. The mounting of the lenses is shown in the inset in the fig.99.b. The flight tube of the optic system was mounted upstream, and downstream the cleaning slits system were used to minimize the diffuse air scattering (see fig.99.b).

The aperture size of the used CRL was about 800 μm horizontally and 200 μm vertically. The distance between CRL and the sample was about 250 mm and the divergence of the beam was about 0.2° in horizontal and 0.05° in vertical directions.

The sample was placed in the vertical position, as it is shown in the fig.99.c, and the diffraction plane was horizontal. The position of the detector in the Bragg conditions is shown in the fig.99.a.

Taking into account the beam size of 10 μm, the scan's step of the ρ_{BSF} map should be not less than 5 μm. The first scans with the rough step of 50 μm were done for the relatively large area of 27 mm^2 for the samples S1 (6 x 4.5mm) and S2 (9 x 3mm).

During the scan of the sample surface about 10000 files were recorded with 2D detector. The calculation of the BSFs density from one single BSFs intensity distribution $I(Q_{str})$ using MC simulation takes hours and therefore, the calculation of the ρ_{BSF} for the ρ_{BSF} map would take months. In order to save the calculation time, first the cuts of intensity along the streak $I(Q_{str})$ were fitted to the Lorentzians and the $FWHM$s were derived and maps of $FWHM$ were organized. As an example the $FWHM$ map of the sample S1 is shown in the fig.100.a. One could further determine the ρ_{BSF} from the $FWHM$ using simple equations of mosaic model.

In order to calculate accurately the ρ_{BSF} map, the map of $FWHM$ was indirect recalculated into ρ_{BSF} using MC simulation. For this purpose, two positions on the sample with the lowest ρ_{BSF} , depicted as A in the fig.100.a, and for the highest ρ_{BSF}, depicted as B in the figure, were chosen. The comparison of the BSFs intensity distributions $I(Q_{str})$ of the positions A and B are presented in the fig.100.b. For these $I(Q_{str})$ the BSFs densities were calculated using MC simulation. The ρ_{BSF} for all intermediate positions were derived by assuming the ρ_{BSF} is proportional to the $FWHM$s and ρ_{BSF} maps were therefore recalculated for the samples S1 and S2 and presented in the fig.101.a and fig.101.b, respectively.

The ρ_{BSF} maps are plotted in the same scale and from their comparison, direct evidence of influence of the SiN mask on the ρ_{BSF} reduction in whole semipolar GaN sample could be observed. Furthermore, the inhomogeneity of ρ_{BSF} in the samples is visible, and ρ_{BSF} distribution seems to be periodic. In order to investigate the local periodicity of the ρ_{BSF}, the scan of the area 0.8 x 0.8 mm in the center of the previous rough scan with the step of

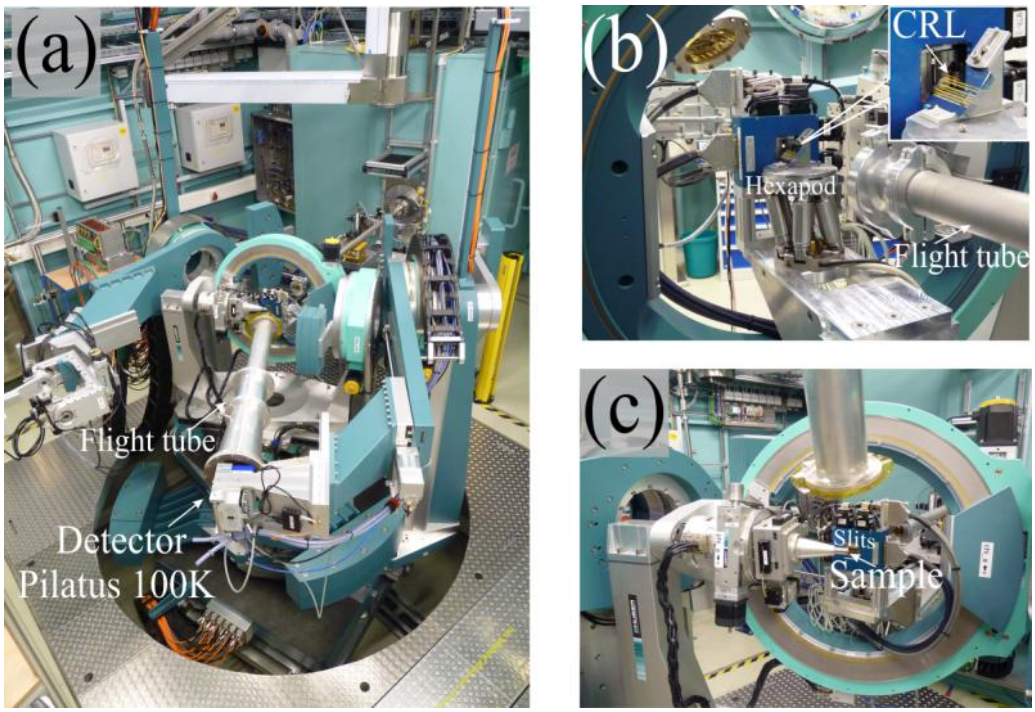

Figure 99: The diffractometer at NANO beamline (a), CRL mounted on hexapod (b), and sample with slits system (c).

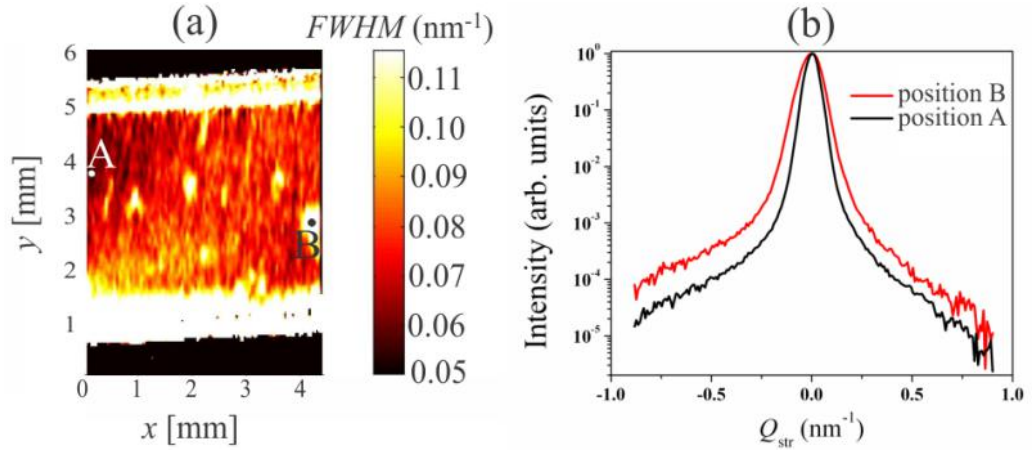

Figure 100: The scan of the sample based on the $FWHM$ of the BSF's $I(Q_{str})$ with two extreme points A and B (a), and comparison of the intensities $I(Q_{str})$ for the positions A and B (b).

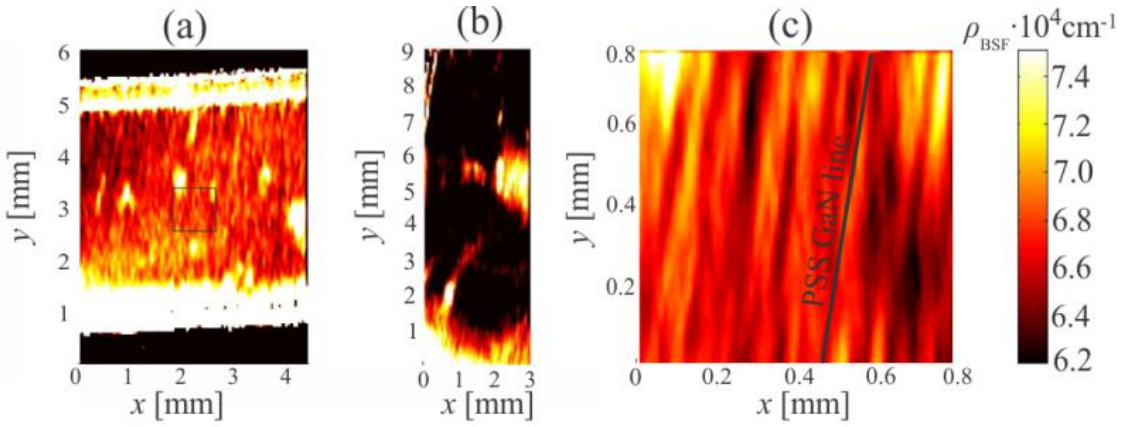

Figure 101: Comparison of the BSFs density scans of the samples S1 without SiN mask (a), and S2 with SiN mask (b).

10 μm was done for the sample S1. The area of the scan is drawn in the fig.101.a as a square, and the ρ_{BSF} map of the scan is presented in the fig.101.c. For the fig.101.c, the periodicity of ρ_{BSF} is visible. Since, the direction of the semipolar GaN stripes is known from the angle δ (see Chapter 8.10.2), the line parallel to the semipolar GaN stripes (parallel to "-c" wings) could be drawn and is depicted in the fig.101.c as "PSS GaN line".

The maximums of the ρ_{BSF} map periodicity are correlated with some deviation with the "PSS GaN line". This deviation is possible to explain as moire pattern of the scan grid with the step of 10 μm and periodicity of the ρ_{BSF} of the sample. The periodicity corresponds to the width of the GaN stripes and is about 5.4 μm for the sample S1 and S2 (see Chapter 8.2). In order to avoid the moire pattern effect one needs to decrease the step size of the scan to 1 μm. Nevertheless, the scan with step 1 μm didn't get better resolution due to the limited beam size of 10 μm.

Sub ten micrometer X-ray beam size will be reached at NANO beamline in the nearest future, and the scan of the same area will show the distribution of the ρ_{BSF} with higher spacial resolution.

8.11 Conclusions

These experiments have shown that the visibility criteria known for the nonpolar GaN are also valid in the case of semipolar GaN. The power of 3D RSM mapping for the diffuse BSF intensity investigation has also been shown to cover the BSF streaks and other diffuse scattering of defects that appear, either in coplanar or in non-coplanar geometries. This has been demonstrated in detail with respect to the semipolar (11$\bar{2}$2) GaN.

In the course of our experiments, the intensity distribution along the BSF streak was recorded for all semipolar GaN samples. A comparison between the tails of diffuse intensity in the log-log scale reveal the slopes of the curves in the range of $Q_{str}^{-3} < Q_{str} < Q_{str}^{-2}$.

The densities of BSFs in samples S1-S4 were calculated using a simple mosaic model and a sophisticated Monte Carlo simulation. The BSF density of the semipolar samples was found to be lower than that for the nonpolar samples. Our 3D RSM mapping of BSFs clearly demonstrates the dependency of the BSFs on the orientation of the GaN crystallographic surface orientation. Comparisons of BSF densities of the (11$\bar{2}$2) and (10$\bar{1}$1) GaN, reveal a lower density in the case of (11$\bar{2}$2)GaN. Moreover, the efficiency of the SiN mask is found to be the same for both orientations, and is equal to about 50%. The ρ_{BSF} for the (11$\bar{2}$2) GaN sample S4 with the SiN mask is found to be the lowest, i.e. equal to $4.4 \cdot 10^3 cm^{-1}$. The PL and CL investigations of samples S3 and S4 confirm the influence of the SiN mask on the reduction of the defect density.

The local distribution of the BSF density, as performed by the microfocus experiment at NANO beamline for the (10$\bar{1}$1) GaN samples S1 and S2, has been shown to enable the determination of the ρ_{BSF} maps from the $FWHM$ of the BSF profile. The ρ_{BSF} maps reveal the inhomogeneity of the ρ_{BSF} distribution. Moreover, the correlation between the ρ_{BSF} periodicity and the semipolar GaN stripes has also been shown. It should be emphasized that resolving a BSF investigation locally, using a microfocus beam, is highly recommended for semipolar GaN grown on patterned sapphire substrate. This is because the BSF distribution is strongly influenced by the GaN stripe formation.

9 Conclusions

The thesis has set out to demonstrate the potential of non-destructive X-ray diffraction for the real structure characterization of defects in group III-nitride epitaxial layers. The mean inter-atomic distances, used for the crystalline structure study, could be derived from the coherent X-ray scattering signal. As demonstrated in Chapter 6 in relation with polar $Al_{0.2}Ga_{0.8}N$, the high resolution X-ray diffraction allows the phase detection of III-nitride alloys. The intensity distribution of diffuse X-ray scattering indicates the crystalline structure imperfections. Depending on the type of defect and its density, the diffuse scattering can give rise to a characteristic distribution of intensity in certain characteristic directions within a reciprocal space.

By measuring and evaluating coherent and diffuse scattered intensity distribution in reciprocal space, we can draw conclusions as to the type of major defects of III-nitrides and their density. Thanks to their position in reciprocal space, the scattering signals can even be attributed to layers of different depths e.g., whether above or below the SiN masks. By using the X-ray methods, it has been shown that mask intercalation is an effective method of TDD and BSF density reduction in polar and semipolar III-nitride layers.

Measurements of complete three dimensional distribution of diffuse intensity in the vicinity of the reciprocal lattice points of semipolar $(11\bar{2}2)$ GaN have also been shown to be a powerful method that enables the intensity extraction of BSF and PSF streaks, as demonstrated in Chapter 8.

The investigation of TDD in polar $Al_{0.2}Ga_{0.8}N$ epilayers with different layer thicknesses shows an exponential decrease of TDD with increasing layer thickness. By comparing the diffuse intensity distribution along BSF streaks in reciprocal space, we were able to demonstrate the influence of the growth direction of semipolar GaN on BSF densities.. Furthermore, lower BSF densities were found for $(11\bar{2}2)$ GaN than for $(10\bar{1}1)$ GaN that had been grown on patterned sapphire.

The microfocus X-ray diffraction experiments at the NANO beamline have shown to be an efficient technique with which to carry out locally-based investigation on crystalline structures and in particular in order to demonstrate periodical fluctuation of BSF densities across the patterned sapphire substrate grooves for the $(10\bar{1}1)$ GaN. The amount of defects in III-nitride layers has been calculated using the Monte Carlo method using diffuse intensity distribution, as demonstrated in Chapters 6, 8.

The work also shows that the mosaic model with the Williamson-Hall plot for TDs in polar $Al_{0.2}Ga_{0.8}N$ and BSFs streak broadening for BSFs in semipolar GaN is a good and relatively fast comparative method of defect density determination. Furthermore, the thesis demonstartes that the Monte Carlo based models can be used as a strong, reliable, but relatively time-consuming quantitative method for absolute defect density determination. In order to increase the accuracy of mosaic model results, additional calibration procedures, based on the results calculated by the Monte Carlo model, should also be performed.

The results of experiments and simulation methods are in agreement with complimentary methods of III-nitride stsructure investigation such as TEM, AFM, SEM, CL, EPD, etc., which goes to prove the reliability of the results received. However, the SEM and AFM were shown to be able to provide information only on thesurface samples. While CL measurements provide information about the total or local emission radiation of semiconductor crystals, they cannot be used for the defect type and density determination. The TEM is both a destructive and time-consuming method, providing only local information about defects and cannot be used for average defect density determination. EPD is a statistical method that is used to determine the average total TDD (edge and screw TDD) but it is also a destructive method that does not allow the edge and screw TDD determination, as shown in Chapter 6. Therefore a non-destructive, tunable diffraction technique covering local to statistical X-ray diffraction, occupies a special position in III-nitride crystal investigation, providing statistical and complimentary information, which can be used in combination with other methods that are also given here.

The work demonstrates advantages of applying the X-ray scattering methods based on synchrotron radiation, even if laboratory X-ray experiments are also considered as a useful tool. Many X-ray diffraction experiments presented in the work could have been performed in principle, using a standard laboratory high-resolution diffractometer. However, only the most recent versions of laboratory diffractometer have the additional degree of freedom to perform GID diffraction experiments, which is crucial for a dominant edge type of investigation on threading dislocations to be carried out on GID reflections. Due to a lower level of flux in laboratory diffractometer intensity, usually only standard scans, such as simple rocking curve measurements, can be applied. Moreover, these RSM techniques are not time-consuming, which might otherwise lead to mistakes in data interpretation, as described in Chapter 6. Finally, the investigation of diffuse scattered intensity of defects in a three dimensional reciprocal space, as described in Chapter 6, requires a high flux and a high brilliance of X-ray beam and a two-dimensional or linear detector. Three-dimensional reciprocal space mapping at standard laboratory diffractometers would take considerable time consuming and with a much lower signal to noise ratio, would in any case be practically impossible to achieve. Synchrotron high resolution X-ray diffraction is thus a requirement for a wide-ranging investigation of

perfection in group III-nitride crystal structures.

Furthermore, it is important to mention that X-ray based techniques for the defect density determination could have been applied not only for ex-situ grown samples, but also for in-situ during the crystal growth. The quality investigation of crystals during the stages of their growth under various growth parameters and with the introduction of various defect reduction techniques is certainly an attractive perspective for the optimization of III-nitride crystals. This makes the synchrotron X-ray diffraction method unique compared to other semiconductor investigation techniques (TEM, SEM, CL, EPD, etc.). Moreover, high-speed growth processes require significant time to be resolved. This means exposing them within short periods of time with a high flux of X-ray beam. As a consequence, this makes in-situ experiments with the laboratory diffractometer practically impossible.

The in-situ X-ray investigation of crystalline structures should be performed in specially manufactured growth chambers. These should be mounted on a heavy duty diffractometer with a synchrotron, which cannot be performed with a standard laboratory high-resolution diffractometer. A MOVPE in-situ growth chamber was produced specially for ANKA and operable with a NANO-beamline. This will open up a new phase of investigation of the crystalline structure growth process of III-nitrides in similar synchrotron radiation facilities and in particular at ANKA. The methodical experience and the scientific results of Chapter 6 could thus be used as a recipe for an investigation of threading dislocation density in polar III-nitride epilayers during layer growth.

Three-dimensional diffuse intensity investigations, as proposed in Chapter 8, can well be performed for in-situ investigation of growth parameters that influence the formation of BSFs in semipolar GaN. Therefore, the results of this thesis might not only go to serve scientific interests but also to optimize the processes of III-nitride growth. This could also pave the way for future on site X-ray investigations of III-nitrides at NANO beamline at synchrotron ANKA.

10 Bibliography

[1] R. Davis, S Einfeldt, E. Preble, A. Roskowski, Z. Reitmeier, and P. Miraglia. Gallium nitride and related materials: challenges in materials processing. *Acta Materialia*, 51(19):5961–5979, 2003.

[2] H. Morkoc. *Handbook of Nitride Semiconductors and Devices: Vol. 1 Materials Properties, Physics and Growth (Handbook of Nitride Semiconductors and Devices)*. Wiley VCH Verlag GmbH Co. KGaA, auflage edition, 2008.

[3] S. C. Jain, M. Willander, J. Narayan, and R. Van Overstraeten. III nitrides: growth, characterization, and properties. *Journal of Applied Physics*, 87(3):965–1006, 2000.

[4] H. Morkoc. *Handbook of Nitride Semiconductors and Devices, GaN-based Optical and Electronic Devices (Handbook of Nitride Semiconductors and Devices VCH*. Wiley-VCH, volume 3 edition, December 2008.

[5] M.R. Krames, O.B. Shchekin, R. Mueller-Mach, G.O. Mueller, Ling Zhou, G. Harbers, and M.G. Craford. Status and future of high-power light-emitting diodes for solid-state lighting. *Journal of Display Technology*, 3(2):160 –175, 2007.

[6] J. S. Speck and S. F. Chichibu. Nonpolar and semipolar group III nitride-based materials. *MRS Bulletin*, 34(05):304–312, 2009.

[7] T. Paskova. Development and prospects of nitride materials and devices with nonpolar surfaces. *Physica Status Solidi (b)*, 245(6):1011–1025, 2008.

[8] M. A. Moram and M. E. Vickers. X-ray diffraction of III-nitrides. *Reports on Progress in Physics*, 72(3):036502, 2009.

[9] F. Scholz. Semipolar GaN grown on foreign substrates: a review. *Semiconductor Science and Technology*, 27(2):024002, 2012.

[10] S. Nakamura. GaN growth using GaN buffer layer. *Japanese Journal of Applied Physics*, 30(Part 2, No. 10A):L1705–L1707, 1991.

[11] O. Ambacher, R. Dimitrov, M. Stutzmann, B.e. Foutz, M.j. Murphy, J.a. Smart, J.r. Shealy, N.g. Weimann, K. Chu, M. Chumbes, B. Green, A.j. Sierakowski, W.j. Schaff, and L.f. Eastman. Role of spontaneous and piezoelectric polarization induced effects in group-III nitride based heterostructures and devices. *Physica Status Solidi (b)*, 216(1):381–389, 1999.

[12] A. Bonfiglio, M. Lomascolo, G. Traetta, R. Cingolani, A. Di Carlo, F. Della Sala, P. Lugli, A. Botchkarev, and H. Morkoc. Well-width dependence of the ground level emission of GaN/AlGaN quantum wells. *Journal of Applied Physics*, 87(5):2289–2292, 2000.

[13] F. Bernardini, V. Fiorentini, and D. Vanderbilt. Spontaneous polarization and piezoelectric constants of III-V nitrides. *Physical Review B*, 56(16):R10024–R10027, 1997.

[14] F. Bernardini and V. Fiorentini. Macroscopic polarization and band offsets at nitride heterojunctions. *Physical Review B*, 57(16):R9427–R9430, 1998.

[15] F. Bernardini and V. Fiorentini. Nonlinear macroscopic polarization in III-V nitride alloys. *Physical Review B*, 64(8):085207, 2001.

[16] P. P. Paskov, R. Schifano, B. Monemar, T. Paskova, S. Figge, and D. Hommel. Emission properties of a-plane GaN grown by metal-organic chemical-vapor deposition. *Journal of Applied Physics*, 98(9).

[17] T. Schwarz and M. Kneissl. Nitride emitters go nonpolar. *Physica Status Solidi (RRL) Rapid Research Letters*, 1(3):A44–A46, 2007.

[18] Z. H. Wu, A. M. Fischer, F. A. Ponce, B. Bastek, J. Christen, T. Wernicke, M. Weyers, and M. Kneissl. Structural and optical properties of nonpolar GaN thin films. *Applied Physics Letters*, 92(17):171904–171904–3, 2008.

[19] P. Waltereit, O. Brandt, A. Trampert, H. T. Grahn, J. Menniger, M. Ramsteiner, M. Reiche, and K. H. Ploog. Nitride semiconductors free of electrostatic fields for efficient white light-emitting diodes. *Nature*, 406(6798):865–868, 2000.

[20] P. Vennegues, J. M. Chauveau, Z. Bougrioua, T. Zhu, D. Martin, and N. Grandjean. On the origin of basal stacking faults in nonpolar wurtzite films epitaxially grown on sapphire substrates. *Journal of Applied Physics*, 112(11):113518–113518–8, 2012.

[21] M. A. Moram, C. F. Johnston, J. L. Hollander, M. J. Kappers, and C. J. Humphreys. Understanding x-ray diffraction of nonpolar gallium nitride films. *Journal of Applied Physics*, 105(11):113501–113501–7, 2009.

[22] M. D. Craven, S. H. Lim, F. Wu, J. S. Speck, and S. P. DenBaars. Structural characterization of nonpolar (110) a-plane gan thin films grown on (102) r-plane sapphire. *Applied Physics Letters*, 81(3):469–471, 2002.

[23] M. Funato and Y. Kawakami. Semipolar III nitride semiconductors: Crystal growth, device fabrication, and optical anisotropy. *MRS Bulletin*, 34(05):334–340, 2009.

[24] Y. Honda, N. Kameshiro, M. Yamaguchi, and N. Sawaki. Growth of (1 10 1) GaN on a 7-degree off-oriented (001)si substrate by selective MOVPE. *Journal of Crystal Growth*, 242(1–2):82–86, 2002.

[25] N. Okada, H. Oshita, A. Kurisu, and K. Tadatomo. Growth mechanism of nonpolar and semipolar GaN layers from sapphire sidewalls on various maskless patterned sapphire substrates. *Japanese Journal of Applied Physics*, 50:035602, 2011.

[26] N. Okada and K. Tadatomo. Characterization and growth mechanism of nonpolar and semipolar GaN layers grown on patterned sapphire substrates. *Semiconductor Science and Technology*, 27(2):024003, 2012.

[27] N. Okada, H. Oshita, K. Yamane, and K. Tadatomo. High-quality 20-21 GaN layers on patterned sapphire substrate with wide-terrace. *Applied Physics Letters*, 99(24):242103–242103–3, 2011.

[28] T. Zimmermann. *Polarisationseffekte in Gruppe-III-Nitriden Anwendung in p-Kanal FETs und elektromechanischen Strukturen*. Suedwestdeutscher Verlag fuer Hochschulschriften, 2010.

[29] R. Cingolani, A. Botchkarev, H. Tang, H. Morkoç, G. Traetta, G. Coli, M. Lomascolo, A. Di Carlo, F. Della Sala, and P. Lugli. Spontaneous polarization and piezoelectric field in GaN/Al(0.15)Ga(0.85)N quantum wells: Impact on the optical spectra. *Physical Review B*, 61(4):2711–2715, 2000.

[30] T. Matsuoka, H. Okamoto, M. Nakao, H. Harima, and E. Kurimoto. Optical bandgap energy of wurtzite InN. *Applied Physics Letters*, 81(7):1246–1248, 2002.

[31] F. C. Frank. On Miller-Bravais indices and four-dimensional vectors. *Acta Crystallographica*, 18(5):862–866, 1965.

[32] P. Krishna and D. Pandey. Close - packed structures. *International Union of Crystallography*, page 7, 1981.

[33] K. Fujito, S. Kubo, and I. Fujimura. Development of bulk GaN crystals and Nonpolar/Semipolar substrates by HVPE. *MRS Bulletin*, 34(05):313–317, 2009.

[34] E. R. Dobrovinskaya, L. A. Lytvynov, and V. Pishchik. *Sapphire: Material, Manufacturing, Applications*. Springer Science and Business Media, LLC 2009, 1 edition, 2009.

[35] H. Ibach and H. Luth. *Solid-State Physics: An Introduction to Principles of Materials Science*. Springer, 2009.

[36] H. Morkoc. *Nitride Semiconductors and Devices*. Springer, 1999.

[37] K. Matsumoto, H. Tokunaga, A. Ubukata, K. Ikenaga, Y. Fukuda, Y. Yano, T. Tabuchi, Y. Kitamura, S. Koseki, A. Yamaguchi, and K. Uematsu. High growth rate MOVPE. In Dirk Ehrentraut, Elke Meissner, and Michal Bockowski, editors, *Technology of Gallium Nitride Crystal Growth*, number 133 in Springer Series in Materials Science, pages 119–133. Springer Berlin Heidelberg, 2010.

[38] C. Hemmingsson, P.P. Paskov, G. Pozina, M. Heuken, B. Schineller, and B. Monemar. Hydride vapour phase epitaxy growth and characterization of thick GaN using a vertical HVPE reactor. *Journal of Crystal Growth*, 300(1):32–36, 2007.

[39] R.J. Molnar, W. Goetz, L.T. Romano, and N.M. Johnson. Growth of gallium nitride by hydride vapor phase epitaxy. *Journal of Crystal Growth*, 178(1-2):147–156, 1997.

[40] C. Abromeit. *Vacancies and Interstitials in Metals and Alloys, Berlin 1986: Proceedings of the 6th International Conference, Berlin, 1986.* Trans Tech Publications Ltd, 1987.

[41] D. Hull and D. J. Bacon. *Introduction to Dislocations.* Butterworth-Heinemann, 5 edition, 2011.

[42] V. Holy, T. Baumbach, D. Lubbert, L. Helfen, M. Ellyan, P. Mikulik, S. Keller, S. P. DenBaars, and J. Speck. Diffuse x-ray scattering from statistically inhomogeneous distributions of threading dislocations beyond the ergodic hypothesis. *Physical Review B*, 77(9):094102, 2008.

[43] Th. Kehagias, Ph. Komninou, G. Nouet, P. Ruterana, and Th. Karakostas. Misfit relaxation of the AlN/Al2O3 (0001) interface. *Physical Review B*, 64(19):195329, 2001.

[44] V. M. Kaganer, R. Kohler, M. Schmidbauer, R. Opitz, and B. Jenichen. X-ray diffraction peaks due to misfit dislocations in heteroepitaxial structures. *Physical Review B*, 55(3):1793–1810, 1997.

[45] D. N. Zakharov, Z. Liliental-Weber, B. Wagner, Z. J. Reitmeier, E. A. Preble, and R. F. Davis. Structural TEM study of nonpolar a-plane gallium nitride grown on 112 by organometallic vapor phase epitaxy. *Physical Review B*, 71(23):235334, 2005.

[46] M. B. McLaurin, A. Hirai, E. Young, F. Wu, and J. S. Speck. Basal plane stacking-fault related anisotropy in x-ray rocking curve widths of m-plane GaN. *Japanese Journal of Applied Physics*, 47(7):5429–5431, 2008.

[47] C. Stampfl and Chris G. Van de Walle. Energetics and electronic structure of stacking faults in AlN, GaN, and InN. *Physical Review B*, 57(24):R15052–R15055, 1998.

[48] H. Blank, P. Delavignette, R. Gevers, and S. Amelinckx. Fault structures in wurtzite. *Physica Status Solidi (b)*, 7(3):747–764, 1964.

[49] R. Liu, A. Bell, F. A. Ponce, C. Q. Chen, J. W. Yang, and M. A. Khan. Luminescence from stacking faults in gallium nitride. *Applied Physics Letters*, 86(2):021908–021908–3, 2005.

[50] M.A. Moram, C.F. Johnston, M.J. Kappers, and C.J. Humphreys. Investigating stacking faults in nonpolar gallium nitride films using x-ray diffraction. *Physica B: Condensed Matter*, 404(16):2189–2191, 2009.

[51] M. Barchuk, V. Hoy, D. Kriegner, J. Stangl, S. Schwaiger, and F. Scholz. Diffuse x-ray scattering from stacking faults in a-plane GaN epitaxial layers. *Physical Review B*, 84(9):094113, 2011.

[52] F. Ernst and P. Pirouz. The formation mechanism of planar defects in compound semiconductors grown epitaxially on {100} silicon substrates. *Journal of Materials Research*, 4(04):834–842, 1989.

[53] R. C. Blish and T. Vreeland. Dislocation velocity on the 221 113 slip systems of zinc. *Journal of Applied Physics*, 40(2):884–890, 1969.

[54] Y. Huang, H. Gao, W.D. Nix, and J.W. Hutchinson. Mechanism-based strain gradient plasticity-II analysis. *Journal of the Mechanics and Physics of Solids*, 48(1):99–128, 2000.

[55] R. Stradling and P. Klipstein. Growth and characterisation of semiconductors : papers contributing to a short course. *Adam Hilger, New York*, (1):1253, 1900.

[56] T. Sugahara, H. Sato, M. Hao, Y. Naoi, S. Kurai, S. Tottori, K. Yamashita, K. Nishino, L. T. Romano, and S. Sakai. Direct evidence that dislocations are non-radiative recombination centers in GaN. *Japanese Journal of Applied Physics*, 37(Part 2, No. 4A):L398–L400, 1998.

[57] T. Sugahara, M. Hao, T. Wang, D. Nakagawa, Y. Naoi, K. Nishino, and S. Sakai. Role of dislocation in InGaN phase separation. *Japanese Journal of Applied Physics*, 37(Part 2, No. 10B):L1195–L1198, 1998.

[58] V. Avrutin, D. J. Silversmith, Y. Mori, F. Kawamura, Y. Kitaoka, and H. Morkoc. Growth of bulk GaN and AlN: progress and challenges. *Proceedings of the IEEE*, 98(7):1302 –1315, 2010.

[59] K. Hiramatsu, S. Itoh, H. Amano, I. Akasaki, N. Kuwano, T. Shiraishi, and K. Oki. Growth mechanism of GaN grown on sapphire with A1N buffer layer by MOVPE. *Journal of Crystal Growth*, 115(1–4):628–633, 1991.

[60] F. Liu, R. Collazo, S. Mita, Z. Sitar, S. J. Pennycook, and G. Duscher. Direct observation of inversion domain boundaries of GaN on c-sapphire at sub-angstrom resolution. *Advanced Materials*, 20(11):2162–2165, 2008.

[61] M.A. Moram, M.J. Kappers, Z.H. Barber, and C.J. Humphreys. Growth of low dislocation density GaN using transition metal nitride masking layers. *Journal of Crystal Growth*, 298:268–271, 2007.

[62] J. Ha, H. Lee, S. Lee, H. Lee, S. Lee, H. Goto, M. Cho, T. Yao, S. Hong, R. Toba, J. Lee, and J. Lee. Reduction of dislocations in GaN films on AlN/sapphire templates using CrN nanoislands. *Applied Physics Letters*, 92(9):091906–091906–3, 2008.

[63] U. Ozgur, Y. Fu, Y. T. Moon, F. Yun, H. Morkoc, and H. O. Everitt. Increased carrier lifetimes in GaN epitaxial films grown using SiN and TiN porous network layers. *Journal of Applied Physics*, 97(10):103704–103704–6, 2005.

[64] J. Hertkorn, F. Lipski, Br&uuml, P. ckner, T. Wunderer, S. B. Thapa, F. Scholz, A. Chuvilin, U. Kaiser, M. Beer, and J. Zweck. Process optimization for the effective reduction of threading dislocations in MOVPE grown GaN using in situ deposited masks. *Journal of Crystal Growth*, 310(23):4867–4870, 2008.

[65] S. Tanaka, M. Takeuchi, and Y. Aoyagi. Anti surfactant in iii nitride epitaxy quantum dot formation and dislocation termination. *Japanese Journal of Applied Physics*, 39(Part 2, No. 8B):L831–L834, 2000.

[66] K. Forghani, M. Gharavipour, M. Klein, F. Scholz, O. Klein, U. Kaiser, M. Feneberg, B. Neuschl, and K. Thonke. In-situ deposited SiNx nanomask for crystal quality improvement in AlGaN. *Physica Status Solidi (c)*, 8(7-8):2063–2065, 2011.

[67] M. Barchuk, V. Holy, B. Miljevic, B. Krause, T. Baumbach, J. Hertkorn, and F. Scholz. X-ray diffuse scattering from threading dislocations in epitaxial gan layers. *Journal of Applied Physics*, 108(4):043521–043521–7, 2010.

[68] A.M. Roskowski, Edward A. Preble, Sven Einfeldt, P.M. Miraglia, and Robert F. Davis. Investigations regarding the maskless pendeo-epitaxial growth of GaN films prior to coalescence. *IEEE Journal of Quantum Electronics*, 38(8):1006–1016, 2002.

[69] B.B. Goldberg, M.S. Unlu, W. D. Herzog, H. F. Ghaemi, and E. Towe. Near-field optical studies of semiconductor heterostructures and laser diodes. *IEEE Journal of Selected Topics in Quantum Electronics*, 1(4):1073–1081, 1995.

[70] L. Kohl. *Transmission Electron Microscopy - Physics of Image Formation*. 2008.

[71] H. Sawada, Y. Tanishiro, N. Ohashi, T. Tomita, F. Hosokawa, T. Kaneyama, Y. Kondo, and K. Takayanagi. STEM imaging of 47-pm-separated atomic columns by a spherical aberration-corrected electron microscope with a 300-kV cold field emission gun. *Journal of Electron Microscopy*, 2009.

[72] L. F. Zagonel, S. Mazzucco, M. Tence, K. March, R. Bernard, B. Laslier, G. Jacopin, M. Tchernycheva, L. Rigutti, F. H. Julien, R. Songmuang, and M. Kociak. Nanometer scale spectral imaging of quantum emitters in nanowires and its correlation to their atomically resolved structure. *Nano Letters*, 11(2):568–573, 2011.

[73] M R Lorenz. Visible light from semiconductors: Luminescence from p-n junctions and potential uses of solid state light sources are discussed. *Science (New York, N.Y.)*, 159(3822):1419–1423, 1968.

[74] F. A. Ponce and D. P. Bour. Nitride based semiconductors for blue and green light-emitting devices. *Nature*, 386(6623):351–359, 1997.

[75] J. Als-Nielsen and D. McMorrow. *Elements of Modern X-ray Physics*. Wiley, 2 edition, April 2011.

[76] U. Pietsch, V. Holy, and T. Baumbach. *High-Resolution X-Ray Scattering: From Thin Films to Lateral Nanostructures*. Springer, August 2004.

[77] M. Schmidbauer. *X-Ray Diffuse Scattering from Self-Organized Mesoscopic Semiconductor Structures*. Springer, 2004.

[78] B. E Warren. *X-ray diffraction*. Addison-Wesley Pub. Co., Reading, Mass., 1969.

[79] O. Yefanov, V. Kladko, M. Slobodyan, and Y. Polischuk. An educational open-source program for demonstration of reciprocal-space construction and diffraction principles. *Journal of Applied Crystallography*, 41(3):647–652, 2008.

[80] O. Yefanov. Accessible reciprocal space region for non coplanar bragg and laue geometries. *Journal of Applied Crystallography*, 41(1):110–114, 2008.

[81] M. Laugt and V. Bousquet. Optimizing scans on asymmetric reflections. *Journal of Physics D: Applied Physics*, 32(10A):A32, 1999.

[82] P. Gay, P.B. Hirsch, and A. Kelly. The estimation of dislocation densities in metals from x-ray data. *Acta Metallurgica*, 1(3):315–319, 1953.

[83] G.K. Williamson and W.H. Hall. X-ray line broadening from filed aluminium and wolfram. *Acta Metallurgica*, 1(1):22–31, 1953.

[84] W. H. Hall. X-ray line broadening in metals. *Proceedings of the Physical Society. Section A*, 62(11):741–743, 1949.

[85] R. Chierchia, T. Boettcher, S. Figge, M. Diesselberg, H. Heinke, and D. Hommel. Mosaicity of gan epitaxial layers: Simulation and experiment. *Physica Status Solidi (b)*, 228(2):403–406, 2001.

[86] V. Srikant, J. S. Speck, and D. R. Clarke. Mosaic structure in epitaxial thin films having large lattice mismatch. *Journal of Applied Physics*, 82(9):4286–4295, 1997.

[87] S. R. Lee, A. M. West, A. A. Allerman, K. E. Waldrip, D. M. Follstaedt, P. P. Provencio, D. D. Koleske, and C. R. Abernathy. Effect of threading dislocations on the bragg peakwidths of gan, algan, and aln heterolayers. *Applied Physics Letters*, 86(24):241904–241904–3, 2005.

[88] R. Chierchia, T. Boettcher, H. Heinke, S. Einfeldt, S. Figge, and D. Hommel. Microstructure of heteroepitaxial GaN revealed by x-ray diffraction. *Journal of Applied Physics*, 93(11):8918–8925, 2003.

[89] T. Lafford, P. Parbrook, and B. Tanner. Direct, independent measurement of twist and tilt mosaic as a function of thickness in epitaxial gan. *Physica Status Solidi (c)*, 10(1):542–545, 2002.

[90] Y. Huang, H. Wang, Q. Sun, J. Chen, D.Y. Li, J. C. Zhang, J. F. Wang, Y.T. Wang, and H. Yang. Evolution of mosaic structure in inn grown by metalorganic chemical vapor deposition. *Journal of Crystal Growth*, 293(2):269–272, 2006.

[91] V. Holy, J. Kubena, E. Abramof, K. Lischka, A. Pesek, and E. Koppensteiner. X-ray double and triple crystal diffractometry of mosaic structure in heteroepitaxial layers. *Journal of Applied Physics*, 74(3):1736–1743, 1993.

[92] T. Metzger, R. Hopler, E. Born, O. Ambacher, M. Stutzmann, R. Stommer, M. Schuster, H. Gobel, S. Christiansen, M. Albrecht, and H. P. Strunk. Defect structure of epitaxial gan films determined by transmission electron microscopy and triple-axis x-ray diffractometry. *Phil. Mag. A*, (77):1013, 1998.

[93] V. M. Kaganer, O. Brandt, A. Trampert, and K. H. Ploog. X-ray diffraction peak profiles from threading dislocations in gan epitaxial films. *Physical Review B*, 72(4):045423, 2005.

[94] A. D. Kurtz, S. A. Kulin, and B. L. Averbach. Effect of dislocations on the minority carrier lifetime in semiconductors. *Physical Review*, 101(4):1285–1291, 1956.

[95] C.G Dunn and E.F Kogh. Comparison of dislocation densities of primary and secondary recrystallization grains of si-fe. *Acta Metallurgica*, 5(10):548–554, 1957.

[96] S. J. Shaibani and P. M. Hazzledine. The displacement and stress fields of a general dislocation close to a free surface of an isotropic solid. *Philosophical Magazine A*, 44(3):657–665, 1981.

[97] S. Lazarev, M. Barchuk, S. Bauer, K. Forghani, V. Holy, F. Scholz, and T. Baumbach. Study of threading dislocation density reduction in AlGaN epilayers by monte carlo simulation of high-resolution reciprocal-space maps of a two-layer system. *Journal of Applied Crystallography*, 46(1):120–127, 2012.

[98] S. Paduano, W. Weyburne, and J. Drehman. An x-ray diffraction technique for analyzing basal-plane stacking faults in GaN. *Physica Status Solidi (a)*, 207(11):2446–2455, 2010.

[99] M. M. Hall Jnr, V. G. Veeraraghavan, H. Rubin, and P. G. Winchell. The approximation of symmetric x-ray peaks by pearson type VII distributions. *Journal of Applied Crystallography*, 10(1):66–68, 1977.

[100] D. T. Gillespie. Markov processes: An introduction for physical scientists. *Academic Press, San Diego.*, 1992.

[101] M. Barchuk, V. Holy, B. Miljevic, B. Krause, and T. Baumbach. Grazing-incidence x-ray diffraction from GaN epitaxial layers with threading dislocations. *Applied Physics Letters*, 98(2):021912–021912–3, 2011.

[102] E. Monroy, F. Calle, J. L. Pau, F. J. Sanchez, E. Munoz, F. Omnes, B. Beaumont, and P. Gibart. Analysis and modeling of AlxGa1xNbased schottky barrier photodiodes. *Journal of Applied Physics*, 88(4):2081–2091, 2000.

[103] I. Ferguson, C.A. Tran, R.F. Karlicek Jr, Z.C. Feng, R. Stall, S Liang, Y. Lu, and C. Joseph. GaN and AlGaN metal semiconductor metal photodetectors. *Materials Science and Engineering: B*, 50(1–3):311–314, 1997.

[104] D. Walker, X. Zhang, P. Kung, A. Saxler, S. Javadpour, J. Xu, and M. Razeghi. AlGaN ultraviolet photoconductors grown on sapphire. *Applied Physics Letters*, 68(15):2100–2101, 1996.

[105] O. Klein, J. Biskupek, K. Forghani, F. Scholz, and U. Kaiser. TEM investigations on growth interrupted samples for the correlation of the dislocation propagation and growth mode variations in AlGaN deposited on SiNx interlayers. *Journal of Crystal Growth*, 324(1):63–72, 2011.

[106] N. Grandjean, J. Massies, I. Grezegory, and S. Porowski. GaN/AlGaN quantum wells for UV emission: heteroepitaxy versus homoepitaxy. *Semiconductor Science and Technology*, (5):2001.

[107] R. Dalmau, B. Moody, R. Schlesser, S. Mita, J. Xie, M. Feneberg, B. Neuschl, K. Thonke, R. Collazo, A. Rice, J. Tweedie, and Z. Sitar. Growth and characterization of AlN and AlGaN epitaxial films on AlN single crystal substrates. *ECS Transactions*, 33(13):43–54, 2010.

[108] S. Kamiyama, M. Iwaya, S. Takanami, S. Terao, A. Miyazaki, H. Amano, and I. Akasaki. UV light-emitting diode fabricated on heteroelogrown Al0.22Ga0.78N with low dislocation density. *Physica Status Solidi (a)*, 192(2):296–300, 2002.

[109] T. Paskova, D.A. Hanser, and K.R. Evans. Gan substrates for iii-nitride devices. *Proceedings of the IEEE*, 98(7):1324 –1338, 2010.

[110] S.k. Mathis, A.e. Romanov, L.f. Chen, G.e. Beltz, W. Pompe, and J.s. Speck. Modeling of threading dislocation reduction in growing GaN layers. *Physica Status Solidi (a)*, 179(1):125–145, 2000.

[111] H.Z Xu, K Takahashi, C.X Wang, Z.G Wang, Y Okada, M Kawabe, I Harrison, and C.T Foxon. Effect of in situ thermal treatment during growth on crystal quality of gan epilayer grown on sapphire substrate by movpe. *Journal of Crystal Growth*, 222(1–2):110–117, 2001.

[112] S. B. Thapa, J. Hertkorn, F. Scholz, G. M. Prinz, M. Feneberg, M. Schirra, K. Thonke, R. Sauer, J. Biskupek, and U. Kaiser. MOVPE growth of high quality AlN layers and effects of si doping. *Physica Status Solidi (c)*, 5(6):1774–1776, 2008.

[113] H. Hirayama, S. Fujikawa, J. Norimatsu, T. Takano, K. Tsubaki, and N. Kamata. Fabrication of a low threading dislocation density ELO-AlN template for application to deep-UV LEDs. *Physica Status Solidi (c)*, 6(S2):S356–S359, 2009.

[114] H. Amano, T. Takeuchi, S. Sota, H. Sakai, and I. Akasaki. Structural and optical properties of nitride-based heterostructure and quantum-well structure. *MRS Online Proceedings Library*, 449, 1996.

[115] S. R. Lee, D. D. Koleske, K. C. Cross, J. A. Floro, K. E. Waldrip, A. T. Wise, and S. Mahajan. In situ measurements of the critical thickness for strain relaxation in algan gan heterostructures. *Applied Physics Letters*, 85(25):6164–6166, 2004.

[116] Y. Golan, X. H. Wu, J. S. Speck, R. P. Vaudo, and V. M. Phanse. Morphology and microstructural evolution in the early stages of hydride vapor phase epitaxy of GaN on sapphire. *Applied Physics Letters*, 73(21):3090 –3092, 1998.

[117] P. R. Tavernier, E. V. Etzkorn, Y. Wang, and D. R. Clarke. Two-step growth of high-quality GaN by hydride vapor-phase epitaxy. *Applied Physics Letters*, 77(12):1804–1806, 2000.

[118] T. Paskova, P. Paskov, V. Darakchieva, S. Tungasmita, J. Birch, and B. Monemar. Defect reduction in HVPE growth of GaN and related optical spectra. *Physica Status Solidi (a)*, 183(1):197–203, 2001.

[119] K. Engl, M. Beer, N. Gmeinwieser, U. T. Schwarz, J. Zweck, W. Wegscheider, S. Miller, A. Miler, H. J. Lugauer, and G. Bruderl. Influence of an in situ-deposited SiNx intermediate layer inside GaN and AlGaN layers on SiC substrates. *Journal of crystal growth*, 289(1):6–13, 2006.

[120] K. Forghani, M. Klein, F. Lipski, S. Schwaiger, J. Hertkorn, R.A.R. Leute, F. Scholz, M. Feneberg, B. Neuschl, K. Thonke, O. Klein, U. Kaiser, R. Gutt, and T. Passow. High quality AlGaN epilayers grown on sapphire using SiNx interlayers. *Journal of Crystal Growth*, 315(1):216–219, 2011.

[121] B. Neuschl, K. J. Fujan, M. Feneberg, I. Tischer, K. Thonke, K. Forghani, M. Klein, and F. Scholz. Cathodoluminescence and photoluminescence study on AlGaN layers grown with SiNx interlayers. *Applied Physics Letters*, 97(19):192108–192108–3, 2010.

[122] A. Bergamaschi, A. Cervellino, R. Dinapoli, F. Gozzo, B. Henrich, I. Johnson, P. Kraft, A. Mozzanica, B. Schmitt, and X. Shi. The MYTHEN detector for x-ray powder diffraction experiments at the swiss light source. *Journal of Synchrotron Radiation*, 17(5):653–668, 2010.

[123] S. Lazarev, S. Bauer, K. Forghani, M. Barchuk, F. Scholz, and T. Baumbach. High resolution synchrotron x-ray studies of phase separation phenomena and the scaling law for the threading dislocation densities reduction in high quality AlGaN heterostructure. *Journal of Crystal Growth*, 2012.

[124] H. Dosch, B. W. Batterman, and D. C. Wack. Depth-controlled grazing-incidence diffraction of synchrotron x radiation. *Physical Review Letters*, 56(11):1144–1147, 1986.

[125] O. Klein, J. Biskupek, U. Kaiser, K. Forghani, S. B. Thapa, and F. Scholz. Simulation supported analysis of the effect of SiNx interlayers in AlGaN on the dislocation density reduction. *Journal of Physics: Conference Series*, 209(1):012018, 2010.

[126] A. E. Romanov, W. Pompe, S. Mathis, G. E. Beltz, and J. S. Speck. Threading dislocation reduction in strained layers. *Journal of Applied Physics*, 85(1):182–192, 1999.

[127] J.E. Ayers. The measurement of threading dislocation densities in semiconductor crystals by x-ray diffraction. *Journal of Crystal Growth*, 135(1–2):71–77, 1994.

[128] M. Asif Khan, M. Shatalov, H. P. Maruska, H. M. Wang, and E. Kuokstis. III-Nitride UV devices. *Japanese Journal of Applied Physics*, 44(10):7191–7206, 2005.

[129] D. A. B. Miller, D. S. Chemla, T. C. Damen, A. C. Gossard, W. Wiegmann, T. H. Wood, and C. A. Burrus. Electric field dependence of optical absorption near the band gap of quantum-well structures. *Physical Review B*, 32(2):1043–1060, 1985.

[130] K. Horino, A. Kuramata, K. Domen, R. Soejima, and T. Tanahashi. Growth of (1100) oriented gan on (1100) 6h-sic by metalorganic vapor phase epitaxy. *Proc. Int. Symp. on Blue Laser and Light Emitting Diodes (Chiba, Japan)*, 71(14):530–533, 1996.

[131] K. Domen, K. Horino, A. Kuramata, and T. Tanahashi. Analysis of polarization anisotropy along the c axis in the photoluminescence of wurtzite GaN. *Applied Physics Letters*, 71(14):1996–1998, 1997.

[132] S. Schwaiger, F. Lipski, Th. Wunderer, and F. Scholz. Influence of slight misorientations of r-plane sapphire substrates on the growth of nonpolar a -plane GaN layers via HVPE. *Physica Status Solidi (c)*, 7(7-8):2069–2072, 2010.

[133] T. J. Baker, B. A. Haskell, F. Wu, P. T. Fini, J. S. Speck, and S. Nakamura. Characterization of planar semipolar gallium nitride films on spinel substrates. *Japanese Journal of Applied Physics*, 44(29):L920–L922, 2005.

[134] J. Hertkorn, P. Brückner, S.B. Thapa, T. Wunderer, F. Scholz, M. Feneberg, K. Thonke, R. Sauer, M. Beer, and J. Zweck. Optimization of nucleation and buffer layer growth for improved GaN quality. *Journal of Crystal Growth*, 308(1):30–36, 2007.

[135] B. B. He. *Two-Dimensional X-Ray Diffraction*. November 2009.

[136] V. Kachkanov, I. P. Dolbnya, K. P. O Donnell, R. W. Martin, P. R. Edwards, and S. Pereira. InGaN epilayer characterization by microfocused x-ray reciprocal space mapping. *Applied Physics Letters*, 99(18):181909–181909–3, 2011.

[137] V. Nazmov, E. Reznikova, M. Boerner, J. Mohr, V. Saile, A. Snigirev, I. Snigireva, M. DiMichiel, M. Drakopoulos, R. Simon, and M. Grigoriev. Refractive lenses fabricated by deep SR lithography and LIGA technology for xray energies from 1 keV to 1 MeV. *AIP Conference Proceedings*, 705(1):752–755, 2004.

[138] V. Nazmov, E. Reznikova, A. Last, J. Mohr, V. Saile, R. Simon, and M. DiMichiel. X-ray lenses fabricated by liga technology. *AIP Conference Proceedings*, 879(1):770–773, 2007.

[139] A. A. Snigirev, I. Snigireva, M. Drakopoulos, V. Nazmov, E. Reznikova, S. Kuznetsov, M. Grigoriev, J. Mohr, and V. Saile. Focusing properties of x-ray polymer refractive lenses from SU-8 resist layer. pages 21–31, 2003.

[140] P. Kraft, A. Bergamaschi, Ch. Broennimann, R. Dinapoli, E. F. Eikenberry, B. Henrich, I. Johnson, A. Mozzanica, C. M. Schleputz, P. R. Willmott, and B. Schmitt. Performance of single-photon-counting PILATUS detector modules. *Journal of Synchrotron Radiation*, 16(Pt 3):368–375, 2009.

[141] J. Marchal, B. Luethi, C. Ursachi, V. Mykhaylyk, and A. Wagner. Low-energy x-ray detection with an in-vacuum PILATUS detector. *Journal of Instrumentation*, 6(11):C11033, 2011.

A. Apendix

List of Acronyms

AFM atomic force microscopy
ANKA Angströmquelle Karlsruhe
AXRD asymmetrical X-ray diffraction
CCD charge coupled device
CL cathodoluminscence
CTR crystal truncation rod
DCM double crystal monochromator
DWBA distorted wave Born approximation
EQE external quantum efficiency
ELO epitaxial layer overgrowth
EPD etch pit density
FWHM full width at the half maximum
GID grazing incidence diffraction
GISAXS grazing incidence small angle X-ray scattering
HRTEM high resolution transmission electron microscopy
HRXRD high resolution X-ray diffraction HVPE hydride vapour phase epitaxy
LD laser diode
LED light emitting diode
MBE molecular beam epitaxy
MOCVD metal-organic chemical vapour deposition
MOVPE metal-organic vapour phase epitaxy
OMVPE organometallic vapour-phase epitaxy
PL photoluminescence
PSD position sensitive detector
QD quantum dot
QW quantum well
RSM reciprocal space map
SAXS small angle X-ray scattering
SCD single crystal diffraction
SEM scanning electron microscopy
SXRD symmetrical X-ray diffraction
TEA triethylaluminium
TEG triethylgallium
TEI triethylindium
TEM transmission electron microscopy
TER total external reflection
TMA trimethylaluminium
TMG trimethylgallium
TMI trimethylindium
UHV ultra high vacuum
XRD X-ray diffraction
XRR X-ray reflectivity